

Edited by
S. C. Singhal

SOLID OXIDE FUEL CELLS

PV89-11

PROCEEDINGS OF
THE FIRST INTERNATIONAL SYMPOSIUM ON

SOLID OXIDE FUEL CELLS

Edited by

Subhash C. Singhal
Westinghouse Research and Development Center
Pittsburgh, Pennsylvania



HIGH TEMPERATURE MATERIALS DIVISION

Proceedings Volume 89-11

THE ELECTROCHEMICAL SOCIETY, INC., 10 South Main St., Pennington, NJ 08534-2896

PROCEEDINGS OF
THE FIRST INTERNATIONAL SYMPOSIUM ON

SOLID OXIDE FUEL CELLS

Edited by

Subhash C. Singhal
Westinghouse Research and Development Center
Pittsburgh, Pennsylvania



HIGH TEMPERATURE MATERIALS DIVISION

Proceedings Volume 89-11

THE ELECTROCHEMICAL SOCIETY, INC., 10 South Main St., Pennington, NJ 08534-2896

Copyright 1989

by

The Electrochemical Society, Incorporated

***Papers contained herein may not be
reprinted and may not be digested by pub-
lications other than those of The Electrochemical
Society in excess of 1/6 of the material presented.***

Library of Congress Catalog Number: 89-85689

Printed in the United States of America

PREFACE

This book contains 33 of the 39 papers presented at the First International Symposium on Solid Oxide Fuel Cells, held at the 176th meeting of the Electrochemical Society in Hollywood, Florida, October 16-18, 1989. These papers represent contributions from authors in several countries, including U.S.A., Japan, The Netherlands, Denmark, France and England, reflecting the widening world-wide interest in solid oxide fuel cells. High-temperature solid oxide fuel cells based on yttria-stabilized zirconia electrolyte have progressed to the point where they are being considered for large-scale power generation by both gas and electric utilities. This symposium attempted to present state-of-the-art knowledge on materials for different cell components as well as on design and performance of different type of solid oxide fuel cells.

The first part of the book covers papers on electrolyte materials and processing. Though majority of the papers in this part deal with yttria-stabilized zirconia electrolyte, papers on few other types of oxygen ion conductors are also included.

The second part of the book presents information on materials and processing of electrodes and interconnection. This part also incorporates papers dealing with interactions at the electrolyte/electrode interfaces.

The remaining three parts of the book deal with design and performance of three different types of solid oxide fuel cells: tubular, monolithic and planar. Taken together, the papers in the book represent a comprehensive sample of the current research in the field of high-temperature solid oxide fuel cells.

I would like to extend my appreciation to Ronak Singhal for compiling the indexes, and to Mrs. Janice Radford for her dedicated efforts with the organization of the symposium and the compilation of the book.

Subhash C. Singhal

Westinghouse R&D Center
Pittsburgh, Pennsylvania

July 1989

TABLE OF CONTENTS

Preface.....	iii
--------------	-----

ELECTROLYTE MATERIALS AND PROCESSING

Effect of Alumina Additions on the Electrical Properties of Yttria-Doped Zirconia.....	3
<i>F. Ishizaki, T. Yoshida and S. Sakurada</i>	
Solid State Oxygen Kinetics in Er_2O_3 Stabilized Bi_2O_3	15
<i>E. D. Wachsman, N. Jiang, D. M. Mason and D. A. Stevenson</i>	
Evaluation of Solid Oxide Electrolytes with the Pyrochlore Structure for Use in Fuel Cells.....	30
<i>P. K. Moon and H. L. Tuller</i>	
Electrochemical Vapor Deposition of Yttria-Stabilized Zirconia Films.....	41
<i>U. B. Pal and S. C. Singhal</i>	
Electrochemical Vapor Deposition of SOFC Components.....	57
<i>J. P. Dekker, N. J. Kwiwet and J. Schoonman</i>	
Thin Electrolyte Layers for SOFC Via Modification of Ceramic Membranes by CVD and EVD.....	67
<i>Y. S. Lin, L. G. J. de Haart, K. J. de Vries and A. J. Burggraaf</i>	
Characteristics of Electrolyte Processed by CO_2 Laser Evaporation Techniques.....	71
<i>H. Nakagawa, S. Kosuge, H. Tsuneizumi, E. Matsuda, H. Mihara and Y. Sato</i>	

ELECTRODES AND INTERCONNECTION MATERIALS AND PROCESSING

Mixed-Conducting Oxide Electrodes for Solid Oxide Fuel Cells.....	81
<i>S. S. Liou and W. L. Worrell</i>	
Morphology and Electrochemistry of Porous Nickel/Zirconia Cermets.....	90
<i>P. H. Middleton, M. E. Seiersten and B. C. H. Steele</i>	

Oxidation of Methane on Oxide Electrodes at 800-1000°C.....	99
<i>M. Mogensen and J. J. Bentzen</i>	
Review of Defect Chemistry of LaMnO_3 and LaCrO_3	111
<i>H. U. Anderson, J. H. Kuo and D. M. Sparlin</i>	
Thermal Expansion Studies on Cathode and Interconnect Oxides.....	129
<i>S. Srilomsak, D. P. Schilling and H. U. Anderson</i>	
Solid Oxide Fuel Cell Electrodes Based on $\text{In}_2\text{O}_3\text{-PrO}_{1.83}\text{-ZrO}_2$	141
<i>J. L. Bates, W. J. Weber and C. W. Griffin</i>	
Strontium-Doped Lanthanum Copper Oxide as a Solid Oxide Fuel Cell Cathode Material.....	157
<i>M. A. Priestnall and B. C. H. Steele</i>	
Synthesis of Air-Sinterable Lanthanum Chromite Powders.....	170
<i>L. A. Chick, J. L. Bates, L. R. Pederson and H. E. Kissinger</i>	
Preparation of LaMnO_3 Thin Film Electrode for Solid Oxide Fuel Cells by Vacuum Evaporation.....	188
<i>H. Michibata, H. Tenmei, T. Namikawa and Y. Yamazaki</i>	
Deposition and Electrical Properties of Thin Porous Ceramic Electrode Layers.....	197
<i>L. G. J. de Haart, R. A. Kuipers, K. J. de Vries and A. J. Burggraaf</i>	
Effect of Pt Additions on the Resistance of $\text{La}_{0.9}\text{Sr}_{0.1}\text{MnO}_3$ Cathode.....	204
<i>A. Tsunoda, T. Yoshida and S. Sakurada</i>	
Measurement of the Chemical Diffusion Coefficient of Oxygen in $(\text{La}_{0.79}\text{Sr}_{0.20})\text{MnO}_{3-\delta}$	214
<i>A. Belzner, T. M. Gur and R. A. Huggins</i>	
Structural, Sintering and Electrical Properties of the Perovskite-Type $(\text{La,Sr})(\text{Cr,Mn})\text{O}_3$	220
<i>R. Koc, H. U. Anderson, S. A. Howard and D. M. Sparlin</i>	
Stability of Perovskite Oxide Electrode with Stabilized Zirconia.....	242
<i>O. Yamamoto, Y. Takeda, R. Kanno and T. Kojima</i>	
Reaction Kinetics and Microstructure of $\text{La}_{0.6}\text{Ca}_{0.4}\text{MnO}_3/\text{YSZ}$ Air Electrode.....	254
<i>J. Mizusaki, H. Tagawa, K. Tsuneyoshi and A. Sawata</i>	

Oxygen Reduction at the $\text{La}_{1-x}\text{Sr}_x\text{MnO}_3$ /Zirconia Electrode.....	265
<i>A. Hammouche, E. Siebert, M. Kleitz and A. Hammou</i>	

TUBULAR SOLID OXIDE FUEL CELLS

Design and Performance of Tubular Solid Oxide Fuel Cells.....	279
<i>N. J. Maskalick</i>	
Thin Film Solid Oxide Fuel Cells with ZrO_2 - and CeO_2 -Based Electrolytes.....	288
<i>H. Arai, K. Eguchi, T. Setoguchi, H. Itoh and T. Inoue</i>	
Temperature Distribution in Tubular Solid Oxide Fuel Cell.....	293
<i>K. Kanamura, S. Yoshioka and Z. Takehara</i>	

MONOLITHIC SOLID OXIDE FUEL CELLS

Forming and Processing of Monolithic Solid Oxide Fuel Cells.....	307
<i>N. Q. Minh, C. R. Horne, F. Liu, P. R. Staszak, T. L. Stillwagon and J. J. Van Ackeren</i>	
Interfacial Effects in Monolithic Solid Oxide Fuel Cells.....	317
<i>D. W. Dees, U. Balachandran, S. E. Dorris, J. J. Heiberger, C. C. McPheeters and J. J. Picciolo</i>	

PLANAR SOLID OXIDE FUEL CELLS

Overview of Planar SOFC Development at NCLL.....	325
<i>M. Dokiya, N. Sakai, T. Kawada, H. Yokokawa, T. Iwata and M. Mori</i>	
Fabrication Technologies for a Planar Solid Oxide Fuel Cell.....	337
<i>P. A. Lessing, L. W. Tai and K. A. Klemm</i>	
Fabrication of Integral Flow-Field/Interconnects for Planar SOFC Stacks.....	361
<i>C. Milliken and A. Khandkar</i>	
Electrode Performance at Planar SOFC Interfaces.....	377
<i>A. Khandkar, K. L. Stuffle and S. Elangovan</i>	

GENERAL

The Present State of SOFC in Japan..... 387
T. Yazawa

Subject Index..... 395

Author Index..... 399

**ELECTROLYTE
MATERIALS AND PROCESSING**

EFFECT OF ALUMINA ADDITIONS ON THE ELECTRICAL
PROPERTIES OF YTTRIA DOPED ZIRCONIA

F. Ishizaki, T. Yoshida and S. Sakurada
Corporate Research and Development Laboratory
Toa Nenryo Kogyo K.K.
3-1 Nishi-tsurugaoka 1-chome, Ohi-machi,
Iruma-gun, Saitama-ken, Japan 354

ABSTRACT

The effect of alumina additions to yttria fully stabilized zirconia (Y-FSZ) has been studied on the microstructure, electrical resistivity, mechanical strength and fuel cell performance. Alumina added Y-FSZ (AAZ) was just a physical mixture. The grain size of Y-FSZ in AAZ reduced with increase in alumina content. The electrical resistivity of AAZ increased with reducing the grain size of Y-FSZ and with increase in volume fraction of alumina. The mechanical strength of AAZ increased with increase in alumina content and was related to the grain size of alumina. The fuel cell performance was determined by the electrical resistivity of AAZ, and AAZ was very stable for use in SOFC. These results indicate that alumina addition to Y-FSZ could provide a self-supported SOFC electrolyte.

INTRODUCTION

In general, fully stabilized zirconia (FSZ) is used as an SOFC electrolyte. But FSZ is mechanically weak, so a porous tube is usually necessary to support FSZ electrolyte when FSZ is used in SOFC. But a support tube prevents an SOFC from improving the volumetric power density, so a self-supported SOFC electrolyte is needed.

On the contrary, partially stabilized zirconia (PSZ) is mechanically very strong but the electrical conductivity of PSZ is fairly inferior to that of FSZ. In our laboratory, PSZ has been studied as an SOFC electrolyte because of the mechanical strength and good performance has been obtained to a certain extent. But PSZ's stability for use in SOFC is not clear at present, and hence, for now, FSZ is the material of choice for an SOFC electrolyte.

Therefore, alumina addition to FSZ was considered in order to improve the mechanical strength of FSZ. Few studies on alumina addition to FSZ have been reported (1-3). In this paper, the effect of alumina additions on electrical resistivity, mechanical strength

and fuel cell performance of FSZ is studied, especially from the standpoint of use as an SOFC electrolyte.

EXPERIMENTAL

Commercial yttria fully stabilized zirconia (Y-FSZ) and alpha-alumina were used as raw materials. Y-FSZ powder contained 7.92mol% yttria and had purity of over 99.9wt%, average particle size of 0.3 μm and specific surface area of 15m²/g. Alumina powder had over 99.99wt%, 0.2 μm and 14m²/g.

Mixed powders of Y-FSZ and alumina were obtained by drying the mixed slurries after milling in a ball mill with ethanol. The tablets (20mm diam. x 3.5mm thickness) of the powders were prepared by pressing at 300kg/cm². They were sintered at 1700°C in air for 3hours.

The density of a sintered tablet was calculated from the volume and weight. The crystal structure was determined by X-ray diffraction (XRD) analysis. The morphology of alumina added Y-FSZ (AAZ) was observed by energy dispersion X-ray (EDX) spectrometry and scanning electron microscopy (SEM).

The electrical resistivity of a tablet was measured by AC impedance method, using YHP 4194A. The electrode preparation procedures are described elsewhere (4).

Sheets of AAZ were fabricated for measurements of bending strength and fuel cell performance. Sheets (25mm diam. x 0.1-0.3mm thickness) of the mixed powders were prepared by doctor blade method, sintering the green sheets at 1700°C in air for 3hours.

The bending strength measurement of a sintered sheet was made by the following method. A sintered sheet was set on the special stand shown in Fig.1. The center of the sheet was slowly pushed by a metal rod of 3mm diam. and the data were obtained from the weight just before the sheets were destroyed.

The electrolyte property of an AAZ sheet was studied on V-I characteristic and current interrupted curve by making a fuel cell. Nickel/zirconia cermet was used as an anode and lanthanum manganese oxide as a cathode, respectively. Hydrogen was supplied to the anodic side of the fuel cell and oxygen to the cathodic side, respectively. The measurement procedures are described elsewhere (5).

RESULTS AND DISCUSSION

The XRD pattern of an AAZ is shown in Fig.2. In this pattern, only peaks of cubic-zirconia and alpha-alumina were found. This indicated that Y-FSZ and alumina did not react with each other. The EDX spectrometry showed that Y-FSZ grains and alumina grains existed independently and that Y-FSZ and alumina did not dissolve each other. These results mean that Y-FSZ and alumina system is stable just as a physical mixture within the fabrication conditions used.

The effect of alumina content on the sintered density of AAZ is shown in Fig.3. The measured densities (open circles) were in good agreement with those of the theoretical curve. These data indicated that the tablets were densified well.

The scanning electron micrographs of base Y-FSZ and AAZ are shown in Fig.4. By the EDX spectrometry, it was confirmed that white grains were Y-FSZ and black grains were alumina. It was revealed from Fig.4, that the grain size of Y-FSZ was reduced by alumina addition and showed more effective results with increase in alumina content. In other words, alumina addition to Y-FSZ controlled the growth of Y-FSZ grains. On the contrary, the grain size of alumina remained constant and independent of alumina content. Fig.5 shows the effect of alumina content on the grain sizes of Y-FSZ and alumina, of which average grain sizes were determined from Fig.4. It shows that an addition of more than 30wt% alumina is not very effective in controlling Y-FSZ grain size in AAZ.

The electrical resistivities of AAZ's as a function of the temperature are shown in Fig.6; the electrical resistivity increased with increase in alumina content. In Table 1, the electrical resistivities at 1000°C are shown. The electrical resistivity is a very important factor from the standpoint of using AAZ as an SOFC electrolyte. At first, the increase in electrical resistivity caused by bulk was considered. From Fig.4, the morphology of alumina in AAZ was regarded as the isolated spherical particles which dispersed well in Y-FSZ. In such a case, the electrical resistivity should be inversely proportional to the volume fraction of Y-FSZ (6). In Table 1, the corrected electrical resistivities R_0/x are shown, where R_0 is the electrical resistivity of base Y-FSZ and x is the volume fraction of Y-FSZ in AAZ. The measured electrical resistivities were larger than those corrected by the volume fraction of Y-FSZ in AAZ.

The increase in electrical resistivity caused by grain boundary was considered for the difference between the measured electrical resistivity and the corrected value. This resistivity increased with increase in grain boundary by reduction of Y-FSZ grain size. Although grain boundary exists in three dimensions, it was assumed that only

one dimension affected the grain boundary electrical resistivity; the two other dimensions which are parallel to the current should not affect this resistivity. It was shown in Fig.7, that the difference between the measured electrical resistivity and the corrected value was proportional to the increase in G_{So}/G_S , where G_{So} is Y-FSZ grain size in base Y-FSZ and G_S is Y-FSZ grain size in AAZ. G_{So}/G_S-1 expresses the increase in grain boundary. These data revealed that the difference between the measured electrical resistivity and the corrected value was due to the increase in grain boundary.

These results show that the increase in electrical resistivity of AAZ is related to the decrease in volume fraction of Y-FSZ and the increase in grain boundary. In other words, the electrical resistivity of AAZ is determined by the alumina content and the grain size of Y-FSZ.

The bending strength of AAZ sheets as a function of thickness is shown in Fig.8. It showed that the bending strength increased with increase in alumina content and that the bending strength was proportional to the square of the thickness.

The relation between the alumina content and the increase in bending strength is shown in Fig.9. It shows that the increase in bending strength is proportional to the alumina content. F.J.Esper et al. have reported that the bending strength of AAZ is determined by the lattice distortions of Y-FSZ and alumina (3). When it is assumed that the lattice distortions occur at the interface between Y-FSZ grains and alumina grains, the bending strength is proportional to the alumina content. It is suggested that the bending strength of AAZ will be increased by smaller grain size of alumina. These results show that alumina addition to Y-FSZ is very effective in improving the bending strength.

The results of the electrical resistivity measurements and the bending strength measurements suggest that alumina addition to Y-FSZ can improve the mechanical strength without large decrease in electrical resistivity. From the standpoint of assembling an SOFC, Y-FSZ electrolyte must be handled carefully because of being very brittle, however, AAZ can play an important role in preparing a self-supported SOFC electrolyte. Therefore, the performance of fuel cells using AAZ sheets was examined in order to check the effect of alumina addition to Y-FSZ.

The V-I characteristic and current interrupted curve are shown in Fig.10. The fuel cells used electrolyte sheets of 0.24mm thickness and had cell area of 0.5cm². V-I characteristic is the performance represented by IR loss and polarization loss. Current interrupted curve includes only polarization loss. That is, the difference

between the V-I characteristic and current interrupted curve indicates IR loss. Reproducibility of making fuel cells was very good, because the current interrupted curves and open circuit voltages corresponded very well.

The fuel cell performances at the current of 1A (current density of $2A/cm^2$) are shown in Table 2. The voltage of V-I characteristic decreased with increase in alumina content and the current interrupted voltage was 1.03V. Therefore, the differences between 1.03V and the voltage of V-I characteristic show IR losses at current of 1A. Table 2 also shows the ohmic resistances obtained by IR loss and the electrolyte resistances calculated by the electrical resistivity in Table 1. The ohmic resistance includes the resistances of the electrolyte and electrodes. The ohmic resistances were a little larger than the electrolyte resistances and the differences showed mostly constant values, 50-60m Ω . This means that the difference is the electrodes' resistance and is not caused by alumina addition.

These results show that the fuel cell performance using AAZ depends mainly on the electrical resistances of AAZ electrolyte and electrodes. Therefore, alumina addition to Y-FSZ has no effect on the fuel cell performance, except increasing the electrical resistance of AAZ electrolyte. Also, alumina addition to Y-FSZ improves the mechanical strength.

The above results show that alumina addition to Y-FSZ can provide a self-supported SOFC electrolyte. Especially, AAZ which has less grain boundary of Y-FSZ and smaller grain size of alumina is desirable.

CONCLUSIONS

1. AAZ system was just a physical mixture of Y-FSZ grains and alumina grains.
2. The grain size of Y-FSZ in AAZ reduced with increase in alumina content. The grain size of alumina did not depend on alumina content.
3. The electrical resistivity of Y-FSZ was increased by alumina addition. The electrical resistivity of AAZ depended on the alumina content and the grain size of Y-FSZ.
4. The mechanical strength of Y-FSZ was increased by alumina addition. The mechanical strength of AAZ was related to the grain size of alumina.

5. The fuel cell performance was determined by the electrical resistivity of AAZ, and AAZ system was very stable when it was used as an SOFC electrolyte.
6. Alumina addition to Y-FSZ could provide a self-supported SOFC electrolyte, which has enough mechanical strength and electrical conductivity.

ACKNOWLEDGEMENT

This work was supported by the Petroleum Energy Center.

REFERENCES

1. E.P.Butler, R.K.Slotwinski, N.Bonanos, J.Drennan and B.C.H.Steele, *Adv. Ceram.*, 12(*Sci. Technol. Zirconia 2*), 572-84 (1984)
2. M.Miyayama, H.Yanagida and A.Asada, *Am. Ceram. Soc. Bull.*, 65(4), 660-4 (1986)
3. F.J.Esper, K.H.Friese and H.Geier, *Adv. Ceram.*, 12(*Sci. Technol. Zirconia 2*), 528-36 (1984)
4. J.E.Bauerle, *J. Phys. Chem. Solids*, 30, 2657-70 (1969)
5. T.Yoshida, T.Hoshina, I.Mukaizawa and S.Sakurada, to be published in *J. Electrochem. Soc.*
6. W.D.Kingery, H.K.Bowen and D.R.Uhlmann, "Introduction to Ceramics," 2nd ed., 518, 634, Wiley-Interscience, New York (1976)

Table 1 Electrical Resistivity of AAZ at 1000°C

Alumina Content [wt%]	0	10	20	30
Electrical Resistivity at 1000°C ; R [Ω cm]	5.84	8.76	11.01	14.83
Volume Fraction of Y-FSZ ; x [-]	1.000	0.875	0.727	0.609
Corrected Electrical Resistivity ; Ro/x [Ω cm]	(5.84)	6.81	8.03	9.59
R-Ro/x [Ω cm]	(0)	1.95	2.98	5.24
Grain Size of Y-FSZ ; GS [μ m]	11.2	3.07	1.63	1.21
GSo/GS-1	(0)	2.65	5.87	8.26

Table 2 Performance of Fuel Cell using AAZ sheet at Current of 1A

Alumina Content [wt%]	0	10	20
Voltage of V-I Characteristic [V]	0.70	0.55	0.44
Current Interrupted Voltage [V]	1.03	1.03	1.03
IR loss [V]	0.33	0.48	0.59
Ohmic Resistance of Cell [$m\Omega$]	330	480	590
Electrolyte Resistance [$m\Omega$]	281	421	529

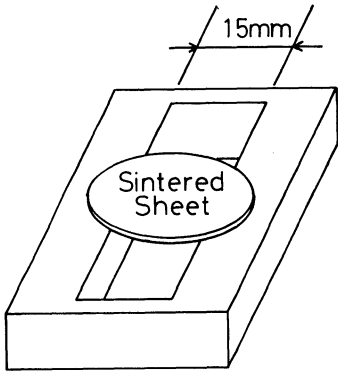


Fig.1 Illustration of Special Stand for Bending Strength Measurement

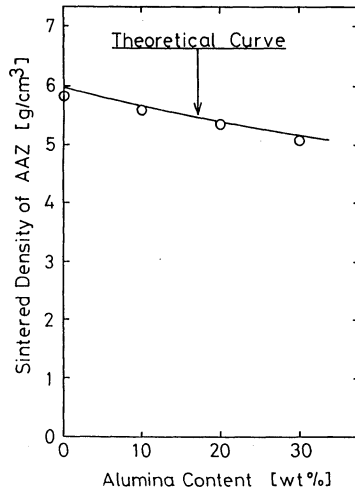


Fig.3 Effect of Alumina Content on Sintered Density of AAZ

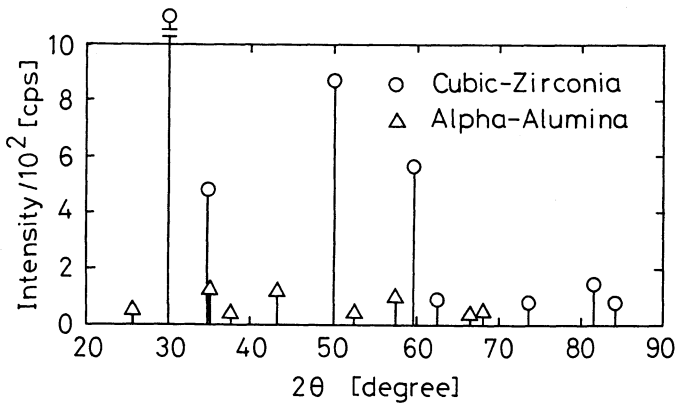
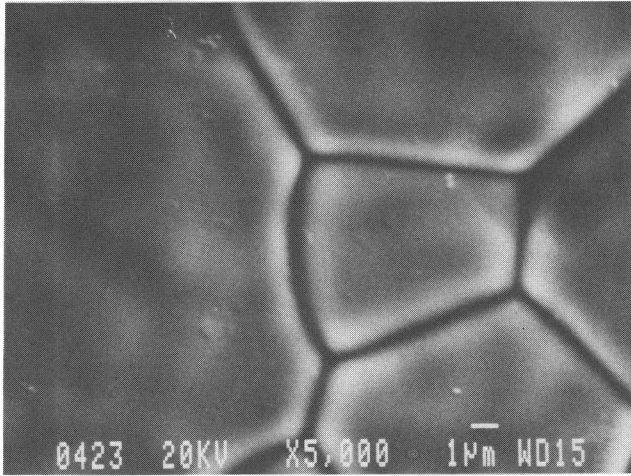
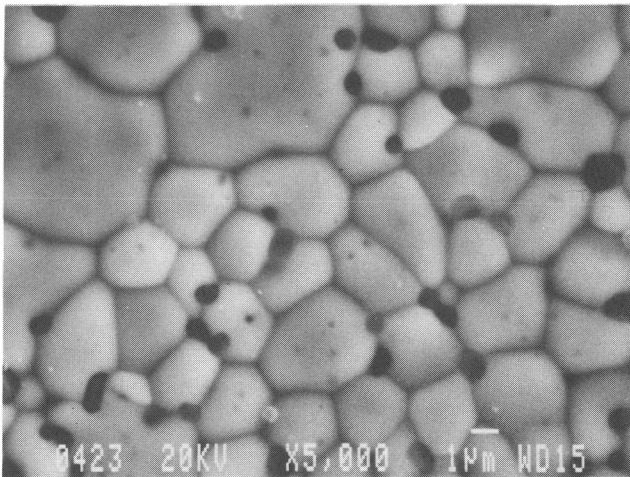


Fig.2 XRD Pattern of AAZ

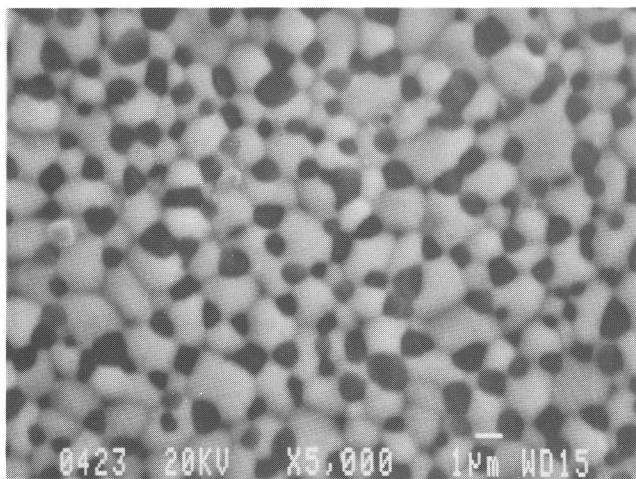


(a) Y-FSZ

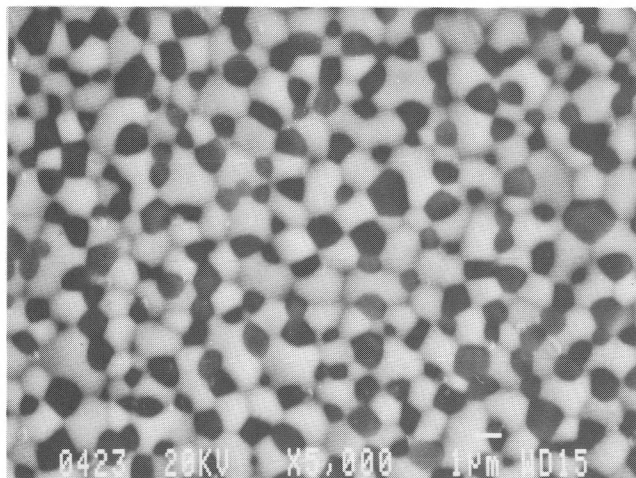


(b) 10wt%-AAZ

Fig.4 Scanning Electron Micrographs of Y-FSZ and AAZ



(c) 20wt%-AAZ



(d) 30wt%-AAZ

Fig.4 Scanning Electron Micrographs of Y-FSZ and AAZ

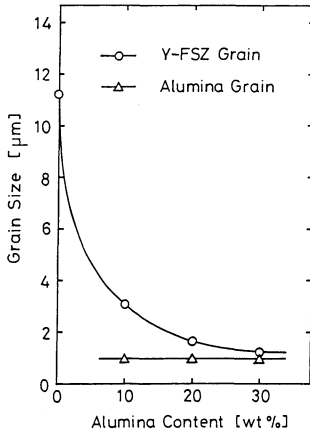


Fig.5 Effect of Alumina Content on Grain Size of Y-FSZ and Alumina in AAZ

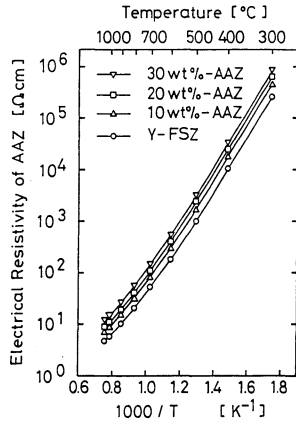


Fig.6 Effect of Alumina Content on Electrical Resistivity of AAZ

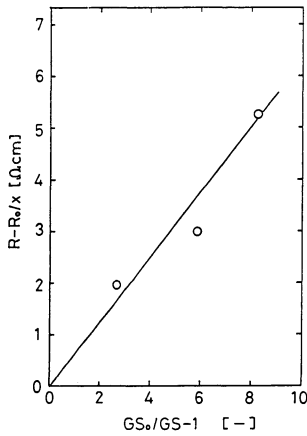


Fig.7 Relation between $G_{So}/GS-1$ and $R-Ro/x$

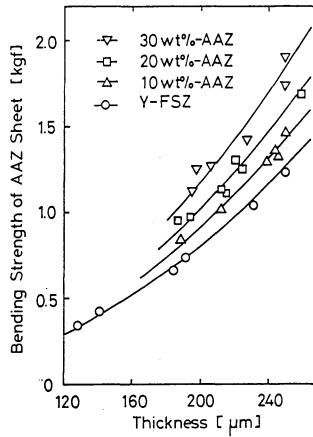


Fig.8 Effect of Alumina Content on Bending Strength of AAZ sheet

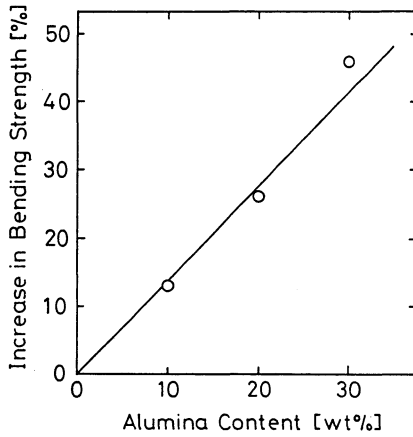


Fig.9 Relation between Alumina Content and Increase in Bending Strength of AAZ

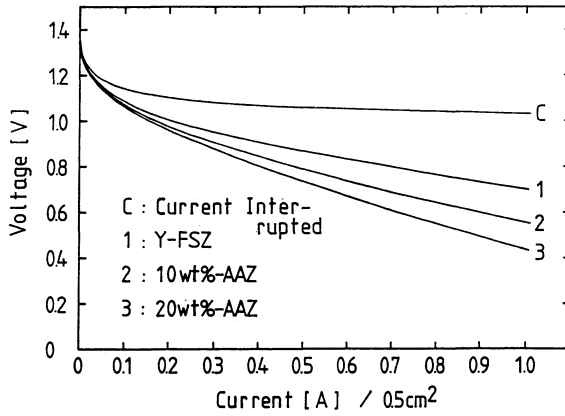


Fig.10 Performance Curve of Fuel Cell using AAZ sheet

SOLID STATE OXYGEN KINETICS IN Er_2O_3 STABILIZED Bi_2O_3

E. D. Wachsman, N. Jiang, D. M. Mason and D. A. Stevenson
Electrocatalysis Laboratory
Departments of Chemical Engineering
and Materials Science & Engineering
Stanford University
Stanford, CA 94305-5025

ABSTRACT

The conductivity and mechanism of oxygen-ion transport in 20 mole % erbia-stabilized bismuth oxide (ESB) was investigated using AC impedance spectroscopy and an equivalent circuit for oxygen-ion transport is described. A change in the slope of conductivity vs. reciprocal temperature, at $\sim 600^\circ\text{C}$, indicating two different conductivity activation processes, is attributed to an order-disorder transition of the oxygen sublattice. At high temperatures, the oxygen sublattice is disordered resulting in a high concentration of mobile oxygen vacancies and a low apparent activation energy. At low temperatures the oxygen sublattice orders. The higher activation energy in this temperature regime is ascribed to the extra energy required to free a vacancy from the ordered state. A reversible aging phenomenon in the conductivity of ESB was observed. When ESB is annealed in the lower temperature region, the conductivity decays with time. Heating above the transition point completely reverses this process and returns the conductivity to its initial value. Differential thermal analysis and x-ray diffraction were used to investigate this conductivity aging phenomenon which is ascribed to ordering of the oxygen sublattice.

1. INTRODUCTION

The anion deficient fluorite structure is common to most of the solid oxide electrolyte systems. It is the structure of the high temperature phase responsible for the observed high conductivity of these electrolytes. The fluorite structure consists of an FCC cation sublattice with oxygen ions in the tetrahedral positions. Zirconia electrolytes are stabilized in this structure by the addition of aliovalent cations and have anion vacancy concentrations proportional to the dopant's concentration and relative charge (typically $\sim 5\%$), which develops reasonable ionic conductivities at high temperatures ($\sim 1 \text{ ohm}^{-1} \text{ cm}^{-1}$ @ 1000°C). Stabilized- Bi_2O_3 electrolytes have an intrinsic vacancy concentration of 25% of the anion sites, and are receiving considerable interest due to their order of magnitude greater ionic conductivity at comparable temperatures. This greater conductivity of stabilized- Bi_2O_3 electrolytes opens the window for lower operating temperatures, thus significantly increasing the number of applications for solid-oxide electrolytes. Among the stabilized- Bi_2O_3 electrolytes, Bi_2O_3 stabilized

with 20 mole % Er_2O_3 (ESB) has the greatest conductivity and is the electrolyte studied in this investigation.

The Arrhenius behavior of the conductivity of several stabilized- Bi_2O_3 electrolytes, including ESB, exhibit an interesting change of slope or "knee" at about 600°C . This change in activation energy is quite different from that observed in typical solid-state conductivity/diffusion processes in that the activation energy is lower at high temperature than at low temperature. This change in activation energy is due to an order-disorder transition of the oxygen sublattice. The question persists as to the nature of the ordered and disordered structures in stabilized- Bi_2O_3 electrolytes and how these structures relate to the ionic conductivity observed in these materials. We address these issues in our present study.

2. EXPERIMENTAL

Polycrystalline erbia-stabilized bismuth oxide (ESB) disks, 2.5 cm in diameter and 0.15 cm thick, of nominal composition $(\text{Bi}_2\text{O}_3)_{0.8}(\text{Er}_2\text{O}_3)_{0.2}$ were obtained from Trans-Tech, Inc. Electron microprobe analysis showed the actual composition to be 81.7 mole % bismuth oxide and 18.3 mole % erbia. Porous Au electrodes were obtained by painting an Engelhard paste onto the surface of the disks and annealing in air at 800°C for 5 hours to drive off the binders. This process was repeated two to three times for each disk in order to obtain a surface resistance of less than 0.2 ohm.

The samples were placed in a quartz sample holder, with spring loaded Au wires for electrical contact and a K-type thermocouple for temperature measurement, inside a quartz tube. The quartz tube was wrapped with a 318 stainless steel wire mesh and grounded in order to minimize any stray inductance and placed inside a Lindberg furnace.

AC impedance measurements were obtained with an HP 4284A Precision LCR Meter over the frequency range 20 Hz to 1 MHz. Compensation for both series and parallel components of the test lead resistance, capacitance and inductance over the entire frequency range was performed using the instruments internal compensation circuitry. Measurements were taken over the temperature range 200 to 750°C in air.

The aging phenomenon was investigated using the above conductivity technique as well as with x-ray and thermal analysis. For the structural and thermal analysis, a disk was broken into several pieces and annealed in air at 500°C in a box furnace. The pieces were aged up to 500 hours and then rapidly quenched to room temperature. Powder diffraction patterns were obtained with $\text{Cu K}\alpha$ radiation over the 2θ range 10 to 70° . Differential thermal analysis data was obtained with a Dupont 2100 Thermal Analysis System using a 1600 DTA cell in air.

3. AC IMPEDANCE

Complex impedance plots for ESB and a variety of other lanthanide stabilized bismuth oxides have been published with varying results. Verkerk and Burggraaf (1) investigated the oxygen transfer on ESB with Pt electrodes over the frequency range 10^{-2} to 10^3 Hz as a function of P_{O_2} at 700°C . For $P_{O_2} = 0.1$ to 1.0 atm, their results indicate a single semicircle shifted along the real axis from the origin. The corresponding equivalent circuit is described by a single resistive element attributable to bulk conductivity, in series with a parallel Warburg impedance - double layer capacitance circuit attributable to the interface. Both Duran (2), for ESB and yttria stabilized bismuth oxide (YSB), and Dordor (3), for YSB, presented results indicating a single parallel circuit element at low temperature ($\sim 200^\circ\text{C}$) followed by two and then three equivalent circuit elements as the temperature is increased. These results are essentially identical to ours, as will be described below. Meng (4) investigated bismuth oxide, both singly and doubly stabilized with Y_2O_3 , Nb_2O_5 , Sm_2O_3 and Pr_6O_{11} , and similarly showed a single semicircle at 253°C which evolved into two semicircles at 400°C . However, as the temperature was increased beyond 500°C the high frequency semicircle exhibited inductive behavior.

At 200°C , a plot of the imaginary vs real components of impedance, Figure 1, consists of a single semicircle, in agreement with the results of Duran, Dordor and Meng (2-4). The equivalent circuit for this high frequency semicircle consists of a single parallel RC circuit and is attributable to the bulk conductivity. As the temperature is increased two more circuit components become evident, Figures 2-4. At the low frequency end of the spectrum another semicircle appears. Extrapolation of the high frequency (bulk conductivity) semicircle results in a high frequency intercept that no longer goes through the origin. Thus there is an additional high frequency (beyond the limits of our equipment) component of the bulk conductivity.

The high frequency end of the low frequency semicircle is linear and intercepts the real axis at 45° . This frequency dispersion is best described by a Warburg impedance, Z_w , in parallel with a capacitance. This low frequency semicircle has been ascribed to the electrolyte-gas phase interface (1) and to a grain boundary effect for ESB (2) and YSB (2,3). Due to the P_{O_2} dependence described by Verkerk and Burggraaf (1) we agree with the assignment of this equivalent circuit element to the electrolyte-gas phase interface. The observed capacitance of this circuit component is therefore due to the double layer, C_{dl} .

Although we can not extend our measurement range to higher frequency, we can tentatively assign the highest frequency component of the bulk conductivity to a series resistance. This is consistent with the typical bulk conductivity circuit for both zirconia (1,5,6) and bismuth (1) based oxygen ion conductors. The overall equivalent circuit is therefore as depicted in Figure 5. The bulk conductivity consists of a resistance, R_f , in series with a parallel circuit, R_d-C_g (the meaning of the resistance subscripts will become evident in the Discussion section). This in turn is in series with a parallel circuit, Z_w-C_{dl} , associated with the interface.

The geometry of our samples is that of a parallel plate capacitor. For the results in Figures 1-4, a disk was cut into an 0.8×0.8 cm square resulting in an area to thickness ratio, A/d , of 6. We have varied the A/d ratio from 6 to 34 and observed that the capacitance is proportional to this ratio. Thus, the capacitive element we observed in the bulk conductivity semicircle can be attributed to the geometric capacitance, C_g .

The differing literature results with respect to the high frequency semicircle warrant explanation. The lack of a high frequency bulk-semicircle in Verkerk and Burggraaf (1) results can be explained by two differences in the experimental conditions. First, they report having only scanned the frequency range up to 1 kHz, which is below the range where this semicircle was observed by Duran (2), Dordor (3) and in this study. Second, they report using a much smaller A/d ratios, ~ 0.98 which would significantly reduce any C_g effect. With regards to the inductive loop described by Meng (4), our only possible explanation is that we also observed an inductive element prior to fully compensating all of the parasitic elements in the test leads.

Several investigators have shown that the conductivity-temperature dependence of a variety of lanthanide stabilized bismuth oxides exhibit two activation energies (7-10). Since the observed conductivity activation energy depends on the measurement frequency, one must obtain the conductivity from the real-axis intercept of a complex impedance plot; otherwise, the Arrhenius behavior will be skewed so as to artificially obtain two slopes (5). A plot of the bulk conductivity, calculated from the real-axis intercept, $R_f + R_d$, as a function of reciprocal temperature is shown in Figure 6. Two slopes are in fact observed, with corresponding activation energies of 15 kcal/mole above 600°C and 28 kcal/mole below 600°C.

The observation of two activation energies requires that two processes are involved in the bulk conductivity mechanism. As such, one would expect to observe two elements in the equivalent circuit attributable to the bulk conductivity with a single activation energy corresponding to each element. This expectation is consistent with our proposed equivalent circuit.

The high frequency intercept of the bulk conductivity semicircle, R_f , varies with temperature. Since the low frequency intercept, $R_f + R_d$, is the sum of the high frequency intercept, R_f , and the resistive element of the semicircle, R_d , one can calculate each of the individual resistive elements by simple subtraction. Above $\sim 500^\circ\text{C}$, the rate of decrease of R_f with increasing temperature becomes proportionally greater than that of R_d . The resulting temperature dependence of the conductivity of each of these resistive elements is plotted in Figure 6. As can be seen from the plot, the conductivity calculated from R_f has the same slope as the low temperature region and the conductivity calculated from R_d has the same slope as the high temperature region of the total conductivity.

4. CONDUCTIVITY AGING

Samples aged at temperatures below the knee in the Arrhenius plot (<600°C) exhibit a monotonic decay in conductivity with time. This aging phenomenon is completely reversible; when samples are heated to temperatures above the order-disorder transition temperature, the conductivity reverts back to its original value. Similar results were observed by Carter for calcia stabilized zirconia, CSZ (11).

A plot of the decay in conductivity of ESB with time is shown in Figure 7. The conductivities measured at several temperatures below 600°C were normalized relative to the initial conductivity at their respective temperature. These curves are best described qualitatively by typical precipitation behavior. This behavior is described first with respect to temperature and then with respect to time. At high temperatures (550-575°C), there is a delay which increases with temperature before the onset of decay. This delay is typical for the dependence of nucleation on supersaturation or the small thermodynamic driving force for small amounts of supercooling below the transition temperature. At lower temperatures (350-500°C), the rate of decay increases with increasing temperature and is controlled by growth kinetics.

The time dependence in the low temperature growth controlled region is shown in Figures 8 and 9. At short times, Figure 8, the logarithm of conductivity is linear with time. At long times, Figure 9, the resistivity is linear with $t^{1/2}$. These results are described in the Discussion section.

5. DIFFERENTIAL THERMAL ANALYSIS

Differential Thermal Analysis (DTA) was used to investigate this aging phenomenon and the order-disorder transition of unaged ESB. ESB was heated and cooled thru the transition temperature and the differential temperature between ESB and a reference thermocouple was measured. The results for no aging, 100 hours and 500 hours at 500°C are shown in Figure 10. The aged samples exhibit an endotherm upon heating, with both the magnitude of the endotherm and the temperature of onset increasing with aging time. The unaged sample exhibits no endotherm upon heating. However, a thermal transition is signified by a change in slope centered at the 600°C conductivity transition point (the onset of the transition is 584°C and the completion is at 615°C, with the extent of the transition region dependent on sample size) and is more evident in the 3X magnification of scale, Figure 11. Below the transition region, the slope is 4.7×10^{-5} °C/mg/°C and above the transition region the slope is 7.6×10^{-5} °C/mg/°C. These slopes are proportional to heat capacity. Hence, the increase in slope above the transition temperature may be related to a greater degree of freedom in the disordered state.

Upon cooling, the reverse change in slope is observed for all of the samples, with some hysteresis of the transition toward lower temperature. Reheating of the aged samples results in identical temperature profiles to that of the unaged sample, thus confirming the reversibility of the aging phenomenon.

6. STRUCTURE

It is generally acknowledged that the structure of δ -Bi₂O₃ consists of a FCC cation sublattice with oxygen ions in six of the eight tetrahedral sites. However, it is still not clear how the oxygen ions are arranged to accommodate the two vacant oxygen lattice sites and the resulting high degree of disorder. Three models have been proposed to account for this disorder.

Gattow and Schroder (12) suggested that the oxygen sites are all randomly occupied, hence a 3/4 occupancy factor for each site. This would result in a FCC diffraction pattern with relative intensities proportional to the structure factors tabulated in Table 1.

Sillen observed diffraction peaks corresponding to the ordering of vacancies in $\langle 111 \rangle$ directions (13). This model is energetically favorable, as calculated by (14). However, several authors have discounted this model as being a result of Si contamination (15,16). Diffraction results from these same authors (15,16), using high temperature neutron diffraction do not show the additional $\langle 111 \rangle$ orientation peaks, Table 1.

The third model by Willis (17) describes the disorder in terms of a displacement δ along four $\langle 111 \rangle$ directions from the normal tetrahedral site, $1/4 \ 1/4 \ 1/4$. This results in 32 possible sites with an oxygen occupancy factor of 3/16. One problem with this model is that in calculating the structure factors, simple multiplication by this occupancy factor allows up to four oxygens arranged with δ displacements around a single tetrahedral site. One should instead consider either the Gattow and Schroder or Sillen models as occupancy disorder with the δ displacement of the Willis model as a local positional disorder superimposed on the occupancy disorder.

Since the aging phenomenon is associated with ordering of the anion lattice, one would expect that additional peaks corresponding to alignment of the vacancies in $\langle 111 \rangle$, $\langle 110 \rangle$ or $\langle 100 \rangle$ directions would become apparent. These peaks would have the structure factors and corresponding relative intensities shown in Table 1. The relative intensities are calculated from the structure factors and the atomic scattering factors where f is the statistical average of the atomic scattering factors of Bi and Er and f_o is the atomic scattering factor of oxygen. As is shown in Table 1, the calculated intensities for the non-FCC peaks are extremely small both due to the structure factor and the fact that the x-ray diffraction (XRD) atomic scattering factor of oxygen is $\sim 1/10$ that of Bi and Er.

Table 1. Structure Factors and Relative XRD Intensities for the Lower Angle Reflections of ESB

	Gattow & Schroder	Sillen <111>	<110>	<100>
Occupancy	3/4	1	1	1
$ F_{110} ^2$	- 0	$4f_o^2$ 0.2	$4f_o^2$ 0.2	- 0
$ F_{111} ^2$	$16f^2+36f_o^2$ 100	$16f^2$ 100	$16f^2+4f_o^2$ 100	$16f^2$ 100
$ F_{200} ^2$	$(4f-6f_o)^2$ 71	$(4f-6f_o)^2$ 72	$(4f-6f_o)^2$ 72	$(4f-6f_o)^2$ 72
$ F_{210} ^2$	- 0	- 0	- 0	$4f_o^2$ <0.2
$ F_{211} ^2$	- 0	$4f_o^2$ <0.2	- 0	$4f_o^2$ <0.2
$ F_{220} ^2$	$(4f+6f_o)^2$ 97	$(4f+6f_o)^2$ 98	$(4f+6f_o)^2$ 98	$(4f+6f_o)^2$ 98
$ F_{221} ^2$	- 0	- 0	$4f_o^2$ <0.2	$4f_o^2$ <0.2
$ F_{310} ^2$	$4f_o^2$ <0.2	$4f_o^2$ <0.2	$4f_o^2$ <0.2	- 0

We investigated the effect of aging on the structure of ESB using XRD. Three important results were observed. First, no peaks corresponding to the formation of additional phases were observed after 500 hours of aging. Second, a qualitative trend was observed in all of the samples with the intensity of the FCC peaks increasing with aging time; after 500 hours the peak intensities increased by a factor of two over the initial sample. This could be related to Willis type ordering where the δ becomes smaller with time; however, one can not fully discount the possible influence of thickness variation in preparation of XRD samples. The third, and possibly most important, observation is that after 500 hrs a small peak at 25.5 degrees 2θ appears, Figure 12, which is not apparent prior to aging. This peak corresponds both in position and relative intensity to that calculated for a reflection from a (110) plane due to either <111> or <110> occupancy-ordering of vacancies. Based on theoretical calculations (14) we believe that <111> type ordering is more likely. Therefore, this aging phenomenon can tentatively be described as ordering of oxygen vacancies along <111> directions.

Further experiments using electron diffraction are underway to confirm (or refute) the observation of <111> ordering. In addition, neutron diffraction results would more clearly identify the presence (or absence) of this peak, as well as some of the other <111> or <110> ordering peaks, as the neutron scattering factor of oxygen is much closer to that of Bi and Er. Previous neutron diffraction experiments (15,16), having not observed the aging phenomenon, may not have taken the time dependence of ordering under consideration.

7. DISCUSSION

The total conductivity for a given material, σ , is defined by:

$$\sigma = \sum_i z_i q [i] b_i \quad (1)$$

where $z_i q$, $[i]$ and b_i are, respectively, the charge, concentration and mobility of each species "i". For solid oxide electrolytes the conducting species are oxygen vacancies and one can neglect the contribution of electronic species over most of the conductivity domain. This simplifies Equation 1 to:

$$\sigma = \sum_i z_i q [V_i] b_i \quad (2)$$

where now the subscript "i" refers only to the different types of oxygen vacancies. The predominate ionic defect in zirconia, M^{+4} , type solid oxide electrolytes are the charged oxygen vacancies, such as $V_O^{\circ\circ}$, due to aliovalent cation substitution and Anti-Frenkel disorder. In addition, however, there are numerous perturbations on the local environment of these vacancies that can have a profound influence on their mobility or partial conductivity. Examples of these perturbations are: ionized vacancies due to the occupation of one or more electrons (i.e. V_O° , V_O^x , V_O' , etc.); the association of a vacancy with an aliovalent cation (i.e. $[V_O^{\circ\circ} Y']^\circ$ in ZrO_2); and, as will be discussed, the structural environment.

In the case of ESB, which has no aliovalent cations, we can ignore the effect of coulombic vacancy-cation association. If we ignore the effect of electron occupation, one can look at the limiting case of structural perturbations on vacancy mobility. This is especially important as the intrinsic vacant 25% of the anion lattice sites are neutral. Therefore, as single entities they do not constitute an ionic defect. Rather, as described by Jacobs (14), charged defects can be formed by a pseudo-Frenkel disorder by transposing oxygen ions and vacancies between neighboring sublattices, hence a structural disorder.

Now consider the case of an ordered vs. a disordered oxygen sublattice. The high oxygen ion mobility in solid oxide electrolytes is attributed to the high degree of disorder of the oxygen sublattice. For a periodic or ordered oxygen sublattice one would expect a significantly lower mobility, possibly approaching that of a typical non-conducting oxide. We believe this structural perturbation plays a significant role in the conductivity of ESB.

The change in activation energy, at $\sim 600^\circ\text{C}$, has been ascribed to an order-disorder transition of the oxygen sublattice (7). Above 600°C the oxygen sublattice is disordered, resulting in a low apparent activation energy for conductivity. Below the transition temperature, the oxygen sublattice attains some degree of ordering and the activation energy is significantly greater. This same type of order-disorder phenomenon of the oxygen sublattice has been described for CSZ, with a

transition temperature of $\sim 1000^\circ\text{C}$ (11). The effect of the order-disorder transition on conductivity can be explained by either of two models. The first, put forth by Carter (11), consists of a single concentration of vacancies whose mobility depends on the local structural environment. Thus, as the oxygen sublattice disorders the mobility increases. This model, however, does not explain the two different activation energies observed in stabilized $\delta\text{-Bi}_2\text{O}_3$. Therefore, we will develop a second model to explain this "knee" in the Arrhenius plot of stabilized $\delta\text{-Bi}_2\text{O}_3$'s.

For diffusion in a cubic solid, the diffusivity, D , is related to the jump frequency, Γ , and the jump distance, α , by:

$$D = \frac{1}{6} \Gamma \alpha^2 \quad (3)$$

For interstitial diffusion, the jump frequency is related to the vibration frequency, ν , the coordination number, z , and the free energy of migration ΔG_m :

$$\Gamma = \nu z e^{-\frac{\Delta G_m}{kT}} \quad (4)$$

However, in a vacancy mechanism an extra term is necessary to account for the formation of vacancies:

$$\Gamma = \nu z X_v e^{-\frac{\Delta G_m}{kT}} \quad (5)$$

where X_v is the equilibrium fraction of vacant sites and is equal to the exponential of the free energy of formation of a vacant site, ΔG_f :

$$X_v = e^{-\frac{\Delta G_f}{kT}} \quad (6)$$

Thus, the diffusivity for vacancy diffusion contains two exponential terms:

$$D = \left(\frac{1}{6} \nu z \alpha^2 \right) e^{-\frac{\Delta G_f}{kT}} e^{-\frac{\Delta G_m}{kT}} \quad (7)$$

and hence two activation energies, ΔH_f and ΔH_m :

$$D = \left(\frac{1}{6} \nu z \alpha^2 e^{-\frac{(\Delta S_f + \Delta S_m)}{k}} \right) e^{-\frac{(\Delta H_f + \Delta H_m)}{kT}} \quad (8)$$

In stabilized $\delta\text{-Bi}_2\text{O}_3$, 25% of all oxygen sites are vacant leading one to expect that X_v plays a minor role in the temperature dependence of diffusion, and hence conductivity. However, consider that the anomalously large oxygen ion conductivity in $\delta\text{-Bi}_2\text{O}_3$ is due to the high degree of disorder in the oxygen sublattice; and that the oxygen sublattice undergoes an order-disorder transition at the knee in the Arrhenius plot of conductivity. Then, one can assume that the local

structural environment has an effect on the mobility of the oxygen vacancies and further that there are two types of structural environments, as signified by the order-disorder transition, with a different type of vacancy associated with each. The vacancies in the disordered regions of the oxygen sublattice have a high mobility, hence mobile vacancies (V_m). Whereas, vacancies in ordered domains of the oxygen sublattice, V_o , have a significantly lower mobility. Then the concentrations of V_m and V_o are related by:

$$X_v = \frac{[V_m]}{[V_m] + [V_o]} \quad (9)$$

where now X_v is the fraction of mobile vacancies. This reasoning then leads to the observed change in activation energy, as the mobile and ordered vacancies are related by a thermodynamic equilibrium similar to that of Equation 6, where now ΔG_f is the free energy of formation of mobile vacancies. In addition, this also explains the aging phenomenon. As a sample of ESB is aged, regions of ordered vacancies grow at the expense of mobile vacancies. This type of solid state transition would follow typical precipitation kinetics with the rate of transformation following first order kinetics at short time and becoming diffusion controlled at long time. The observed aging phenomenon shows this type of behavior.

The rate equation for first order kinetics, of species "i", is:

$$\frac{\partial [i]}{\partial t} = k [i] \quad (10)$$

Integrating Equation 10 and substituting V_m for species "i" yields:

$$\ln\left(\frac{[V_m]}{[V_m]_0}\right) = k t \quad (11)$$

where $[V_m]_0$ is the initial concentration of mobile vacancies. Assuming the mobility of ordered vacancies is negligible and that mobility is not concentration dependent, the ratio of conductivity to initial conductivity (σ/σ_0) is:

$$\left(\frac{\sigma}{\sigma_0}\right) = \left(\frac{(zq [V_m] b)}{(zq [V_m]_0 b)}\right) = \left(\frac{[V_m]}{[V_m]_0}\right) \quad (12)$$

Substitution of Equation 12 into Equation 11 yields:

$$\ln\left(\frac{\sigma}{\sigma_0}\right) = k t \quad (13)$$

Thus, if the aging phenomenon follows first order kinetics a plot of the natural logarithm of the conductivity is linear with time, as is displayed in Figure 8.

Carter attributed an observed linear increase in resistivity with the square root of time, for samples aged below 1100°C, to a diffusional process related to anion ordering (11). This is identical to our results for ESB at long times, Figure 9, thus indicating diffusion control.

The temperature dependence of the conductivity and the associated order-disorder transition can therefore be described in terms of the formation and migration of mobile vacancies. Above 600°C, the oxygen sublattice is disordered, X_v approaches unity and the observed activation energy is that of migration of mobile vacancies. Below 600°C, the oxygen sublattice tends to order, X_v approaches zero and the apparent activation energy is the enthalpy of formation of mobile vacancies. In terms of the equivalent circuit, R_f is the resistance associated with the formation of mobile vacancies and R_d is a diffusion resistance associated with the migration of mobile vacancies.

Further evidence for this can be seen by comparing the activation energies in Table 2. The activation energies of the conductivity calculated from R_f and the aging kinetics are both comparable with that of the bulk conductivity at low temperature. Similarly, the activation energy of the conductivity calculated from R_d is comparable with that of the bulk conductivity at high temperature. Since the aging phenomenon is due to the consumption of mobile vacancies rather than their formation the observed activation energy, ΔH^\ddagger , is not expected to be identical to, but only comparable to, that of the conductivity in the low temperature region. Due to the long time involved in these solid state transitions, aging of samples at temperatures less than 500°C has not as yet progressed to the point where diffusion is limiting; therefore, an activation energy for the diffusion controlled region of the aging phenomenon has not yet been calculated.

Table 2. Activation Energies in ESB (kcal/mole)

Bulk Conductivity	Individual Components	Rate Constant
<u><600°C</u>	<u>R_f</u>	<u>ΔH^\ddagger</u>
28	28	25
<u>>600°C</u>	<u>R_d</u>	
15	12	

8. CONCLUSION

An order-disorder transition of the oxygen sublattice in ESB is proposed to explain the knee in the Arrhenius plot of conductivity. At high temperatures (>600°C) the oxygen sublattice is in a disordered state, conceptually a disordered array of mobile oxygen ions and oxygen vacancies, with a corresponding low activation barrier to migration. As ESB is cooled below the transition temperature, the vacancies tend to form domains of some lower-energy ordered-state with a concomitant reduction in the population of mobile vacancies. Preliminary diffraction results indicate that this ordered state can be described by

the arrangement of oxygen vacancies in <111> directions. The apparent activation energy in the low temperature region is then related to the formation of mobile vacancies.

The kinetics of the reversible aging phenomenon is related to the rate the oxygen vacancies attain this lower-energy ordered-state. Domains of the ordered state grow by consuming mobile vacancies, thus reducing the concentration of conducting species. These results, when compared with those for CSZ (11), indicate a commonality in the transport kinetics and aging phenomenon between zirconia and bismuth oxide electrolytes.

ACKNOWLEDGEMENTS

We are grateful for the financial support of the Electric Power Research Institute, grant RP8002-13, and the Department of Energy, Pittsburgh Energy Technology Center, contract DE-FG22-88PC914.

REFERENCES

1. M. J. Verkerk and A. J. Burggraaf, *J. Electrochem. Soc.*, **130**, 78 (1983).
2. P. Duran, J. R. Jurado, C. Moure, N. Valverde and B. C. H. Steele, *Mat. Chem. Phys.*, **18**, 287 (1987).
3. P. J. Dordor, J. Tanaka and A. Watanabe, *Solid State Ionics*, **25**, 177 (1987).
4. G. Meng, M. Zhou and D. Peng, *Solid State Ionics*, **18 & 19**, 756 (1986).
5. T. M. Gur, I. D. Raistrick and R. A. Huggins, *Mat. Sci. Eng.*, **46**, 53 (1980).
6. J. E. Bauerle, *J. Phys. Chem. Solids*, **30**, 2657 (1969).
7. M. J. Verkerk and A. J. Burggraaf, *Solid State Ionics*, **3/4**, 463 (1981).
8. M. J. Verkerk, K. Keizer and A. J. Burggraaf, *J. Appl. Electrochem.*, **10**, 81 (1980).
9. H. T. Cahen, T. G. M. Van Den Belt, J. H. W. De Wit and G. H. J. Broers, *Solid State Ionics*, **1**, 411 (1980).
10. E. D. Wachsman, N. Jiang and D. M. Mason, *Proc. 1988 Fuel Cell Seminar*, 65 (1988).
11. R. E. Carter and W. L. Roth, *EMF Measurements in High Temperature Systems* (C. B. Alcock, ed.), Institute of Mining and Metallurgy, London (1968).
12. G. Gattow and H. Schroder, *Z. Anorg. Allg. Chem.*, **318**, 176 (1962).
13. L. G. Sillen, *Ark. Kemi. Mineral. Geol.*, **12A**, 1 (1937).
14. P. W. M. Jacobs and D. A. Mac Donnell, *Solid State Ionics*, **18 & 19**, 209 (1986).
15. H. A. Harwig, *Z. Anorg. Allg. Chem.*, **444**, 151 (1978).
16. M. J. Verkerk, G. M. H. Van De Velde, A. J. Burggraaf and R. B. Helmholtz, *J. Phys. Chem. Solids*, **43**, 1129 (1982).
17. B. T. M. Willis, *Acta Cryst.*, **18**, 75 (1965).

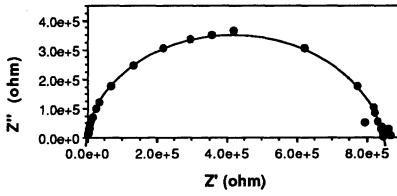


Figure 1. Complex impedance plot of ESB at 200°C.

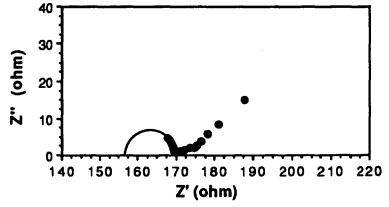


Figure 3. Complex impedance plot of ESB at 400°C.

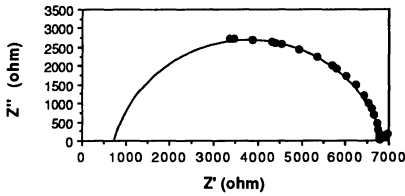


Figure 2. Complex impedance plot of ESB at 300°C.

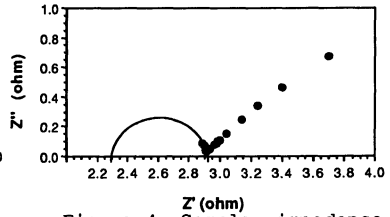


Figure 4. Complex impedance plot of ESB at 575°C.

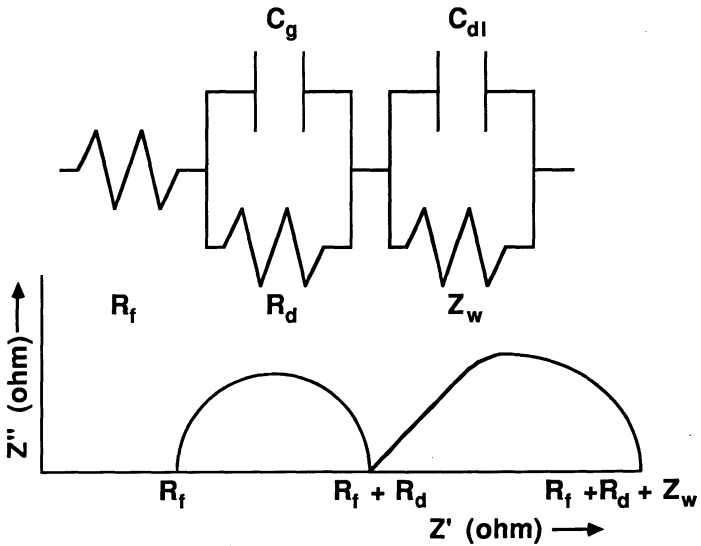


Figure 5. Equivalent circuit for ESB.

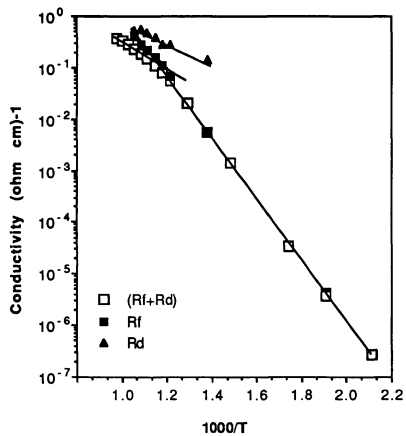


Figure 6. Bulk and individual component conductivities from (Rf+Rd), Rf and Rd intercepts, respectively, as a function of reciprocal temperature for ESB.

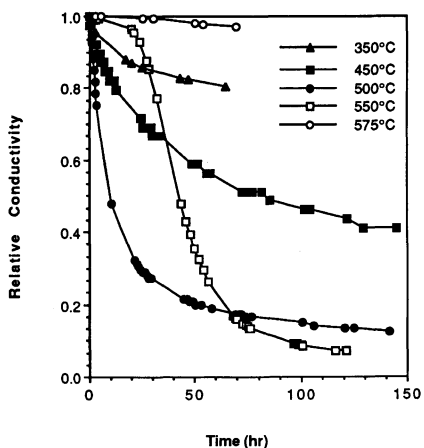


Figure 7. Aging phenomenon in ESB; normalized conductivity as a function of time and temperature.

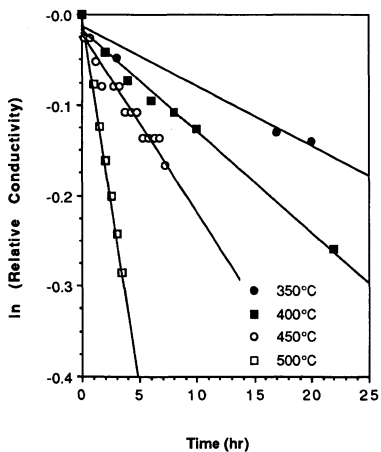


Figure 8. Aging phenomenon in ESB indicating first order kinetics at short time.

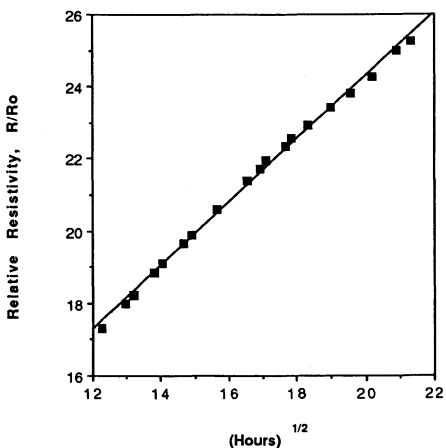


Figure 9. Aging phenomenon in ESB at 500°C indicating diffusion control at long time.

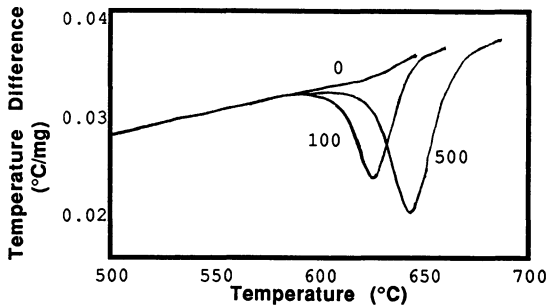


Figure 10. DTA of ESB; temperature difference upon heating for no aging, 100 and 500 hours at 500°C.

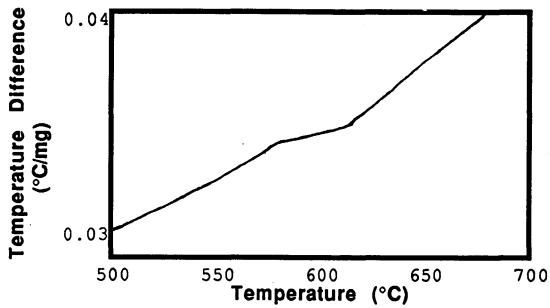


Figure 11. DTA of un-aged ESB indicating change in slope.

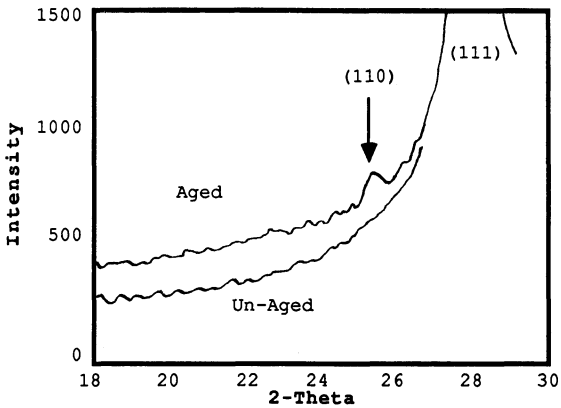


Figure 12. X-ray diffraction of ESB indicating (110) reflection after 500 hours at 500°C.

EVALUATION OF SOLID OXIDE ELECTROLYTES WITH THE PYROCHLORE
STRUCTURE FOR USE IN FUEL CELLS

P.K. Moon* and H.L. Tuller
Crystal Physics & Optical Electronics Laboratory
Department of Materials Science & Engineering
Massachusetts Institute of Technology
Cambridge, MA 02139

ABSTRACT

Compositions in the pyrochlore system $Gd_2(Zr_xTi_{1-x})_2O_7$ (GZT) are examined as possible alternatives to stabilized zirconia as solid oxide electrolytes in fuel cells. The GZT system is shown in general to be a mixed ionic/electronic conductor with the titanate end member being predominantly semiconducting and the zirconate end member achieving intrinsic fast oxygen ion conductivity. A defect model is utilized to assist in the deconvolution of ionic and electronic contributions to the total conductivity. This data is then used to construct electrolytic domain boundaries which are shown to broaden rapidly with increasing x . The key features which make the GZT system attractive as a fuel cell element are discussed.

1. INTRODUCTION

Due to an increased concern with atmospheric pollution and repeated volatility in the supply of fossil fuels, there is a renewed incentive to examine alternative energy conversion approaches which are inherently more efficient and non-polluting. High temperature fuel cells utilizing solid electrolytes are receiving increased attention due to⁽¹⁾ (a) their ability to utilize hydrocarbon fuels resulting from rapid electrode kinetics at elevated temperatures, (b) potential for higher current densities and thereby higher power densities, and (c) the absence of liquids and the attendant problems with electrode wetting, corrosion, and sealing.

High temperature fuel cells utilizing stabilized zirconia as the oxygen-ion solid electrolyte were first seriously considered nearly 25 years ago.^(2,3) In the

*Present Address: Intel Corp., Hillsboro, OR 97124-6497

interim, most of the attention has been directed towards cell engineering and development and testing of electrodes rather than on alternative electrolytes. Stabilized zirconia still remains the electrolyte of choice although several others including δ -Bi₂O₃,⁽⁴⁾ CeO₂,^(5,6) and α -Ta₂O₅^(7,8) have been examined from time to time. In this paper, we discuss our findings regarding the transport properties of the pyrochlore solid solution Gd₂(Zr_xTi_{1-x})₂O₇ (GZT) in relation to its potential as a solid electrolyte in fuel cells.

Acceptable solid electrolytes must satisfy a number of criteria⁽⁹⁾ including high oxygen ion conductivity, low electronic conductivity, chemical compatibility with electrodes and/or substrates, good mechanical strength, thermal shock resistance and imperviousness to gases. Stabilized zirconia has remained the material of choice primarily because of the first two criteria. Its relatively high oxygen ion conductivity (e.g. $\sim 10^{-1}$ S/cm at 1000°C) is coupled to an excellent stability with respect to reduction or oxidation, which limits its electronic conductivity to below 1% of the total between $10^{+8} < P_{O_2} < 10^{-25}$ atm. Other materials, such as δ -Bi₂O₃ and doped CeO₂, although they have higher ionic conductivities, reduce much more readily, thereby reducing the size of their electrolytic domains with resultant decreases in output voltage and energy conversion efficiency.⁽¹⁰⁾ Although the GZT system is not generally as conductive as stabilized zirconia at elevated temperatures, it does, as we illustrate below, exhibit a number of attractive features which make it interesting as a solid oxide electrolyte candidate.

The pyrochlore structure has a cubic unit cell with a lattice constant of roughly 10Å and a general molecular formula of A₂B₂O₆X, where A and B are cations and O and X are anions. A diagram of a portion of the pyrochlore structure projected onto the (100) plane is shown in Fig. 1. Detailed descriptions of the pyrochlore structure can be found elsewhere.⁽¹¹⁾

The pyrochlore structure is a superstructure of the defect fluorite structure with exactly twice the lattice parameter. Pyrochlore and ideal defect fluorite differ in that pyrochlore has additional ordering on both the cation and the anion sublattices and some of the oxygen ion positions are slightly distorted from their fluorite position. Oxygen vacancies occur at random throughout the anion sublattice in fluorite but are ordered onto particular sites (8b) in the pyrochlore structure.

Structural disorder occurs in pyrochlore compounds when the superstructure ordering, which distinguishes pyrochlore from fluorite, is partially lost. Two types of disorder are prevalent: antisite disorder on the cation sublattice where the A and B cations switch positions and quasi-Frenkel disorder on the anion sublattice where oxygen ions leave their normal sites (8a and 48f) and enter interstitial sites (8b). It is the latter feature which we believe results in intrinsic fast oxygen ion conductivity in a number of pyrochlores including $Gd_2Zr_2O_7$ and $Y_2Zr_2O_7$.⁽¹²⁾ Both types of disorder can be expected to occur to a substantial degree for certain compositions owing to the similarity of the fluorite and pyrochlore structures.

Detailed studies of the electrical properties of $Gd_2Zr_2O_7$ and $Nd_2Zr_2O_7$ were initiated by Van Dijk et al⁽¹³⁾ who found a local maximum in ionic conductivity (e.g. 5×10^{-3} S/cm at 720°C) and minimum in activation energy (~0.87eV) for the $GdO_{1.5}$ - ZrO_2 system for 50 mol% $GdO_{1.5}$, i.e. $Gd_2Zr_2O_7$. At least for high Gd_2O_3 levels, the pyrochlore structure gave higher ionic conductivities than neighboring fluorite phases. Comparing conductivities more globally, fluorite compositions can be found which exhibit higher conductivities than the pyrochlore phase, e.g. $Gd_{0.19}Zr_{0.81}O_{1.905}$ (fluorite) and $Gd_{0.5}Zr_{0.5}O_{1.675}$ (pyrochlore) exhibit ionic conductivities of 9.3×10^{-3} S/cm and 4.8×10^{-3} S/cm at 723°C respectively.⁽¹⁴⁾ Attempts to increase the ionic conductivity of $Gd_2Zr_2O_7$ by acceptor doping have resulted in either no change⁽¹⁵⁾ or a decrease in conductivity⁽¹⁶⁾ pointing to the intrinsic nature of the ionic disorder.

Studies of $Y_2Ti_2O_7$ by Uematsu et al⁽¹⁷⁾ show it to be a mixed ionic-electronic conductor. In a more complete study, recently completed by the authors on GZT and YZT systems,⁽¹⁵⁾ the ionic conductivity of the undoped titanate end members was shown to be many orders of magnitude lower than the zirconate end members and strongly impurity dependent. Conversely, the electronic conductivities of the titanates were substantial at elevated temperatures, in contrast to the zirconates. $Gd_2(Zr_xTi_{1-x})_2O_7$ was found⁽¹²⁾ to exhibit a very large increase in ionic conductivity (~3 orders of magnitude) between $x=0.15$ and $x=0.4$ with further substantial increases thereafter. This is illustrated in Fig. 2. At the same time, the electronic conductivity decreases markedly with $x > 0.2$.⁽¹⁸⁾ This provides an opportunity to control the mix of ionic and electronic conductivity - a feature of interest in developing electrodes with high oxygen-exchange kinetics.

2. THEORY

Ionic Conductivity. We have previously demonstrated that compositions in the GZT system with $x > 0.4$ are intrinsically highly disordered on the oxygen sublattice leading to high concentrations of both oxygen vacancies and interstitials. We have also shown, explicitly for GZT with $x=0.3$,⁽¹⁹⁾ that oxygen vacancies are far more mobile than oxygen interstitials and expect the same to be true for other values of x .

The ionic disorder can be viewed as Frenkel-type in nature which is given by

$$nil \Rightarrow V_o'' + O_i'' \quad (1)$$

or

$$[V_o''] [O_i''] = K_F(T) = K_F^0 \exp(-\Delta H_F/kT) \quad (2)$$

where $K_F(T)$ is the Frenkel equilibrium constant. The oxygen ion conductivity can therefore be written as

$$\sigma_i = 2qK_F^{1/2}(T) (\mu_V + \mu_{int}) \quad (3a)$$

$$\approx 2qK_F^{1/2}(T) \mu_V \quad (3b)$$

where μ_V and μ_{int} represent oxygen vacancy and interstitial mobilities, respectively.

Nonstoichiometry and Electronic Conductivity. The reduction reaction which leads to nonstoichiometry and thereby the generation of excess electrons is



which leads to the mass action relation

$$[V_o''] n^2 P_{O_2}^{1/2} = K_R(T) = K_R^0 \exp(-\Delta H_R/kT) \quad (5)$$

where $K_R(T)$ is the equilibrium constant for the reduction reaction and P_{O_2} the oxygen partial pressure. Combining Eq. 2 with 5, we find the electron density to be

$$n = (K_R/K_F^{1/2})^{1/2} P_{O_2}^{-1/4} \quad (6)$$

Since the electron-hole product given by

$$np = K_e(T) = N_e N_v \exp(-E_g/kT) \quad (7)$$

is a constant, one readily finds the hole density to be

$$p = K_e(K_F^{1/2}/K_R)^{1/2}Po_2^{1/4} \quad (8)$$

The total conductivity can therefore be written as

$$= A + B Po_2^{-1/4} + C Po_2^{+1/4} \quad (9)$$

where the first term is the Po_2 -independent ionic conductivity given by Eq. 3b, the second term is the electron contribution, $nq\mu_e$, with n given by Eq. 6, and the third term is the hole contribution, $pq\mu_h$, with p given by Eq. 8. Note, that the three partial conductivities can readily be distinguished by their Po_2 dependencies.

Although ionic defects substantially outnumber electronic defects under all experimental conditions of interest, the electronic conductivity can become appreciable (i.e. $\sigma_{\text{electronic}} = \sigma_{\text{ionic}}$ at sufficiently oxidizing ($Po_2=P_p$) or reducing conditions ($Po_2=P_n$) given the much higher electronic mobilities (see Eq's 8 and 6, respectively). P_n and P_p are readily established at each temperature by setting

$$A = B Po_2^{-1/4} \quad (10)$$

$$A = C Po_2^{+1/4} \quad (11)$$

and solving for the respective partial pressures.

One may readily demonstrate that expressions for P_n and P_p are given by⁽¹⁰⁾

$$\ln P_n = -4[(E_n - E_i)/k] 1/T + 4 \ln(\sigma_n^\circ / \sigma_i^\circ) \quad (12)$$

$$\ln P_p = -4[(E_i - E_p)/k] 1/T + 4 \ln(\sigma_i^\circ / \sigma_p^\circ) \quad (13)$$

where E_i , E_n and E_p are the activation energies for the ionic, n-type and p-type partial conductivities, respectively, and σ_i° , σ_h° , and σ_p° are the corresponding pre-exponential terms in A, B, and C, respectively. The region in $\ln Po_2$ vs. $1/T$ space bounded by Equations 12 and 13, represents the ionic domain within which the ionic transference number remains equal to or greater than 1/2.

3. EXPERIMENTAL

Powder samples were prepared by the "liquid-mix" technique⁽²⁰⁾ which enables close control of the cation

stoichiometries. Powders were dry pressed at 10Kpsi, isopressed at 40Kpsi, and then sintered at 1600°C for 16 hours.

Electrical measurements were performed with an HP4192a impedance analyzer operating between 5Hz and 13MHz which enabled the separation of the bulk conductance from the grain boundary and electrode contributions. Similar results were obtained from disc (12 mm dia, x2 mm) and bar (2x3x12 mm³) geometries. Oxygen partial pressures (1-10⁻²⁰atm) were controlled by use of either O₂/Ar or CO/CO₂ gas mixtures and monitored with a stabilized ZrO₂ concentration cell. A more detailed description of experimental techniques may be found in Ref. (15).

4. RESULTS

The isothermal Po₂ dependence of the electrical conductivity of Gd₂(Zr_{0.4}Ti_{0.6})₂O₇ is shown in Fig. 3. These data were found to fit well to Equation (9) outside of several points at the highest temperatures and lowest Po₂'s. It is obvious from Fig. 3 that, at 700°C, the total conductivity is nearly ionic, while at 1400°C, it is nearly entirely n-type electronic. P_n and P_p were readily determined at each temperature with the assistance of Eq's. (10 and 11) and are shown plotted in Fig. 4. As is the case for stabilized ZrO₂,⁽¹⁰⁾ the ionic domain is observed to shrink rapidly with increasing temperature. The rapid shrinkage of the domain with temperatures under reducing conditions is a consequence of E_n = 3.0eV >> E_i = 0.82eV while the weak dependence of the other domain boundary is a result of E_p = 1.0eV ≈ E_i = 0.82eV (see Eq's. 12 and 13).

If we examine the corresponding isothermal conductivity of the x=0.6 composition, i.e. Gd₂(Zr_{0.6}Ti_{0.4})₂O₇ shown in Fig. 5, we see that the ionic component of the conductivity now dominates at all but the highest temperatures and lowest Po₂ values. This is a consequence of two factors. First, as discussed above, the ionic conductivity increases sharply with increasing x, owing to a systematic disordering of the oxygen sublattice. Second, we find⁽¹⁸⁾ that the electronic component of the conductivity drops orders of magnitude with x over the same range of x (0.3 < x < 0.6) which, we believe, is due to a narrowing of the Ti 3d-like conduction band and an increase in the reduction enthalpy, ΔH_R, as titanium is replaced by zirconium.

The increase in ionic and decrease in electronic conductivity with increasing x is reflected in a systematic shift of the electrolytic boundary P_n towards lower Po₂ with

increasing zirconium content, as illustrated in Fig. 6. The fact that the boundaries remain parallel is due to the fact that E_i and E_n remain relatively independent of x . For $Gd_2Zr_2O_7$, we find no evidence of electronic conductivity over the ranges of P_{O_2} and temperature that we have examined.

In Fig. 7, we plot the ionic conductivity of $Gd_2Zr_2O_7$ versus reciprocal temperature and compare it with that of yttria stabilized zirconia $(Zr_{0.91}Y_{0.09})O_2$.⁽²²⁾ The ionic conductivity of the pyrochlore is clearly somewhat smaller than stabilized zirconia with the difference decreasing at lower T due to the lower activation energy of the pyrochlore (0.84 eV versus 0.9-1.0 eV).

5. DISCUSSION

The two key criteria that a solid oxide electrolyte must satisfy, namely high oxygen ion conductivity and low electronic conductivity, are satisfied by compositions in the GZT system with high values of x . The ionic conductivity of $Gd_2Zr_2O_7$ is high, e.g. $\sim 2 \times 10^{-2}$ S/cm at 1000°C, which is approximately 1/5 of yttria stabilized zirconia. The activation energy of ~ 0.84 eV is approximately 0.10-0.15 eV lower than that of stabilized zirconia. The ionic domain as illustrated in Fig. 6 is already quite broad for GZT with $x=0.6$, e.g. $P_n = 10^{-21}$ atm at 1000°C and we estimate $P_n = 10^{-32}$ atm for $x=1.0$ based upon our observed increase in σ_{ion} with x and an extrapolated decrease in $\sigma_{electron}$ between $x=0.6$ and 1.0.⁽¹⁸⁾ This compares favorably with P_n values estimated for stabilized zirconia.

Although somewhat lower in ionic conductivity, the GZT system exhibits a number of characteristics which make it an attractive candidate vis-a-vis stabilized zirconia. Since GZT with large values of x is an intrinsic fast ion conductor, it requires no dopants. Further, since the pyrochlore phase is the equilibrium phase, no long term aging effects are expected, as are found for "stabilized" zirconia⁽²¹⁾ and $\alpha-Ta_2O_5$.⁽⁸⁾

Perhaps what is most interesting about the GZT system is its flexibility. By controlling x , its lattice parameter may be varied from ~ 10.18 at $x=0$ to ~ 10.53 at $x=1$. This can be advantageous in lattice matching with substrate or electrode material, thereby reducing strain. Furthermore, the ratio of $\sigma_{ion}/\sigma_{electron}$ can be controlled over a wide spectrum by varying x and/or doping which can be of

significant importance in modifying surface regions in order to enhance oxygen exchange rates leading to lower electrode polarization.

Further work is required to determine whether these attributes can overcome GZT's somewhat lower ionic conductivities.

6. ACKNOWLEDGEMENTS

The authors wish to thank the Basic Science Division, U.S. Department of Energy, for their generous support under contract DE-FG02-86ER45261.

7. REFERENCES

1. H. Obayashi and T. Kudo in Solid State Chemistry of Energy Conversion and Storage, Eds. J.B. Goodenough and M.S. Wittingham, American Chemical Society, Washington, DC, 1977, p. 316.
2. O. Antonsen, W. Baukal, W. Fischer, Brown Boveri Rev., 53 21 (1966).
3. T.L. Markin, R.J. Bones, R.M. Dell in Superionic Conductors, Eds. G.D. Mahan and W.L. Roth, Plenum Press, New York, 1976, p.15.
4. T. Takahashi and H. Iwahara, Mat. Res. Bull., 13 1447 (1978).
5. H.L. Tuller and A.S. Nowick, J. Electrochem Soc., 122 255 (1975).
6. T. Kudo and H. Obayashi, J. Electrochem. Soc., 123 415 (1976).
7. A.E. McHale and H.L. Tuller, Solid State Ionics, 5 515 (1984).
8. G.M. Choi, H.L. Tuller, and J.S. Haggerty, J. Electrochem. Soc., 136 835 (1989).
9. H.L. Tuller and P.K. Moon, Mat. Sci. and Eng., B1 171 (1988).
10. H.L. Tuller in Non-Stoichiometric Oxides, Ed. O.T. Sorensen, Academic Press, New York, 1981, p. 271.
11. R.A. McCauley, J. Appl. Phys., 51 290 (1980).

12. P.K. Moon and H.L. Tuller in Proc. Symp. Solid State Ionics, Materials Research Society Fall meeting, November 28-December 2, 1988, Boston, MA, in press.
13. T. Van Dijk, K.J. de Vries, and A.J. Burggraaf, *Phys. Stat. Sol. (b)*, 101 765 (1980).
14. T. Van Dijk, K.J. de Vries, and A.J. Burggraaf, *Phys. Stat. Sol. (a)*, 58 115 (1980).
15. P.K. Moon, PhD Thesis, Massachusetts Institute of Technology, Cambridge, MA, 1988.
16. T. Fournier, J.Y. Nots, J. Muller, and J.C. Joubert, *Solid State Ionics*, 15 71 (1985).
17. K. Uematsu, S. Shinuzaki, O. Sakurai, N. Mizutani, and M. Kato, *J. Am. Ceram. Soc.*, 62 219 (1979).
18. P.K. Moon, M.A. Spears, and H.L. Tuller in Proc. Symp. Char. Struct. Chem. Defects. Mat., Materials Research Society, Fall Meeting, November 28-December 2, 1988, Boston, Ma, in press.
19. P.K. Moon and H.L. Tuller, *Solid State Ionics*, 28-30 470 (1988).
20. M.P. Pechini, U.S. Patent 3,330,697 (11 July 1967).
21. M. Kleitz, H. Bernard, E. Fernandez and E. Schouler, *Adv. Cer.*, 3 310 (1981).
22. E.C. Subbarao (ed.), *Solid Electrolytes and Their Applications*, Plenum Press, New York, 1980.

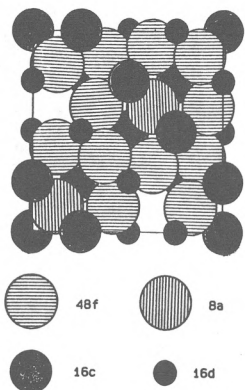


Fig. 1: A (100) projection of a portion of one unit cell of the pyrochlore structure.

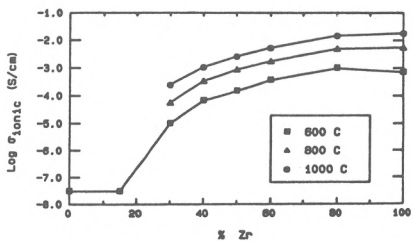


Fig. 2: Log σ vs. mole fraction of zirconium in $Gd_2(Zr_xTi_{1-x})_2O_7$ at 600°C, 800°C, and 1000°C.⁽¹²⁾ The sharp rise in ionic conductivity for $x > 0.2$ should be noted.

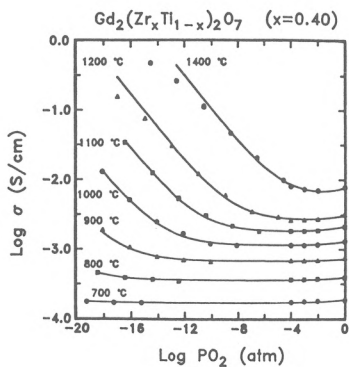


Fig. 3: Log σ vs. log P_{O_2} for $Gd_2(Zr_{0.4}Ti_{0.6})_2O_7$.⁽¹⁵⁾

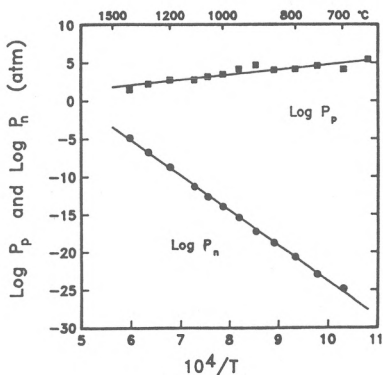


Fig. 4: The extent of the electrolytic zone for $Gd_2(Zr_{0.4}Ti_{0.6})_2O_7$ as a function of inverse temperature (from Ref. 9).

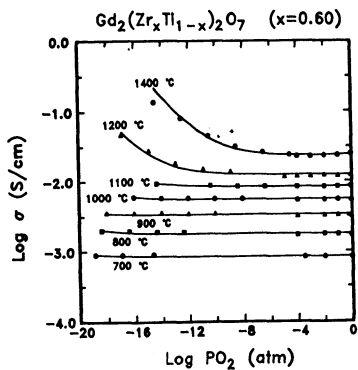


Fig. 5: $\text{Log } \sigma$ vs. $\text{log } P_{\text{O}_2}$ for $\text{Gd}_2(\text{Zr}_{0.6}\text{Ti}_{0.4})_2\text{O}_7$.⁽¹⁵⁾

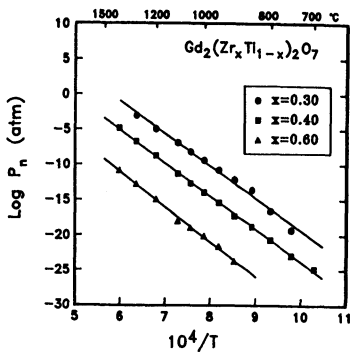


Fig. 6: The extent of the electrolytic zone under reducing conditions as a function of the composition of $\text{Gd}_2(\text{Zr}_x\text{Ti}_{1-x})_2\text{O}_7$ (from Ref. 9).

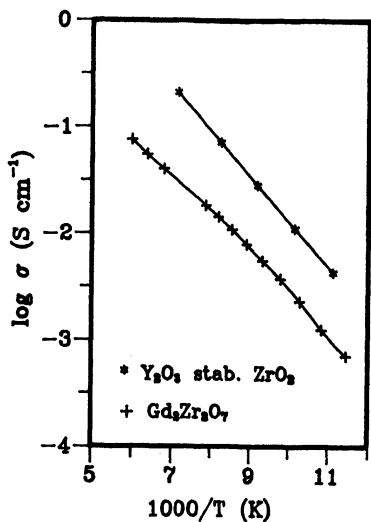


Fig. 7: A comparison of the temperature dependent conductivities of $\text{Gd}_2\text{Zr}_2\text{O}_7$ and $(\text{Y}_{0.09}\text{Zr}_{0.91})\text{O}_2$ (* = YSZ; + = GZ).

ELECTROCHEMICAL VAPOR DEPOSITION OF YTTRIA-STABILIZED ZIRCONIA FILMS

U. B. Pal and S. C. Singhal
Westinghouse Research and Development Center
1310 Beulah Road
Pittsburgh, Pennsylvania 15235

ABSTRACT

Tubular solid oxide fuel cells employ yttria-stabilized zirconia electrolyte film as an oxygen ion conductor at high temperatures. These yttria-stabilized zirconia electrolyte films are deposited by an electrochemical vapor deposition (EVD) process. The electrochemical transport of oxygen ions during the EVD process is analyzed by measuring the film growth as a function of EVD reaction time; the film growth is found to be parabolic with time. Wagner's transport theory for parabolic growth and the defect model for yttria-stabilized zirconia have been used to calculate the average electronic transport number and the partial electronic conductivity of the electrolyte film. The analysis of the data revealed that the electrolyte film growth is controlled by diffusion of electrons. It is also shown that the electrochemical transport that occurs during EVD of the electrolyte is similar to the phenomena of oxygen semi-permeability wherein electrons migrate from the low oxygen partial pressure side to the high oxygen partial pressure side and oxygen ions migrate in the reverse direction maintaining charge neutrality.

1. INTRODUCTION

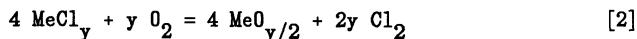
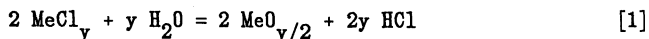
Solid oxide fuel cells employ yttria-stabilized zirconia electrolyte to operate as an oxygen ion conductor at high temperatures (1,2). A schematic cross-section of the tubular solid oxide fuel cell is shown in Figure 1. In this design, the cell components viz. air and fuel electrodes, electrolyte and cell interconnection, are deposited as thin layers over a porous calcia-stabilized zirconia tube; this porous tube functions both as a structural member supporting other cell components and as a functional member allowing oxygen and/or air to permeate through its pores to the air electrode. Table 1 summarizes the materials and fabrication processes for the various cell components (2,3).

For optimum cell performance, the yttria-stabilized zirconia electrolyte must be free of porosity so as not to allow gases to permeate from one side of the electrolyte to the other; it should be uniformly thin

to minimize ohmic loss; and it should have high oxygen ion conductivity with transport number for oxygen ions close to unity and a transport number for electrons as close to zero as possible (4). Therefore, an understanding of the growth mechanism of the yttria-stabilized zirconia electrolyte film is necessary to identify the rate controlling step and to determine the conditions for depositing electrolyte films with desired properties. In this paper, the growth of thin films of yttria-stabilized zirconia electrolyte by an electrochemical vapor deposition process is described and analyzed.

2. EXPERIMENTS AND RESULTS

The electrochemical vapor deposition process for depositing thin films of different cell components including the electrolyte has been discussed previously (5-8). Briefly, to deposit yttria-stabilized zirconia electrolyte films, chlorides of zirconium and yttrium are volatilized in a predetermined ratio and passed over outer surface of the porous air electrode. Oxygen mixed with steam at a predetermined ratio is passed inside the porous calcia-stabilized zirconia tube over which the porous air electrode is deposited. In the first stage of the reaction, designated as the chemical vapor deposition (CVD) stage, molecular diffusion of oxygen, steam and metal chlorides occurs through the porous air electrode and these react to fill the air electrode pores with the yttria-stabilized zirconia electrolyte according to the following reactions:



where Me is the cation specie (zirconium and/or yttrium);
and y is the valency associated with the cation.

The temperature, the pressure and the different gas flow rates are so chosen that the above reactions are thermodynamically and kinetically favored.

During the second stage of the reaction after the pores in the air electrode are closed, electrochemical transport of oxygen ions maintaining electroneutrality occurs, through the already deposited electrolyte in the pores, from the high oxygen partial pressure side (oxygen/steam) to the low oxygen partial pressure side (chlorides). The oxygen ions upon reaching the low oxygen partial pressure side react with the metal chlorides and the electrolyte film grows in thickness. This second stage of the reaction is termed the electrochemical vapor deposition (EVD) stage.

The forementioned two stages of reaction, viz. the CVD stage and the EVD stage, responsible for the growth of the yttria-stabilized zirconia

electrolyte film, are schematically shown in Figure 2. In this deposition process, the flows of the metal chloride vapors are maintained above a critical level to eliminate any gas phase control of the EVD reaction. Furthermore, the ratio of yttrium chloride to zirconium chloride is so chosen that the electrolyte deposited contains about 10 mole% yttria; this composition ensures the highest oxygen ion conductivity in yttria-stabilized zirconia (9,10).

For an analysis of the growth of the yttria-stabilized zirconia film, films were deposited at 1473°K for different EVD reaction times. The equilibrium calculations indicated that at this temperature the oxygen partial pressures inside and outside the air electrode tube were about 1.0×10^{-4} atm and 4.3×10^{-18} atm, respectively. A representative electrolyte film is shown in the metallographic cross-section in Figure 3. The film thicknesses were measured metallographically, and the square of the film thickness is plotted in Figure 4 as a function of the EVD reaction time. This plot was found to be a straight line indicating that the electrolyte film growth is parabolic with time. The rate of growth of the electrolyte film, dx/dt , can therefore be expressed as:

$$\frac{dx}{dt} = \frac{K'}{x} \quad \text{or} \quad x^2 = 2 K' t \quad [3]$$

where x is the electrolyte film thickness in cm;
 t is the reaction time in seconds;
and K' is the parabolic rate constant in cm^2/sec .

From the slope of the straight line in Figure 4, K' is calculated as being equal to $0.37 \times 10^{-8} \text{ cm}^2/\text{sec}$.

3. GROWTH MECHANISM OF THE YTTRIA-STABILIZED ZIRCONIA ELECTROLYTE FILM

In this section, Wagner's transport theory for parabolic growth is used to identify the rate controlling step during the EVD growth of the electrolyte and the rate controlling transport parameters are estimated. Next, the defect structure of the yttria-stabilized zirconia is described and applied to the film growth data to determine the partial electronic conductivity of the electrolyte as a function of oxygen partial pressure. Based on this analysis, the actual electrochemical transport reactions that occur during EVD growth of the electrolyte are elucidated. Finally, the possible use of such growth rate measurements as a function of temperature to arrive at a model for the electrolyte EVD growth rate is outlined.

(a) Rate Controlling Step in the EVD Growth of the Yttria-Stabilized Zirconia Electrolyte:

It was found in the previous section that the EVD growth of the

electrolyte is parabolic with time; the parabolic rate constant, K' , being equal to $0.37 \times 10^{-8} \text{cm}^2/\text{sec}$. This parabolic rate constant can also be expressed in terms of the rate of equivalents of oxygen consumed in the reaction as follows:

$$K' = K_{\gamma} V_{\text{eq}} \quad [4]$$

where K_{γ} is the parabolic specific rate constant in equiv./cm-sec;
and V_{eq} is the equivalent volume of oxygen in ZrO_2 -10% Y_2O_3
in cm^3/equiv .

Substituting the values of K' and V_{eq} in Equation [4], one gets:

$$K_{\gamma} = 0.7 \times 10^{-9} \text{ equiv/cm-sec} \quad [5]$$

Using Wagner's transport theory for parabolic growth (11), the specific rate constant, K_{γ} , can be written as:

$$K_{\gamma} = \frac{R T}{2 |Z| F^2} \int_{P_{\text{O}_2}'}^{P_{\text{O}_2}''} \frac{(\sigma_1 + \sigma_2) \sigma_3}{(\sigma_1 + \sigma_2 + \sigma_3)} d \ln P_{\text{O}_2} \quad [6]$$

where R is the gas constant (1.987 cal/deg-mole);
 T is the EVD reaction temperature (1473°K);
 Z is the valence of oxygen (2);
 F is the Faraday constant (23060 cal/volt-mole);
 σ_1 , σ_2 and σ_3 are the partial cationic, anionic and electronic
conductivities of the electrolyte, respectively, in $\Omega\text{-cm}^{-1}$;
and P_{O_2}' and P_{O_2}'' are oxygen partial pressures at the electrolyte-
chloride and the electrolyte-oxygen/steam interfaces (4.3×10^{-18}
and 1.0×10^{-4} atm, respectively).

It is known from previous work (10,12) that in yttria-stabilized zirconia, at oxygen partial pressures from 1 atm to about 10^{-20} atm, the partial electronic conductivity (σ_3) and the partial cationic conductivities (σ_1) are negligible as compared to the partial anionic (oxygen ion) conductivity (σ_2). Therefore:

$$\sigma_2 \approx \sigma_1 + \sigma_2 \approx \sigma_1 + \sigma_2 + \sigma_3 \quad [7]$$

Substituting Equation [7] in Equation [6]:

$$K_{\gamma} = \frac{R T}{2 |Z| F^2} \left. \right\}_{P_{O_2}'}^{P_{O_2}''} \sigma_3 d \ln P_{O_2} \quad [8]$$

In order to calculate the electronic transport number of the electrolyte film, t_3 , from Equation [8], we need to substitute σ_3 with the following expression:

$$\sigma_3 = t_3 (\sigma_1 + \sigma_2 + \sigma_3) = t_3 \sigma_{\Gamma} \quad [9]$$

where σ_{Γ} is the total conductivity of the yttria-stabilized zirconia electrolyte, which is virtually independent of oxygen partial pressure from 1 atm to about $10^{-2.2}$ atm between 873°K and 1573°K (10,12).

Substituting Equation [9] in Equation [8]:

$$K_{\gamma} = \frac{R T \sigma_{\Gamma}}{2 |Z| F^2} \left. \right\}_{P_{O_2}'}^{P_{O_2}''} t_3 d \ln P_{O_2} \quad [10]$$

or

$$\tilde{t}_3 = \frac{2 K_{\gamma} |Z| F^2}{R T \sigma_{\Gamma} (\ln P_{O_2}'' - \ln P_{O_2}')} \quad [11]$$

where \tilde{t}_3 is the average electronic transport number of the electrolyte film.

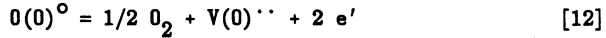
Using the average value of σ_{Γ} at 1473°K for ZrO_2 -10% Y_2O_3 as equal to $0.3 \Omega\text{-cm}^{-1}$ (9,10,12,13), \tilde{t}_3 is calculated to be 0.6×10^{-4} .

From Equation [8], it is clear that the partial electronic conductivity (σ_3) controls the parabolic specific rate constant, K_{γ} ; in other

words, the EVD growth of the electrolyte film is controlled by the electronic transport through the electrolyte with the rate controlling average electronic transport number being 0.6×10^{-4} .

(b) Determination of Partial Electronic Conductivity of Yttria-Stabilized Zirconia:

In this section, the defect structure of the yttria-stabilized zirconia is combined with the EVD growth data to determine the partial electronic conductivity of the yttria-stabilized zirconia electrolyte film. In low oxygen pressures, the defect equilibrium reaction of yttria-stabilized zirconia with oxygen can be expressed as (14-16):



$$K_{12} = \frac{P_{O_2}^{1/2} [V(O)^{\cdot\cdot}] [e']^2}{[O(O)^{\circ}]} \quad [13]$$

where K_{12} is the equilibrium constant for Reaction [12];
 $O(O)^{\circ}$, $V(O)^{\cdot\cdot}$ and e' are neutral oxygen, oxygen vacancy with two positive charge and free electron, respectively;
 and []'s are the respective concentrations.

It is known that in yttria-stabilized zirconia, the concentration of the majority defect, oxygen vacancies, is much larger than the concentration of the minority defect, free electrons (4,17). Hence, the concentration of oxygen vacancies, $[V(O)^{\cdot\cdot}]$, is not affected by Reaction (12) and is independent of the oxygen partial pressure, P_{O_2} . Equation [13] can therefore be written as:

$$[e'] = K_e P_{O_2}^{-1/4} \quad [14]$$

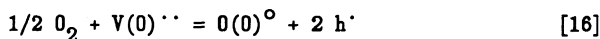
where K_e is a thermally activated constant.

If the free electron mobility is concentration-independent, then the partial free electronic conductivity, σ_e , is proportional to the concentration of electrons, $[e']$, and

$$\sigma_e = \sigma_e^{\circ} P_{O_2}^{-1/4} \quad [15]$$

where σ_e° is the partial electronic conductivity at $P_{O_2} = 1$ atm and it is also a thermally activated constant.

Under high to medium oxygen pressures, the defect equilibrium reaction of yttria-stabilized zirconia with oxygen can be written as (14-16):



$$K_{16} = \frac{[O(O)^{\circ}] [h^{\cdot}]^2}{[V(O)^{\cdot\cdot}] P_{O_2}^{1/2}} \quad [17]$$

where K_{16} is the equilibrium constant for Reaction [16]; and h^{\cdot} and $[h^{\cdot}]$ are free electron hole and its concentration, respectively.

Similar derivation as done above for low oxygen pressure conditions can be performed on Equations [16] and [17], and the free electron-hole conductivity, σ_h , under high to medium oxygen pressures can be expressed as:

$$\sigma_h = \sigma_h^{\circ} P_{O_2}^{1/4} \quad [18]$$

where σ_h° is the free-electron hole conductivity at $P_{O_2} = 1$ atm and is also a thermally activated constant.

In the oxygen partial pressure range of the EVD experiments (between 10^{-4} and 10^{-18} atm), the partial free electronic conductivity, σ_e , is much greater than the partial free electron-hole conductivity, σ_h (14,15). Therefore, one can write:

$$\sigma_3 = \sigma_e + \sigma_h \approx \sigma_e \quad [19]$$

Substituting Equation [19] in Equation [8]:

$$K_{\gamma} = \frac{R T}{2 |Z| F^2} \int_{P'_{O_2}}^{P''_{O_2}} \sigma_e d \ln P_{O_2} \quad [20]$$

Substituting for σ_e from Equation [15] in Equation [20]:

$$K_\gamma = \frac{R T}{2 |Z| F^2} \int_{P_{O_2}'}^{P_{O_2}''} (\sigma_e^\circ P_{O_2}^{-1/4}) d \ln P_{O_2} \quad [21]$$

or

$$K_\gamma = \frac{4 R T \sigma_e^\circ}{2 |Z| F^2} \left(P_{O_2}'^{-1/4} - P_{O_2}''^{-1/4} \right) \quad [22]$$

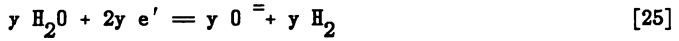
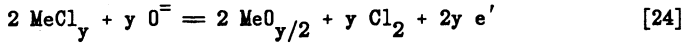
Using the value of K_γ from Equation [5] and solving Equation [22], we find that the partial electronic conductivity at 1473°K and 1 atm oxygen pressure, σ_e° , is equal to $0.6 \times 10^{-8} \text{ atm}(\Omega\text{-cm})^{-1}$; this value of σ_e° compares favorably with σ_e° calculated by earlier workers (14). Substituting this value of σ_e° in Equation [15], the partial free electronic conductivity at 1473°K can be expressed as:

$$\sigma_e = 0.6 \times 10^{-8} P_{O_2}^{-1/4} \quad [23]$$

Similar EVD growth rate measurements at other temperatures can be used for the determination of the partial electronic conductivity of yttria-stabilized zirconia as a function of temperature.

(c) Electrochemical Transport During EVD Growth of the Yttria-Stabilized Zirconia Electrolyte:

It has been shown above that the migration of electrons controls the EVD growth of the electrolyte. From Equation [14], it is obvious that the migration of electrons in the electrolyte film occurs from the chloride side (low oxygen partial pressure side) to the oxygen/steam side (high oxygen partial pressure side). Furthermore, the majority defects which are also the compensating defects for the electrons in yttria-stabilized zirconia are oxygen vacancies, (Equation [12]). Therefore, the migration of electrons in the electrolyte must be accompanied by the migration of oxygen vacancies in the same direction maintaining electroneutrality. The migration of oxygen vacancies can also be viewed as the migration of oxygen ions, O^{2-} , in the opposite direction, i.e., from the oxygen/steam side (high oxygen partial pressure side) to the chloride side (low oxygen partial pressure side). This electrochemical transport can be expressed in the form of general reaction equations as shown below:



The EVD growth rate measurements, described in this paper, were obtained only at one temperature (1473°K). However, such growth rate measurements can be made as a function of temperature to model the growth of yttria-stabilized zirconia films by electrochemical transport. For instance, the values of σ_e° can be obtained as a function of temperature from film growth rate measurements at different temperatures. Since σ_e° is a thermally activated constant, it can be expressed as:

$$\sigma_e^{\circ} = A \exp (-E_e/RT) \quad [26]$$

where A is a constant related to the total concentration of electrons; and E_e is the activation energy for free electronic conduction.

Plotting $\ln \sigma_e^{\circ}$ as a function of $(1/T)$, E_e can be estimated from the slope of the line and A can be estimated from the intercept at $1/T = 0$. Now, substituting Equation [26] in Equation [22]:

$$K_{\gamma} = \frac{4 R T A \exp(-E_e/R T) (P'_{\text{O}_2}{}^{-1/4} - P''_{\text{O}_2}{}^{-1/4})}{2 |Z| F^2} \quad [27]$$

This equation can be used to predict the parabolic growth of the yttria-stabilized zirconia film at any given temperature and oxygen partial pressures employed during EVD process.

4. SIMILARITY BETWEEN EVD GROWTH ANALYSIS AND OXYGEN SEMI-PERMEABILITY FLUX ANALYSIS

Oxygen semi-permeability in an electrolyte is defined by the flux of oxygen ions that occurs through the electrolyte when the electrolyte is kept in an oxygen potential gradient. Kleitz (14) showed that when the electrolyte is kept in an oxygen potential gradient, a flux of free electrons or electron holes streams continuously through the electrolyte; it is electrically compensated by a counter migration of oxygen ions. The net effect is a flux of oxygen through the electrolyte. In the oxygen partial pressure range where the free electron conductivity is dominant, the oxygen semi-permeability flux, J_{O_2} is given by the expression (14,18):

$$\tilde{J}_{O_2} = \frac{R T}{4 F^2 L} (\sigma_e' - \sigma_e'') \quad [28]$$

where σ_e' and σ_e'' are the partial free electronic conductivities in the low oxygen partial pressure side and the high oxygen partial pressure side of the electrolyte, respectively;
and L is the thickness of the electrolyte.

Combining Equation [15] and Equation [22], the parabolic specific EVD growth rate constant of the electrolyte, K_γ , can be written as:

$$K_\gamma = \frac{4 R T}{2 |Z| F^2} (\sigma_e' - \sigma_e'') \quad [29]$$

Substituting the value of Z (2 for oxygen):

$$K_\gamma = \frac{R T}{F^2} (\sigma_e' - \sigma_e'') \quad [30]$$

K_γ can also be expressed in terms of flux of oxygen through the electrolyte film as:

$$\frac{K_\gamma}{\Delta x} = \frac{\dot{n}}{A} = 4 J_{O_2} \quad [31]$$

where \dot{n}/A is the flux of oxygen equivalents expressed in equiv/cm²-sec;
 Δx is the thickness of the electrolyte film;
and J_{O_2} is the flux of oxygen through the growing electrolyte film.

Combining Equations [31] and [29], one can write:

$$J_{O_2} = \frac{K_\gamma}{4 \Delta x} = \frac{R T}{4 F^2 \Delta x} (\sigma_e' - \sigma_e'') \quad [32]$$

It is seen that the expressions for flux obtained in Equation [32] from the EVD growth analysis and in Equation [28] from oxygen semi-permeability analysis are similar. This suggests that the EVD growth of the yttria-stabilized zirconia electrolyte films can also be interpreted in terms of the phenomena of oxygen semi-permeability.

5. CONCLUSIONS

The growth of yttria-stabilized zirconia electrolyte films, by the electrochemical vapor deposition (EVD) process, is found to be parabolic with time and the rate controlling step in the EVD process is identified to be the electronic transport (diffusion of electrons) through the electrolyte film. The average electronic transport number of the electrolyte during EVD at 1473°K is calculated to be 0.6×10^{-4} . Using the defect structure of yttria-stabilized zirconia and the transport theory for parabolic growth, the partial electronic conductivity of the EVD grown electrolyte has been estimated as a function of oxygen partial pressure. It is shown that such growth rate measurements as a function of temperature can be used to predict a model for the electrolyte EVD growth as a function of temperature and oxygen partial pressures. Finally, it is demonstrated that the electrochemical transport that occurs during EVD is similar to the phenomena of oxygen semi-permeability wherein electrons migrate from the low oxygen partial pressure side to the high oxygen partial pressure side and oxygen ions migrate in the reverse direction maintaining electroneutrality.

ACKNOWLEDGMENTS

The authors would like to acknowledge the dedicated efforts of G. R. Folser and J. A. Fraino in conducting the EVD experiments and Mrs. J. A. Radford for her patience in typing the manuscript. The help of T. A. Manion in preparing the metallographic mounts and R. W. Palmquist in analyzing the samples with electron microprobe is greatly appreciated. This work was funded by the U.S. Department of Energy under Contract Number DE-AC21-80ET17089 and the Westinghouse Electric Corporation.

REFERENCES

1. R. J. Ruka and J. Weissbart, "A Solid Electrolyte Fuel Cell," J. Electrochemical Society, 109, (1962), p. 723.
2. W. Feduska and A. O. Isenberg, "High Temperature Solid Oxide Fuel Cell-Technical Status," J. of Power Sources, 10, (1983), p. 89.
3. S. C. Singhal, "Materials for High Temperature Solid Oxide Fuel Cells," Extended Abstracts, 87-2, Abstract No. 180, The Electrochemical Society Fall Meeting, Honolulu, Hawaii, (1987), p. 265.
4. H. Rickert, "General Aspects of Solid Electrolytes," in Fast Ion Transport in Solids, Solid State Batteries and Devices, Edited by W. van Gool, North Holland Publishing Company, Amsterdam, (1973), p. 3.

5. A. O. Isenberg, "Growth of Refractory Oxide Layers by Electrochemical Vapor Deposition (EVD) at Elevated Temperatures", in Proceedings of the Symposium on Electrode Materials and Processes for Energy Conversion and Storage, The Electrochemical Society, Inc., 77-6, (1977), p. 572.
6. A. O. Isenberg, "Processing and Performance of High Temperature Solid Electrolyte Fuel Cells - State of the Art," Abstracts, National Fuel Cell Seminar, San Diego, CA, (1980), p. 135.
7. A. O. Isenberg, "Energy Conversion via Solid Oxide Electrochemical Cells at High Temperatures," *Solid State Ionics*, 314 (1981), p. 431.
8. U. B. Pal and S. C. Singhal, "Growth Mechanism of Perovskite Films by Electrochemical Vapor Deposition," in Proceedings of the Sixth (IUPAC) International Conference on High Temperatures - Chemistry of Inorganic Materials, Gaithersburg, MD, (1989).
9. D. W. Strickler and W. G. Carlson, "Ionic Conductivity of Cubic Solid Solutions in the System (CaO-Y₂O₃-ZrO₂)," *J. of the American Ceramic Society*, 47, (1964), p. 122.
10. E. C. Subbarao, "Zirconia - An Overview," in Advances in Ceramics - Science and Technology of Zirconia, 3, Edited by A. H. Heuer and L. W. Hobbs, The American Ceramic Society, Inc., Columbus, OH, (1981), p. 254.
11. C. Wagner, "Contribution to the Theory of Formation of Oxidation Films," *Zeitschrift fur Physikalische Chemie B*, 21, (1933), p. 25.
12. C. B. Choudhary and E. C. Subbarao, "Electrical Conduction in the Cubic Fluorite Phase in the System ZrO₂-YO_{1.5}-TaO_{2.5}," in Fast Ion Transport in Solids, Electrodes and Electrolytes, Edited by P. Vashista, J. N. Mundy and G. K. Shenoy, North Holland Publishing Company, Amsterdam, (1979), p. 665.
13. Y. Suzuka and K. Sugiyama, "The Temperature Dependence of the Electrical Conductivity of ZrO₂-12 mole% Y₂O₃ Single Crystal," *J. of Ceramic Society of Japan*, 95, ²(1987), p. 480.
14. M. Kleitz, E. Fernandez, J. Fouletier and P. Fabry, "Determination of Electronic Conductivities and Ionic Domains of ZrO₂-Y₂O₃ by Semipermeability Measurements," in Advances in Ceramics - Science and Technology of Zirconia, 3, Edited by A. H. Heuer and L. W. Hobbs, The American Ceramic Society, Inc., Columbus, OH, (1981), p. 349.
15. J. W. Patterson, E. C. Bogren, and R. A. Rapp, "Mixed Conduction in Solid Electrolytes," *J. Electrochemical Society*, 114, (1967), p. 752.

16. C. Wagner, "Mechanism of Electric Conduction in Nernst Glower," *Naturwissenschaften*, 31, (1943), p. 265.
17. H. Schmalzried, "Transport Theory of Oxide Electrolytes," in Advances in Ceramics - Science and Technology of Zirconia, 3, Edited by A. H. Heuer and L. W. Hobbs, The American Ceramic Society Inc., Columbus, OH, (1981), p. 254.
18. F. A. Kroger, "Chemical Effects Related to the Presence of Imperfections," in The Chemistry of Imperfect Crystals, 3, North Holland Publishing Company, Amsterdam, (1974), p. 105.

TABLE 1
Cell Components, Materials and Fabrication Processes

<u>Component</u>	<u>Material</u>	<u>Fabrication Process</u>
Support Tube	$ZrO_2(CaO)$	Extrusion-sintering
Air Electrode	$La(Sr)MnO_3$	Slurry coat-sintering
Electrolyte	$ZrO_2(Y_2O_3)$	Electrochemical vapor deposition
Interconnection	$La(Mg)CrO_3$	Electrochemical vapor deposition
Fuel Electrode	$Ni-ZrO_2(Y_2O_3)$	Slurry coat-electrochemical vapor deposition

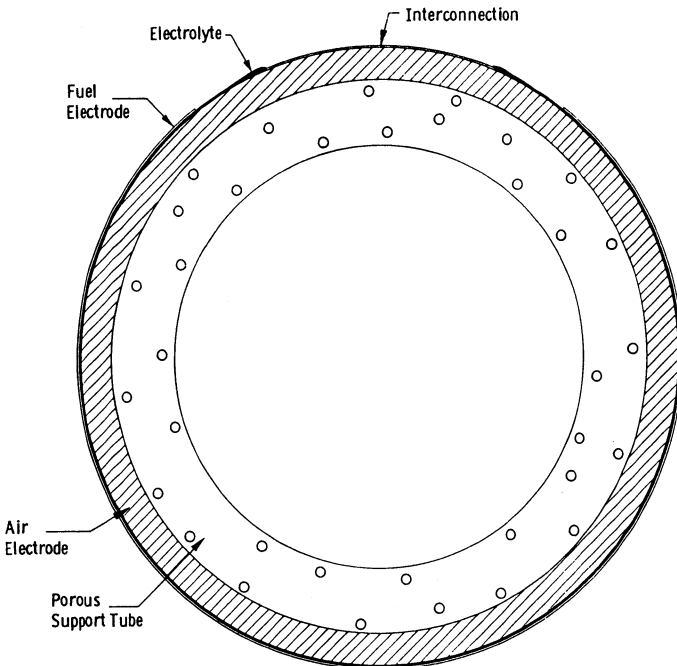
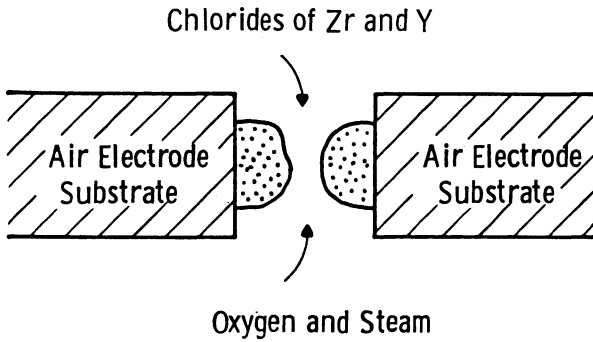


Figure 1 - Schematic cross-section of the tubular solid oxide fuel cell.

Reaction Stage I (CVD)
Molecular Diffusion



Reaction Stage II (EVD)
Electrochemical Transport

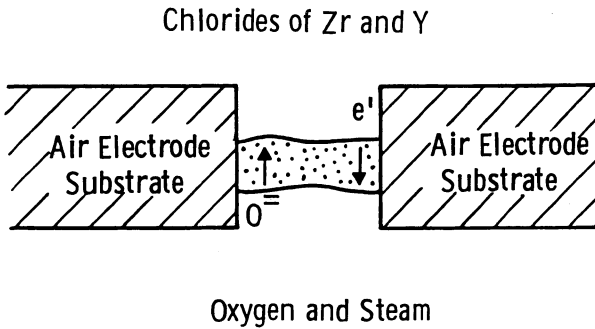


Figure 2 - Two stages of reaction occurring during the deposition of the yttria-stabilized zirconia.

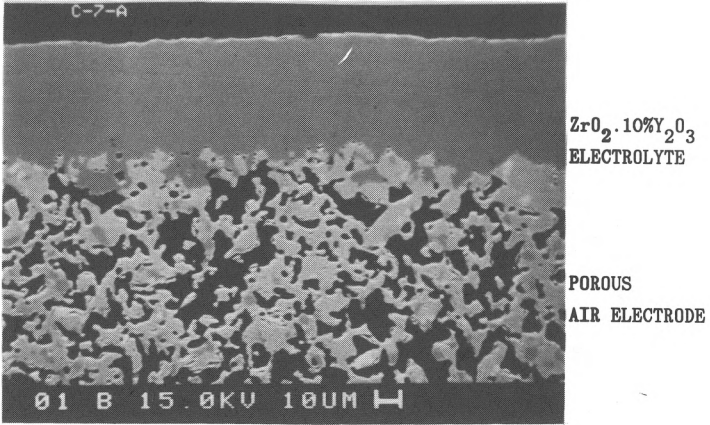


Figure 3 - Metallographic cross section of the EVD grown yttria-stabilized zirconia film over porous air electrode substrate.

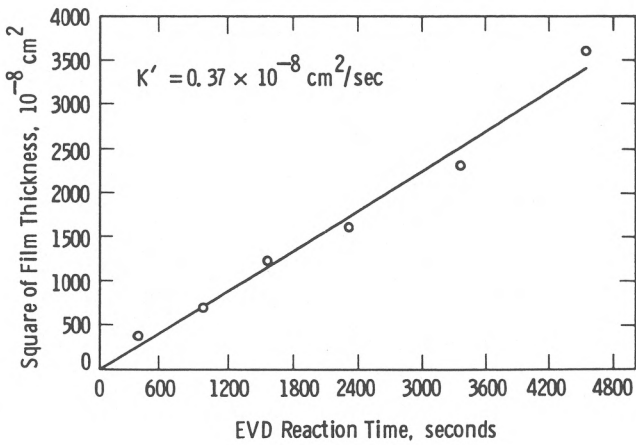


Figure 4 - Square of electrolyte film thickness versus deposition time at 1473^oK.

ELECTROCHEMICAL VAPOR DEPOSITION OF SOFC COMPONENTS

J.P. Dekker, N.J. Kiewiet*, J. Schoonman
Laboratory for Inorganic Chemistry,
Delft University of Technology
P.O. Box 5045, 2600 GA Delft, the Netherlands
*also: Institute of Applied Chemistry TNO
P.O. Box 108, 3700 AC Zeist, the Netherlands

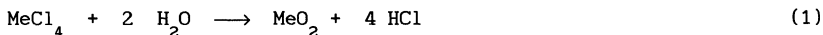
ABSTRACT

The kinetics for film growth of yttria doped zirconia are modeled considering a Wagner oxidation process. The growth kinetics are examined as a function of reaction temperature, yttria content in the film, as well as the oxygen partial pressure gradient across the film. Calculated results indicate that only at temperatures above 1300 K, and low doping levels is the growth rate governed by the diffusion of electrons. With decreasing temperature and increasing yttria content the diffusion of holes becomes increasingly important in the growth rate. These model studies are used to explain differences in observed morphologies of EVD grown films of YSZ.

1. Introduction

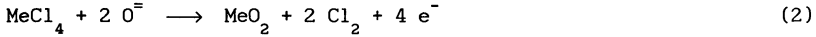
Electrochemical vapor deposition (EVD) is a technique for producing thin (10-50µm) gas tight layers of metal oxides upon porous substrates (1). The first step in film formation proceeds by a normal CVD type reaction.

Step 1, Pore closure:



The substrate separates the reactant metal chlorides from a mixture of H₂ and steam. Deposits of the metal oxide forming in the pores of the substrate eventually lead to pore closure. Once pore closure is complete the reactants are no longer in direct contact. Film growth proceeds due to the large oxygen partial pressure gradient which exists across the film. Typically, on the H₂O/H₂ side the oxygen partial pressure (P_{O₂}) is 10⁻⁴ atm, whereas on the metal chloride side it is on the order of 10⁻¹⁶ atm. This large P_{O₂} gradient results in the diffusion of oxygen anions from the H₂O/H₂ side to the metal chloride side. The second step, scale growth, proceeds due to the reaction of oxygen anions with metal chlorides:

Step 2, Scale growth:



Carolan *et al.* have modeled the dynamics of the CVD step leading to pore closure for the growth of yttria doped zirconia (2). In this work the dynamics of the second step are examined as a function of the reaction temperature, yttria content in the film, and oxygen partial pressure gradient across the film.

2. Model

The kinetics for film growth are calculated considering a Wagner oxidation process (3,4). In this case film growth is governed by solid state diffusion through the oxide. The diffusion processes which take place during EVD growth are shown schematically in Figure 1. The partial pressure of oxygen on the $\text{H}_2\text{O}/\text{H}_2$ side of the substrate (P_{O_2}) is determined by the equilibrium between the gases. Similarly the oxygen partial pressure on the metal chloride side (P_{O_2}') is determined by the equilibrium between MeCl_4 , Cl_2 , and MeO_2 . The large oxygen partial pressure gradient across the film results in a flux of oxygen anions (O^{\ominus}) to the metal chloride side. Electroneutrality is preserved through an opposing electronic flux. At steady state the sum over the ionic (i), electronic (e') and hole (h') fluxes is given by:

$$i = 0 = \sum_{i,e,h} Z_k J_k \quad (4)$$

where Z_k is the charge on species k, and J_k the flux of species k. In Wagner oxidation the rate of scale growth is inversely proportional to the oxide thickness, L (3).

$$\frac{dL}{dt} = K \frac{1}{L} \quad (5)$$

The integrated form of equation 5 yields the parabolic rate law

$$L^2 = 2Kt + C_0 \quad (6)$$

where C_0 is a constant of integration.

Alternatively the growth rate can be expressed in terms of the ionic flux. Assuming that all anions that pass through the film react to produce electrolyte, the growth rate is given by:

$$\frac{dL}{dt} = \frac{1}{2} J_1 \frac{mw}{\rho} \quad (7)$$

where ρ and mw are the density and molecular weight of the growing oxide. For an ionic conductor the general expression for the ionic flux is given by (4):

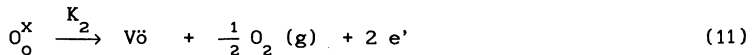
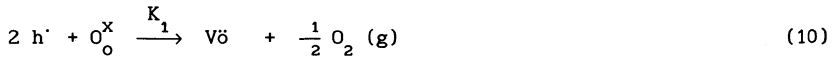
$$J_1 = - \left[\frac{kT}{8e^2} \int_{P_{O_2}}^{P_{O_2}'} \sigma_{e1} d \ln P_{O_2} \right] \frac{1}{\Delta L} \quad (8)$$

where k is Boltzmann's constant, T is absolute temperature, e is the charge of an electron, and σ_{e1} the sum of the electron and hole conductivities. From equations 7 and 8 the rate constant for film growth can be derived yielding:

$$K = - \frac{1}{16} \left[\int_{P_{O_2}}^{P_{O_2}'} [h'] D_h + \int_{P_{O_2}'}^{P_{O_2}'} [e'] D_e \right] d \ln P_{O_2} \quad (9)$$

where $[h']$ and $[e']$ represent the mole fraction of holes and electrons and D_h and D_e their respective diffusion coefficients. The pressure at which the electronic conductivity changes from n type to p type is represented by P_{O_2}' .

The rate constant is integrated in parts to take into account the variation in $[h']$ and $[e']$ with oxygen partial pressure. The pressure dependence of $[h']$ and $[e']$ can be understood by considering the defect reactions responsible for their formation. In YSZ, the formation of doubly charged oxygen vacancies $[V\ddot{o}]$ results in the formation of quasi-free electrons and the annihilation of holes. In Kröger-Vink notation these defect reactions are written as:



Solving for $[h']$ and $[e']$ from the above reactions yields the equilibrium expressions:

$$[h'] = \frac{[V\ddot{o}]^{1/2} P_{O_2}^{1/4}}{[O_o^X]^{1/2} K_1^{1/2}} \quad (12)$$

$$[e'] = \frac{[O_o^X]^{1/2} K_2^{1/2}}{[V\ddot{o}]^{1/2} P_{O_2}^{1/4}} \quad (13)$$

Thus, the hole concentration varies with $P_{O_2}^{1/4}$ whereas the electron concentration varies with $P_{O_2}^{-1/4}$.

Under typical EVD growth conditions the oxygen partial pressure gradient ranges from 10^{-4} atm to 10^{-16} atm. The variation of the electronic conductivity over this pressure range is shown in Figure 2. At high P_{O_2} holes dominate the electronic conductivity whereas at low P_{O_2} electrons dominate the electronic conductivity. As shown in Figure 2, the log of P_{O_2} varies linearly with temperature. With increasing yttria content (X) this line shifts to higher oxygen partial pressures.

To obtain numerical values for K the functional dependence, $f(X, T, P_{O_2})$, for σ as well as D_h , D_e , K_1 , K_2 and $V\ddot{o}$ were calculated. The data necessary for these calculations was derived from the work of Weppner (5,6) and Honke (7). The lower limit of integration, P_{O_2} , was determined by the equilibrium of the H_2O , H_2 , O_2 gas mixture at a given temperature. The integration limit P_{O_2}' was taken to vary with X and T according to the functional dependence given in Figure 2. The upper limit, P_{O_2}'' , is taken to be 10^{-16} atm throughout these calculations.

3. Results

The total rate constant for film growth is the sum of the electronic (K_e) and hole contributions (K_h). The effect of increasing temperature upon the relative magnitudes of K_e and K_h is shown in Figure 3. At low temperatures, $T < 1300$, K_e is of the same order of magnitude as K_h and both contribute of the overall growth rate. With

increasing temperatures K_e rapidly becomes orders of magnitude greater than K_h . The contribution of holes is so small at high temperatures that film growth is rate limited by the diffusion of electrons alone.

Not only does temperature affect the relative magnitudes of K_e and K_h but also the mole fraction dopant (Y_2O_3) affects the film growth rate. Addition of Y_2O_3 to ZrO_2 results in the formation of oxygen vacancies. From the equilibrium expressions for $[h']$ and $[e']$, it is clear that with increasing V_o , $[h']$ increases and $[e']$ decreases. Consequently, with increasing Y_2O_3 , K_h increases while K_e decreases (Figure 4). At very low reaction temperatures and high X the diffusion of holes dominate the film growth kinetics, $K_h > K_e$.

Under most conditions ($T > 1100$ K and $X < 0.10$) the overall rate constant decreases with increasing yttria content (Figure 5). The Arrhenius plot (Figure 6) yields an activation energy of 3.85 eV for the growth of 10 mole percent Y_2O_3 in ZrO_2 . These calculations predict a relatively slow growth rate for YSZ. The average K is on the order of 10^{-10} (cm^2/sec). Applying the parabolic rate law yields an average growth rate of 6 $\mu m/hour$. Similar growth rates have been observed by Isenberg *et al.* (1).

4. Experimental

A schematic drawing of the EVD reactor used to grow thin films of YSZ is shown in Figure 7. Films were grown on calcium stabilized zirconia. Typically, the open porosity of the substrate was 40 % having an average pore diameter of 5 μm . A 80:20 mixture of H_2 in steam was passed along one side of the substrate. On the other side a mixture of volatilized yttrium and zirconium chlorides was passed in an argon stream. Films were grown under reduced pressure (10 torr) and temperatures between 1200-1375 K.

Scanning electron micrographs were taken with a JEOL JSM35 operating at 25 kV. Films grown under these conditions are shown in Figure 8. Two types of morphologies are observed: a somewhat faceted surface for films grown below 1300 K and a cauliflower textured surface for films grown above 1300 K. The turning point in observing one morphology over the other occurs at the same temperature in which the kinetics of film growth becomes dominated by electron diffusion. The change from a faceted surface to a cauliflower surface can be explained by a change in kinetics. A faceted surface forms when the reaction proceeds slowly through the diffusion of both electrons and holes. At temperatures above 1300 K and $X < 0.10$, the growth rate is determined by the diffusion of electrons. Film growth is much

faster when limited only by electron diffusion and results in the cauliflower textured surface.

6. Conclusions

Kinetic model studies yield an average growth rate of 6 $\mu\text{m}/\text{hour}$ for the EVD scale growth of yttria stabilized zirconia. The activation energy is calculated to be 3.85 eV for the growth of 10 mole percent Y_2O_3 in ZrO_2 . These results are in quantitative agreement with experimental observations (1). Model studies indicate that film growth is rate limited by the diffusion of both electrons and holes. The hole contribution to the overall growth rate is greatest at low temperatures and high doping levels. At temperatures above 1300 K film growth becomes dominated by the diffusion of electrons. The change in kinetics which occurs at 1300 K can account for the different film morphologies which form at temperatures above and below 1300 K.

References

1. A.O. Isenberg, in : ECS Symposium Electrode Materials, Processes Energy Conver. Storage 77-6, 562 (1977).
2. M.F. Carolan, J.N. Micheals, Solid State Ionics 25, 207, (1987).
3. C. Wagner, Z. Physik. Chem. B21, 25, (1933).
4. P. Kofstad, Nonstoichiometry, Diffusion, and Electrical Conductivity in Binary Metal Oxides (Wiley: New York, 1972).
5. W. Weppner, J. Solid State Chem. 20, 305 (1977).
6. W. Weppner, Electrochim. Acta 22, 721 (1977).
7. D.K. Hohnke, "Ionic Conduction in Doped Zirconia", Fast Ion Transport in Solids, eds. P. Vashishta, J.N. Mundy, and G.K. Shenoy (North-Holland: New York, 1979) pp. 669-672.

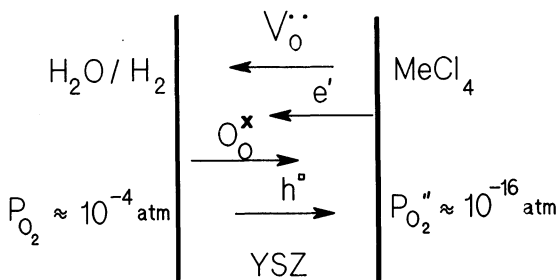


Figure 1: Diffusion processes occurring during the EVD growth of YSZ.

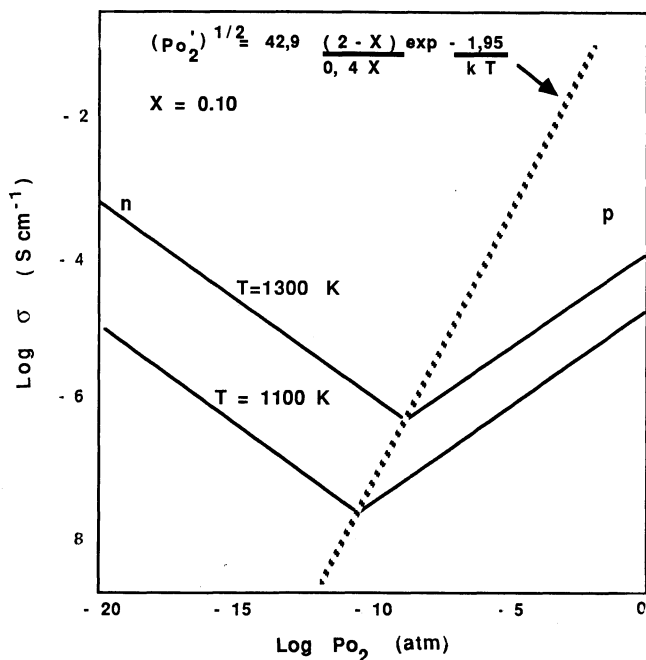


Figure 2: Dependence of the partial conductivity as a function of oxygen partial pressure. (Data adapted from Weppner (5,6).)

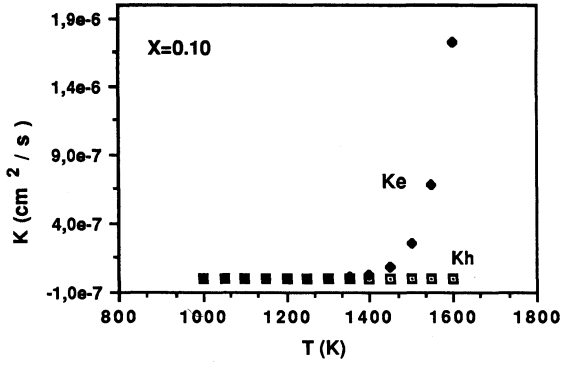


Figure 3: Temperature dependence of K_e and K_h for $ZrO_2 + 10 \text{ m/o } Y_2O_3$.

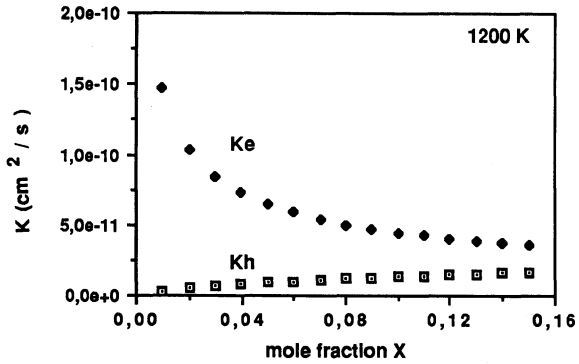


Figure 4: Dependence of K_e and K_h upon mole fraction (X) of Y_2O_3 at 1200 K.

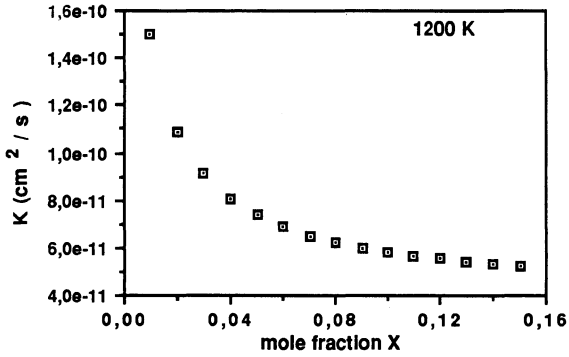


Figure 5: Plot of the overall rate constant ($K = K_e + K_h$) versus mole fraction (X)

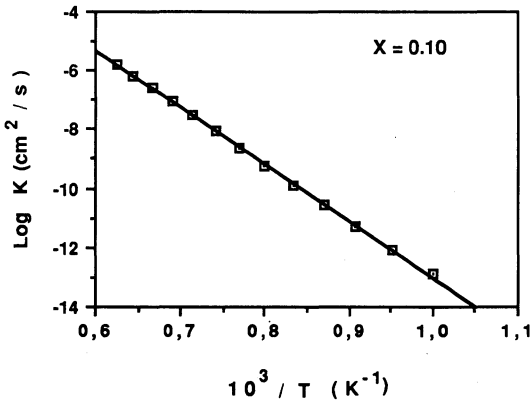


Figure 6: Arrhenius plot of overall rate constant for $\text{ZrO}_2 + 10 \text{ m/o } \text{Y}_2\text{O}_3$.

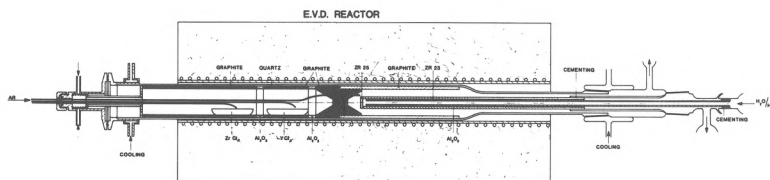


Figure 7: Schematic of EVD reactor used to grow thin films of YSZ.

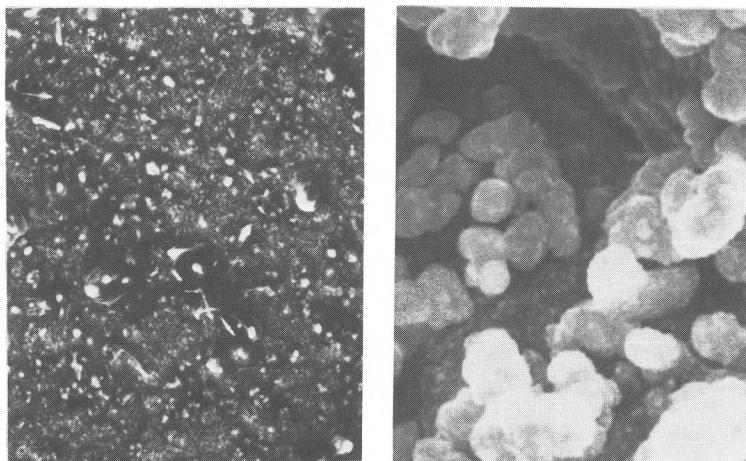


Figure 8: Scanning electron micrographs of EVD grown films of YSZ. Left: Film grown at 1273 K for 150 min. at 10 torr (500X). Right: Film grown at 1334 K for 135 min. at 10 torr (5000X).

THIN ELECTROLYTE LAYERS FOR SOFC
VIA MODIFICATION OF CERAMIC MEMBRANES
BY CVD AND EVD

Y.S. Lin, L.G.J. de Haart, K.J. de Vries
and A.J. Burggraaf

Laboratory of Inorganic Chemistry, Materials Science
and Catalysis, University of Twente, P.O.Box 217
7500 AE Enschede, The Netherlands

ABSTRACT

The efficiency of state-of-the-art solid oxide fuel cells can be improved by applying YSZ electrolyte layers with thicknesses reduced to a few micrometers. This will allow the operating temperature of reactors made of these SOFC's to be lowered to 800 - 900 °C. The membrane-based thin electrolyte layer SOFC technology is therefore being developed. A ceramic membrane is deposited on and integrated with the supported porous cathode layer. A modified-CVD process combined with an Electrochemical Vapor Deposition (EVD) process is used to grow a (very) thin gas tight YSZ layer on this composite layer system. Preliminary experimental depositions on alumina substrates show the formation of a gas tight YSZ layer (thickness of a few microns) after 6 hours of deposition.

1 INTRODUCTION

Solid oxide fuel cells (SOFC) reactors are attractive energy conversion systems. They have a very reasonable efficiency compared to the conventional systems based on fuel combustion. Increase in usefulness of SOFC reactors can be achieved when the limitations of presently developed reactors can be avoided or at least decreased. There are two main limitations. The first is related to the use of cubic yttria-stabilized zirconia (YSZ) as electrolyte. The value of the (specific) conductivity of this material requires SOFC reactor operating temperature of 1000 °C in order to reach an acceptable high conductivity of the applied electrolyte layers, which have a thickness of about 60 - 150 μm . This high operating temperature lowers the obtainable OCV considerably. The second limitation is the perovskite-type cathode material, usually Sr-doped LaMnO_3 , which causes too high electrode polarization losses, besides ohmic $I \cdot R$ losses, when the current path from the electrolyte/electrode interface through the cathode layer to the interconnection material (ICM) is too long.

In this contribution we present the membrane-based thin YSZ electrolyte layer SOFC technology. We aim to present a technology to reduce the layer thickness of the presently applied YSZ electrolyte layers to thicknesses of a few microns or less. This will decrease the ohmic polarization losses. Such a considerable reduction of the electrolyte layer thickness will allow the SOFC reactors to be operated at lower temperatures (800-900 °C).

These (very) thin electrolyte layers require to be supported when produced. A suitable production technique for thin supported YSZ layers is Electrochemical Vapor Deposi-

tion (EVD). The EVD technique has been used (1-3) demonstrating its unique ability to form relatively thin gas tight YSZ films on porous substrates. In order to apply EVD in the production of very thin gas tight YSZ layers, a ceramic toplayer with porous membrane characteristics has to be developed.

The procedure for constructing the membrane-based thin electrolyte layer SOFC includes: (i) deposition of a (thin) porous cathode layer on a coarse-pore ceramic support; (ii) deposition on and integration with the supported porous cathode layer of a porous ceramic toplayer with membrane properties; (iii) growth of a very thin and gas tight YSZ layer by a combined CVD and EVD procedure onto the supported porous membrane toplayer and (iv) providing a porous anode layer by filmcoating onto the thin gas tight YSZ layer.

The deposition process of YSZ starts with a CVD step in which YSZ is deposited in the membrane pores due to the reaction between water vapor and a mixture of $ZrCl_4$ and YCl_3 vapor in a desired ratio. The two separate gas streams, one with the chloride vapors and one with the water, enter the system from the membrane side and from the coarse-pore support side respectively. After closure of the membrane pores by the formation of a YSZ plug, layer growth starts due to the EVD process (3,4).

In the present investigation we report on the theoretical study of the kinetics of the EVD phase of the deposition process and on preliminary experimental results of growing thin YSZ films on porous alumina substrates.

2 THEORETICAL AND EXPERIMENTAL

An important aspect of the CVD phase of the YSZ deposition in the membrane pores is, that plug formation in the pore occurs near the upper surface of the membrane toplayer, i.e. near the surface of the supported system at which the metalchloride mixture is delivered. Then the formed gas tight YSZ layer can be kept as thin as possible.

Mathematical analysis (4) shows that the CVD process is mainly determined by six independent parameters. The main parameter governing the location of pore-closure in the membrane toplayer is the Thiele modulus ϕ . Approximately the Thiele modulus can be considered to be proportional to the ratio of the reaction rate constant (K) to the effective pore diffusivity for the metalchloride mixture (D_{cg}):

$$\phi = K / D_{cg} \quad (1)$$

A larger Thiele modulus results in location of pore-closure nearer to the metalchloride delivery side.

In the EVD phase of the YSZ layer deposition process the film growth is determined by four mass transfer steps: (i) water (or oxygen) diffusion in the substrate pore, (ii) charge-transfer reaction at the interface between the EVD film and the water vapor, (iii) electrochemical transport in the EVD layer and (iv) charge-transfer reaction (formation of solid oxide) at the interface between the EVD film and metal chloride vapor. Assuming a quasi steady-state and using Wagner-type approach, the kinetics of the EVD film growth is described by a mathematical model which considers all four mass transfers.

From the solution of the model it is found, that the function of EVD film thickness versus deposition time, $H(t)$, is parabolic only when electrochemical transport in the growing

EVD film is the rate-limiting step:

$$H(t) = k \cdot t \quad (2)$$

If any one of the other three mass transfer steps is the rate-limiting step, $H(t)$ should be a linear relation. Mathematical analysis further shows that the rate-limiting step for deposition of YSZ on the porous substrate under the conditions as reported previously (1,3) as well as in the present investigation is water (oxygen) diffusion in the substrate pore.

As a preliminary experimental investigation, the EVD experiments were concentrated on the deposition of YSZ layers on porous alumina substrate disks. The experiments were performed in a CVD/EVD apparatus. The main part of the apparatus is an alumina tube reactor heated by a six zone furnace. All the experimental conditions such as reaction zone temperature, gas delivery and system pressure could be controlled in this apparatus. Typical experimental conditions were: total concentration of metal chloride vapor = 2.0×10^{-9} mol/ml; $YCl_3/ZrCl_4$ ratio in vapor phase = 1:5; total pressure in reaction zone = 1.5 mbar; total water vapor concentration = 3.5×10^{-9} mol/ml and the deposition temperature = 1000 °C. The two substrates used were porous alumina disks with mean pore sizes of 11.0 and 0.16 μm , respectively. The deposition results were characterized by XRD, SEM and EDS.

It was found, that after 6 hours deposition (or longer) a gas tight YSZ layer was formed on the side of the substrate exposed to the metal chloride vapor. The XRD and EDS data show that this layer has a FCC crystal structure with an Y_2O_3/ZrO_2 ratio of about 8%. This is apparently being determined by the $YCl_3/ZrCl_4$ ratio in the metal chloride vapor. The deposit of the solid oxide penetrates only a few microns deep into the substrate pores. Figure 1 shows a SEM photograph of a deposit. The deposited film thickness is in the range of a few microns. The deposition time required for depositing approximately the same thickness of EVD film on two substrates with different pore-sizes was determined in order to examine the predictability of the film growth theory. Based on these preliminary experimental results, as well as on theoretical understanding of the film growth kinetics, the deposition of the solid electrolyte layer by the EVD process will be optimized.

ACKNOWLEDGEMENT

The investigations were partly supported by the Dutch Ministry of Economical Affairs (Research Project 'ECVD Synthesis and Properties of Porous Composite Systems', IOP Technical Ceramics, No. 87 A045) and partly performed under contract with the Commission of the European Communities (CEC) within the Non-Nuclear Energy R and D Programme (contract no. EN3E-175-NL).

REFERENCES

- (1) A.O. Isenberg, ECS Symp. Electrode Materials, Processes for Energy Conversion and Storage, Vol. 77-6 (1977) 572
- (2) G. Dietrich and W. Schäfer, J. Hydrogen Energy 9 (1984) 747
- (3) M.P. Carolan and J.N. Micheals, Solid State Ionics 25 (1987) 207
- (4) Y.S. Lin, K.J. de Vries and A.J. Burggraaf, accepted for presentation at EURO CVD 7, June 19-23, 1989, Perpignan, France
- (5) P. Kofstad, High Temperature Oxidation of Metals, Ch. 5, Wiley (1966)

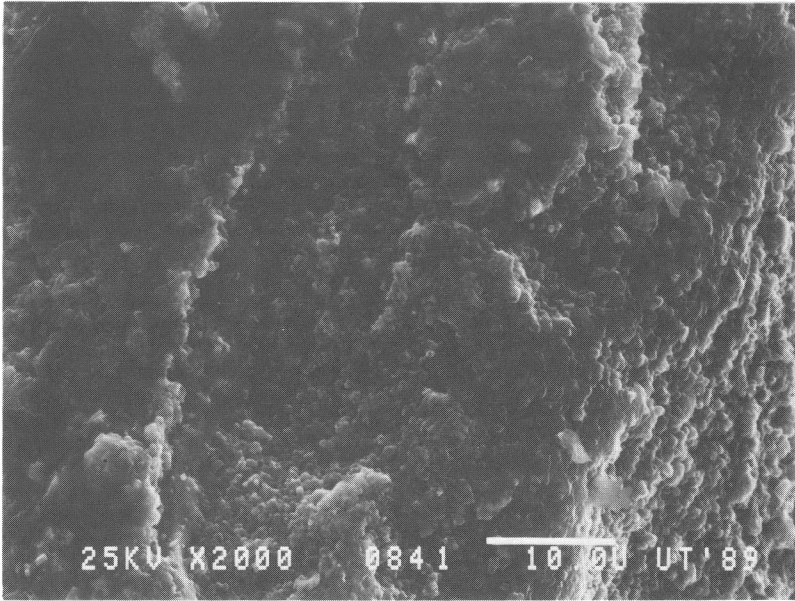


FIGURE 1

SEM photograph of a CVD/EVD deposit of yttria-stabilized zirconia (YSZ) on a porous alumina substrate. The left-hand side of the picture shows the YSZ deposit, while the fracture surface of the alumina substrate is visible on the right-hand side. Near the fracture surface the YSZ deposit has been peeled off, leaving still a small part of the deposit visible at the top-center of the picture.

Characteristics of Electrolyte Processed
by CO₂ Laser Evaporation Techniques

H. Nakagawa, S. Kosuge, H. Tsuneizumi,
E. Matsuda, H. Mihara and Y. Sato
N K K Corporation
1-1 Minamiwatarida-cho Kawasaki-ku
Kawasaki 210, Japan

ABSTRACT

The CO₂ laser evaporation (laser PVD) technique was studied to form dense and thin 8 mol% yttria stabilized zirconia (YSZ) electrolyte films. The process parameters for laser PVD were determined on the basis of YSZ physical properties and Al₂O₃ evaporation conditions. Small-size cells of which electrolytes had been made by laser PVD were tested and their performances compared with low pressure plasma spraying, plasma spraying and detonation spraying cells. On the laser PVD cells, highest open circuit voltage and lowest IR drop obtained. A scanning electron microscope study and other characteristics measurements of the electrolyte films suggested laser PVD as one of the best electrolyte forming processes.

1. INTRODUCTION

In order to improve the SOFC performance, we have studied reducing the thickness of the electrolyte and its electric resistance by making dense and thin film of 8 mol% yttria stabilized zirconia (YSZ) by laser evaporation technique.

The CO₂ laser evaporation (laser PVD) technique has been recently developed in our laboratory(1). In this paper, we describe this CO₂ laser technique for dense and thin YSZ electrolyte film formation and compare it with other conventional processes such as plasma spraying, low pressure plasma spraying(2) and detonation spraying. By comparison of I-V characteristics of different fuel cells and physical properties of YSZ films, most desirable process for electrolyte film formation was determined.

2. CO₂ LASER EVAPORATION PROCESS FOR YSZ FILM

As a laser beam does not charge the target material with electricity, evaporation process in a vacuum chamber using the CO₂ laser as heating source has an advantage in comparison with thin film formation methods such as ion plating: it can stably melt and

evaporate the target material. Above all, CO₂ laser beam energy can be easily absorbed on oxides such as YSZ and Al₂O₃ because of CO₂ laser beam length (=10.6μm), resulting in high evaporation rate of oxides as shown in Fig.1.

However, laser beam irradiates the target in the vacuum chamber through a KCl window. Therefore, some amount of deposition on the window is inevitable and the window is more apt to break after absorbing beam energy during PVD processing than the conventional systems. In our laboratory, a special mechanism was devised to prevent the deposition on the KCl window and conduct laser PVD without cracking a window.

Fig.2 illustrates the schematic drawing of the the CO₂ laser evaporation technique. Target used consisted of powder, wherein the laser beam was irradiated on the target surface and target received lower laser energy density compared to a solid target, resulting in fairly uniform evaporation of the target material. The composition of the target was not adjusted.

The YSZ film was deposited at a pressure of 5×10^{-4} Torr. The targets consisting of powder were prepared from YSZ used for plasma spraying without composition adjustment because it did not change after evaporation. The powder size distribution was 10~44μm. The target was mounted about 75 mm apart from the substrate which was heated to 450°C during deposition, and irradiated by defocussed CO₂ laser beam ($\lambda=10.6\mu\text{m}$) at an incident angle of 12° through a KCl window, on which evaporated particles were prevented from depositing by a suitable technique. The process parameters were determined on the basis of YSZ physical properties and Al₂O₃ evaporation conditions. Table 1 shows laser PVD conditions used for YSZ film formation.

The YSZ electrolyte films deposited by laser PVD were characterized by scanning electron microscope, X-ray diffraction, gas permeability and electrical resistivity. Gas permeability of the coated film was compared by gas leaking rate calculated from leak time at room temperature by means of the apparatus shown in Fig. 3. YSZ film coated on the Ni porous plate was bonded to the steel box A by silicon rubber adhesive and the time of initial N₂ gas pressure (500mmH₂O) changing to 300mmH₂O was measured. Electrical resistivity was also measured by conventional DC fourprobe technique at 500~1000°C. The films formed by other techniques were also characterized in the same manner.

3. PREPARATION OF SMALL-SIZE CELL

Fabrication method of mini-size cell is shown in Fig.4. The porous Al₂O₃ was used as substrate on which Pt mesh(#80) was attached partially by Al₂O₃ cement. Fuel electrodes were formed on the substrate by acetylene gas flame spraying of NiO powder. The electrolytes were formed by plasma spraying, detonation spraying, low pressure plasma spraying and laser PVD. Finally, La(Sr)MnO₃ as air

electrode was coated by acetylene gas flame spraying and connected to the Pt mesh(#80).

4. RESULTS AND CONCLUSIONS

YSZ film composition and structure did not change after laser PVD and spraying. Fig.5 gives the electric resistances of YSZ electrolytes formed by laser PVD, low pressure plasma spraying and plasma spraying. At 1000°C, only a slight difference of resistivity owing to the film formation technique was observed. Electrical resistivity of YSZ at 1000°C was $\sim 10 \Omega \cdot \text{cm}$. Gas permeability of SOFC components is presented in Fig.6. Air electrode formed by flame spraying and fuel electrode formed by plasma spraying were of rather high permeability at the level of $1 \sim 10 \text{ cc/sec} \cdot \text{cm}^2$. On the other hand, electrolyte should be highly dense and less gas-permeable. YSZ film formed by laser PVD had the lowest permeability of $10^{-3} \sim 10^{-2} \text{ cc/sec} \cdot \text{cm}^2$.

The cells, of which electrolytes were formed by different processes, were tested at $\sim 1000^\circ\text{C}$ with hydrogen as fuel gas and air as oxidizing gas. Fuel gas flow rate was $\sim 1 \text{ l/min}$. Fig.7 shows the I-V characteristics of the cells. Open circuit voltage was dependant on the electrolyte forming process. Detonation and plasma spraying cells showed lower OCV values; the highest OCV value was observed in laser PVD cell of which electrolyte was rather dense. IR drop was found to be related to the electrolyte thickness and it was thinnest in laser PVD cell as can be seen in the the micro-structure SEM photos of YSZ electrolytes(Fig.8). Also in Fig.8, YSZ film formed by plasma spraying has many pores which explain the lower OCV value. Much fewer pores in the low pressure plasma spraying and laser PVD films are consistent with higher OCV values observed in mini-cell test. But detonation spraying cell did not give higher OCV although its SEM photo of YSZ film showed no significant pores. This is thought to be related to several cracks caused by detonation shocks during spraying.

It is concluded that electrolyte made by CO_2 laser evaporation technique was highly dense and thin, and CO_2 laser evaporation technique is considered the best electrolyte forming process.

REFERENCES

1. K.Tachikawa, I.Watanabe, S.Kosuge and M.Ono. Mater.Res. Soc. Proc. 99, Boston, 1987 pp.723-726.
2. K.Tachikawa, S.Kosuge, M.Ono and N.Nakada. Appl.Phys.Lett. vol.52 1988 p1011.

TABLE I

Deposition condition of YSZ films

Laser power	500W
Target	YSZ (8mol%Y ₂ O ₃)
Pressure	10 ⁻² torr in air
Substrate temperature	450°C
Distance between target and substrate	75 mm

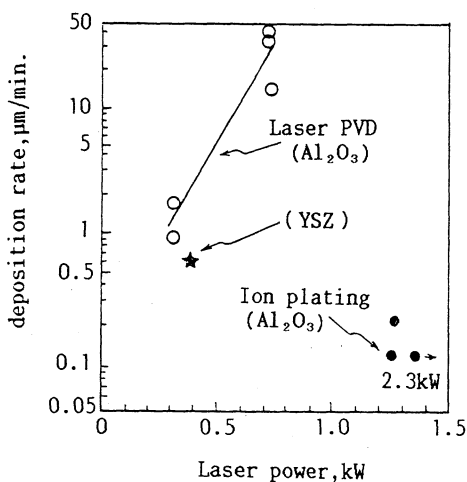


Fig.1 Effect of laser power on deposition rate of oxide film.

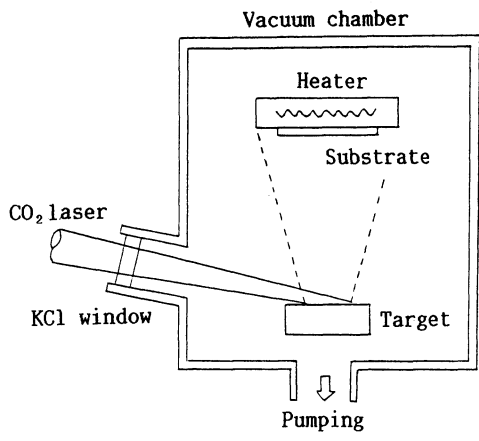


Fig.2 Schematic diagram of CO₂ laser deposition apparatus.

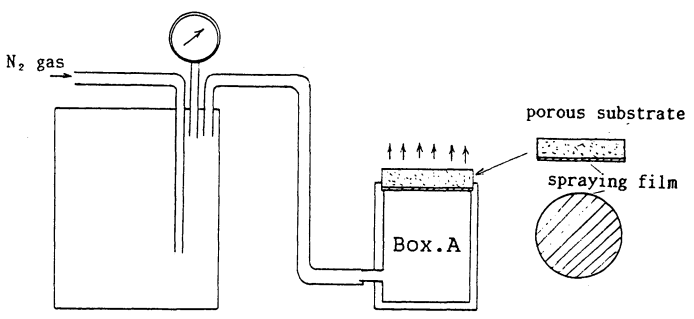


Fig.3 Measuring apparatus for gas permeability of SOFC components.

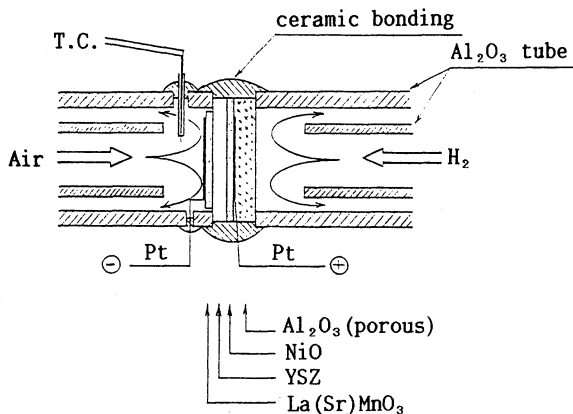


Fig.4 Small-size cell structure.

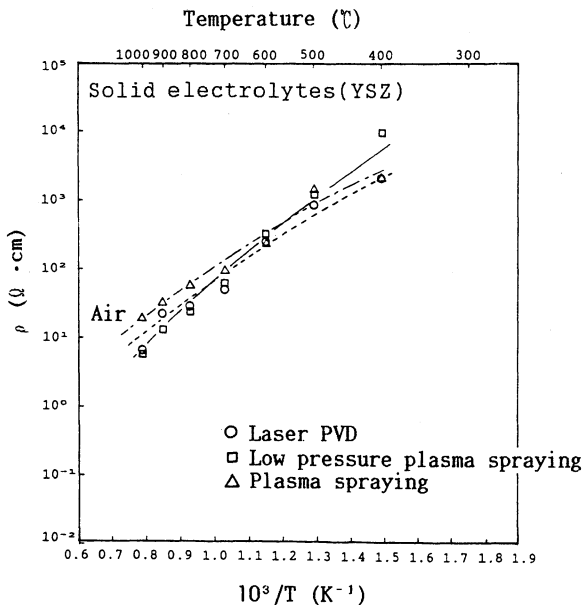


Fig.5 Electric resistance of YSZ electrolytes.

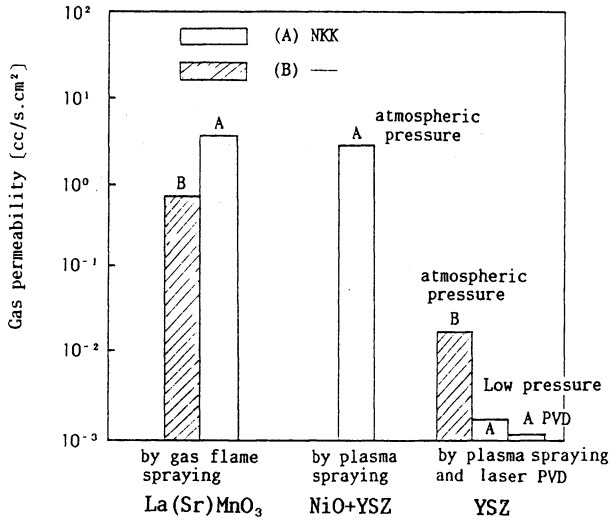


Fig.6 Gas permeability of SOFC components.

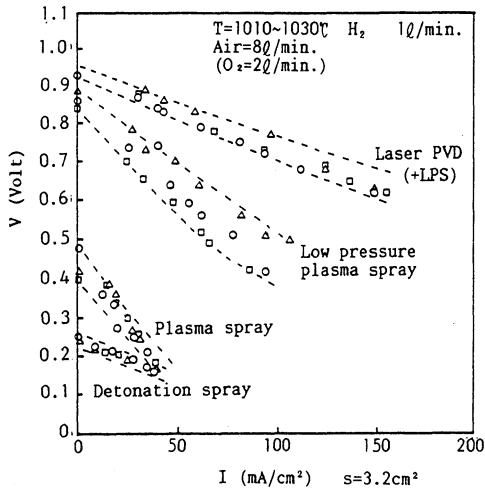


Fig.7 I-V characteristics of small cells.

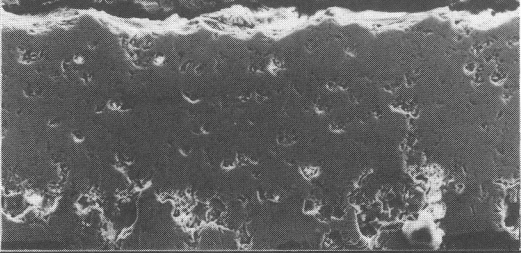
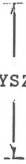
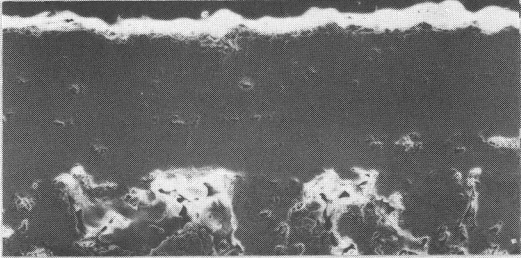
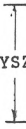
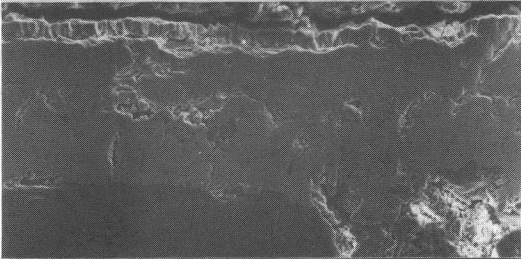
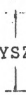
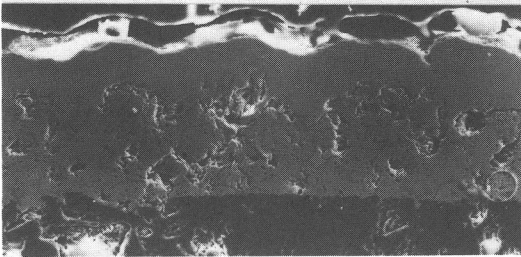

electrolyte formation process	cross section of cell	
Plasma spray		
Low pressure plasma spray		
LPV+ Laser PVD		
Detonation spray		

Fig.8 Micro-structure of YSZ electrolytes.

100μm

**ELECTRODES AND INTERCONNECTION
MATERIALS AND PROCESSING**

MIXED-CONDUCTING OXIDE ELECTRODES FOR SOLID OXIDE FUEL CELLS

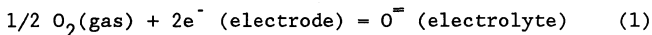
Shian-Shyang Liou and Wayne L. Worrell
Department of Materials Science and Engineering
University of Pennsylvania
3231 Walnut Street
Philadelphia, PA 19104

ABSTRACT

Novel mixed-conducting yttria-stabilized zirconia-titania solutions have been synthesized and electrically characterized. The dissolution of titania into yttria-stabilized zirconia increases significantly the percentage of electronic conductivity in this oxygen-ion conductor. The total electrical, lattice and grain-boundary conductivities have been determined using impedance spectroscopy at temperatures between 350 and 900°C and at oxygen pressures between 10^{-23} and 0.21 atm. The electronic conductivity has been measured at temperatures between 800 and 1000°C using a platinum electrode to block oxygen-ion transport. The percentage of electronic conductivity is calculated from the electronic/total electrical conductivity ratios and from separate Emf cell measurements. The percentage of electronic conductivity increases with increasing titania concentration and with decreasing temperature. Our results establish not only the magnitudes of the electronic and oxygen-ion conductivities but also the optimum compositions of the yttria-stabilized zirconia-titania solutions for mixed conduction. The results are used to estimate the electrode current densities of these new mixed-conducting oxides in solid oxide fuel cells.

1. INTRODUCTION

Mixed-conducting oxides, which exhibit oxygen-ion and electronic conductivity, are novel materials. Particularly attractive applications of these materials are as electrodes in solid oxide fuel cells (SOFC). Current electrode materials (nickel-zirconia cermets and strontium-doped manganite) are electronic conductors, and the charge-transfer reactions such as expressed in Eq. (1) are



restricted geometrically to the intersection lines of the gas, electrode and electrolyte phases. With a mixed-conducting oxide electrode, the charge transfer-reaction, Eq. (1), occurs over the entire electrode surface because both electrons and oxygen ions are mobile in the electrode material. Thus polarization losses at the

electrode-electrolyte interface will be reduced significantly due to the large increase in the charge-transfer reaction area.

There are other major advantages of using mixed-conducting oxide electrodes in SOFC. These materials would eliminate the necessity to fabricate and to maintain the intricate, porous electrode structures in the present cells. Although such electrode structures are necessary to maximize the intersection lines of the gas, electrode and electrolyte phases, it is very difficult to avoid sintering and the associated reduction of the optimum porous electrode structure during cell operation. Secondly, mixed-conducting oxide electrodes which are based on stabilized zirconia should have excellent chemical compatibility and interfacial adhesion with the yttria-stabilized zirconia electrolyte currently used in SOFC. For example, the chemical composition and thermal-expansion coefficients of the mixed-conducting stabilized zirconias described in this paper should be very similar to yttria-stabilized zirconia. Thirdly, mixed-conducting oxide electrodes should exhibit superior sulfur tolerances over the metal cermet currently used as fuel electrodes.

The paper is a summary of the synthesis and electrical characterization of new, mixed-conducting yttria-stabilized zirconia-titania solutions. The concept is to introduce electron-hopping or small polaron conduction into an oxygen-ion conductor such as yttria-stabilized zirconia by dissolution of an oxide such as titania which has a multivalent cation. Our results establish not only the magnitudes of the electronic and oxygen-ion conductivities, but also the optimum compositions in the yttria-stabilized zirconia-titania solutions for mixed-conduction. The results are used to estimate the electrode current densities of these new mixed-conducting oxides in SOFC.

2. PREVIOUS WORK

Some previous researchers also have recognized the advantages of mixed-conducting stabilized zirconias. Transition-metal oxides such as iron oxide, manganese oxide and cobalt oxide were dissolved into stabilized zirconia [1]. However, only small solubilities of these oxides in stabilized zirconia were observed, and the percentage of electronic conductivity was low. More recently, mixed-conducting zirconia-ceria-yttria solutions have been prepared [2]. Significant percentages of electronic conductivity were observed only at very high temperatures (above 1200°C). Furthermore, the mixed conduction was a strong function of temperature and oxygen pressure.

3. SYNTHESIS AND PHASE CHARACTERIZATION

New ternary-oxide solutions containing 10 or 12 mole percent (m/o) yttria-stabilized zirconia containing between 0 and 30 m/o titania have been prepared [3,4]. The starting powders are isostatically cold-pressed and then sintered in air at 1400°C for 12 hours to obtain the cubic-fluorite phase and then sintered at 1600°C for 12

hours to densify and chemically homogenize the oxide solutions. After sintering, the polycrystalline specimens are opaque and pale yellow with a density of 5.18 g/cm^3 (88% of the theoretical value). No leakage of helium through the specimens is detected using a Veeco leak detector. The average grain size, determined from scanning electron micrographs (SEM's), is 20 to 40 microns for the 10 m/o yttria-stabilized zirconia-titania solutions and 10 to 20 microns for the 12 m/o yttria solutions.

Figure 1 shows that the lattice parameters for yttria-stabilized zirconia containing no titania are in excellent agreement with previous studies [5,6]. The results also indicate that the single-phase fluorite structure is retained in the 10 and 12 m/o yttria-stabilized zirconia solutions with titania concentrations as high as 12.5 and 15 m/o, respectively. The observed decrease in the lattice parameter with increasing titania concentration is presumably due to the substitutional replacement of zirconia ions with the smaller titanium ions. The 12 m/o yttria-stabilized zirconia has a higher lattice parameter, and the titania solid solubility is less in 10 m/o yttria-stabilized zirconia than in the 12 m/o yttria solution. Although a second phase has been observed in the SEM's of the 20 and 25 m/o titanium solutions, we have been unable to determine its composition using EDAX.

4. ELECTRICAL CHARACTERIZATION

Impedance spectroscopy has been used to determine the electrical conductivity of our polycrystalline oxide solutions. Its major advantage over d.c. conductivity measurements is that one can determine the lattice and grain-boundary contributions to the total electrical conductivity. The impedance spectra have been interpreted in terms of the brick-layer model [7,8] which assumes a well-developed microstructure and uniform grain size. Results have been obtained at temperatures between 350 and 900°C and at oxygen pressure between 0.21 and 10^{-23} atm. The lattice, grain-boundary and total electrical conductivities are independent of oxygen pressure. Our results for the lattice and total electrical conductivities for 12 m/o yttria-stabilized zirconia containing no titania are in excellent agreement with previous results using single-crystals [9,10] and a four probe d.c. technique [10,11]. This agreement indicates the quality of our polycrystalline materials and the reliability of our impedance-spectroscopy data.

The temperature variation of the total electrical conductivity for 10 and 12 m/o yttria-stabilized zirconia containing 0 to 10 m/o titania is shown in Figs. 2 and 3, respectively. The electrical conductivity of 10 and 12 m/o yttria-stabilized zirconia increases with the addition of 5 m/o titania and then decreases for the 7.5 and 10 m/o titania solutions. The initial increase is due to an increase in the grain-boundary conductivity, while the observed decreases at higher titania concentrations reflect the decreases in grain-boundary and lattice conductivities.

The electronic conductivity of 10 and 12 m/o yttria-stabilized zirconia containing 5, 7.5 or 10 m/o titania has been determined at temperatures between 800 and 1000°C using a platinum electrode to block oxygen-ion conductivity. The results shown in Fig. 4 indicate that the electronic conductivity increases significantly with increasing titania concentration. This reflects the increase in the number of electronic charge carriers, i.e. Ti'_{Zr} , with increasing titania concentration. Figure 4 also indicates that the activation energy of 0.73 (\pm 0.3) eV is constant for all the yttria-stabilized zirconia-titania solutions.

5. PERCENTAGE OF ELECTRONIC CONDUCTIVITY

The percentage of electronic conductivity has been determined using two approaches. The values have been calculated from the blocking-electrode results by dividing the electronic conductivity shown in Fig. 4 by the total electrical conductivity (Figs. 2 and 3). Electromotive force (Emf) cells with the mixed-conducting oxides as electrolytes have also been used to determine the percentage of electronic conductivity. The measured open-circuit cell voltage is divided by the value which would be observed if the electrolyte exhibited negligible electronic conductivity. Results from the blocking-electrode and Emf-cell measurements are compared in Figs. 5 and 6. There is excellent agreement between the results obtained from the two difficult experimental techniques. The large scatter in the results for the 10 m/o titania composition shown in Fig. 6 is believed due to the high percentage (55 to 89%) of electronic conductivity and the associated difficulty in obtaining steady, consistent Emf values.

The results shown in Figs. 5 and 6 confirm our initial concept that the dissolution of titania into yttria-stabilized zirconia should introduce significant amounts of electronic conductivity. The percentage of electronic conductivity clearly increases with increasing titania concentration, presumably due to electron hopping or small polaron conduction via multivalent titanium cations. The results also show that the percentage of electronic conductivity decreases with increasing temperature. This reflects the fact that the activation energy (0.90 eV) for oxygen-ion conductivity at temperatures above 700°C is higher than that for electronic conductivity (0.73 eV). Thus increasing temperature has a larger effect on the oxygen-ion conductivity.

6. EVALUATION OF ELECTRODE CURRENT DENSITIES

For a given total electrical conductivity, the optimum composition for a mixed-conducting electrode is that at which the transference numbers or percentages of electronic and oxygen-ion conductivity are equal. If they are not equal, the species with the lowest percentage will control the transport of electrons and oxygen ions through the mixed conductor. The titania compositions at which the electronic conductivity equals the oxygen-ion conductivity are shown in Table I for the 10 m/o yttria-stabilized zirconia-titania

solutions. The resistivity of these optimum compositions is also tabulated.

The resistivities (ρ) shown in Table I are used to estimate electrode current densities for mixed-conducting 10 m/o yttria-stabilized zirconia-titania solutions. The oxygen-pressure gradients across the electrodes currently used in SOFC vary from 10 to 10^4 . We have assumed an oxygen-pressure gradient of 100 to calculate values for the potential (E) across the mixed-conducting electrode and the current density (i). The calculated current densities tabulated in Table II vary from 223 to 9,621 mA/cm² depending upon temperature and electrode thickness. These values indicate that mixed-conducting yttria-stabilized zirconia-titania solutions should have attractive electrode applications in SOFC.

ACKNOWLEDGEMENTS

The financial support of the U.S. Department of Energy through the Morgantown Energy Technology Center is gratefully acknowledged. The work was carried out at the University of Pennsylvania in the Materials Research Laboratory which is supported by the U.S. National Science Foundation.

REFERENCES

1. R. Fullman and S.P. Mitoff, U.S. Patent 3,410,728 (1968).
2. B. Cales and J.F. Baumard, J. Electrochem. Soc., Vol.131 (1984) p. 2407.
3. S.S. Liou and W.L. Worrell, in press, App. Phys. A: Solids and Surfaces (1989).
4. S.S. Liou, Ph.D. Dissertation, Univ. of Pennsylvania, Phila., PA (1989).
5. J. Lefevre, Ann. Chim. (Paris), Vol.8 (1963) p. 117.
6. R.E.W. Casselton, Phys. Stat. Sol. (A), Vol.2 (1970) p. 571.
7. M.J. Vrkerk, B.J. Middelhuis and A.J. Burggraaf, Solid State Ionics, Vol.6 (1982) p. 159.
8. T. Van Dijk and A.J. Burggraaf, Stat. Sol. (A), Vol.63 (1981) p. 229.
9. P. Abelard and J.F. Baumard, Proceed. of Second Europ. Conf. on Solid State Chemistry, Veldhoven, The Netherlands, June (1982).
10. S.P.S. Badwal and M.V. Swain, J. of Mat. Sci. Letters, Vol.4 (1985) p. 4.
11. D.W. Strickler and W.G. Carlson, J. Am. Ceram. Soc., Vol.48 (1965) p. 286.

TABLE I

Titania composition and resistivity when the percentage of electronic conductivity equals the oxygen-ion conductivity for 10 m/o yttria-stabilized zirconia-titania solutions.

Temperature(^o C)	Titania (Mole%)	Resistivity (ohm-cm)
800	7.4	120
900	8.3	63
1000	9.3	33

TABLE II

Variation of the calculated current density (i) with temperature and electrode thickness (t) for mixed-conducting 10 m/o yttria-stabilized zirconia-titania electrodes.

T(^o C)	t(microns)	$\rho \cdot t$ (ohm-cm ²)	E (mV)	i(mA/cm ²)
1000	10	3.3×10^{-2}	127	962
"	5	1.7×10^{-2}	"	1,868
"	1	3.3×10^{-3}	"	9,621
900	10	6.3×10^{-2}	117	464
"	5	3.2×10^{-2}	"	914
"	1	6.3×10^{-3}	"	4,643
800	10	12×10^{-2}	107	223
"	5	6×10^{-2}	"	446
"	1	1.2×10^{-2}	"	2,229

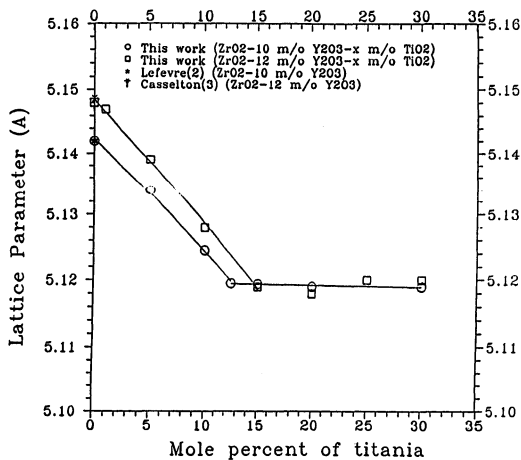


Fig. 1 Variation of the lattice parameter with titania concentration in 10 and 12 mole % yttria-stabilized zirconia.

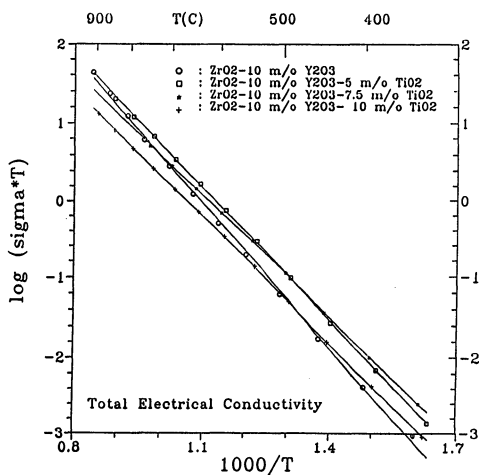


Fig. 2 Variation of the total electrical conductivity with temperature for polycrystalline 10 mole % yttria-stabilized zirconia containing 0 to 10 mole % titania.

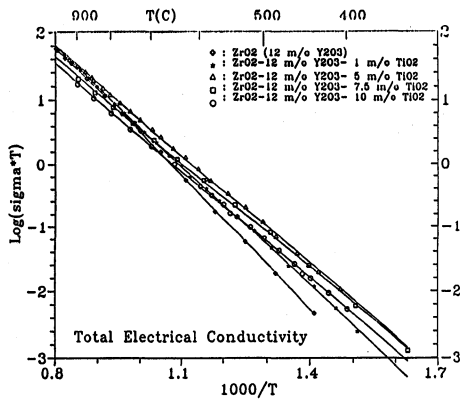


Fig. 3 Variation of the total electrical conductivity with temperature for polycrystalline 12 mole % yttria-stabilized zirconia containing 0 to 10 mole % titania.

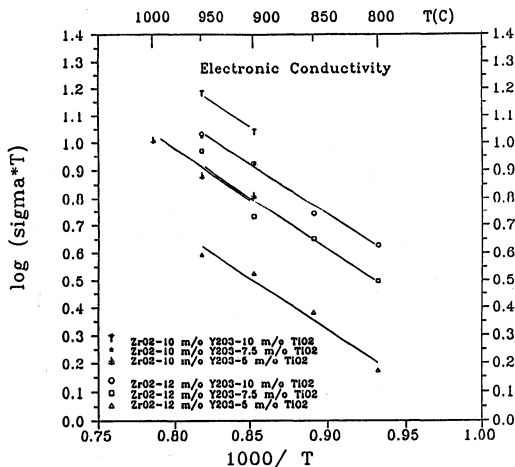


Fig. 4 Temperature variation of the electronic conductivity for 10 and 12 mole % yttria-stabilized zirconia containing 5, 7.5 or 10 mole % titania.

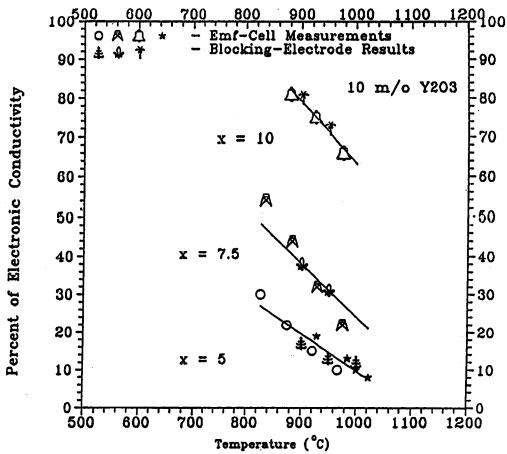


Fig. 5 Temperature variation of the percentage of electronic conductivity in 10 mole % yttria-stabilized zirconia containing 5, 7.5 or 10 mole % titania.

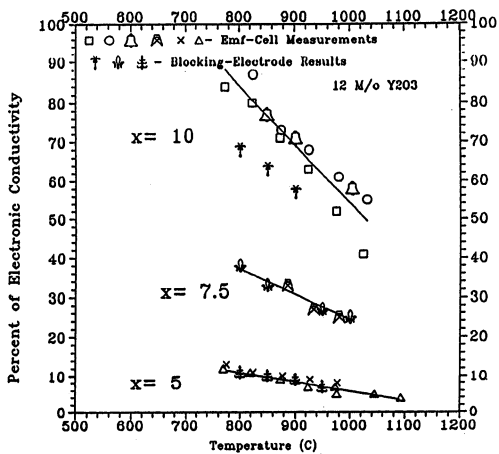


Fig. 6 Temperature variation of the percentage of electronic conductivity in 12 mole % yttria-stabilized zirconia containing 5, 7.5 or 10 mole % titania.

MORPHOLOGY AND ELECTROCHEMISTRY OF POROUS NICKEL/ZIRCONIA CERMETS

P.H. Middleton, M.E. Seiersten* and B.C.H. Steele.
Department of Materials,
Imperial College of Science, Technology and Medicine,
London SW7 2BP. UK.

*Senter For Industriforskning,
P.O. Box 124 Blindern, 0314 Oslo 3, Norway.

ABSTRACT

This paper investigates the morphology and electrochemistry of tape cast nickel/zirconia cermet anodes in solid oxide fuel cells. Films containing 45 volume% Ni exhibited a porous structure after reduction in hydrogen, but particles larger than $3\mu\text{m}$ were found to retain a core of NiO. Electrochemical measurements by cyclic voltammetry showed that the cermet anode is readily oxidised at potentials more positive than -0.3V , resulting in an increase in the film resistance. The cell was run with hydrogen, using the residual resistance in the leads as load, and the observed current decayed by 80% over a period of 60 hours which was consistent with a rise in the anode film resistance. The loss of performance was attributed to the electrochemical oxidation of Ni at the low cell voltage attained.

1. INTRODUCTION

In solid oxide fuel cells (SOFC), the commonest anode material is a nickel/zirconia cermet comprising an intimate mixture of Ni and $\text{ZrO}_2\text{-Y}_2\text{O}_3$ (1). However, there is very little in the published literature about the properties of this material (2) though several patents cover the preparation and properties of cermets fabricated by a combination of slurry and vapour deposition techniques (3-6). The preparation of porous nickel cermets by a tape casting route has been discussed by Dees and Fee *et al* (2), who prepared free standing films, and studied the effects of Ni content, particle size and surface area on the conductivity of the reduced cermet.

In the present work, we have produced tape cast Ni/zirconia cermets on flat plate pre-sintered zirconia sheets for SOFC application and describe their morphology and electrochemistry.

2. EXPERIMENTAL

2.1 *Cermet preparation*

Commercial grade nickel oxide powder (Hopkin and Williams) was ball milled for 72 hours in a media of ethanol and dispersant (fish oil) yielding a powder of average particle size $3\mu\text{m}$ and containing no particles $> 10\mu\text{m}$.

Tape casting slurries were made up whose composition were such that 45 volume% (v/o) nickel was present in the reduced state. Appropriate mixtures of NiO, zirconia powder (Tosoh containing 8 mol% Y_2O_3) and dispersant (fish oil) were ball milled for 24 hours in ethanol, after which binder (polyvinylbutyral) and plasticiser (polyethylene glycol and dibutylphthalate) were added and the mixture ball milled for a further 24 hours. An example batch recipe is given below:

60 g ceramic ($\text{ZrO}_2 + \text{NiO}$)
1 g dispersant
9 g binder
4.5 g plasticiser
36 g solvent

Samples were made by casting a $200\mu\text{m}$ thick layer of the slurry onto $200\mu\text{m}$ thick sheets of zirconia (pre-sintered Tosoh 8 mol% Y_2O_3). After drying for 12 hours, the sheets were heated slowly at 1°C min^{-1} to remove the binder and plasticiser. Once all the organics had burnt out, the heating rate was then increased to $10^\circ\text{C min}^{-1}$. The samples were sintered at 1350°C for 2 hours followed by cooling to room temperature at 5°C min^{-1} . The NiO was then reduced to metallic nickel by reduction in an atmosphere of hydrogen (10% H_2 in N_2) in the temperature range 850 to 1000°C .

2.2 *Electrochemical measurements*

A 4-electrode cell arrangement was used as shown in figure 1. A $2.5\text{cm} \times 2.5\text{cm}$ square sheet of zirconia was coated with a $2\text{cm} \times 2\text{cm}$ area of cermet material as described above and contact made to two opposite edges with platinum wires bonded by a conducting glass ceramic adhesive. Measurements between these two working electrodes labelled W.E.1 and W.E.2 in figure 1 enabled the surface film resistance to be monitored. Care was taken to ensure that the points of contact were distant from the ionic current flux, thus avoiding any possibility of signals interfering. The opposite face of the zirconia sheet was coated with circular areas of platinum acting as counter and reference electrodes (C.E. and R.E. in figure 1). Platinum wires were attached to these areas using a conducting ceramic glass and platinum paste. The working electrode area was 1.2cm^2 .

The cell was then attached to the end of an impermeable zirconia support tube (Corning 8 mol% Y_2O_3) using a ceramic adhesive (Aremco 516). The whole assembly was placed in a large diameter silica tube fitted with water cooled brass end caps and facilities for atmosphere control. The gas supply to the fuel electrode was through a 10mm diameter heated quartz tube terminating in a small orifice

(0.1mm diameter). The resulting wall-jet configuration allowed the gas stream to impinge directly onto the working area of the anode. The counter and reference electrodes were supplied with air through a small bore quartz tube placed down the inside of the zirconia support tube. The assembly was placed inside a split-level furnace and temperature control maintained with a thermocouple placed close to the working electrode.

Resistance measurements were made by applying a constant current of $100\mu\text{A}$ between the two working electrodes and measuring the voltage developed across the film with a differential buffer amplifier and a y/t recorder; the results were adjusted for iR losses in the measuring leads. Cyclic voltammetry was performed using a potentiostat constructed at Imperial College with output to a Bryans 60000 x/y recorder. Fuel cell mode performance was achieved using a Sycopel DD10M zero resistance ammeter with output to a Gould BS-232 y/t recorder. Gases were obtained from BOC Ltd. as high purity Argon ($\text{PO}_2 \approx 10^{-6}\text{atm.}$) and 10% hydrogen in nitrogen.

3. RESULTS AND DISCUSSION

3.1 Morphological Studies

The structure of the nickel cermet was studied by SEM analysis. Figure 7, a micrograph of a sample after reduction in hydrogen, shows a surface composed of small pores and larger cracks. Figure 8 is a cross-section of the same sample in which the porous structure of the cermet film is clearly evident. The interface region shows a thin diffusion layer between the cermet and the electrolyte substrate, indicating good adhesion between the two layers. The thickness of the cermet in this example is about $30\mu\text{m}$.

A metallographical cross-section was made and its image in figure 9 shows how the nickel was distributed in the cermet after reduction, where the darker areas correspond to nickel oxide, and the lighter areas to nickel metal. Evidently the nickel oxide was not completely reduced, the larger particles ($> 3\mu\text{m}$) having a NiO core, but despite this, the film was electronically conducting. Quantitative metallographic measurements by a Kontron image analyser on the polished cross-sections showed that the Ni content in the solid was 30v/o instead of the 45v/o aimed for. This result suggests that the nickel content in the cermet film was close to the threshold of conductivity stated in the work of Dees et al (2) but finer control of the NiO particle size prior to making up the slurry should alleviate this problem. The porosity of the cermet layer was measured as 40v/o.

3.2 Electrochemical Studies

The final reduction of the nickel oxide in the cermet was performed *in situ* whilst monitoring the surface film resistance. The initial resistance in an argon atmosphere was $4\text{k}\Omega$ ($\sigma = 8.3 \times 10^{-2}\Omega^{-1}\text{.cm}^{-1}$), but rapidly fell to 5Ω ($\sigma = 67\Omega^{-1}\text{.cm}^{-1}$) after introduction of hydrogen. The response is shown in figure 2. The

equilibrium PO_2 for the reaction $2Ni + O_2 = 2NiO$ at $850^\circ C$ is $\approx 10^{-13} atm.$, indicating instability of the anode at oxygen partial pressures above this value. Thus in the presence of argon ($PO_2 \approx 10^{-6} atm$) the surface film resistance was observed to increase from 5Ω to $1k\Omega$ over a period of 8 hours (figure 3). Re-introduction of hydrogen rapidly restored the anode to its conducting state.

Cyclic voltammetry (CV) was performed both in argon and hydrogen. The CV in argon is shown by the solid line in figure 4, where anodic currents were observed at potentials more positive than $-0.3V$ which can be ascribed to the formation of nickel oxide. The cathodic peak obtained in the reverse scan (labelled A in figure 4) can be ascribed to the reduction of the oxide back to free metal. It was observed that the current fell rapidly to zero when the potential exceeded $+0.4V$, indicating the formation of an insulating oxide layer; however on reverse sweeping the electrode could be revitalised. Analysis of the cathodic peak by observing the variation of peak height with scan rate resulted in a linear response (figure 5) indicative a surface adsorption process (7). This supports the assignment of peak A to the removal of oxygen from the surface.

The cyclic voltammogram obtained in hydrogen is given by the dashed line in figure 4. This shows an almost linear response, indicating currents that were limited by the residual iR losses in the circuit rather than mass transport or the kinetics of hydrogen oxidation. There appeared to be no significant variation of current with flow rate. The open circuit voltage of $-1.0V$ corresponded to a PO_2 of $\approx 10^{-13} atm.$

The cell was operated as a fuel cell using the potentiostat as a zero resistance ammeter and the combined resistance of 7Ω in the leads as the load. A plot of current against time is given in figure 6, in which the performance is seen to decay by 80% over a period of 50 hours. The open circuit voltage was still $-1.0V$ at the end of the experiment. The same plot also shows the variation of anode film resistance over the same period of time. Clearly the performance is related to a change in the conductivity of the anode.

The initial cell voltage was estimated to be $0.22V$ and it is suggested that this value may have been sufficiently low to bring about electrochemical oxidation of the nickel. A counter argument that oxygen may have penetrated the anode compartment of the cell was discounted on the grounds that the open circuit potential was maintained at $-1.0V$. The possibility of surface oxidation by the formation of water in the reactor was also considered. The oxygen partial pressure for the reaction $H_2 + \frac{1}{2}O_2 = H_2O$ can be obtained from the thermodynamic relationship:

$$PO_2 = \left[\frac{PH_2O}{PH_2} \exp(\Delta G^\circ/RT) \right]^2$$

where ΔG° is the standard free energy per mole of hydrogen. Under steady state conditions the ratio of steam and hydrogen partial pressures can be compared with the ratio of fluxes of steam and hydrogen maintained in the wall-jet reactor. The flux of water jH_2O produced on the electrode is given by

$$jH_2O = -i/nFA$$

where i is the measured current, n is the number of electrons in the charge transfer step, F is the Faraday constant and A is the electrode surface area. The flux of hydrogen j_{H_2} entering the reactor is given by

$$j_{H_2} = P\nu/ART$$

where P is the pressure, ν is the volume flow rate, R is the gas constant and T is the absolute temperature. Whence

$$\frac{PH_2O}{PH_2} = \frac{j_{H_2O}}{(j_{H_2} - j_{H_2O})}$$

A value of 0.17 was calculated for the fuel cell experiment corresponding to a PO_2 of $10^{-1.9}$ atm, but the equilibrium PO_2 value for the formation of nickel oxide at $850^\circ C$ is $\approx 10^{-1.3}$ atm, indicating that the nickel electrode could not have been oxidised by the formation of water alone.

4. CONCLUSIONS

These results suggest that the performance of nickel anodes is very much dependent on the degree of surface oxidation. The observation of incomplete reduction in the fabrication process suggests that the conducting pathway occurs around the outside of the larger particles. This pathway may be blocked under fuel cell operation if the voltage falls sufficiently for the electrochemical formation of nickel oxide to occur. It is thought that the performance problem can be overcome in part by controlling the NiO particle size prior to making up the slurry.

ACKNOWLEDGEMENTS

Part of this work was done while one of the authors (M.E.S.) was visiting Imperial College. The support from Borgestad stipend and SI which made that possible is gratefully acknowledged. P.H.M. would like to express thanks to the EEC under contract EM3E/0167/E for financial support.

REFERENCES

1. D.C. Fee and J.P. Ackerman. Abstracts of the 1983 Fuel Cell Seminar Orlando, FL. November 13-16 1983. PP 11-14.

2. D.W. Dees, T.D. Claar, T.E. Easler, D.C. Fee, and F.C. Mrazek, "Conductivity of Porous Ni/ZrO₂-Y₂O₃ Cermets" *J. Electrochem. Soc.* vol. 134 (1987) p 2141.
3. R. Schmidberger, "Cermet Electrodes for Solid-Electrolyte Cells and Process for their Manufacture". (To Dornier System G.m.b.H., Friedrichshafen, Germany, F.R.). German Patent 2,747,467/B/. 22 Feb 1979.
4. A.O. Isenberg and G.E. Zymboly, "High Performance Cermet Electrodes". (To Westinghouse Electric Corp., Pittsburgh, Pa.), US Patent 4,582,766. 15 April 1986.
5. A.O. Isenberg, "Methods of Making an Electrode". (To Westinghouse Electric Corp., Pittsburgh, Pa.), US Patent 4,597,170. 1 July 1986.
6. *idem.* "Sulfur Tolerant Composite Cermet Electrodes for Solid Oxide Electrochemical Cells". (To Westinghouse Electric Corp., Pittsburgh, Pa.), US Patent 4,702,971. 27 Oct. 1987.
7. A.J. Bard and L.R. Faulkner, Electrochemical Methods, Fundamentals and Applications, John Wiley and Sons, Inc., New York 1980. p522.

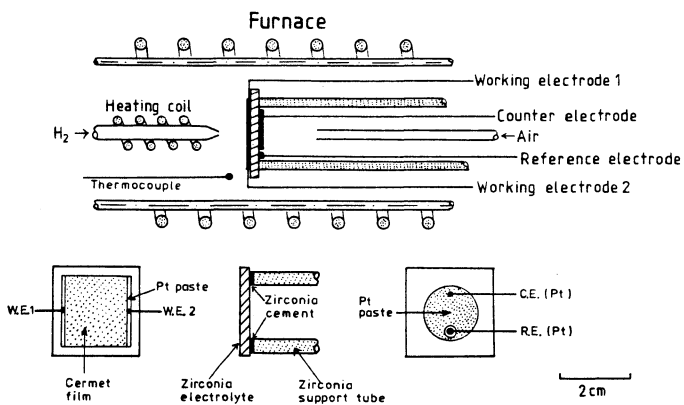


Fig. 1 - Schematic diagram of wall-jet reactor and electrode configuration.

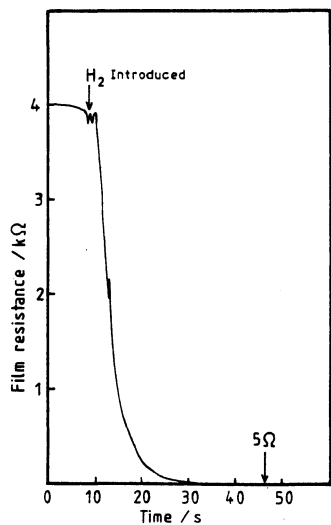


Fig. 2 - Cermet film resistance during hydrogen reduction at 850°C. Measurements made between W.E.1 and W.E.2.

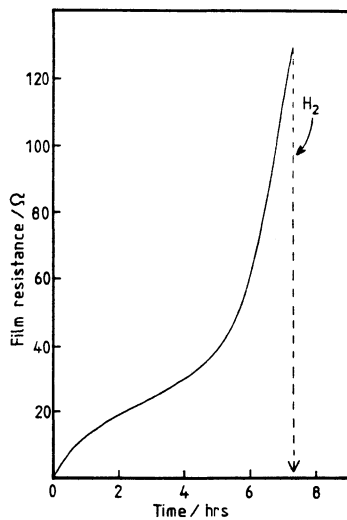


Fig. 3 - Increase in cermet film resistance during argon purging.

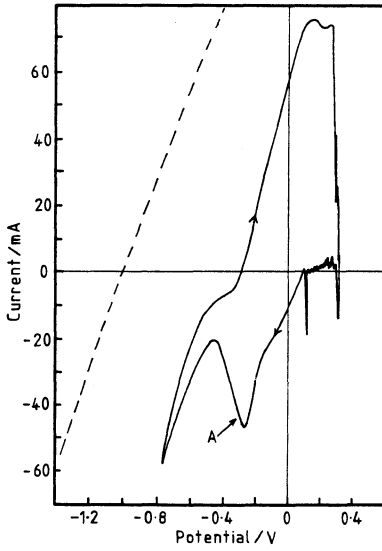


Fig. 4 - Cyclic voltammetry of a cermet film at 850°C exposed to Ar (solid line) and H₂ (dashed line). The scan rates were 50 mV s⁻¹. (A):NiO reduction peak.

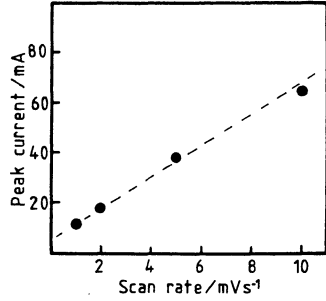


Fig. 5 - Variation of peak current with scan rate for the reduction of NiO.

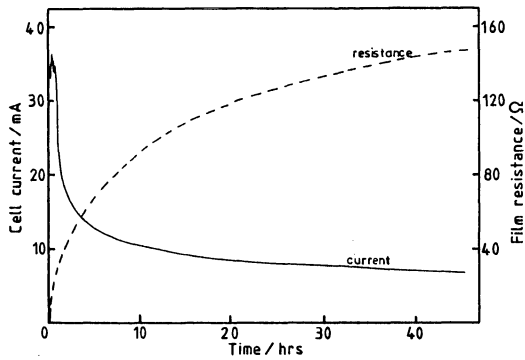


Fig. 6 - Variation of fuel cell performance and cermet resistance with time.

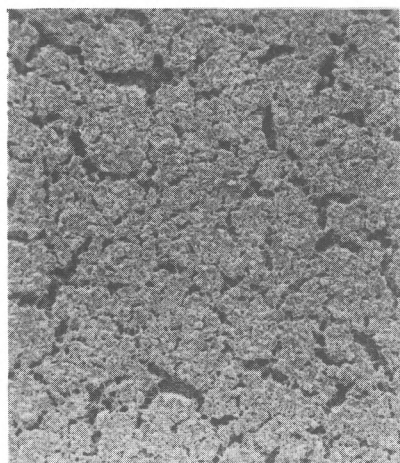


Fig. 7 - SEM image of a cermet surface after reduction in H_2 .

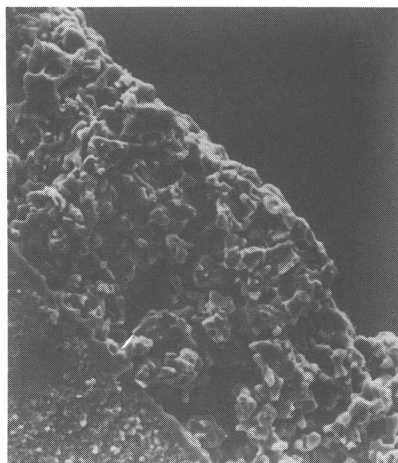


Fig. 8 - SEM image of a fractured sample showing the porous cermet layer bonding to the zirconia electrolyte sheet.

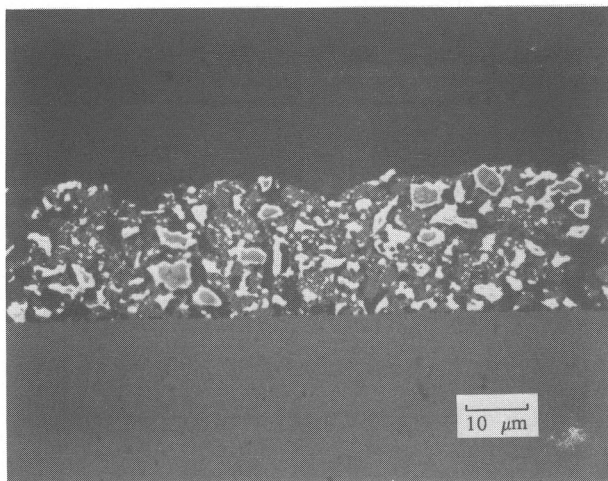


Fig.9 - Metallographical cross-section of a $Ni/ZrO_2-Y_2O_3$ cermet film lying above a sheet of zirconia electrolyte.

OXIDATION OF METHANE ON OXIDE ELECTRODES AT 800-1000°C

M. Mogensen and J.J. Bentzen
Metallurgy Department,
Risø National Laboratory
DK-4000 Roskilde, Denmark

ABSTRACT

Preliminary experimental results on oxidation of methane on oxide anodes with mixed ionic and electronic conductivity are reported. Two compositions of oxide electrodes were used. One consisted of a mixture of 67.3 mole% $\text{Ce}_{0.85}\text{Gd}_{0.15}\text{O}_{1.925}$ and 32.7 mole% $\text{Zr}_{0.945}\text{Y}_{0.055}\text{O}_{1.973}$, and another was a mixture of 40.7 mole% $\text{Ce}_{0.85}\text{Gd}_{0.15}\text{O}_{1.925}$ and 59.3 mole% $\text{Zr}_{0.945}\text{Y}_{0.055}\text{O}_{1.973}$. Cyclic voltametry on these electrodes in CH_4 and H_2 revealed polarisation resistances of less than $0.8\Omega\cdot\text{cm}^2$ and $0.4\Omega\cdot\text{cm}^2$ for CH_4 and H_2 , respectively, at 1000°C in the best cases. A considerable hysteresis was observed in the case of CH_4 . In H_2 it was much less. Possible reaction mechanisms are mentioned. No carbon deposition from CH_4 was observed but problems of cracking of the oxide electrodes were encountered.

1. INTRODUCTION

The principal advantage of mixed ionic and electronic conductivity in solid oxide fuel cell (SOFC) electrodes was pointed out long ago by Takahashi, Iwahara and Suzuki (1). They also demonstrated it experimentally on porous anodes of $\text{Ce}_{0.6}\text{La}_{0.4}\text{O}_{1.8}$ and $\text{Ce}_{0.6}\text{Y}_{0.4}\text{O}_{1.8}$ in H_2 . Later Nguyen, Lin and Mason (2) observed that "blackening" of the surface of a Sc_2O_3 - ZrO_2 (SSZ) electrolyte with Pt-electrodes increased the current density two to three orders of magnitude for a number of fuels including H_2 and CH_4 . The "blackening" process was identified as inducing electronic conductivity into the SSZ oxygen ion conductor by reducing it electrochemically.

Furthermore Steele, Kelly, Middleton and Rudkin (3) have shown that SOFC's with ceramic anodes can be operated on 100% CH_4 without any carbon deposition. This indicates that CH_4 can be oxidized in SOFC's without the incorporation of ex-situ or in-situ reforming stages.

On this background, work has been initiated at Risø National Laboratory with the purpose of developing mixed ionic- and electronic conducting oxide anodes for direct oxidation of CH_4 in SOFC. Some preliminary results are reported below for electrodes consisting of mixtures of $\text{Ce}_{0.85}\text{Gd}_{0.15}\text{O}_{1.925}$ and $\text{Zr}_{0.945}\text{Y}_{0.055}\text{O}_{1.973}$.

2. PROPERTIES OF CeO₂ CONTAINING CERAMICS

The ionic and electronic conductivities of doped cerium oxides and the dependence on O₂ partial pressure have been reviewed by H.L. Tuller (4). At pO₂ < 10⁻¹⁵ atm together with temperatures above 800°C di- and trivalent cation doped CeO₂ becomes predominantly electronic conducting for doping levels up to 15%. The ionic conductivity is independent of pO₂. The electronic conductivity is in the range of 1 to 4 S/cm and the ionic conductivity varies from about 0.02 to 0.1 S/cm from 800 to 1000°C.

Gales and Baumard (5,6) investigated solid solutions of ((1-x) ZrO₂ - xCeO₂)_{0.9} (Y₂O₃)_{0.1}, 0 ≤ x ≤ 1. They found a minimum in ionic conductivity of 0.012 S/cm at x = 0.5 and pO₂ = 1 atm at 1000°C. Furthermore they found that the electronic conductivity went through a maximum when decreasing pO₂. The maxima of the conductivity versus pO₂ curves correspond to a ratio of [Ce⁺³]/[Ce⁺⁴] ~ 0.1. At 1000°C the maximum is found around pO₂ values of 10⁻¹³ to 10⁻¹⁴ atm. For x = 0.5 the electronic conductivity maximum value is about 0.2 S/cm at 1000°C.

3. EXPERIMENTAL

The experimental setup was a three electrode configuration as sketched in Fig. 1. The CeO₂ containing working electrodes were sintered onto the end of a cylinder made of tetragonal Y₂O₃ doped ZrO₂. The diameter was 11 mm and the length was 12 mm. A center hole, 3 mm diameter, was drilled in order to accommodate the reference electrode at a position not too far from the working electrode (see Fig. 1). Gas tightness was assured with Pt-gaskets 0.1 mm thick and 1.25 mm wide. These also functioned as current collectors.

The accessible electrode area was taken to be 0.75 cm². The H₂ and CH₄ flow rates were about 2 ml/s each and the air flow rate 1 ml/s.

The test sample was made by uniaxial pressing (34 MPa) of about 7 g of tetragonal Y₂O₃ doped zirconia powder (Zr_{0.945}Y_{0.055}O_{1.973} called TZ3YA) from Tosoh. On top of that was pressed about 150 mg of the electrode powder. After this the sample was sintered in air according to the scheme: 20-350°C 5 h, 350-400°C 5 h, 400-1600°C 2 h, at 1600°C 2 h, and 1600°C-20°C 10 h. This yielded an almost 100% dense electrolyte cylinder with a less dense (80-90%) electrode layer.

The electrode powders were made from TZ3YA and a Ce_{0.85}Gd_{0.15}O_{1.925} powder produced via chemical precipitation (7). The powders were mixed dry by shaking them in a bottle. Two mixtures were made. One composition was 67.3 mole% Ce_{0.85}Gd_{0.15}O_{1.925} + 32.7 mole% Zr_{0.945}Y_{0.055}O_{1.973} (this one is referred to as electrode 1), and the other was 40.7 mole% Ce_{0.85}Gd_{0.15}O_{1.925} + 59.3 mole% Zr_{0.945}Y_{0.055}O_{1.973} (referred to as electrode 2).

XRD showed that the sintered electrode layers were inhomogeneous consisting of solid solutions of zirconium-yttrium-oxide in cubic cerium-gadolinium-oxide and of solid solutions of Ce-Gd-oxide in tetragonal Zr-Y-oxide. These inhomogeneities were also observed with optical microscopy along with very fine cracks perpendicular to the surface.

Homogeneous electrodes with the same overall composition were also made but no electrochemical measurements were performed on them. These electrodes had in hydrogen a too low total electrical conductivity to facilitate measurements through a reasonable current range. The low conductivities are in accordance with the extrapolation of the findings given by Cales and Baumard (5).

The fuels used in all tests were either H_2 or CH_4 , both saturated with H_2O at room temperature which means about 3 vol% H_2O .

Electrode 2 was three times during its life oxidized with argon having $pO_2 = 10^{-2}$ atm. In the first and last case (referred to as redox cycle 1 and 3) the electrode was exposed to H_2 or CH_4 with 3% H_2O both before and after the oxidation. In the case of redox cycle 2, it was exposed to dry CH_4 before the oxidation.

The current-voltage curves were measured by means of a PAR 273 potentiostat. All curves were corrected for simple ohmic voltage drop. The ohmic resistances were measured by means of impedance spectroscopy (Solartron 1250) before and after the cyclic voltametry. As the ohmic resistance was in the range of 15 to 60 Ω and the electrode polarisation was often only a fraction of an ohm, a considerable uncertainty exists in the determination of the latter. In order to be conservative the lowest measured ohmic resistance was consistently used for the correction, i.e. the true polarisation is always less than or equal to those shown on the curves in Figures 2-5.

The curves were measured with a sweep rate of 10 mV/s either without any or with partly automatic ohmic drop compensation. In order to overcome the ohmic drop it was in some cases necessary to polarise the system 2000 mV which means that the time necessary to go through a cycle was $2 \times 200 \text{ s} = 400 \text{ s}$.

It was proved by blank experiments with the Pt-gasket on pure TZ3YA that this gives no significant current contribution either in H_2 or in CH_4 .

4. RESULTS

Figure 2 shows current-voltage curves for oxidation of H_2 and CH_4 on electrode 1, the 67.3 mole% $Ce_{0.85} Gd_{0.15} O_{1.925}$ electrode, at 1000°C. It reveals that the oxidation current in both cases varies roughly linearly with the potential. The H_2 -curve shows a polarisation

resistance of about $0.4\Omega\cdot\text{cm}^2$ and the CH_4 -curve about $1.2\Omega\cdot\text{cm}^2$. The CH_4 -oxidation displays a considerable larger hysteresis than the H_2 -oxidation.

During these experiments it was observed that the free electrode potential in H_2 with 3% H_2O was very stable and close to the theoretical value of -1065 mV vs Pt/air whereas the potential was very much unstable in CH_4 varying slowly from about -950 mV to -1100 mV in an irregular manner. The theoretical potential in $\text{CH}_4 + 3\%$ H_2O is about -1060 mV vs Pt/air. The thermodynamic data for the calculation of the theoretical values were taken from Hartung and Mübius (8) and from Broers and Treijtel (9). According to Broers and Treijtel a mixture of $\text{CH}_4 + 3\%$ H_2O will at 1000°C precipitate almost all the carbon in CH_4 as free carbon if equilibrium is obtained. However, no carbon deposition at the electrode was observed. Only in the quartz tube (see Fig. 1) minor carbon precipitation was seen in an intermediate temperature zone estimated to be in the range of 600 - 700°C .

Fig. 3 shows current-voltage curves for electrode 2, the 40.7 mole% $\text{Ce}_{0.85}\text{Gd}_{0.15}\text{O}_{1.925}$ + 59.3 mole% $\text{Zr}_{0.945}\text{Y}_{0.055}\text{O}_{1.973}$ -electrode, in $\text{H}_2 + 3\%$ H_2O at 800 , 900 and 1000°C . Fig. 4 gives the corresponding curves for $\text{CH}_4 + 3\%$ H_2O . The free potential of electrode 2 was stable at all three temperatures in hydrogen, and it was close to the theoretical. As for electrode 1, the free potential in methane at 1000°C was very unstable. The zero current potentials of the 1000°C -cycle in Fig. 4 span almost the entire potential range over which the free potential varies. In fact this sweep was deliberately started when the free potential was close to its most negative value. In contrast to the unstable free-potential of electrode 2 in methane at 1000°C , the potentials were stable within ± 10 mV at 900 and 800°C . The free potential at 900°C was -920 mV and at 800°C it was -870 mV vs Pt/air. After the end of the sweeps, the potential returned to these values in few minutes.

Even though the curves of Figs. 3 and 4 were measured at the same electrode and at the same temperatures in H_2 and CH_4 , respectively, the corresponding curves are not directly comparable. Between the two sets of measurements several other experiments were made, one of which changed the electrode irreversibly. After two measurements at 1000°C in CH_4 -3% H_2O showing good reproducibility in the high current density range, the gas was switched to pure (99.99%) CH_4 and the free potential dropped for a short period (5 min.) to -1170 mV vs Pt/air. Afterwards it increased to about -1060 mV. Impedance measurements showed a clear decrease in ohmic resistance (from 21.4Ω to 15.3Ω). These observations were taken as indicating that dry CH_4 induced some electronic conductivity into the TZ3YA electrolyte. The electrode was then flushed with argon ($p_{\text{O}_2} = 10^{-2}$ atm.) and left overnight at 1000°C in order to reoxidize the electrolyte (and the electrode). Next CH_4 -3% H_2O was introduced again. Fig. 5 shows the current-voltage curves before and after this event which is called redox cycle 2. A current-voltage curve was also measured in the dry CH_4 giving a result very

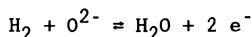
similar to the one measured after the redox cycle.

It is seen (Fig. 5) that before the treatment of electrode 2 with dry CH_4 the oxidation of CH_4 was quite fast, the average polarisation resistance being $0.8\Omega\cdot\text{cm}^2$.

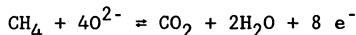
As mentioned previously the ohmic resistance seen by the reference electrode was measured by impedance spectroscopy before and after each current-voltage curve measurement. A clear trend of an increasing ohmic resistance during the sweeps was observed. Furthermore significant increases were observed when the electrode (no. 2) was reoxidized in argon ($p_{\text{O}_2} = 10^{-2}$ atm) and reduced again. At 800°C the starting value of the ohmic resistance was 45.8Ω . After two redox cycles it had increased to 57.8Ω and finally after the third cycle it was 80.3Ω . After this third redox cycle it was decided to cool down the electrode in order to make visual inspection of the electrode. It was then revealed that some of the very fine and small cracks present in the electrode layer after sintering had grown down into the TZ3YA pellet and caused parts of the electrode and electrolyte to break off. This decreased the electrode area as well as the electrolyte cross sectional area causing an increase in the ohmic resistance. No current-voltage curves were measured after the third redox cycle.

5. DISCUSSION

In the case of $\text{H}_2/\text{H}_2\text{O}$ oxidation or reduction on these oxide electrodes at $800\text{-}1000^\circ\text{C}$ the simple chemical equilibrium



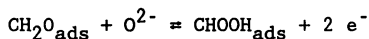
exists when the electrode is not polarized as evidenced by the measurement of stable free potentials approximately equal to the thermodynamically calculated values. No true equilibrium exists in the case of CH_4 oxidation. First of all the chemical reaction between CH_4 and H_2O forming free carbon, H_2 , CO and CO_2 does not take place as no carbon deposition is seen. Also the electrochemical oxidation reaction



is probably not in equilibrium. Three circumstances point to this. First: the feed gas does not contain any CO_2 , second: this equilibrium potential should be approximately independent of temperature while in fact a significant variation is observed, and third: the free potential at 1000°C is not stable.

The rather stable free potentials in CH_4 at 800 and 900°C , however, point to a quasi equilibrium. Even though it cannot be determined with any certainty based on the present data which type of reaction results in stable potentials, one can speculate. If for instance

an intermediate product like CH_2O is formed in some reaction step, part of it might adsorb on the electrode surface and an electrochemical equilibrium might be obtained like



Such a type of mechanism can also explain the more unstable free potentials at higher temperatures because the adsorbed species would become less stable at higher temperatures.

Adsorbed species can furthermore explain the large hysteresis seen on cyclic voltametry in CH_4 . The small hysteresis seen in H_2 for electrode 1 might be due to changes in the electrode. The change in potential will also change the ratio of $[\text{Ce}^{3+}]/[\text{Ce}^{4+}]$ in the electrode. Thereby the number of oxygen vacancies in the electrode surface (and in the bulk) will be changed. If these vacancies are the electrochemical active sites, as assumed by Nguyen, Lin and Mason (2), a vacancy change will also change the reaction rate but not necessarily in a simple manner because the vacancies are also the sites of intermediate adsorption. In the case of H_2 oxidation, OH-intermediates might be present.

The cause of the permanent change of electrode 2 by the treatment with dry CH_4 (Fig. 5) is not clear. The change in average polarisation resistance was from $0.8\Omega\cdot\text{cm}^2$ to $3.2\Omega\cdot\text{cm}^2$, i.e. a factor of 4. The cracking of the electrode was monitored by the measurement of ohmic resistance (impedance spectroscopy). After redox cycle 2 which included the dry CH_4 , the ohmic resistance had increased less than 30% compared to the initial value. It seems reasonable to assume as a first approximation that the reduction in electrode area is inversely proportional to the increase in ohmic resistance and thus the cracking cannot explain the 4 times increase in the average reaction polarisation resistance.

The cracking of the electrode on redox cycling is assumed to be caused by the expansion of the CeO_2 containing oxides on reduction and the contraction on oxidation. If further experiments confirm this, the problem can be solved by sintering the Ce-containing electrode in a reducing atmosphere. If such anode electrode material is to be used in a fuel cell, it may be necessary to use an oxygen potential during its sintering such that the oxygen electrode material is not reduced.

6. CONCLUSION

The mixed ionic and electronic conducting oxide electrodes studied have shown interesting electrochemical properties. It was possible to oxidize CH_4 with 3% H_2O at a rate which is not far from what is demanded in an SOFC. Problems of cracking of the electrodes on reduction and oxidation cycles were observed. Means of solving this problem must be found if this type of Ce-containing oxide anode is to be used in a SOFC.

ACKNOWLEDGEMENTS

This work was supported by the Danish Ministry of Energy under contract no. 1443/89-6. We are grateful to Kjeld Larsen for experimental assistance, to Lone Jørgensen for typing the manuscript and to Dr. Finn Willy Poulsen for valuable discussions.

REFERENCES

1. T. Takahashi, H. Iwahara and Y. Suzuki: Proceedings of Third International Symposium on Fuel Cells, Bruxelles 16-20-VI 1969, Presses Academiques Europeennes, Bruxelles, pp. 113-119.
2. B.C. Nguyen, T.A. Lin and d.A. Mason: J. Electrochem. Soc. 133 (1986) pp. 1807-1815.
3. B.C.H. Steele, I. Kelly, H. Middleton and R. Rudkin: Solid State Ionics 28-30 (1988) pp. 1547-1552.
4. H.L. Tuller, in: Nonstoichiometric Oxides, (O. Toft Sørensen ed.) Academic Press (1981) pp.317-322.
5. B. Cales and J.F. Baumard: Rev. Int. Hautes Temper. Refract. Fr., 17 (1980) pp. 137-147.
6. B. Cales and J.F. Baumard: J. Electrochem. Soc., 131 (1984) pp. 2407-2413.
7. J.J. Bentzen, P.L. Husum and O.T. Sørensen, in: High Tech Ceramics, (P. Vincenzini ed.) Elsevier (1987) pp. 385-398.
8. R. Hartung and H.H. Mübius: Chemic-Ing.-Techn., 40 (1968) pp. 592-600.
9. G.H.J. Broers and B.W. Treijtel: Advanced Energy Conversion, 5 (1965) pp. 365-382.

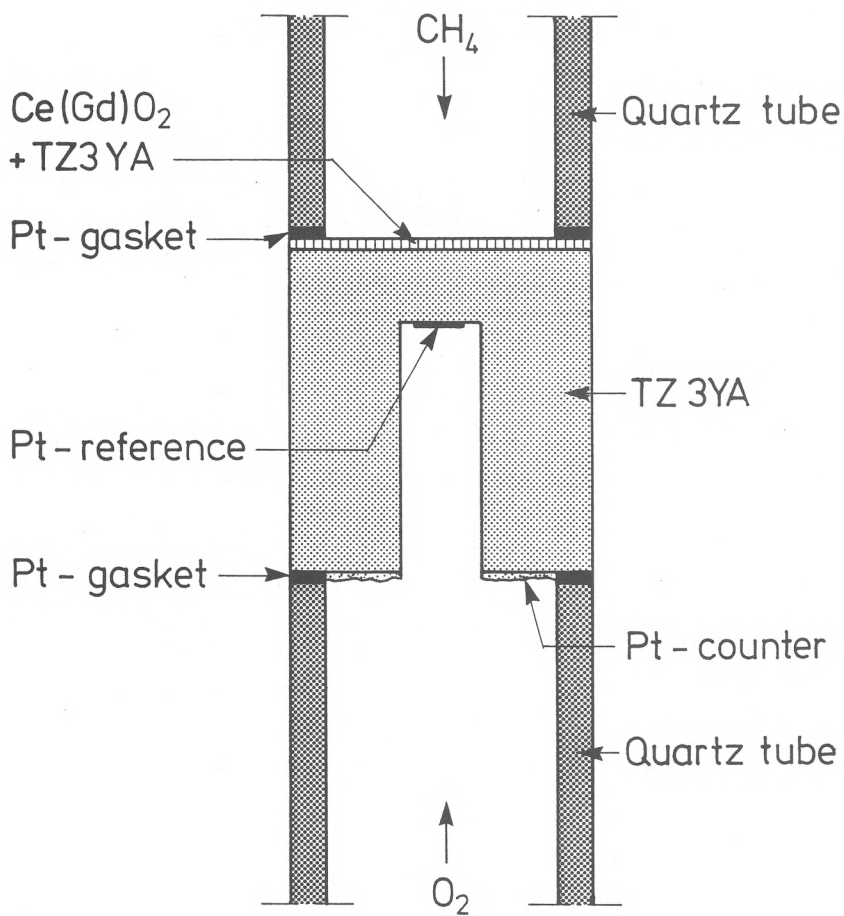


Fig. 1. A sketch of the experimental setup.

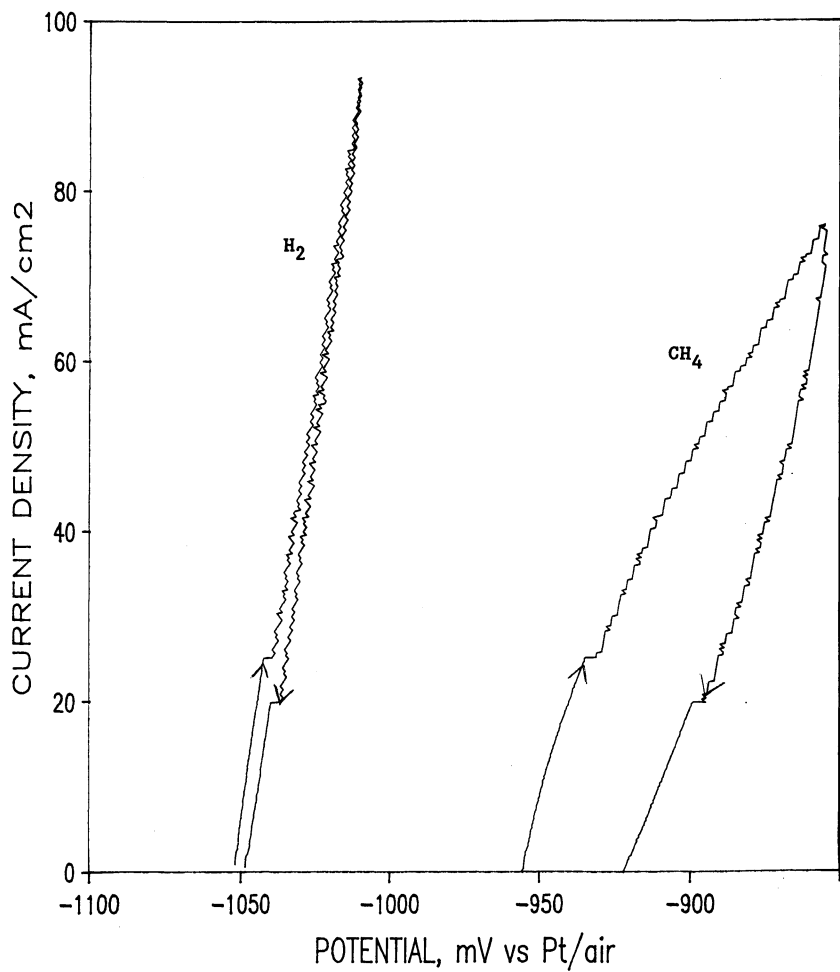


Fig. 2. Current density as a function of potential for electrode 1 in $\text{H}_2 + 3\% \text{H}_2\text{O}$ and $\text{CH}_4 + 3\% \text{H}_2\text{O}$ at 1000°C .

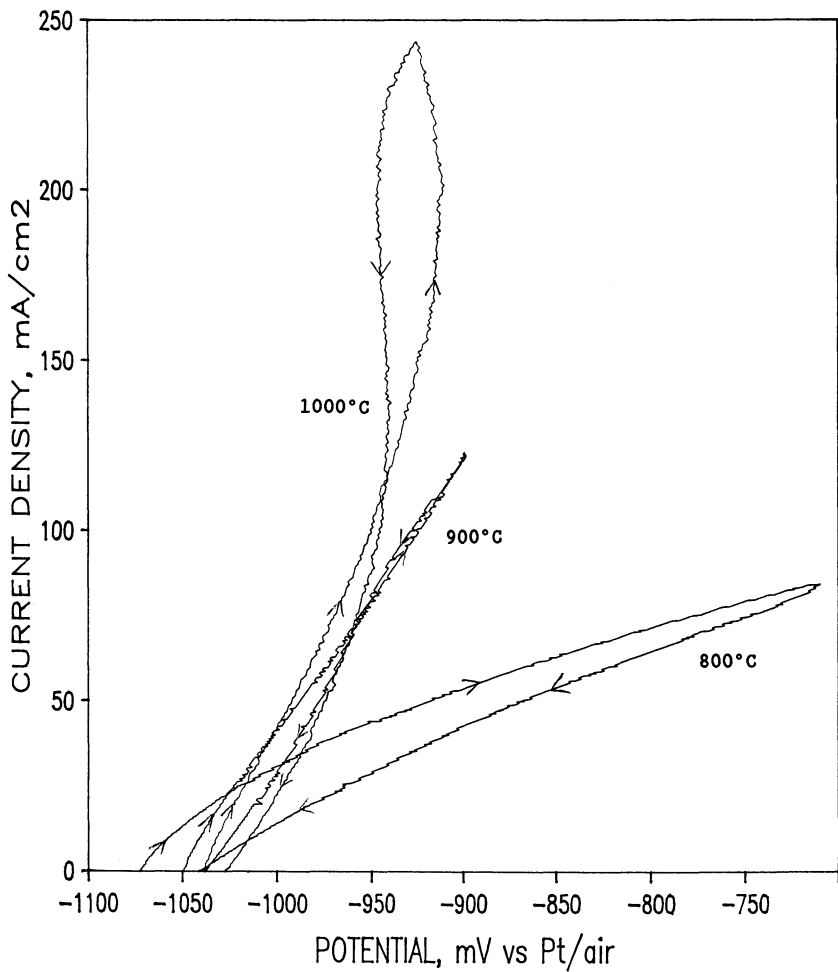


Fig. 3. Current density as a function of potential for electrode 2 in $H_2 + 3\% H_2O$ at 800, 900 and 1000°C.

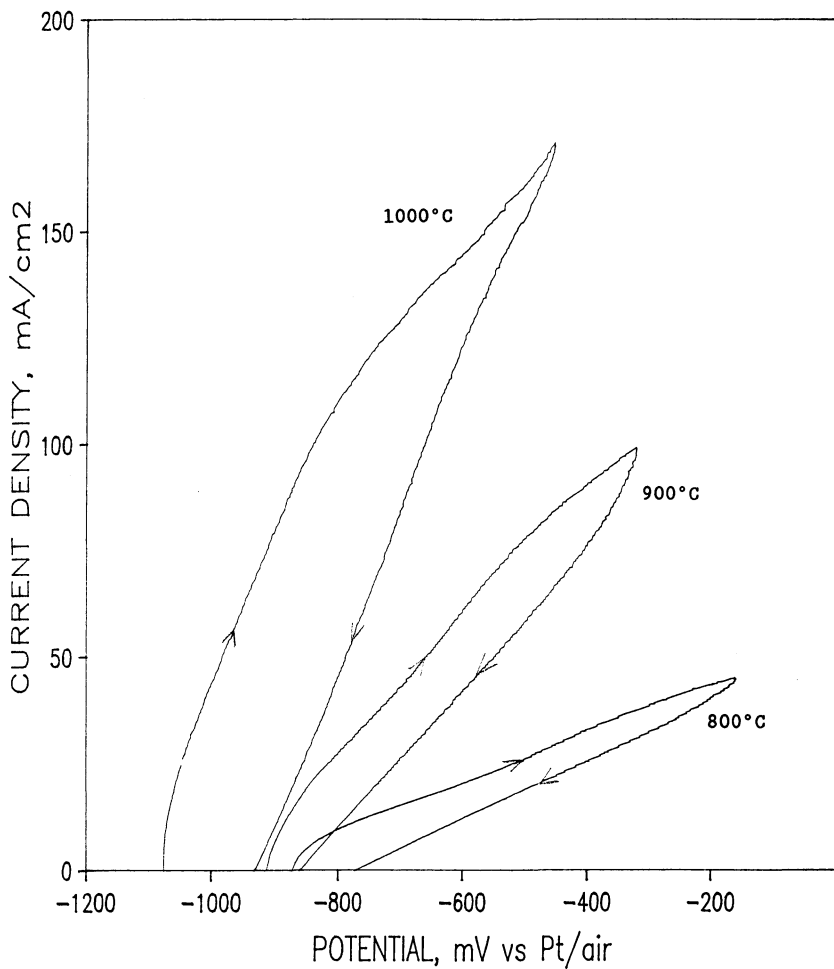


Fig. 4. Current density as a function of potential for electrode 2 in $\text{CH}_4 + 3\% \text{H}_2\text{O}$ at 800, 900 and 1000°C.

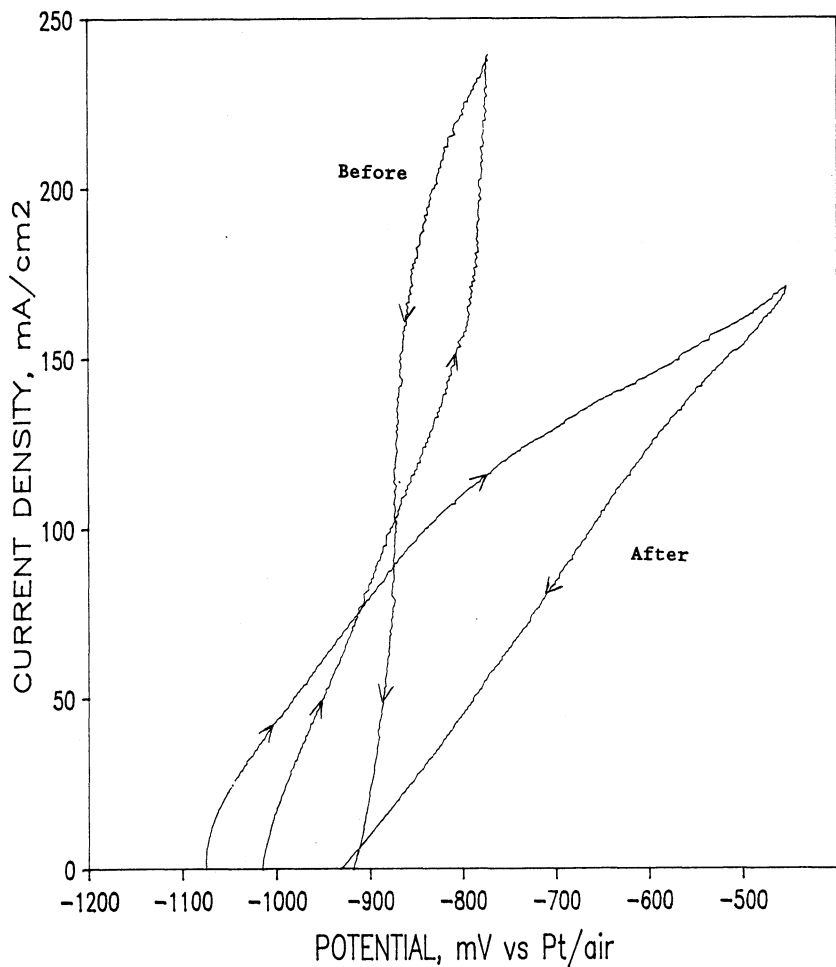


Fig. 5. Current density as a function of potential for electrode 2 in $\text{CH}_4 + 3\% \text{H}_2\text{O}$ at 1000°C before and after redox cycle 2 (i.e. the reduction in pure dry CH_4 , oxidation in argon with $p_{\text{O}_2} = 10^{-2}$ atm and finally reduction in $\text{CH}_4 + 3\% \text{H}_2\text{O}$).

REVIEW OF DEFECT CHEMISTRY OF LaMnO_3 AND LaCrO_3 *

H. U. Anderson, J. H. Kuo and D. M. Sparlin
University of Missouri-Rolla
Ceramic Engineering Department
278 McNutt Hall
Rolla, Missouri 65401

ABSTRACT

Chemical stability and cation stoichiometry determine the applicability of LaCrO_3 and LaMnO_3 as high temperature solid oxide fuel cell (SOFC) interconnects and cathodes respectively. Models for the oxidation-reduction behavior of acceptor doped LaCrO_3 and acceptor doped LaMnO_3 are reviewed. Experimental data are presented which agree with the models and show the regimes of oxygen activities and temperature over which these oxides can be expected to be stable.

1. INTRODUCTION

It is essential for the long term reliability of fuel cells that the electrodes and interconnects of fuel cells be stable, both electrically as well as structurally, at elevated temperatures in the presence of the required electrolytes and oxygen activities. A number of oxides are candidates for this application with some of the most promising being from the perovskite family. For many of the ABO_3 compounds, sufficient electrical conductivity is obtainable by substitution on either the A or B sites by acceptor- or donor-type cations, depending on the intrinsic defect structure of the parent oxide. However, it is known that under certain oxygen activity conditions the electrical conductivity can decrease until the material becomes unsuitable as an electrode.

It is the purpose of this report to review the defect chemistry of the perovskite-type oxides LaMnO_3 and LaCrO_3 to show how the defect structure and electrical conductivity change as they equilibrate under various oxygen activities at elevated temperatures. Models for the oxidation-reduction behavior of both of these p-type oxides are presented.

The electrical conductivity of LaCrO_3 and LaMnO_3 is essentially due to the 3d band of the Cr ions,⁽¹⁾ thus an increase in conductivity can be expected as lower valence ions are substituted on either the La^{3+} , Cr^{3+} or Mn^{3+} sites, resulting in the formation of Cr^{4+} or Mn^{4+} . If such a substitution is compensated by the formation of oxygen vacancies, no contribution to the electronic conductivity

*Sponsored by Office of Basic Energy Science, Department of Energy.

is anticipated. The conditions under which equilibration of LaCrO_3 and LaMnO_3 take place will determine whether electronic or ionic compensation will be favored.

The behavior of LaCrO_3 and LaMnO_3 as shown in the relationships among its electrical conductivity, carrier concentration, oxidation-reduction kinetics, defect structure, and temperature, at various oxygen activities and dopant levels, need to be determined to fully characterize the materials. Such parameters are essential in order to construct a Kröger-Vink-type diagram showing the stability regimes.

Over the past several years we have been preparing Mg and Sr doped LaCrO_3 and Sr doped LaMnO_3 and relating the properties to proposed defect structure models.^(2,3) In this review, the models will be presented and the particular differences between LaCrO_3 and LaMnO_3 discussed. The principle model will be developed using Mg doped LaCrO_3 as an example. However, it is equally applicable to either Sr doped LaCrO_3 or Sr doped LaMnO_3 .

2. PROPOSED DEFECT STRUCTURE⁽⁴⁾

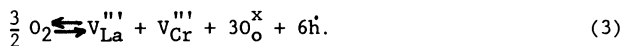
For simplicity, it will be assumed that p-type disorder prevails in nonstoichiometric LaCrO_3 , all defects are fully ionized, and the large cation-to-small cation ratio is unity. Furthermore, it is assumed that the acceptor dopant, Mg^{2+} , substitutes for Cr^{3+} on a normal lattice site. Using Kröger-Vink notation,⁽⁵⁾ the Schottky reaction for this compound is expressed by



and the equilibrium constant is

$$K_s = [V_{\text{La}}'''] [V_{\text{Cr}}'''] [V_{\text{O}}'']^3 \quad (2)$$

From our assumption, the cation stoichiometry must remain constant unless a second phase has exsolved. Therefore, $[V_{\text{Cr}}'''] = [V_{\text{La}}''']$ throughout the entire single-phase region. The p-type nonstoichiometric reaction is given by



The equilibrium constant for this reaction is

$$K_3 = [V_{\text{Cr}}''']^2 [p]{}^6 P_{\text{O}_2} \quad (4)$$

$$= \exp(-\Delta G_3/RT)$$

where ΔG_3 is the Gibbs free energy for Eq.3. When doped, the acceptor impurity, Mg_{Cr}' , will possess one effective negative charge which can be compensated for either by a $\text{Cr}^{3+} \rightarrow \text{Cr}^{4+}$ transition or

by the formation of oxygen vacancies. This leads to the following electrical neutrality condition

$$2[V_O^{''}] + p = 6[V_{Cr}^{''}] + [Mg_{Cr}^{\prime}] \quad (5)$$

At high activity, assuming that both $[V_O^{''}]$ and $[V_{Cr}^{''}]$ are smaller than the impurity content, the neutrality condition becomes

$$p = [Mg_{Cr}^{\prime}]$$

and from Eqs.2 and 4

$$[V_{Cr}^{''}] = \frac{(K_3)^{1/2}}{[Mg_{Cr}^{\prime}]^3} P_{O_2}^{3/4} \quad (6)$$

and

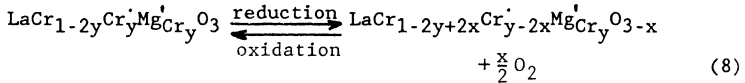
$$[V_O^{''}] = \frac{K_S^{1/3}}{K_3} [Mg_{Cr}^{\prime}]^2 P_{O_2}^{-1/2} \quad (7)$$

respectively.

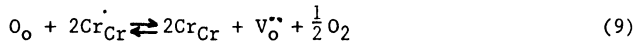
At low oxygen activities, oxygen may be lost and ionic compensation takes place through the formation of oxygen vacancies. In this case the neutrality condition becomes

$$p = [Mg_{Cr}^{\prime}] - 2[V_O^{''}]$$

This condition can be expressed by



or



where y is the amount of dopant and x is the concentration of oxygen vacancies.

The equilibrium constant for reaction 9 can be expressed as either

$$K_9 = \frac{[Cr_{Cr}^{\prime}]^2 [V_O^{''}]^{1/2}}{[Cr_{Cr}^{\prime}]^2} P_{O_2}^{1/2}$$

or

$$K_9 = \frac{(1-2y+2x)^2 x}{(y-2x)^2} P_{O_2}^{1/2} \quad (10)$$

The mass action equation then becomes

$$K_9 = \exp[-(\Delta G_S - \Delta G_3)/3RT]$$

where ΔG_s - free energy of formation for Schottky defects, ΔG_3 is free energy of formation for cation vacancies, and $(\Delta G_s - \Delta G_3)/3$ is the free energy of formation for one mole of V_o'' in acceptor-doped LaCrO_3 .

Equation 10 can be solved to yield

$$2x = y \frac{P_{O_2}^{1/2}}{4K_9} [(8yK_9P_{O_2}^{-1/2} + 1)^{1/2} - 1]. \quad (11)$$

The electrical conductivity σ is given by

$$\sigma = e\mu p$$

where e is the electron charge, μ the mobility, and p the concentration of carriers which, from the model, is equal to $y - 2x$. Thus Eq.11 can be rearranged to give

$$\sigma = \frac{e}{4K_9} P_{O_2}^{1/2} [(8yK_9P_{O_2}^{-1/2} + 1)^{1/2} - 1]. \quad (12)$$

At the high- P_{O_2} limit, Eq.11 reduces to $x = 0$ and Eq.12 reduces to $\sigma = e\mu y$, whereas in the low- P_{O_2} regime the respective equations are reduced to:

$$p = \frac{y-2x}{y} = \frac{P_{O_2}^{1/4}}{(2yK_9)^{1/2}} \quad (13)$$

or

$$\sigma = e\mu \frac{y^{1/2}}{2K_9} P_{O_2}^{1/4} \quad (14)$$

and

$$\sigma/\sigma_R = \frac{P_{O_2}^{1/4}}{(2K_{11}y)^{1/2}}, \quad (15)$$

where σ_R is the conductivity when acceptors are compensated electronically.

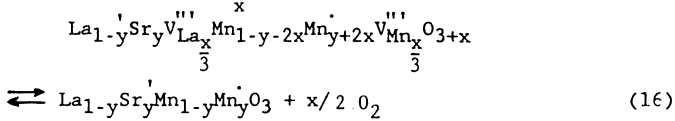
In this P_{O_2} limit, the acceptors become compensated by oxygen vacancies and $[Mg_{Cr}] = 2[V_o'']$. Thus, it is anticipated that σ will decrease with decreasing P_{O_2} , as $P_{O_2}^{1/4}$, as the electrical compensation changes from electronic to ionic.

Thermogravimetric and electrical-conductivity measurements as a function of P_{O_2} and temperature are used to evaluate the equilibrium constants. Diagrams showing the predominant defects under various thermal and oxygen activity conditions can then be constructed. This allows the behavior of the electrical conductivity to be predicted under variable oxidizing and reducing conditions.

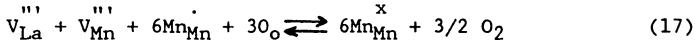
The model developed for LaCrO_3 describes the electrical conductivity of LaMnO_3 quite well. However, LaMnO_3 , even when Sr doped, has excess oxygen at high oxygen activity and in the lowest

oxygen activity Mn^{2+} tends to form and the structure dissociates into its binary components. Thus to explain the defect concentrations the influence of cation vacancies and Mn^{2+} must be considered. (3)

In the oxygen excess region the reduction of $La_{1-y}Sr_yMnO_{3+x}$ may be expressed as



where y represents the dopant and x the excess oxygen concentration. In terms of reactants this reaction can be simplified to be



If it is further assumed that $[V_{La}^{\prime\prime\prime}] = [V_{Mn}^{\prime\prime\prime}]$, then the equilibrium constant for this reaction is given by

$$K_{17} = [Mn_{Mn}^x]^6 P_{O_2}^{3/2} / ([V_{La}^{\prime\prime\prime}]^2 [Mn_{Mn}^{\cdot}]^6 [O_2]^3) \quad (18)$$

which in terms of mole fraction becomes

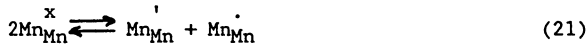
$$K_{17} = (1-y-2x)^6 P_{O_2}^{3/2} / ((x/3)^2 (y+2x)^6 (3+x)^3) \quad (19)$$

For a given dopant level y, K_{17} can be found from the weight loss vs. P_{O_2} experimental data by using Eq.19. Theoretical curves in the high P_{O_2} region were generated by using K_{17} and the proposed metal vacancy model.

As further reduction occurs the Sr dopants are compensated by holes and Eq.9 prevails and the equilibrium constant is given by Eq.10. Since at very low P_{O_2} part of the Mn ions are expected to be divalent, the general neutrality condition can be represented by

$$[Sr_{La}^{\cdot}] + [Mn_{Mn}^{\cdot}] = 2[V_o^{\cdot}] + [Mn_{Mn}^{\cdot}]. \quad (20)$$

The relation between $[Mn_{Mn}^{\cdot}]$ and $[Mn_{Mn}^{\cdot}]$ is given by



with

$$K_{21} = [Mn_{Mn}^{\cdot}] [Mn_{Mn}^{\cdot}] / [Mn_{Mn}^x]^2. \quad (22)$$

In order to maintain the fixed A/B ratio, the following equation has to be maintained

$$[Mn_{Mn}^x] + [Mn_{Mn}^{\cdot}] + [Mn_{Mn}^{\cdot}] = 1. \quad (23)$$

By combining the experimental TG data with the equation 19 the equilibrium constants can be calculated and the theoretical isotherms for the P_{O_2} range investigated generated.

3. EXPERIMENTAL PROCEDURE

The undoped and Sr-doped $LaMnO_3$ and Mg and Sr doped $LaCrO_3$ specimens were prepared by a liquid mix method similar to that first described by Pechini.⁽⁶⁾ In all cases, the A/B ratio (ABO_3) was maintained as unity. The starting chemicals were reagent grade La carbonate, Mn carbonate, Sr carbonate, Cr nitrate and Mg carbonate. The desired compositions were prepared by dissolving quantitative amounts of selected carbonates into solutions of citric acid, ethylene glycol and water. Upon removal of the excess solvent by heating, transparent solid resins containing the metals in solid solution were formed. Calcination of the resin intermediates at 800°C for 8 hours removed the organic constituents, leaving the desired ceramic compositions in a fine, uniform and chemically combined state. For all compositions, X-ray diffraction analysis showed only the perovskite structure. No second phase was detected, implying that the desired solid solution was achieved.

Thermogravimetric measurements were made in a TG system designed to measure weight changes on a powder sample, 70-80 g, to an accuracy of ± 1 mg ($\pm 6 \times 10^{-5}$ mole oxygen). Measurements were conducted at 1000 to 1400°C at an oxygen activity of 10^{-17} to 1 atm, with the oxygen activity being monitored by a calibrated zirconia sensor. Details of the apparatus are given elsewhere⁽⁴⁾.

Electrical conductivity measurements were conducted on dense and porous rectangular bars with four embedded Pt wires welded to Pt leads and attached to a four-terminal digital voltmeter. Conductivity measurements were carried out at 1000 - 1400°C in an oxygen activity of 10^{-17} to 1 atm.

In another apparatus, the Seebeck coefficient and dc electrical conductivity were sequentially measured on the same specimen. The specimen was situated between two Pt blocks. Two Pt - (Pt-10%Rh) thermocouples were used to monitor the temperatures at the ends of the specimen. A Pt wire heater was wound on the lower end of the holder to generate a temperature gradient along the longitudinal direction.

4. RESULTS AND DISCUSSION

A. $LaCrO_3$

Typical TG results for $LaCrO_3$ are displayed in Figs. 1 and 2, which show the experimental data plotted in terms of oxygen deficiency as a function of temperature and oxygen activity for a

constant dopant concentration, and as a function of dopant content and oxygen activity at a constant temperature, respectively. Figure 1 shows that the oxygen activity at which maximum nonstoichiometry occurs shifts to lower values as the temperature is decreased from 1366 to 1014°C, whereas Fig. 2 shows that the degree of nonstoichiometry increases as the amount of dopant increases at any given oxygen activity. The solid lines are those predicted from the model and represent the best fit solution of the equilibrium constant expression.

The temperature dependence of the equilibrium constant, K_0 for reaction⁽⁹⁾ was determined. It was found that for up to 10 at% Mg the enthalpy of the reaction appears to be independent of Mg content; however, at higher Mg content this is not true. For example, up to 10 at% Mg, this value was found to be 272 ± 16 kJ/mol (2.8 ± 0.2 eV), whereas it increased to 331 ± 12 kJ/mol (3.4 ± 0.1 eV) for 20 at% Mg. X-ray diffraction data⁽⁷⁾ indicate that the 20-at% Mg sample is a two-phase system and that under oxidizing conditions the phase boundary is at about 15 at% Mg. Accordingly, an expression for the equilibrium constant of the reaction within the single phase region (up to 10 at% Mg) was found to be

$$K_0 = (2.1 \times 10^4) \exp(-\Delta H/RT) \quad (24)$$

where $\Delta H = 272 \pm 16$ kJ/mol (2.8 ± 0.2 eV) and represents the enthalpy of formation of oxygen vacancies in Mg-doped LaCrO_3 .

Figure 3 displays typical conductivity results plotted as \log conductivity versus $\log P_{\text{O}_2}$ and compared to a calculated plot, using the equilibrium constants determined by the TG data. While there is considerable scatter present and the truncation of the reaction restricts the ionically compensated region, there still is good correlation with the model throughout the entire composition range except for the 20% Mg sample where the dopant concentration appears to exceed the solubility limit⁽⁷⁾ and notable deviation from the model was observed. The activation energy for the mobility was determined from Arrhenius plots of $\ln(\sigma T)$ vs. $1/T$ and found to be 22.3 ± 7 KJoule/mole (0.23 ± 0.07 eV) which is in reasonable agreement with Karim and Aldred's⁽⁸⁾ data. However, our mobility values appear to be about an order of magnitude lower than those for the Sr doped samples implying that Mg which substitutes for Cr on the "B" sites is significantly different than Sr substituting La on the "A" sites.

A plot of conductivity vs. carrier concentration ($y-2x$) is shown in Figure 4 which confirms the assumption that the V_{O} directly compensate the Mg ions and that the mobility does not change under the experimental conditions. Our data show a slight depression at about 80-90% of the maximum expected carrier concentration, this might be due to a band component that exists in doped but uncompensated LaCrO_3 and scattering or trapping by V_{O} . Otherwise, the results show a linear dependence of carrier concentration on conductivity for $y-2x$ values less than 0.05 regardless of the dopant

level, implying that the mobility is constant and approximately equal $5 \times 10^{-6} \text{ m}^2/\text{V}\cdot\text{sec}$. which is about a factor of 5 lower than that reported by Karim and Aldred⁽⁸⁾ ($2.5 \times 10^{-5} \text{ m}^2/\text{V}\cdot\text{sec}$ for 2% Sr). This tends to agree with the higher conductivities that they observed.

B. LaMnO_3

For Sr-doped LaMnO_3 , the oxidized samples exhibited single phase X-ray patterns while the reduced samples were multiphase. The X-ray diffraction analysis showed that under the most reducing conditions (1200°C , 10^{-16} atm) Sr-doped LaMnO_3 completely dissociated into La_2O_3 , MnO , SrMnO_3 and La_2MnO_4 . Upon reoxidation, the reduced samples regained their original single phase X-ray patterns indicating that the redox cycle is reversible. The TG results for $\text{La}_{1-y}\text{Sr}_y\text{MnO}_3$ ($y=0.01, 0.1$ and 0.2) are shown in figures 5 and 6 in which the symbols represent the experimental data while the lines were calculated. As can be seen in figures 5 and 6 the calculated isotherms fit the data quite well.

The electrical conductivity was measured from room temperature to 1200°C as function of P_{O_2} and Sr content. The results are shown in figures 7 and 8. Typical results for the effects of Sr content on conductivity are presented in figure 8.

Both undoped and Sr-doped LaMnO_3 showed common characteristics:

- Little P_{O_2} dependence was observed in a range of high P_{O_2} and this range narrows with increasing temperature.
- As reduction proceeded, the electrical conductivity decreased as $P_{\text{O}_2}^{1/4}$ which agrees well with Eq.14.
- An abrupt decrease of the electrical conductivity occurred under very reducing conditions. These data were too low to be included in figures 7 and 8. However, by comparing with the previous TG data, it was found that the abrupt decrease in electrical conductivity was due to the decomposition of the perovskite phase. For each isotherm shown in figures 7 and 8, the symbol at the lowest P_{O_2} value indicates the "critical" point, i.e., the lowest P_{O_2} before the oxide dissociated into multiple phases. Upon reoxidation, very good reversibility was found.
- The critical P_{O_2} shifted to higher P_{O_2} when the temperature and/or the dopant concentration was increased.

When the temperature was below 1000°C , the electric conductivity increased rapidly with increasing temperature. For temperature above 1000°C , the temperature dependence of electric conductivity shows a transition from positive to negative temperature dependence as the Sr content increased to 20% suggesting a semiconducting to metallic transition. According to the previous studies for LaCoO_3 ,⁽⁹⁾ such a

semiconducting-metallic transition may be due to a localized to collective electron transition. Similar results were also found for other La-site substituted lanthanum manganites of the type $\text{La}_{1-x}\text{M}_x\text{MnO}_3$ ($\text{M}=\text{Pb}^{+2}, \text{Ba}^{+2}, \text{Ca}^{+2}$).^(10,11)

At temperature below 1000°C, the activation energies were determined using the expression derived for the small polaron mechanism,

$$\sigma = (A/T)\exp(-E/kT) \quad (25)$$

where A is the pre-exponential factor, k is Boltzmann's constant, T is the absolute temperature and E is the activation energy. With the application of Eq.9, the hopping energy for undoped LaMnO_3 under oxidizing conditions was calculated to be 0.19 ± 0.01 eV which is lower than the 0.25 eV reported by Goodenough.⁽¹²⁾ Since LaMnO_3 possesses different Mn^{+4} content depending upon the preparation conditions, this small difference in activation energy is understandable. Hopping energies were calculated as 0.19 ± 0.01 , 0.16 ± 0.01 , and 0.09 ± 0.01 eV for 5, 10 and 20 Mol % Sr doped LaMnO_3 , respectively.

The Seebeck coefficients for undoped LaMnO_3 , and 5, 10 and 20 Mol % Sr-doped LaMnO_3 were measured as a function of temperature with the results shown in figure 9. The positive Seebeck coefficients indicate that these oxides are p-type. The variation of Q for these $(\text{La,Sr})\text{MnO}_3$ samples in the temperature range investigated is relatively small when compared with that observed for other kinds of La perovskites such as LaCrO_3 and $(\text{La,Sr})\text{FeO}_3$.^(13,14) According to Eq.10, the weak temperature dependence of Q implies that the carrier concentration is nearly temperature independent. Therefore, the temperature dependence of electrical conductivity would depend largely on the mobility.

Seebeck measurements were made as a function of P_{O_2} and temperature. Typical results for Sr-doped LaMnO_3 are shown in figure 10. With decreasing P_{O_2} , the Seebeck coefficient increased to a maximum after which it became negative. These negative values are not included in figure 10. The P_{O_2} at which the Seebeck coefficient changed from positive to negative was the same as the "critical P_{O_2} " observed in TG and electrical conductivity data.

Even though the absolute values of the measured Seebeck coefficients in the $(\text{La,Sr})\text{MnO}_3$ system are smaller than the $100 \mu\text{V}/^\circ\text{K}$ criterion suggested by Goodenough,⁽¹⁵⁾ for the following we assume the small polaron hopping mechanism derived by Heikes.⁽¹⁶⁾

This relationship is

$$Q = \pm(k/e) [\ln((1-x)/x) + S^*/k] \quad (26)$$

where the plus and minus signs indicate p-type and n-type carriers, respectively, K is Boltzmann's constant, x is the fraction of hopping sites which are occupied, and S^* is the vibrational entropy. When S^* is assumed small enough to be negligible, the Seebeck coefficient depends only on the concentration term. This equation leads to a temperature-independent Seebeck coefficient. By using Eq.26 and assuming that the entropy S^* is negligible, the fraction of sites occupied at 1000°C in an oxygen atmosphere was calculated to be 0.39 and 0.41 for undoped and 20 Mol% SrO-doped LaMnO_3 , respectively. These calculated fractions of hopping sites are clearly too high to result from doping alone. Similar behavior has been reported in the $\text{La}_{1-y}\text{Sr}_y\text{CoO}_{3-x}$ system.⁽¹⁷⁾ This may indicate that the conduction mechanism is more complicated than that proposed by Heikes in that another source of carriers may be involved in the transport mechanism. For example, carriers originating from the band to band transition may be contributing to the conduction at elevated temperatures. Analogous to the (La,Sr) CoO_3 system, at elevated temperatures (La,Sr) MnO_3 may have a position between a metal and semiconductor. Furthermore, since the calculated carrier concentrations for $\text{La}_{0.8}\text{Sr}_{0.2}\text{MnO}_3$ and undoped LaMnO_3 are nearly the same, it may be concluded that the electrical conductivity for these LaMnO_3 based perovskites is dominated by the mobility rather than by the carrier concentration.

The mobility was determined by combining the Seebeck and electrical conductivity data. Figures 11 and 12 show the results as a function of temperature, P_{O_2} , and Sr content. At 1000°C the maximum mobility for undoped LaMnO_3 and $\text{La}_{0.8}\text{Sr}_{0.2}\text{MnO}_3$ was calculated to be 0.045 and 0.071 $\text{cm}^2\text{V}^{-1}\text{sec}^{-1}$, respectively. These results showed that the mobility of undoped LaMnO_3 was appreciably increased by the addition of Sr. From the previous sections, the electrical conductivity of undoped LaMnO_3 was found to be enhanced by the addition of Sr without appreciably altering the carrier concentration. It is concluded that the electrical conductivity for these LaMnO_3 based perovskites is dominated by the mobility rather than by the carrier concentration.

Note that the values of mobility for LaMnO_3 based perovskites calculated above are only approximate, since the Heikes formula which assumed that both spin and orbital degeneracy were negligible was used in the calculation.⁽¹⁶⁾ The real situation may be more complicated than that described by Heikes formula. However, these small mobility values are consistent with the criteria given by Goodenough.⁽¹⁵⁾

5. CONCLUSIONS

1. Both LaCrO_3 and LaMnO_3 are p-type conductors.
2. Both the TG and electrical conductivity data support the models for the oxidation-reduction behavior of both oxides.

3. At 1000°C LaCrO_3 is stable towards reduction, but LaMnO_3 dissociates for $P_{\text{O}_2} \leq 10^{-14}$ atm.
4. LaCrO_3 obeys the small polaron hopping mechanism of conductivity from room temperature to 1400°C on oxygen atmospheres as low as 10^{-18} atm.
5. LaMnO_3 obeys the small polaron mechanism only to about 1000°C after which metallic type behavior is observed.
6. The mobilities for each oxide ranged from 0.05 to 0.1 $\text{cm}^2/\text{v}\cdot\text{sec}$ at 1000°C.

REFERENCES

1. I.G. Austin and N.E. Mott, *Adv. Phys.* 18, 41 (1969).
2. H.U. Anderson, M.M. Nasrallah, B.K. Flandermeyer, and A.K. Agarwal, "High-Temperature Redox Behavior of Doped SrTiO_3 and LaCrO_3 ", *J. Solid State Chem.* 56, 325 (1985).
3. J.H. Kuo, H.U. Anderson, and D.M. Sparlin, "Oxidation-Reduction Behavior of Undoped and Sr-doped LaMnO_3 - Nonstoichiometry and Defect Structure", submitted to *J. of Solid State Chem.*
4. B.K. Flandermeyer, M.M. Nasrallah, A.K. Agarwal, and H.U. Anderson, "Defect Structure of Mg-Doped LaCrO_3 Model and Thermogravimetric Measurements", *J. Amer. Cer. Soc.*, 67, 195-198 (1984).
5. F.A. Kröger and H.J. Vink, *Solid State Physics, Vol. 3*, ed. F. Seitz and D. Turnbull, Academic Press, New York, 1965; p. 307.
6. M.P. Pechini, "Method of Preparing Lead and Alkaline Earth Titanates and Niobates and Coating Method Using the Same to Form a Capacitor", U.S. Patent No. 3,330,697, July 1967.
7. D. Schilling, "The Solubility of MgO in LaCrO_3 as a Function of Stoichiometry", M.Sc. Thesis, University of Missouri-Rolla, 1983.
8. D.P. Karim, and A.T. Aldred, "Localized Level Hopping Transport in $\text{La}(\text{Sr})\text{CrO}_3$ ", *Phys. Rev. B*, 20 2255 (1979).
9. P.M. Raccach and J.B. Goodenough, "First Order Localized-Electron \rightleftharpoons Collective Electron Transition in LaCoO_3 ", *Phys. Rev.* 155 932 (1967).
10. G. Matsumoto, "Magnetic Structure and Electrical Properties of $(\text{La}_{1-x}\text{Ca}_x)\text{MnO}_3$ ", Proc. Int. Conf. on Ferrites, Japan, July 1970.

11. V.I. Pavlov, A.K. Bogush, and G.L. Bychkov, "Influence of Impurity Centers on the Electrical Conductivity of Manganites with a Perovskite Structure", *Inorganic Materials*, 20, No. 5, 752 (1984).
12. J.B. Goodenough, "Theory of the Role of Covalence in the Perovskite-Type Manganites [La,M(II)]MnO₃", *Physical Review*, 100, 564 (1953).
13. J. Mizusaki, T. Sasamoto, W.R. Cannon, and H.K. Bowen, "Electronic Conductivity, Seebeck Coefficient, and Defect Structure of LaFeO₃", *J. of Am. Cer. Soc.* 65, 363 (1982).
14. J. Mizusaki, T. Sasamoto, W.R. Cannon and H.K. Bowen, "Electronic Conductivity, Seebeck Coefficient, and Defect Structure of La_{1-x}Sr_xFeO₃ (x=0.1,0.25)", *J. of Am. Cer. Soc.* 66, 247 (1983).
15. J.B. Goodenough, "Metallic Oxides", *Prog. in Solid State Chem.*, 5, 238 (1971).
16. R.R. Heikes, Thermoelectricity, Interscience, New York, 1961.
17. F.R. van Buren and J.H.W. deWit, "The Thermoelectric Power of La_{1-x}Sr_xCoO_{3-x}", *J. Electrochem. Soc.*, 126, 1817 (1979).

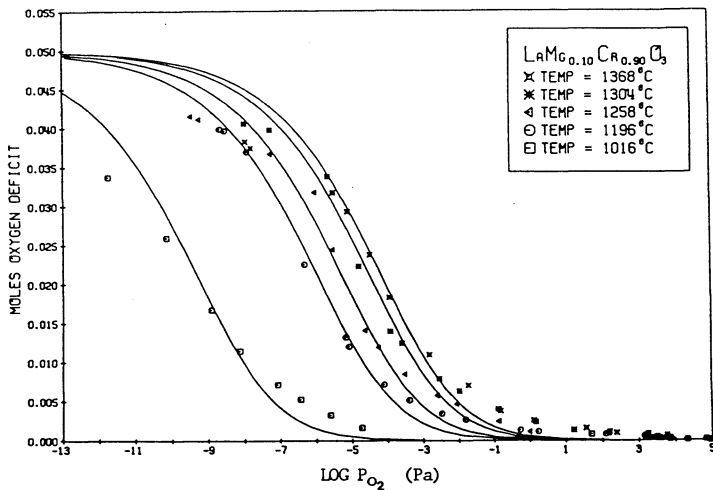


Figure 1. Moles oxygen weight loss per mole sample as a function of $\log P_{\text{O}_2}$ at various temperatures for 5 at% Mg-doped LaCrO_3 .

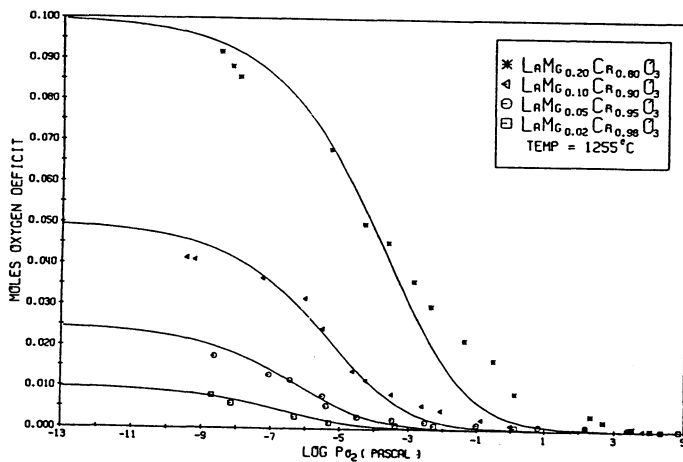


Figure 2. Moles oxygen weight loss per mole sample as a function of $\log P_{\text{O}_2}$ and dopant content at 1255°C.

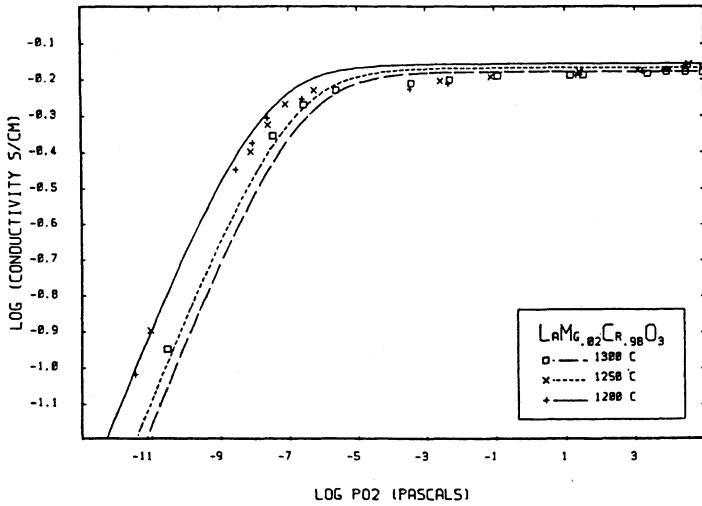


Figure 3. Plots of log conductivity vs. log P_{O_2} at 1200°, 1250° and 1300°C for 2 at% Mg-doped LaCrO_3 .

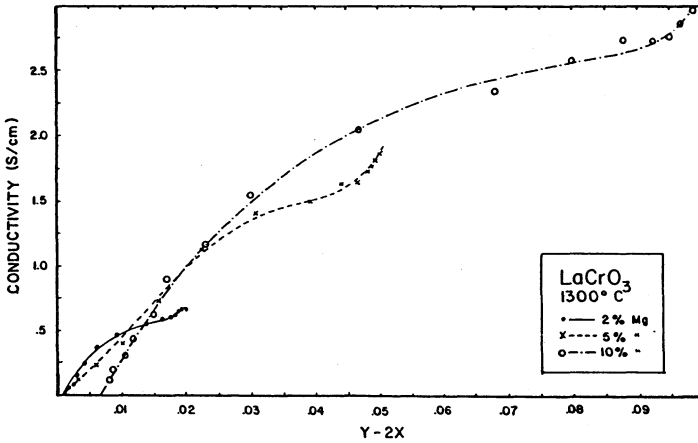


Figure 4. Plots of conductivity vs. $(y-2x)$ for various levels of Mg-doped LaCrO_3 .

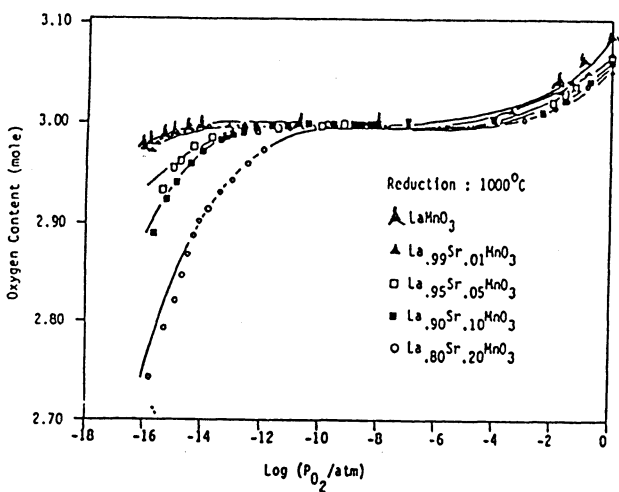


Figure 5. Moles oxygen weight loss per mole sample vs. $\text{Log } P_{\text{O}_2}$ for various Sr-dopant levels. The solid lines are calculated from model and the linearized equilibrium constants.

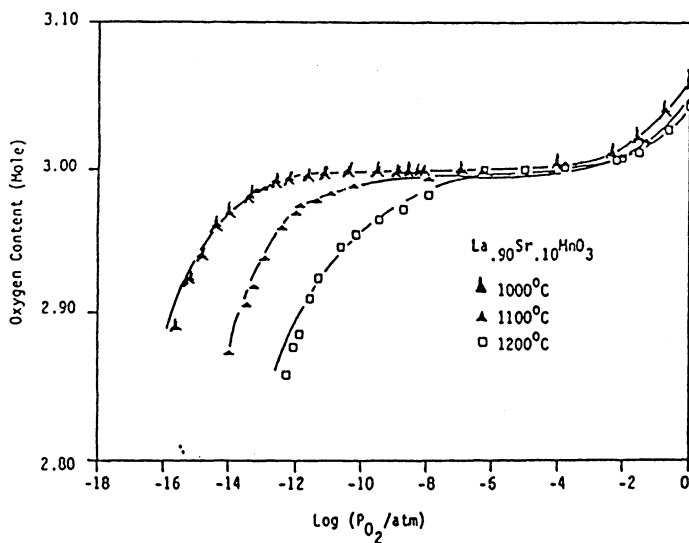


Figure 6. Moles oxygen weight loss per mole sample as a function of $\text{Log } P_{\text{O}_2}$ at various temperatures.

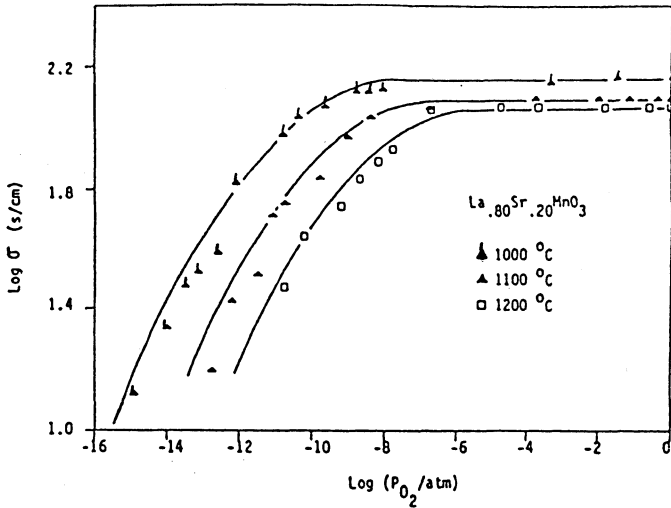


Figure 7. Log conductivity vs. Log P_{O_2} for $\text{La}_{0.8}\text{Sr}_{0.2}\text{MnO}_3$ at various temperatures. The solid lines are calculated from the model.

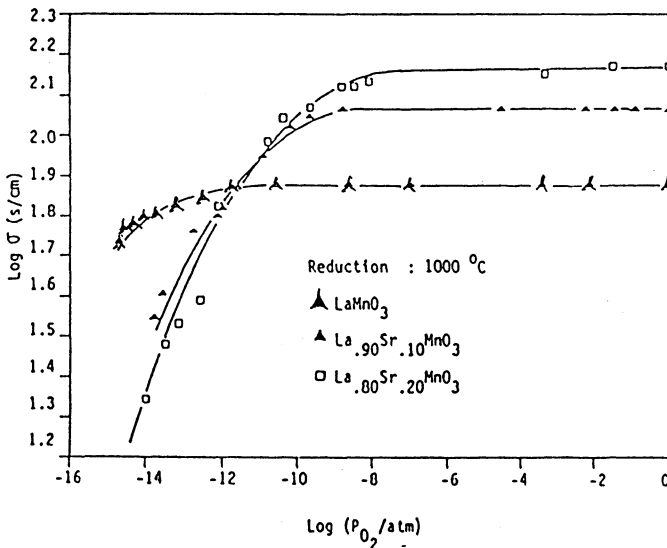


Figure 8. Log conductivity vs. Log P_{O_2} for various Sr-dopant levels at 1000°C.

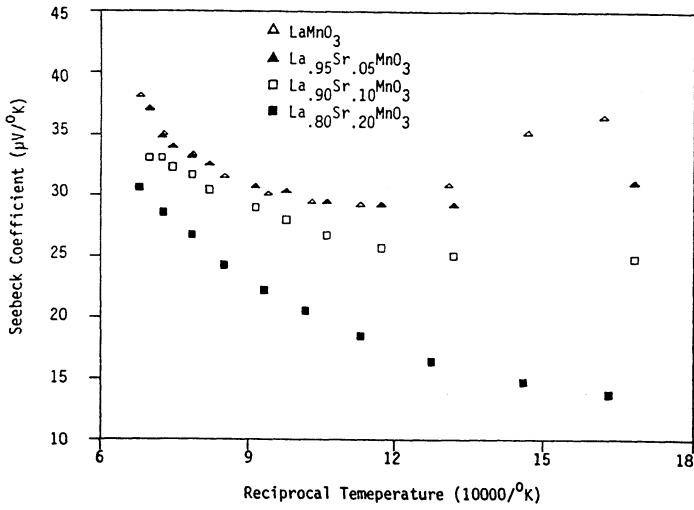


Figure 9. Seebeck coefficient vs. temperature for various Sr-dopant levels.

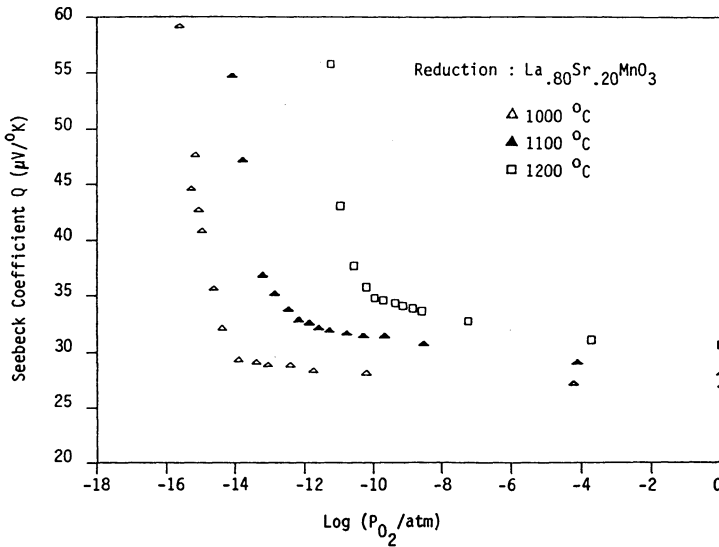


Figure 10. Seebeck coefficient vs. $\text{Log } P_{\text{O}_2}$ for $\text{La}_{.8}\text{Sr}_{.2}\text{MnO}_3$ at various temperatures.

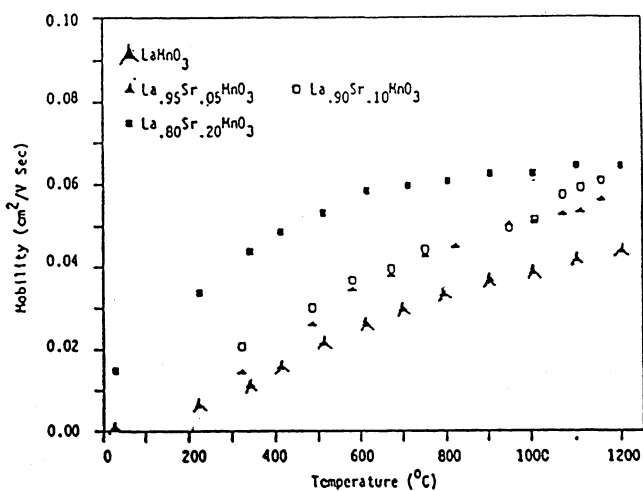


Figure 11. Mobility vs. temperature for LaMnO₃, Sr-doped LaMnO₃. The measurements were done in O₂.

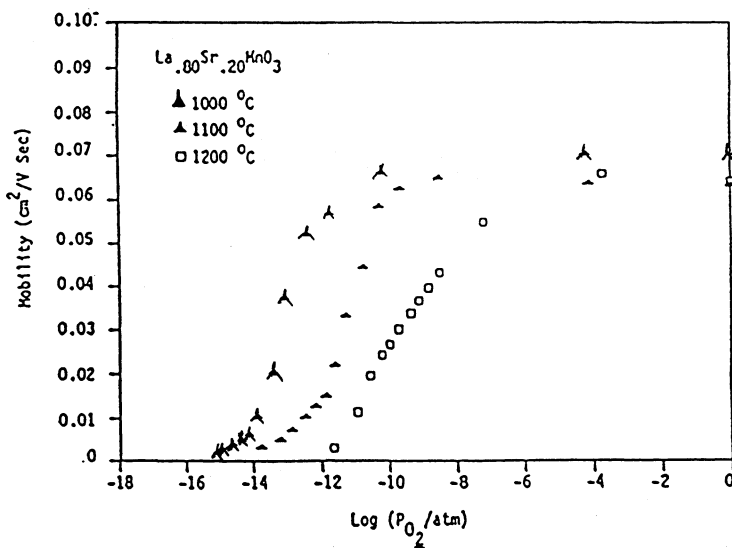


Figure 12. Mobility vs. Log P_{O₂} for La_{0.8}Sr_{0.2}MnO₃ at various temperatures.

THERMAL EXPANSION STUDIES ON CATHODE AND INTERCONNECT OXIDES *

S. Srilomsak, D.P. Schilling** and H.U. Anderson
University of Missouri-Rolla
Ceramic Engineering Department
278 McNutt Hall
Rolla, MO 65401
**Motorola Corporation
Albuquerque, NM 87120

ABSTRACT

The thermal expansion of both the cathode and interconnect of the high temperature solid oxide fuel cell is reviewed. The influence of dopants such as Al, Mg and Sr are discussed. Data are presented which suggest that Sr doped LaCrO_3 matches the thermal expansion of zirconia best, but this composition is more susceptible to expansion upon reduction than Mg doped LaCrO_3 . Data also show that Sr doped LaMnO_3 has too high of a thermal expansion coefficient and that to make a structurally sound cathode, alternate compositions need to be considered.

1. INTRODUCTION

High temperature solid oxide fuel cells (SOFC) are fabricated as a composite of four different oxides:

1. Y stabilized ZrO_2 (Y-PSZ) as electrolyte,
2. Ni- ZrO_2 cermet as anode,
3. $\text{La}_{1-x}\text{Sr}_x\text{MnO}_3$ (LSM) as cathode, and
4. $\text{La}_{1-x}\text{Sr}_x\text{CrO}_3$ (LSC) or $\text{LaCr}_{1-x}\text{Mg}_x\text{O}_3$ (LMC) as interconnect.

It is important that the thermal expansion coefficients (TEC's) of all components are the same if the SOFC is to remain stable during thermal cycling. Since the electrolyte, Y-PSZ is fixed in this cell with a TEC of about $10.3 \times 10^{-6}/^\circ\text{C}$, the TEC's of the other components must be adjusted to match that of Y-PSZ.

*Sponsored by Office of Basic Energy Science, Department of Energy.

In this report the influence of cation stoichiometry, dopant and dopant concentration on the TEC of the cathode and interconnect oxides, LSM and LSC or LMC respectively are reviewed.

2. EXPERIMENTAL

The required compositions were prepared with a chemical preparation technique which allowed precise compositional control and produced highly sinterable powders of $<0.1\mu\text{m}$ crystallite size.⁽¹⁾ The compositions were then dry pressed and sintered into disc-shaped and bar-shaped test specimens whose densities all exceeded 93% of theoretical density with no surface porosity. X-ray diffraction analysis showed that all of the compositions were single phase. Thus it was felt that the preparation technique was such that the thermal expansion measurements should reflect variation in dopant content or cation stoichiometry rather than extraneous influences which may result from the preparation process.

3. RESULTS AND DISCUSSION

A. LaMnO_3

Table I tabulates the average TEC's measured for LSM as function of Sr content. As can be seen the TEC of LSM is greater than that of Y-PSZ particularly for the Sr content of 10-20 m% which is currently being used. With such large differences in TEC's, cracking at the Y-PSZ-LSM interfaces may occur during thermal cycling. However, this does not appear to be a problem, probably due to the porosity of the cathode. This is a potential problem and the differences in TEC's should be corrected.

In order to lower the TEC of LSM, substitutions with smaller cations will have to be made. The addition of either Ca or Y for La will probably lower the TEC. Compositions with these additives are being fabricated and the results will be discussed in a later report.

B. LaCrO_3

1. Pure LaCrO_3

From room temperature to about 240°C , LaCrO_3 is orthorhombic with a TEC of about $6.7 \times 10^{-6}/^\circ\text{C}$. At approximately 240°C the structure becomes rhombohedral with a TEC of about $9.2 \times 10^{-6}/^\circ\text{C}$. As can be seen in figure 1, the TEC is not influenced by the cation stoichiometry⁽²⁾ at least over a range of ± 10 m% variation of La.

No phase equilibria studies in the $\text{La}_2\text{O}_3\text{-Cr}_2\text{O}_3$ system show any appreciable Cr_2O_3 or La_2O_3 solubility into LaCrO_3 . Paulikov et. al.⁽³⁾ conducted a detailed study of the $\text{Gd}_2\text{O}_3\text{-Cr}_2\text{O}_3$ system and found

no apparent solubility. Because of the similarity of the two rare earths, Gd and La, they generalized that LaCrO_3 existed only in the stoichiometric state. Another study by Berjoan⁽⁴⁾ also detected no excess cation solubility in LaCrO_3 , although excess Cr_2O_3 volatilization precluded any precise high temperature X-ray diffraction measurements between the limits of $\text{La}_{0.9}\text{CrO}_3$ and $\text{La}_{1.1}\text{CrO}_3$.

Khattak and Cox⁽⁵⁾ studied samples heated to 500°C in air. No solubility was found in excess La_2O_3 formulations. In excess Cr_2O_3 material, the corundum phase was not detected until the La/Cr ratio was lower than 0.985.

However, as can be seen in figure 2, the temperature over which the orthorhombic to rhombohedral transformation occurs is dependent upon La content. The onset temperature of the transformation ranges from 240°C to 251°C for La/Cr ratios of 0.9 and 1.1 respectively. The transformation is somewhat sluggish, it is small ($<2 \times 10^{-2}\%$) and occurs over about a 10°C temperature range. Upon cooling, the onset of the transformation is depressed by about 10°C . The extent of the hysteresis does not appear to be dependent upon the La content.

2. $\text{LaCr}_{1-x}\text{Al}_x\text{O}_3$

Aluminum ion is isovalent with Cr so only alters the electrical conductivity by a dilution effect. However, Al additions do markedly change the TEC.

The thermal expansion as function of Al content is shown in figure 3. As can be seen the addition of Al does two things: 1) increases the thermal expansion coefficient of the rhombohedral phase from $9.1 \times 10^{-6}/^\circ\text{C}$ to $11.3 \times 10^{-6}/^\circ\text{C}$ as it increases from 0 to 100 m%; and 2) shifts the orthorhombic to rhombohedral transformation temperature to lower temperatures. Figures 4 and 5, illustrate the temperature shift of the transformation temperature. No measurements were made below room temperature so only specimens containing less than 15 m% Al could be measured. An extrapolation of the data suggests that 13 m% of Al is sufficient to shift the transformation temperature to room temperature. About 30 m% Al is required for the TEC to match that of Y-PSZ.

3. $\text{La}_{1-x}\text{Sr}_x\text{CrO}_3$

The addition of Sr to LaCrO_3 also shifts the orthorhombic to rhombohedral transformation to lower temperature. As can be seen in figure 6, as little as 10 m% Sr is sufficient to shift the transformation to below room temperature. From Table II, it is evident that only 5 m% Sr will increase the TEC to that of Y-PSZ. This makes Sr to be very attractive dopant for LaCrO_3 .

4. $\text{LaCr}_{1-x}\text{Mg}_x\text{O}_3$

Magnesium has long been used as an acceptor dopant to increase the conductivity of LaCrO_3 . However, its addition does little to the TEC as can be seen in figure 7 and Table II. Neither the orthorhombic-rhombohedral transformation nor the average TEC's show much dependence on Mg content. Part of the reason that Mg is not very effective is that it has limited solubility in LaCrO_3 . This is particularly evident if excess B cation exists (figure 8). Evidently, in the presence of excess B cation, the Mg reacts with Cr to form MgCr_2O_4 until the A to B ratio becomes unity. This suggests, a possible phase diagram for $\text{MgO-La}_2\text{O}_3\text{-Cr}_2\text{O}_3$ at 1000°C as shown in figure 9. At this temperature the maximum Mg solubility is about 20%, but as can be seen it depends upon the A to B ratio.

5. Influence of Oxygen Activity on Lattice Dimensions

A study was made in which the expansion (or contraction) and lattice parameter changes resulting from cycling Sr and Mg-doped LaCrO_3 from 10^{-20} to 1 atm oxygen at temperatures as high as 1200°C were determined. The dimensional change measurements were made in a controlled atmosphere dilatometer at 1000°C as dense specimens were oxidized and reduced. Results of these measurements are illustrated in figures 10 and 11. As can be seen, the Mg-doped specimens experience about 5 times less expansion with reduction than do the Sr-doped specimens.

Room temperature lattice parameter measurements were also made on powdered specimens which were quenched from a given atm and 1200°C . The atmosphere was maintained during quenching. These data agreed with the dilatometer measurements in that expansion of the lattice occurred as oxygen was lost from the lattice (see figure 12). This suggests that when used as an interconnect Sr doped LaCrO_3 is more susceptible to cracking and leaking due to expansion at the fuel interface than that containing Mg.

4. CONCLUSIONS

1. The TEC's of both LaCrO_3 and LaMnO_3 do not match that of Y-PSZ.
2. The addition of either Al or Sr to LaCrO_3 can adjust the TEC to that of Y-PSZ.
3. The addition of Mg to LaCrO_3 does not alter the TEC with the highest value occurring for 10-15 m% Mg addition $\sim 9.6 \times 10^{-6}/^\circ\text{C}$.
4. The addition of Sr to LaMnO_3 increases the TEC from the base value of about $11.3 \times 10^{-6}/^\circ\text{C}$.

5. In order to lower the TEC of LaMnO_3 , additives other than Sr must be employed. Experience suggests that either Y or Ca additions are likely candidates but there are no data to quantify this supposition.

REFERENCES

1. M.P. Pechini, "Method of Preparing Lead and Alkaline Earth Titanates and Niobates and Coating method Using the Same to Form a Capacitor", U.S. Pat. 3,330,697, July 11, 1967.

2. H.U. Anderson, R. Murphy, K. Humphrey, B. Rossing, A. Aldred, W. Procarione, R. Ackermann and J. Bates, "Influence of Composition and Cation Stoichiometry on the Volatility, Electrical Conductivity and Thermal Expansion of LaCrO_3 Based Oxides", pp. 55-61 in The Rare Earths in Modern Science and Technology, ed. G.J. McCarthy and J.J. Rhyne, Plenum, New York, 1978.

3. V.N. Parlikov, A.V. Shevchenko, L.M. Lopato and S.G. Tresvyatskii, "Chromites of the Rare-Earth Elements and Some of Their Physicochemical Properties", Chemistry of High Temperature Materials, 8 57-62, (1965).

4. R. Berjoan, "Contribution a l'Etude des Reactions de l'Oxygene avec les Melanges d'Oxyde de Lanthane et el d'Oxyde de Chrome III ou de Chromite de Lanthane", Rev. int. Hautes Temperatures et. Refract., 13 199-135, (1976).

5. C.P. Khattak and D.E. Cox, "Structural Studies of The $(\text{La,Sr})\text{CrO}_3$ System", Materials Research Bulletin, 12 463-472, (1977).

TABLE I

Thermal Expansion of $\text{La}_{.99-x}\text{Sr}_x\text{MnO}_3$
(25 to 1100°C)

<u>Composition</u>	<u>$\alpha \times 10^6 / ^\circ\text{C}$</u>
$\text{La}_{.99}\text{MnO}_3$	11.2 ± 0.3
$\text{La}_{.94}\text{Sr}_{.05}\text{MnO}_3$	11.7
$\text{La}_{.89}\text{Sr}_{.10}\text{MnO}_3$	12.0
$\text{La}_{.79}\text{Sr}_{.20}\text{MnO}_3$	12.4
$\text{La}_{.69}\text{Sr}_{.30}\text{MnO}_3$	12.8

TABLE II

Thermal Expansion Coefficients of Mg and Sr-Doped $\text{La}_{.99}\text{CrO}_3$

<u>Compounds</u>	<u>Thermal Expansion Coefficient ($\times 10^{-6} / ^\circ\text{C}$)</u>
$\text{La}_{.99}\text{CrO}_3$	9.48
$\text{La}_{.99}\text{Cr}_{.98}\text{Mg}_{.02}\text{O}_3$	9.46
$\text{La}_{.99}\text{Cr}_{.95}\text{Mg}_{.05}\text{O}_3$	9.57
$\text{La}_{.99}\text{Cr}_{.90}\text{Mg}_{.10}\text{O}_3$	9.48
$\text{La}_{.99}\text{Cr}_{.85}\text{Mg}_{.15}\text{O}_3$	9.55
$\text{La}_{.97}\text{Sr}_{.02}\text{CrO}_3$	10.24
$\text{La}_{.94}\text{Sr}_{.05}\text{CrO}_3$	10.89
$\text{La}_{.89}\text{Sr}_{.10}\text{CrO}_3$	10.74
$\text{La}_{.84}\text{Sr}_{.15}\text{CrO}_3$	10.84
$\text{La}_{.79}\text{Sr}_{.20}\text{CrO}_3$	11.10
Y-PSZ	10.3

*Temperature range from 350 to 1000°C.

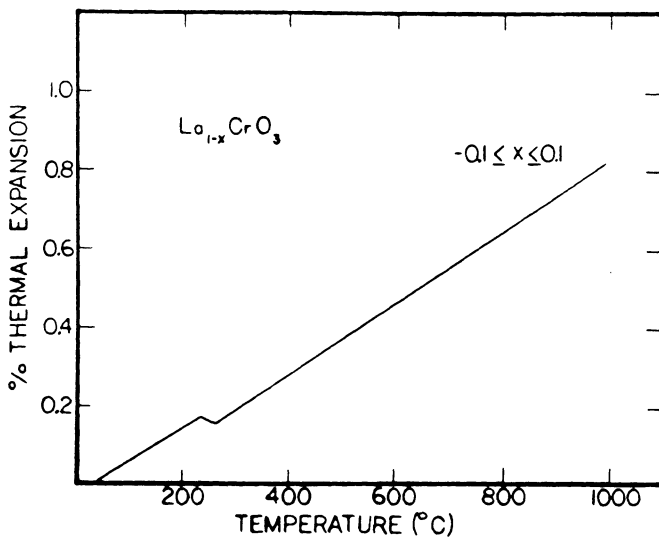


Figure 1. Thermal expansion of $\text{La}_{1-x}\text{CrO}_3$.

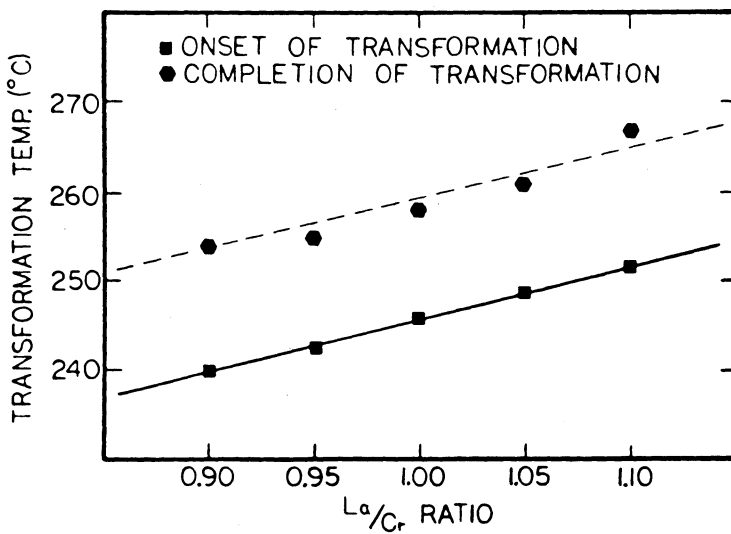


Figure 2. Dependence of orthorhombic-rhombohedral transformation upon La/Cr ratio.

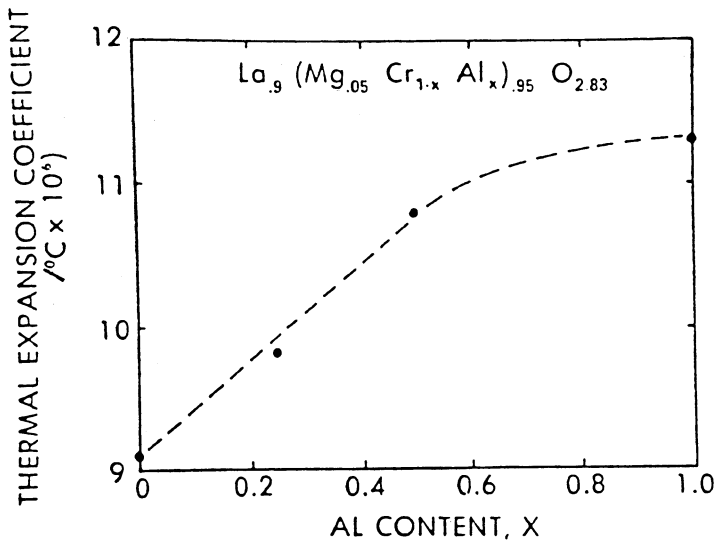


Figure 3. Thermal expansion coefficient of $\text{La}_{0.9}(\text{Mg}_{0.05}\text{Cr}_{1-x}\text{Al}_x)_{0.95}\text{O}_{2.83}$ as a function of Al content.

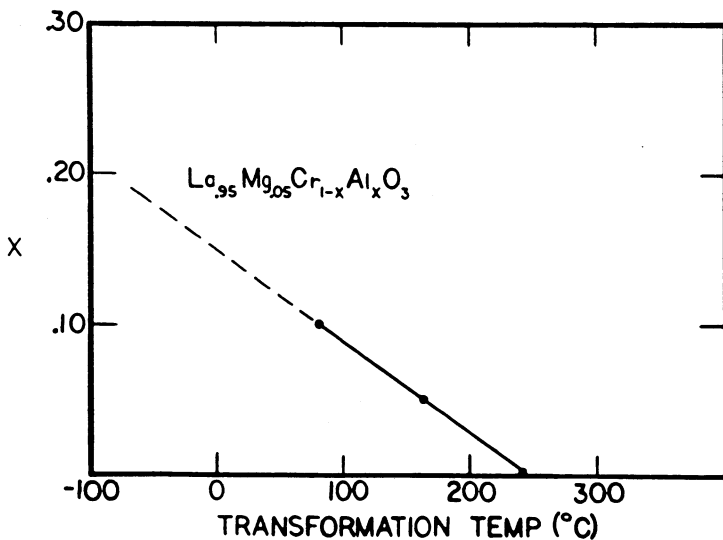


Figure 4. Temperature of onset of orthorhombic-rhombohedral transformation.

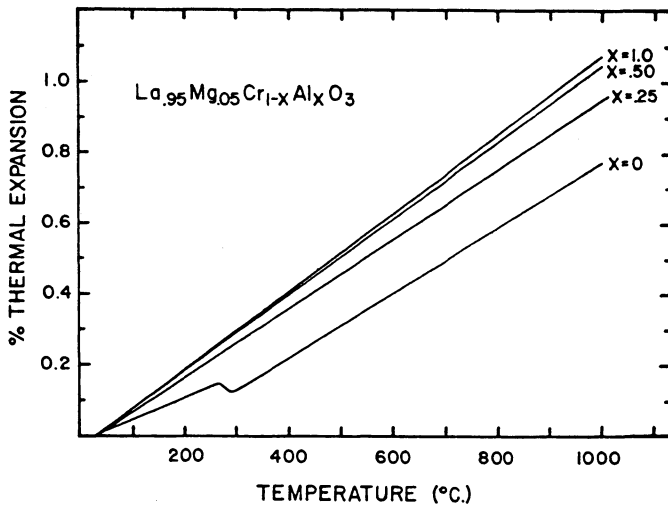


Figure 5. Thermal expansion of $\text{La}_{0.95}\text{Mg}_{0.05}\text{Cr}_{1-x}\text{Al}_x\text{O}_3$.

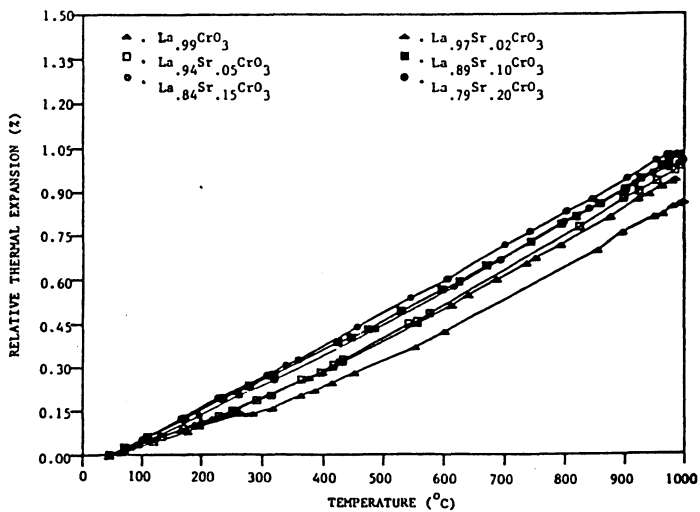


Figure 6. Relative thermal expansion for $\text{La}_{0.99-x}\text{Sr}_x\text{CrO}_3$.

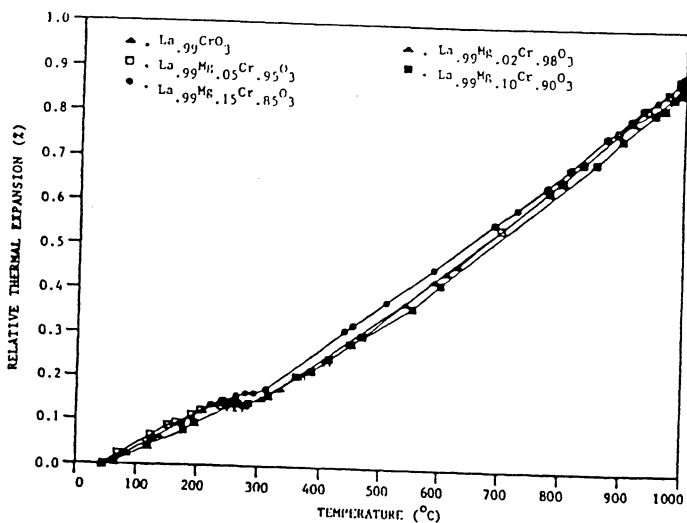


Figure 7. Relative thermal expansion for $\text{La}_{0.99}\text{Mg}_y\text{Cr}_{1-y}\text{O}_3$. (dimensions at 45°C)

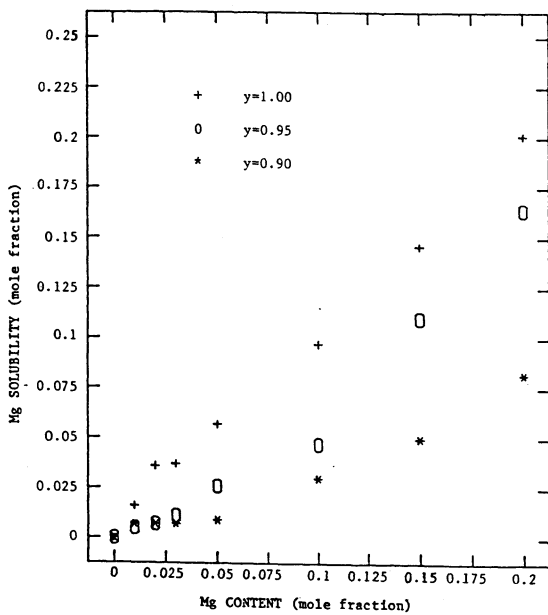


Figure 8. Mg solubility in $\text{La}_y\text{Cr}_{1-x}\text{Mg}_x\text{O}_3$ at 1000°C.

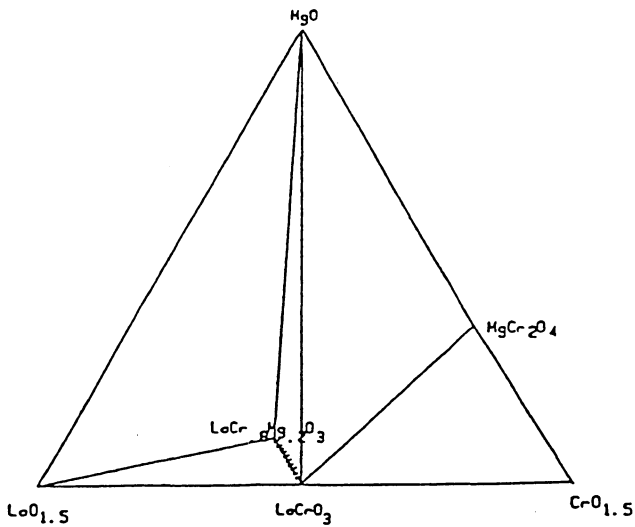


Figure 9. MgO-La₂O₃-Cr₂O₃ phase diagram at 1000°C.

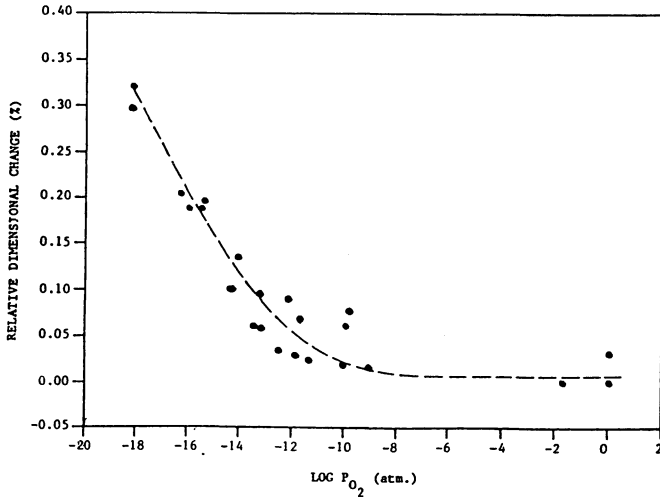


Figure 10. Relative dimensional change as a function of Log P_{O₂} for La_{0.99}Mg_{0.15}Cr_{0.85}O₃. (ref.-dimension at P_{O₂} = 0.2 atm.; 1000°C)

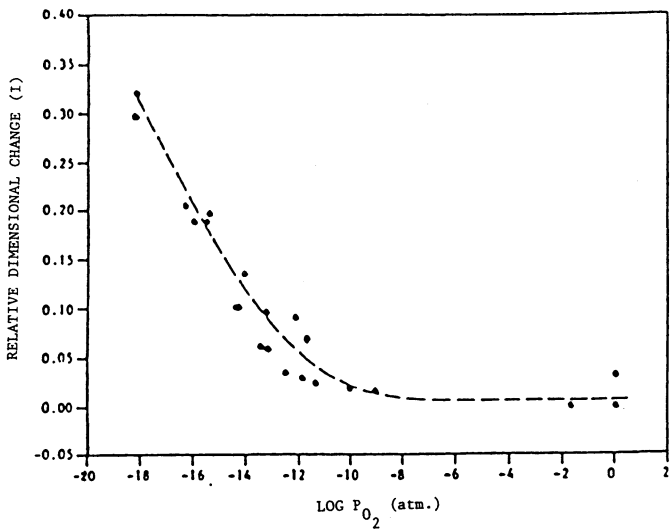


Figure 11. Relative dimensional change as function of Log P_{O₂} for La_{0.79}Sr_{0.20}CrO₃.

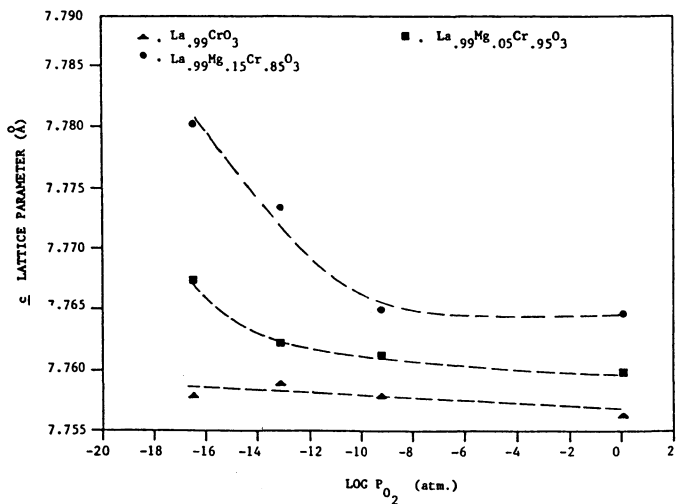


Figure 12. c lattice parameter of Mg-doped La_{0.99}CrO₃ quenched from 1200°C, different oxygen atmospheres.

SOLID OXIDE FUEL CELL ELECTRODES BASED ON $\text{In}_2\text{O}_3\text{-Pr}_{0.83}\text{-ZrO}_2$

J. Lambert Bates, William J. Weber and Curtis W. Griffin*
Materials Sciences Department,
Pacific Northwest Laboratory(a)
Richland, Washington 99352

*Ceramatec
Salt Lake City, Utah

ABSTRACT

Oxides based on $\text{In}_2\text{O}_3\text{-Pr}_{0.83}\text{-ZrO}_2$ and having high electrical conductivity were developed as cathode materials for solid oxide fuel cells (SOFCs). A ternary phase diagram developed at 1823 K relates the electrical, thermal and electrochemical properties to compositions and structures of the material. The bcc In_2O_3 solid solution containing ZrO_2 and PrO_2 exhibits the highest electrical conductivity. Two-phase fcc-bcc structures provide high electrical conductivity with mixed ionic-electronic conduction, thermal expansion characteristics and fabricability compatible with other SOFC materials. The oxides are thermally stable in air to 1473 K, but are easily reduced at 1273 K. Electrochemical testing of an fcc-bcc composition with an externally applied current showed some densification of interface and exsolution of In_2O_3 at the cathode-electrolyte interface.

1. INTRODUCTION

Solid oxide fuel cell (SOFC) performance can benefit from the use of air electrodes with high-electrical conductivity and with mixed ionic/electronic conduction. The higher electrical conductivity will reduce the internal resistance of the fuel cell. The mixed ionic/electronic conductivity will enhance charge transfer and gas adsorption by effectively increasing the potential area for these electrolyte-electrode reactions to occur. A reduced polarization will also result. Presently, the state-of-the-art electrodes are the lanthanum manganites containing strontium.

The purpose of this work was to investigate new and advanced electrode systems that could provide a high electrical conductivity, mixed ionic/electronic transport, a thermal expansion match with the electrolyte and interconnection and still be thermally and electrochemically

(a) Pacific Northwest Laboratory is operated by Battelle Memorial Institute for the U.S. Department of Energy under Contract DE-AC06-76RLO 1830.

stable during cell fabrication and use. The $\text{In}_2\text{O}_3\text{-PrO}_{1.83}\text{-ZrO}_2$ system was selected for this study. The approach was to select 1) a rare-earth oxide that forms fluorite and/or similar distorted fluorite structures that are compatible with the fcc ZrO_2 -stabilized fluorite lattice and 2) a second oxide that will combine with the ZrO_2 and the RE_xO_y to maintain a compatible, related structure that will increase significantly the electronic conduction and not inhibit oxygen ion conduction. The goal is a structurally compatible and stabilized oxide with mixed electronic/ionic conduction and with a thermal expansion similar to that of the Y_2O_3 -stabilized ZrO_2 . Because these advanced electrode materials are synthesized with similar structures and thermal expansion properties, they can be fabricated together simultaneously into a SOFC. In addition, this combination of materials and properties has the potential for minimizing deleterious material interaction with other SOFC components while still retaining the necessary interfacial contact between the electrode and the electrolyte.

ZrO_2 was selected as the composition base for the advanced electrode materials because it is also the major component of the Y_2O_3 -stabilized ZrO_2 electrolyte. Praseodymium oxide was selected because of its ability to stabilize the ZrO_2 in the fluorite phase. Praseodymium also has multiple +3 and +4 valencies and can form a number of oxide phases, providing a favorable defect structure to enhance high-electronic conduction. Y_2O_3 was initially selected as the stabilizing oxide; however, the electrical conductivity did not significantly increase as the other conducting metal oxides were added. This was attributed to the singular valence of yttrium, which has only one oxide. Other rare earth oxides, such as Yb_2O_3 , were considered; however, more was known about $\text{PrO}_{1.83}$.^(a)

In_2O_3 was selected as the oxide added to the $\text{PrO}_2\text{-ZrO}_2$ base because of the rare-earth sesquioxide phase, its high electrical conductivity in air [on the order of 10^3 mhos/cm near room temperature; increasing with additions such as SnO_2 and ZrO_2 (1)], and its ability to stabilize ZrO_2 into the fcc fluorite phase.

This paper considers materials based on the $\text{In}_2\text{O}_3\text{-PrO}_{1.83}\text{-ZrO}_2$ system as advanced air electrodes for the SOFC. The relationships of the electrical transport and thermal properties to structure, phase equilibria and composition are reported. Some thermal and electrochemical stabilities are also discussed. A method, developed for fabricating these oxides, is also described.

(a) Praseodymium oxide at room temperature can exist as either PrO_2 or $\text{PrO}_{1.83}$. For convenience in this report, $\text{PrO}_{1.83}$ is generally used, unless specific reference is made to PrO_2 .

2. FABRICATION

The mixed oxides were synthesized using a coprecipitation process similar to that reported by Dole et al.(2). This technique was important for the preparation of powders and samples with reproducible properties. The nitrates of Pr and In were mixed in proper proportions with either the oxychlorides or sulfates of Zr in water. The solutions were filtered through a 0.2- μm millipore filter to remove both impurities and a gelatinous oxychloride residual. The mixed acids were spray-dried through an ultrasonic pressure nozzle, producing small acid droplets of less than 100 μm in diameter, into an ammonium hydroxide solution to a final pH of 8.5. The precipitates were washed sequentially with water, acetone, toluene and then anhydrous acetone.

The powders were dried, calcined in air between 1073 to 1271 K for 4 h and ball-milled using Y_2O_3 -stabilized ZrO_2 balls in a fluorinated hydrocarbon media. The final surface areas of the powders varied between 12 and 17 m^2/g . The powders were cold-pressed at 69 MPa, then passed through a -145 Tyler mesh screen. The granulated powder was pressed uniaxially into rectangular bars at 152 MPa and isostatically pressed at 228 MPa. These bars were sintered in air in a ZrO_2 -lined furnace with the samples surrounded by sintered powders of compositions close to that of the sample. The sintering temperatures varied between 1823 and 1850 K for periods of 8 to 20 h, with 5-h heating and cooling times. The final density of the samples was >95% TD. Samples were cut from the center of each bar for characterization, property measurements and electrochemical evaluation.

3. PHASE EQUILIBRIA

The ternary phase diagram for the In_2O_3 - $\text{PrO}_{1.83}$ - ZrO_2 system was determined at 1823 K using optical microscopy, scanning electron microscopy (SEM) coupled with energy-dispersive x-ray analysis (EDX) and x-ray diffraction (XRD). Quantitative SEM-EDX is a relatively new technique employed to study phase equilibria. In multiple-phase field, the overall composition is determined quantitatively by scanning large areas containing all phases. The composition of each individual phase was determined by focussing the electron beam on single-phase grains of sufficient size so that the beam did not penetrate or scatter beyond the volume of the single-phase region. The smallest volume that could be examined had to exceed a 1- μm -diameter deep volume probed by the 10-kV electron beam. These quantitatively determined compositions represent the vortex compositions of a three-phase region and points on opposite boundary lines of a two-phase region.

The EDX spectra was calibrated quantitatively at the same electron beam energy using dense, single-phase sintered samples of known compositions that were verified by wet chemistry. The spectral data for the unknown were analyzed and compared with the standard spectra using a computer analog system. The accuracy of the quantitative

SEM-EDX data was within ± 1 mole%. In contrast, XRD is accurate to ± 5 wt%. SEM-EDX was a very rapid and valuable technique since many of the compositions were either two or three-phase.

The proposed ternary phase diagram for the In_2O_3 - $\text{PrO}_{1.83}$ - ZrO_2 in air at 1823 K is shown in Figure 1. This became the basis for selecting compositions and structures for the electrical transport and thermal property measurements. Only those areas that are of interest as potential cathodes that are necessary in understanding property behavior will be discussed in detail in this paper.

$\text{PrO}_{1.83}$ - ZrO_2 The $\text{PrO}_{1.83}$ - ZrO_2 binary has not been reported previously, although a single-phase cubic $\text{Pr}_2\text{Zr}_2\text{O}_7$ has been reported (3-5). The expected phases were anticipated from the isomorphous $\text{PrO}_{1.83}$ - HfO_2 system that had been studied previously (6). The ZrO_2 remains monoclinic (M) to about 6 mol% $\text{PrO}_{1.83}$, monoclinic plus fcc (F) to 17 mol% and is fully stabilized into the fcc phase at 34 mol% $\text{PrO}_{1.83}$ with a lattice parameter of 0.523 nm. The structure is two-phase F plus a $\text{Pr}_2\text{Zr}_2\text{O}_7$ pyrochlore (P) from 40 to 45 mol% $\text{PrO}_{1.83}$. The single-phase $\text{Pr}_2\text{Zr}_2\text{O}_7$ pyrochlore structure exists from 45 to 55 mol% and is a distorted fluorite lattice. The lattice parameter of the In_2O_3 -free pyrochlore is 1.0695 ± 0.001 nm, which is about twice that of the fluorite structure. The reported lattice parameter is 1.0662 ± 0.004 nm (4-5). The structural similarities of $\text{Pr}_2\text{Zr}_2\text{O}_7$ and fluorite PrO_2 make it hard to distinguish between the two structures by XRD, and make the definition of the phases and phase boundaries between the $\text{Pr}_2\text{Zr}_2\text{O}_7$ and $\text{PrO}_{1.83}$ difficult; they are not discussed in this paper. The solubility of In_2O_3 in $\text{Pr}_2\text{Zr}_2\text{O}_7$ is estimated to be near 5 mol%.

$\text{PrO}_{1.83}$ - In_2O_3 The binary phase diagram for $\text{PrO}_{1.83}$ - In_2O_3 has been reported in detail (6). An orthorhombic PrInO_3 phase (O) is the major phase of interest in this portion of the phase diagram. It has a high electrical resistivity.

In_2O_3 - ZrO_2 The ZrO_2 is stabilized as a fcc phase (F) with the additions of In_2O_3 . The ZrO_2 is monoclinic up to 5 mol% In_2O_3 and becomes partially stabilized with the fluorite phase to 12 mol% In_2O_3 . Between 12 and 24 mol%, the ZrO_2 is fully stabilized as fcc. The lattice parameter of the fully stabilized ZrO_2 is 0.5119 ± 0.0005 nm, but increases with increasing In_2O_3 concentrations at both higher and lower In_2O_3 concentration. The lattice parameter also increases as $\text{PrO}_{1.83}$ is added. From 24 to 36 mol% In_2O_3 , the structure is two-phase containing the fcc In_2O_3 -stabilized ZrO_2 and the bcc In_2O_3 solid solution (B) containing 7 mol% ZrO_2 . The lattice parameter is 1.013 ± 0.001 nm. The bcc lattice parameter decreases as the In_2O_3 content is decreased. These results agree with the results reported by Schusterius and Padurow (8) with the exception of small differences in lattice parameters and phase boundaries. However, the XRD data suggest the possibility of a distorted fluorite, rhombohedral phase near 35 mol% In_2O_3 that may be stabilized with additions of $\text{PrO}_{1.83}$. It may also be a high-temperature phase and similar to a rhombohedral $\text{In}_2\text{Hf}_2\text{O}_7$ phase

reported in the isomorphous $\text{In}_2\text{O}_3\text{-PrO}_{1.83}\text{-HfO}_2$ system (6). The indications for the existence of the $\text{In}_2\text{Zr}_2\text{O}_7$ increase as $\text{PrO}_{1.83}$ is added.

$\text{In}_2\text{O}_3\text{-PrO}_{1.83}\text{-ZrO}_2$ The interior portions of the ternary phase diagram are made up of at least two fields containing three phases, i.e. (O + P + B), (P + B + F) and questionable (P + O + C). The two three-phase fields that were determined for certain are separated by a narrow two phase field of P + B and surrounded by four two-phase fields: (P + O), (C + B), (P + O) and (O + B). Because of the interest in high electrical conductivities and structures similar to the fcc fluorite lattice, the property investigations were concentrated in the high- ZrO_2 and In_2O_3 portions of the ternary phase diagram between the In_2O_3 and $\text{PrO}_{1.83}$ fcc-stabilized ZrO_2 and the bcc In_2O_3 solid solution.

4. ELECTRICAL TRANSPORT PROPERTIES

An understanding of the electrical transport properties is critical in the selection of compositions, structures and performance of materials for SOFCs. The dc electrical conductivity, Seebeck coefficients and transference numbers were measured and related to the structures and compositions of the $\text{In}_2\text{O}_3\text{-PrO}_{1.83}\text{-ZrO}_2$ phase diagram.

Electrical Conductivity The dc electrical conductivity was measured to 1700 K in air using a four-point method. Direct currents did not exceed 0.05 A/cm². Temperatures were controlled to within ± 1 K and measurements are accurate to $\pm 5\%$. The data were fitted to a $\log \sigma$ versus $1/K$ relationship with coefficients of determination generally > 0.98 . The electrical conductivities of some selected compositions are summarized in Figure 2.

Orthorhombic PrInO_3 : The PrInO_3 is an electrical insulator with an activation energy of 1.77 eV and the lowest electrical conductivity in the $\text{In}_2\text{O}_3\text{-PrO}_{1.83}\text{-ZrO}_2$ system. The conductivity increases with increasing In_2O_3 as the bcc phase is increased.

$\text{Pr}_2\text{Zr}_2\text{O}_7$ Pyrochlore: The pyrochlore phase has higher electrical conductivity than the fcc fluorite phase (F), but exhibits extensive hysteresis on heating and cooling. This instability is attributed to the many possible praseodymium oxide phases.

$\text{In}_2\text{O}_3\text{-ZrO}_2$: The $\text{In}_2\text{O}_3\text{-ZrO}_2$ binary composition received only limited study because of the interest in the anticipated higher stability of the fcc-bcc phase field containing $\text{PrO}_{1.83}$. The electrical conductivity of the fcc In_2O_3 -stabilized ZrO_2 is close to that measured for a $0.096\text{Y}_2\text{O}_3\text{-}0.904\text{ZrO}_2$ single crystal. However, this composition also exhibited some hysteresis during heating cycles, suggesting the existence of the possible rhombohedral phase discussed earlier. The electrical conductivity measured in this study is higher than that reported by Plotkin et al.(9). The ionic conductivity of the fcc

phase is reported by Hohnke (10) to be comparable to that for ZrO_2 stabilized with 9 to 19 mol% Y_2O_3 .

In_2O_3 - $PrO_{1.83}$ - ZrO_2 : The electrical conductivities of compositions in the center of the In_2O_3 - $PrO_{1.83}$ - ZrO_2 ternary diagram were emphasized because of the potential increased stability of the oxides. The electrical conductivities were found to be dependent on both structure and composition. These results are summarized in Figures 3 to 5. The highest electrical conductivity was associated with the bcc In_2O_3 containing approximately 6 to 10 mol% $PrO_{1.83}$ and/or ZrO_2 .

The electrical conductivity at 1300 K varies with both In_2O_3 and the other oxide phases, as shown in Figure 6. The conductivities were also found to be dependent on the second and/or third phases present along with the bcc phase. The logarithm of the electrical conductivity does not increase linearly with In_2O_3 , but increases rapidly between 20 and 50 mol% In_2O_3 . The highest electrical conductivities in the multi-phase oxides occur when the bcc In_2O_3 solid solution phase is associated with either the pyrochlore or fcc fluorite phase (Figure 7). Increasing the concentration of the orthorhombic phase resulted in decreased electrical conductivity. The presence of either the pyrochlore or fluorite structures also appears to enhance the conductivity much more than the volume ratio for each phase might indicate. The conductivity does not vary linearly with the volume % of the bcc phase, suggesting possible compositional or defect interactions of the bcc with the fcc In_2O_3 -stabilized ZrO_2 and/or the pyrochlore structures; such interactions make them more conductive than the single phase alone.

Seebeck Coefficients The Seebeck coefficient (or thermoelectric power) was determined by applying a temperature gradient along the length of the same samples used to measure the electrical conductivity. Four thermocouples contacted the sample along the length of the bar without holes or bonding. Six voltage-temperature values were obtained from the four combinations of temperatures and voltages. The absolute thermoelectric power was determined from the least-squares analysis of the six data points.

The Seebeck coefficient as a function of temperature for compositions and structures containing the bcc (B), fcc (F) or the pyrochlore (P) phase are illustrated in Figure 8. For compositions containing large fractions of the bcc phase with high electrical conductivity, the Seebeck coefficients were negative (n-type conduction) and increased nearly linearly to higher negative values as the temperature increased; this behavior coupled with high n-type conductivity is representative of degenerate semiconduction. As the fraction of bcc phase decreased and the amount of fcc increased, the Seebeck coefficient became less negative. At the higher fcc contents, the Seebeck coefficients were negative at the lower temperatures and decreased more negatively as the temperature increased. However, at the higher temperatures, the Seebeck coefficient became positive and increased with further

increases in temperature. For the nearly 100% fcc structures, the Seebeck coefficient was positive and increased rapidly to higher positive values (p-type conduction) with increasing temperature, indicative of the oxygen ion vacancy conduction expected for the fcc stabilized structures. These results indicate mixed ionic/electronic conduction in the fcc-pyrochlore-bcc structures.

Transference Numbers The transference numbers were measured with an electrochemical, oxygen half-cell to 1275 K. These results are shown in Figure 9. The electronic transference number (t_e) for the In_2O_3 solid solution is greater than 0.99. As the fraction of bcc decreased, t_e decreased. This change is very rapid, since the electrical conductivity of the bcc phase at 1273 K is 3 to 4 orders of magnitude higher than the stabilized ZrO_2 . However, on a log t_i scale, it is clear that the changes in the transference number relate to the ratio of bcc to fcc in the sample and to the In_2O_3 content. Thus, the B + F + P oxides appear to exhibit mixed ionic-electronic conduction, with t_i increasing with increasing temperature.

More precise transference numbers were determined for analogous compounds in the In_2O_3 - $\text{PrO}_{1.83}$ - HfO_2 system using a coulombic-titration method. For an $0.21\text{In}_2\text{O}_3 \cdot 0.39\text{PrO}_{1.8} \cdot 0.39\text{HfO}_2 \cdot 0.01\text{Yb}_2\text{O}_3$ at 1073, 1123, 1173 and 1223 K, the values of t_i were 0.16, 0.1, 0.07 and 0.05 (6). Thus, these fcc-bcc oxides have a significant ionic conduction, near or greater than 0.1 mhos/cm. However, this significant ionic conduction is often masked by the high electronic conduction near 100 mhos/cm. The total ionic conductivity is estimated to be equal to or higher than the ionic conductivity of the Y_2O_3 -stabilized ZrO_2 at 1273 K.

The proper balance between electronic and ionic conduction can improve the electrode-electrolyte interface reactions, reduce related polarization and increase the fuel cell efficiency. Heyne (11) has shown that as the electronic conduction of an ionic conductor increases, the ionic conduction also should increase. For those In_2O_3 - $\text{PrO}_{1.83}$ - ZrO_2 compositions with sufficient electronic conduction (near 100 mhos/cm) to be a SOFC cathode, such as the 40 mol% bcc phase, the t_i is near 0.01. However, the absolute ionic conduction may be equal to or greater than the total 100% ionic conductivity of the fcc structure, which is near 0.1 mhos/cm at 1273 K. Therefore, in mixed conductors, the total ionic conductivity may exceed that of the fcc phase, even with an electronic conductivity near 100 mhos/cm. Normally, an oxygen half-cell cannot measure ionic transference numbers less than 0.01; therefore for these highly electronic conductors, the total ionic conductivity of these electrode materials, even with a t_i of 0.01, could be higher than that for the >99% ionic fcc electrolyte. Thus, for the In_2O_3 - $\text{PrO}_{1.83}$ - ZrO_2 systems measured, the t_i values of 0.005 and 0.01 represent absolute ionic conductivities near those of the Y_2O_3 -stabilized ZrO_2 .

5. THERMAL PROPERTIES

The thermal expansion and thermal stability in oxidizing and reducing atmospheres are important factors for cathodes in SOFC.

Thermal Expansion The thermal expansion was determined in air to 1473 K using a push-rod dilatometer. The thermal expansion coefficients (α) were compared with values for single-crystal and sintered 9.4 mol% Y_2O_3 -stabilized ZrO_2 , which were 11 and $10.5 \times 10^{-6}/K$, respectively. The coefficient for the In_2O_3 bcc solid solution is $9.3 \times 10^{-6}/K$ and increases with increasing fraction of fcc phase from $9.6 \times 10^{-6}/K$ at 20 mol% In_2O_3 to $10.2 \times 10^{-6}/K$ at 70 mol% fcc (Figure 10). The compositions with the bcc and fcc phases and with In_2O_3 <40 mol% have thermal expansions which best match that of the electrolyte.

Thermal Stability The thermal stability of sintered samples with wide variations in composition was determined by measuring the weight changes after heating at 1273 and 1473 K in air for 98 h. The compositions represented all structures and phase fields that contain significant amounts of the high-bcc solid solution In_2O_3 (20 to 90 mol% In_2O_3). Most samples exhibited a slight gain (<0.02%) in weight on heating at 1273 K, with one sample, which was high in the orthorhombic phase, exhibiting a 0.04% gain. Three of the 13 samples showed a slight weight loss between 0.01 and 0.02%. However, these changes are near to the precision limits ($\pm 0.01\%$) of the measurements. The highest loss was associated with a 75% In_2O_3 -25% ZrO_2 sample that did not contain $PrO_{1.83}$. With this exception, there does not appear to be any direct relationship of weight change to structure, In_2O_3 content or composition.

The thermal stability at 1473 K was less than at 1273 K, exhibiting about four times greater weight loss. Those samples with the orthorhombic structure continued to gain weight, with the highest gain near 0.10% at 1473 K. All other compositions and structures exhibited weight losses of $0.04 \pm 0.01\%$. Thus, stability is reduced with the increase from 1273 to 1473 K. The highest weight losses at both 1273 and 1473 K in air were associated with the $PrO_{1.83}$ -free, 0.75 In_2O_3 -0.25 ZrO_2 bcc - fcc structure. Additions of 5 mol% $PrO_{1.83}$ to the samples containing higher concentrations of In_2O_3 and the bcc phases resulted in a significantly reduced weight losses.

The samples were also heated to 1473 K in reducing 4% H_2 -96% Ar to evaluate the properties of these compositions as anodes for SOFC. All of the samples exhibited significant weight losses for 25 to 64%. The reduction was sufficient to decompose the In_2O_3 - $PrO_{1.83}$ - ZrO_2 to indium metal. The highest weight losses were again associated with the $PrO_{1.83}$ -free, 0.75 In_2O_3 -0.25 ZrO_2 bcc - fcc structure with significantly better stability for similar compositions containing small amounts of $PrO_{1.83}$.

Electrochemical Stability The electrochemical interactions and cation migration between the $\text{In}_2\text{O}_3\text{-PrO}_{1.83}\text{-ZrO}_2$ and Y_2O_3 -stabilized ZrO_2 electrode were studied as a fuel cell and with a voltage applied across the components of cathode-electrolyte to simulate higher current densities of SOFC. Simple half-cells were fabricated by cold pressing together layers of electrode and electrolyte powders into thin discs. The discs were sintered in air at 1823 K for 12 h. Each disc was reduced in thickness and Pt electrodes were attached to both surfaces. The sintered electrode was a fcc - bcc structure with a composition of $0.43\text{In}_2\text{O}_3\cdot 0.24\text{PrO}_{1.83}\cdot 0.33\text{ZrO}_2$, and the composition of the electrolyte was $0.094\text{Y}_2\text{O}_3\cdot 0.906\text{ZrO}_2$; densities were 98 and 95% TD, respectively. The assembly was placed in a furnace at 1273 K in air with a constant current maintained across the half-cell and the voltage monitored during the test. Two separate tests were conducted at current densities of 0.3 and 0.5 A/cm² for 316 and 332 h, respectively. After testing, the samples were sectioned and examined by optical microscopy and SEM-EDX to determine interfacial interactions, compositional variations and structural changes.

The microstructure of a pristine sample before testing exhibited a significant amount of porosity with some localized densification (15 μm wide) at the cathode-electrolyte interface. The two-phase cathode microstructure of $0.43\text{In}_2\text{O}_3\cdot 0.24\text{PrO}_{1.83}\cdot 0.33\text{ZrO}_2$ contained nearly equimolar amounts of a continuous fcc phase with a composition near $0.16\text{In}_2\text{O}_3\cdot 0.56\text{PrO}_{1.83}\cdot 0.28\text{ZrO}_2$ and an irregularly-shaped, approximately 7.5- μm -long and 2- μm -wide discontinuous bcc phase of $0.92\text{In}_2\text{O}_3\cdot 0.02\text{PrO}_{1.83}\cdot 0.06\text{ZrO}_2$. The electrolyte was fcc single-phase Y_2O_3 -stabilized ZrO_2 . A significant amount of In_2O_3 was found in the electrolyte near the interface, apparently having diffused from the electrode into the electrolyte during sintering. This may also have had some impact on the interface densification. However, these small amounts did not alter the fcc structure.

Results from the two tests were similar. The voltages in both tests increased with time from 1.7 to 3.2 volts (0.3 A/cm²) and 1.8 to 4.0 volts (0.5 A/cm²). The microstructure of electrolyte and cathode interfaces in both tests were similar. An example is shown in Figure 10. The thickness of the densified area at the interfaces was approximately twice that of the untested sample and was concentrated in the paths between the pores, although the porosity did not appear to increase. A large second phase of 96 to 98% In_2O_3 with 2 to 4% ZrO_2 and $\text{PrO}_{1.83}$ was found near the interface. Y_2O_3 was not found in this phase. This phase is considered to have resulted from the consolidation of the smaller bcc In_2O_3 solid solution phases present in the untested cathode. The concentration of In_2O_3 in the electrolyte was slightly less than found in the untested sample. The densification at the interface and consolidation and exsolution of the bcc phase was concentrated in the paths between pores, suggesting current densities were higher in these areas than the average current densities being applied at the exterior surfaces.

The In_2O_3 in the bcc phase appears to be very mobile, both during sintering and electrochemical testing. The application of an electrical field has resulted in enhanced densification at the interface, the consolidation of the bcc second phase and the formation of large bcc particles near the electrolyte-cathode interface. This diffusion and densification could limit the use of this composition as a SOFC cathode.

A third test was conducted with a $0.3\text{In}_2\text{O}_3\cdot 0.35\text{PrO}_{1.83}\cdot 0.35\text{ZrO}_2$ cathode and $0.094\text{Y}_2\text{O}_3\cdot 0.906\text{ZrO}_2$ electrolyte at 1273 K in fuel cell geometry using 4% H_2 - 96%Ar as fuel and air as the oxidant. Pt was used as current connections. At 1273 K, the cell had an open circuit voltage of 0.98 volts. With a load of 25 ohms in series with the cell, the current density was 5 to 6 mA/cm² and the power was 2.1 to 2.9 mW (1.2 to 1.7 mW/cm²). The efficiency was low, between 18 and 21%. This was expected since the density of the cathode was very high and was free of porosity. The cell was operated for 468 h and no interactions were observed at the electrolyte-cathode interface.

6. CONCLUSIONS

- The structures and compositions in the phase equilibria of the In_2O_3 - $\text{PrO}_{1.83}$ - ZrO_2 have been related to the electrical and thermal properties and developed as cathode materials for SOFCs.
- The high electrical conductivity is directly related to a bcc In_2O_3 solid-solution phase containing from 4 to 10 mol% ZrO_2 and/or $\text{PrO}_{1.83}$.
- A two-phase fcc and bcc structure containing between 30 and 40 mol% bcc phase provides the high electrical conductivity and thermal characteristics compatible with other SOFC materials.
- The oxides are stable in air to 1473 K, but are easily reduced at 1273 K in a SOFC fuel environment.
- Densification and exsolution of In_2O_3 occur at the cathode/electrolyte interface during electrochemical testing.

ACKNOWLEDGMENTS

The authors acknowledge the contributions of David D. Marchant who participated in the initial research at PNL and D. I. Boget, W. E. Gerry and G. E. Davison who conducted many of the experiments.

REFERENCES

1. J. L. Bates, C. W. Griffin, D. D. Marchant and J. E. Garnier. "Electrical Conductivity, Seebeck Coefficient and Structure of $\text{In}_2\text{O}_3\text{-SnO}_2$ ", *Bull. Am. Cer. Soc.* 65(4) (1986) p 673-678.
2. S. L. Dole, "Technique for Preparing Highly Sinterable Oxide Powders", *Materials Science and Engineering*, Vol. 32 (1978) p 277-281.
3. G. K. Brauer and B. Willaredt, "Oxidation of Praseodymia in Ternary Rare Earth Oxide Phases", *The Rare Earths in Modern Science and Technology*, Vol 2. (J. Gregory, J. McCarthy, J. Rhyme, and H. B. Silber eds.), Plenum Press, New York (1980) p 187-188.
4. V. B. Glushkova and V. A. Krzhizkanovskaya, "The Interaction of In_2O_3 with ZrO_2 and HfO_2 at High Temperatures", *Colloques Internationaux C.N.R.S. No. 205 - Etude des Transformations Cristallines a Haute Temperature* (1973).
5. M. A. Rouanet, "Study of the Zirconia-Rare-Earth Oxide Systems in the Melting Vicinity", *C.R. Acad. Sci, Paris*, Vol. 266 (1968) p 1230-33.
6. J. L. Bates, C. W. Griffin and W. J. Weber, "Advance Materials for Solid Oxide Fuel Cells: Hafnium-Praseodymium-Indium Oxide System", PNL-6575, Pacific Northwest Laboratory, Richland, WA (1988).
7. M. V. Kravchinskaya, A. K. Kuznetsov, P. A. Takhonov and E. K. Koehler. "Phase Diagrams of the Systems $\text{HfO}_2\text{-Pr}_2\text{O}_3$ and $\text{Dy}_2\text{O}_3\text{-Pr}_2\text{O}_3$." *Ceramurgia International*, Vol. 1 (1973) p 14-17.
8. Von C. Schusterius and N. N. Padurow, "Isomorphiebesiehungen in System $\text{In}_2\text{O}_3\text{-Y}_2\text{O}_3\text{-ZrO}_2$ ". *Ber. Deut. Ker. Ges.*, 30(10) (1953) p 235-239.
9. S. S. Plotkin, V. E. Plyushchev and I. A. Rosdin, "Electrical Properties of Ceramics Containing ZrO_2 , HfO_2 and In_2O_3 ", *Investiya Akademii Nauk SSSR, Meorganicheskie Materially*, 11(9) (1975) p 1709-1710.
10. D. K. Hohnke, "Ionic Conductivity of $\text{Zr}_{1-x}\text{In}_2\text{xO}_2\text{-x}$ ", *J. Phys. Chem. Solids*, 41 (1980) p 777-784.
11. L. Heyne, "Ionic Conductivity in Oxides, Experimental Problems; Survey of Existing Data", in *Mass Transport in Oxides*, (J. B. Wachtman and A. D. Franklin, Eds.), National Bureau of Standards Special Publication 296, U.S. Department of Commerce, Washington D.C. (1968) p 149-164.

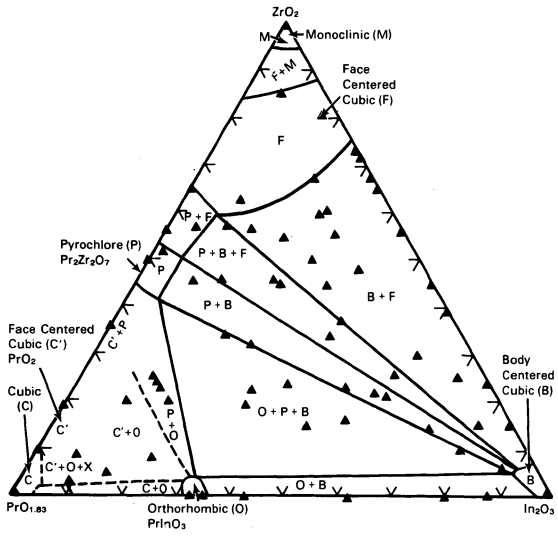


FIGURE 1. Phase Diagram for $In_2O_3-Pr_{0.83}-ZrO_2$ in air at 1823 K.

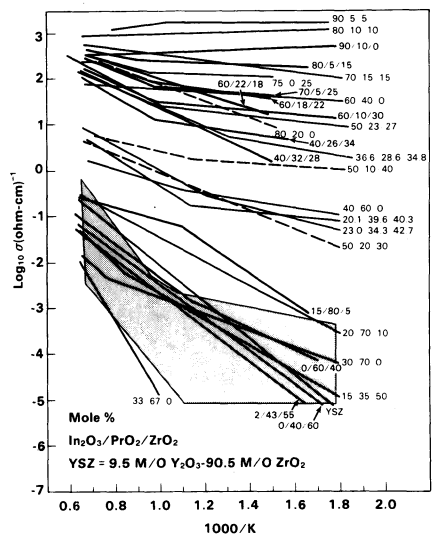


FIGURE 2. Electrical Conductivities of $In_2O_3-Pr_{0.83}-ZrO_2$ in Air.

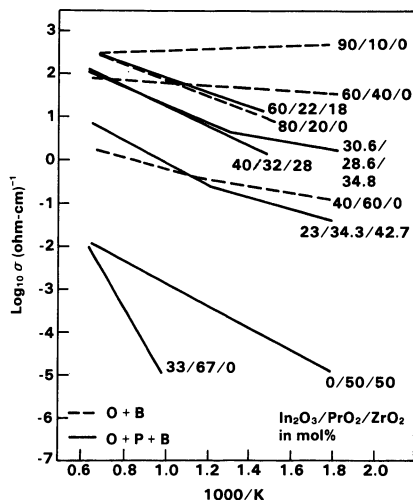


FIGURE 3. Electrical Conductivities of $\text{In}_2\text{O}_3\text{-PrO}_{1.83}\text{-ZrO}_2$ For Compositions with Orthorhombic, Pyrochlore and BCC Phases.

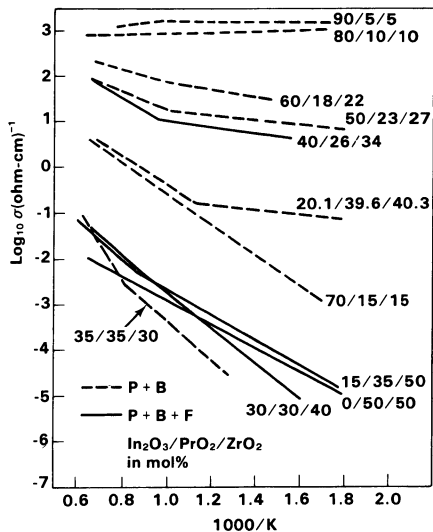


FIGURE 4. Electrical Conductivities of $\text{In}_2\text{O}_3\text{-PrO}_{1.83}\text{-ZrO}_2$ for Compositions With Pyrochlore, BCC and FCC Phases.

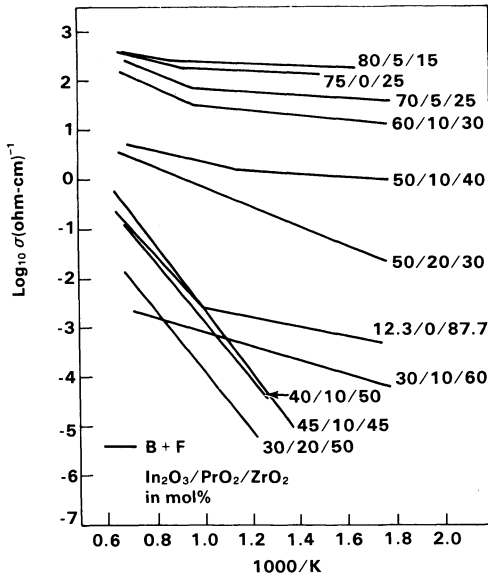


FIGURE 5. Electrical Conductivities of $\text{In}_2\text{O}_3\text{-PrO}_{1.83}\text{-ZrO}_2$ for Compositions Containing BCC and FCC Phases.

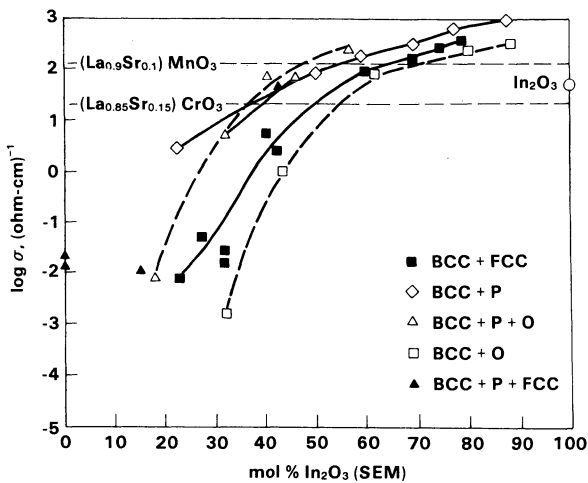


FIGURE 6. Electrical Conductivities of $\text{In}_2\text{O}_3\text{-PrO}_{1.83}\text{-ZrO}_2$ at 1273 K as Function of In_2O_3 Content.

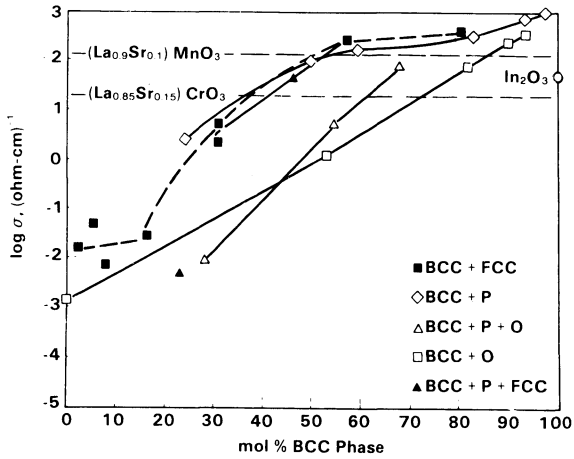


FIGURE 7. Electrical Conductivities of In_2O_3 at 1273 K as Function of BCC In_2O_3 Solid Solution.

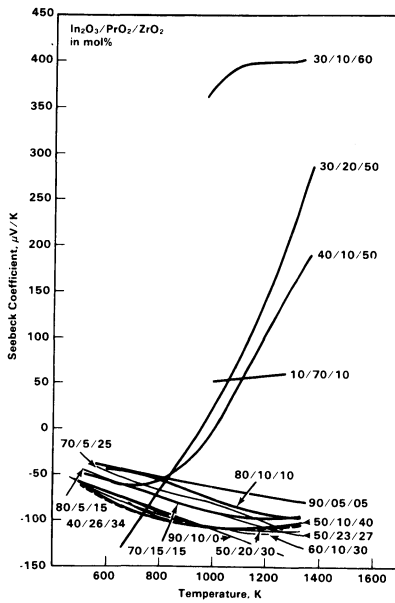
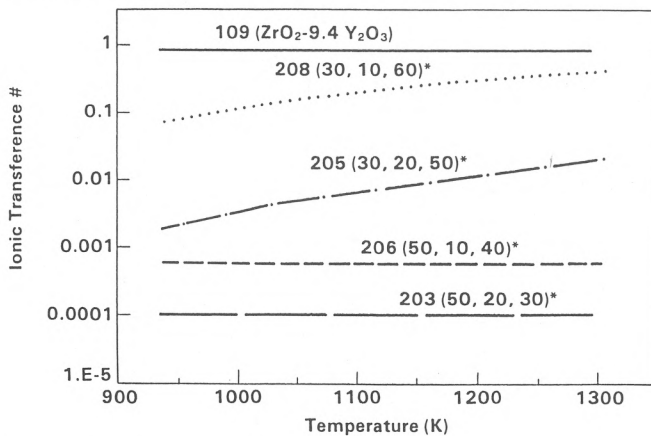


FIGURE 8. Seebeck Coefficient of Some $\text{In}_2\text{O}_3\text{-PrO}_{1.83}\text{-ZrO}_2$ Compositions as Function of Temperature.

Half Cell Results



*Mole % of In₂O₃, PrO₂, ZrO₂, Respectively

FIGURE 9. Ionic Transference Number for Some In₂O₃-PrO_{1.83}-ZrO₂ Compositions At 1273 K.

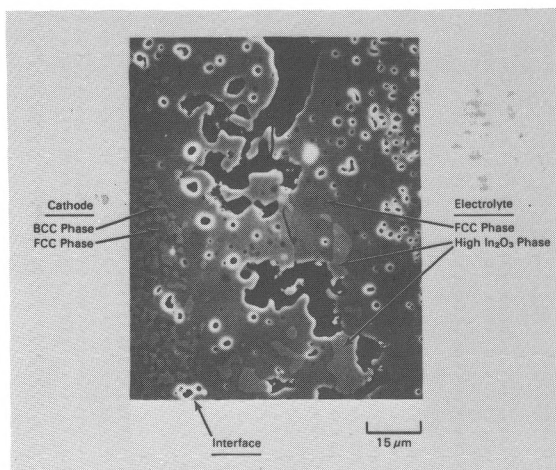


FIGURE 10. Microstructure of the Interface Electrochemical Test with a 0.43In₂O₃·0.24PrO_{1.83}·0.33ZrO₂ cathode and 0.094Y₂O₃·0.906ZrO₂ Electrolyte After an Electrochemical Test with an Externally Applied Current of 0.5 A/cm² for 332 Hours.

Strontium-Doped Lanthanum Copper Oxide as a Solid Oxide Fuel Cell Cathode Material

M.A. Priestnall, B.C.H. Steele
Department of Materials
Imperial College of Science Technology & Medicine
London SW7 2BP, UK

ABSTRACT

$\text{La}_{1-x}\text{Sr}_x\text{CuO}_{3.85+\delta}$ has been investigated as a possible electrode material for high temperature (1123K) oxygen reduction in SOFCs. Preparation routes for the oxide powder and electrodes, including sol-gel, amorphous glass, metal-organic decomposition, co-precipitation and mist pyrolysis, have been studied in detail. Measurements on the bulk oxide and on the electrode films using XRD, SEM, EDAX, TGA, 4-point DC and DC blocking electrodes show that the material is highly compatible with a YSZ electrolyte substrate and promising as a cathode.

1. INTRODUCTION

Solid oxide fuel cells (SOFCs) operate at high temperatures (~1050-1200K) in oxidizing (air/oxygen) and reducing (fuel) environments. Materials selection is therefore critical for the components to survive over the lifetime of a SOFC. For the electrode materials which catalyse the fuel cell reactions and act as current collectors, additional requirements must be met. These criteria can be summarised as:

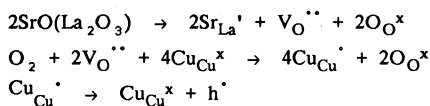
- 1 stable within the range of $p\text{O}_2$ encountered at the anode or cathode
- 2 no reaction with other fuel cell components at the operating temperature
- 3 low volatility of oxide components at the operating temperature
- 4 no destructive phase transition within the operating temperature range
- 5 thermal expansion compatible with the electrolyte substrate
- 6 ability to be formed into films adherent to the electrolyte
- 7 high electronic conductivity
- 8 high ionic conductivity
- 9 high catalytic activity for reduction (cathode) or oxidation (anode)
- 10 low electrode polarization losses
- 11 moderate cost

Perovskite-type non-stoichiometric oxides are a class of materials in which the defect structures, and p-type electronic behaviour, give rise to a range of electrical properties. Their high-temperature stability has led to them being investigated as possible electrode materials for SOFCs. Some of them show promise in this role,

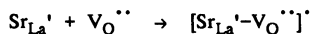
although, to date, strontium-doped lanthanum manganite is the only satisfactory material that is widely used as a SOFC cathode. Other materials are frequently ideal in certain characteristics, but fail on other selection criteria. For example, the high values of electronic conductivity reported for lanthanum strontium cobaltite, at 1120K, range from $\sim 10^2 \text{Scm}^{-1}$ to $\sim 10^4 \text{Scm}^{-1}$ (1,2). However, its thermal expansion coefficient has been measured as twice that of the yttria-stabilised zirconia (YSZ) electrolyte, giving rise to spalling of the electrode film from its substrate. The range of conductivity for this material highlights another aspect of these defect oxides - that their electrode properties are highly dependent upon the level of dopant and upon oxygen non-stoichiometry. Frequently, temperature-dependent conductivities reported for nominally identical materials, vary by orders of magnitude. This emphasises the importance of correlating the electrical properties of an oxide with preparation route, firing conditions, oxygen partial pressure, stoichiometry and bulk and electrode film morphologies.

High ionic conductivity is necessary for oxygen ions to pass through the thickness of an electrode. High electronic conductivity is required since current is collected along its length. Both of these parameters are, therefore, inversely related by the porosity and thickness of the electrode, and a low value of one may be acceptable if compensated by an enhanced value of the other.

Preliminary data reported in the literature (3,4,5) indicate that strontium-doped lanthanum cuprate may meet many of the requirements of a SOFC cathode material. Approximately constant metallic electronic conductivity has been reported in the range $10^2 - 10^3 \text{Scm}^{-1}$ from room temperature up to 600K. This appears to reach a maximum with 15mol% strontium doping (6,7). Self-diffusion experiments using O^{18} at lower levels of strontium doping indicate that the oxide has a significant ionic conductivity, highly dependent upon dopant level (8). When La_2CuO_4 is doped with strontium, additional ionic and electronic (hole) charge carriers are created:



The two competing mechanisms of vacancy formation and hole formation moderate the oxygen stoichiometry in $\text{La}_{2-x}\text{Sr}_x\text{CuO}_{4-x/2+\delta}$, so that δ is a function of x , $p\text{O}_2$ and temperature (7). It is believed that as the concentration of oxygen vacancies increases, it becomes energetically favourable for them to be ordered in fixed positions, possibly located around strontium centres (6,7,9,10):



This suggests that both ionic and electronic conductivity should go through maxima as strontium concentration increases. Raveau and others (6,7) have shown that for electronic conductivity, this maximum is at around 15%Sr. A maximum in ionic conductivity has not been identified in the literature, although the self-diffusion measurements by Routbort (8) suggest that this may be in the range 0-5%Sr.

2. OXIDE PREPARATION METHODS

From the wide variation in bulk electrical properties reported in the literature for nominally identical perovskite-type oxide compounds, it is evident that differences in preparation method can have a significant effect. An important factor in this can be identified as variations in defect structure caused by inhomogeneities in the oxide. When deposited as a ceramic electrode film, it is important that the oxide has consistent and reproducible electrical characteristics. Additionally, deposition techniques must give an electrically continuous electrode layer that remains adherent to the YSZ electrolyte substrate during subsequent thermal cycling. For large scale application in SOFCs, the electrode preparation method must also be convenient, cost-effective and appropriate to the cell geometry.

The suitability of several preparation techniques has been investigated. All of these involve the formation of a precursor to the oxide which is homogenous on an atomic scale. In some cases an electrode film can be formed directly from the decomposition of the precursor, in others the precursor is first decomposed to the oxide powder which is then applied to a YSZ substrate. In all cases, the homogenous atomic mixing results in the desired tetragonal oxide phase being formed more quickly and at much lower temperatures than can be achieved with conventional solid state mixing of oxide, hydroxide or carbonate components.

(i) Sol-Gel

A sol-gel route had earlier been developed for the preparation of YSZ powders, involving the slow hydrolysis of a mixed solution of the metal isopropoxides. Limited success was achieved in adapting this technique for other mixed-metal oxides. However, the combination of solubility difficulties, severe gel shrinkage and the very high cost of the metal alkoxides, led to further work on this oxide preparation route being abandoned.

(ii) Amorphous Glass Decomposition (AGD)

A second technique involved the preparation of amorphous glass precursors which were thermally decomposed to the oxide by calcining at around 1120K for two hours. Several variations of this route were investigated in which a poly-functional hydroxy-carboxylic acid, such as citric acid, was added to a stoichiometric solution of metal salts. The metal ions were coordinated by the carboxylic acid groups into an homogenous, partially-polymeric amorphous complex. The solution was dried below 370K in a rotary evaporator and evacuated desiccator, becoming increasingly viscous and ultimately a brittle transparent glass. Amorphous citrate glasses were prepared in this way using nitrates or acetates of lanthanum strontium and copper, with either water or ethylene glycol as the solvent. Some glasses were also made by replacing citric acid with mono-functional pyridine-N-oxide. For the stoichiometric metal ratio La(1.7):Sr(.3):Cu(1), these methods gave a total of eight different glass types. In all cases, the glasses were transparent blue or blue-green, and X-ray diffraction showed them to be amorphous.

It proved extremely difficult to completely dry or calcine the glasses without them foaming. In some preparation routes described in the literature (11), the nitrate-ethylene glycol solutions were boiled before adding the complexing agent, in

order to partially decompose the nitrates and prevent subsequent NO_2 foaming. For the combination of lanthanum and copper, however, the solution was too unstable for this to be done, possibly due to the formation of the di-nitrate ester of ethylene glycol (11,12). The glasses readily decomposed above 900K to the oxide, retaining a very friable foamed structure of partially sintered particles.

It was possible to produce adherent films of the oxide on YSZ from all of the glassy precursors, by painting the dilute complex solution onto the substrate. With very slow drying and calcination, it was possible to avoid foaming of the layers, but the high degree of shrinkage caused severe film cracking (Figure 1). Additional films of the oxide were deposited on top, to improve the electrode conductivity, but adherence was found to be very poor. For lanthanum strontium cuprate, it is concluded that the AGD route can be used to prepare highly homogenous powders, but is unsuitable for the direct deposition of electrode films.

(iii) Metal-Organic Decomposition (MOD)

Using the method described by Vest (13), quantitative stock solutions of lanthanum and strontium 2-ethyl hexanoate and copper neodecanoate in xylene were prepared. These were mixed together to give the desired stoichiometric metal ratios and painted onto YSZ plates. Drying the films under a heat lamp and firing to 1273K at 1K per minute, produced very thin but adherent layers of black $\text{La}_{1.5}\text{Sr}_{3.5}\text{CuO}_4$. Using faster decomposition rates, or painting on thicker organic films, tended to cause the oxide layers to crack and detach. As with the amorphous glass decomposition route, conductivity could be improved by depositing multiple thin layers, but at the expense of poorer adherence. Loading the organic precursor solutions with previously calcined oxide powder gave thicker films, but no improvement in adherence. X-ray diffraction showed the MOD films to consist of the desired tetragonal oxide phase, with some residual strontium carbonate being detected up to 1323K. Similar experiments carried out with lanthanum strontium manganite, gave much more adherent and continuous electrode films. For $\text{La}_{1.5}\text{Sr}_{3.5}\text{CuO}_4$, the MOD technique can be used to deposit thin oxide layers on YSZ, but does require very slow rates of drying and firing.

(iv) Co-Precipitation

Carbonate co-precipitation of the metals in their stoichiometric ratios was investigated in order to prepare tens of grams of the oxide for bulk electrical measurements. A mixed aqueous solution of the metal nitrates was added dropwise to a slight excess of sodium carbonate solution in a high-shear stirrer. The milky-blue precipitate was centrifuged and washed several times before drying and calcining at 1100K for two hours. X-ray diffraction showed the oxide to consist of the desired phase, with only a small level of strontium carbonate contamination. However, the technique was deemed unsatisfactory on a number of grounds. Firstly, a small proportion of the copper was retained in solution due to the formation of a soluble sodium complex, $\text{Na}_2[\text{Cu}(\text{CO}_3)_2] \cdot 3\text{H}_2\text{O}$. Secondly, repeated washing of the precipitate, in order to remove sodium ions, would also tend to dissolve the very slightly soluble strontium carbonate. Thirdly, during the drying stage, the carbonate powder formed solid cakes which led to large aggregates in the calcined oxide powder.

A brief study of the solubilities and stabilities of lanthanum, strontium and copper salts in various solvent systems was carried out in order to determine a more

appropriate precipitation technique. Co-precipitation of the oxalates from a solution of the metal acetates in ethanol, was found to offer the most reliable route. The bidentate nature of the oxalate ligand enabled its two COO^- groups to coordinate to two different metal cations, and consequently for each metal cation to be chemically linked to several others. Under the SEM, the precipitated, washed and dried oxalate particles appeared as flakes $0.5\text{--}3\mu\text{m}$ in diameter, reducing to $0.5\text{--}1\mu\text{m}$ spheroidal particles when calcined.

The high degree of homogeneity in the oxalate product minimises the temperature and time required for calcination to the oxide. Thermogravimetric decomposition was carried out in air from room temperature to 1250K at 5K per minute. Three distinct decomposition stages were recorded in the temperature ranges $550\text{--}570\text{K}$, $640\text{--}690\text{K}$ and $720\text{--}770\text{K}$, as shown in Figure 2. XRD of powder samples, calcined at a series of temperatures, confirmed that the precursor had been completely converted to the desired tetragonal oxide phase after two hours at 923K . Gradual sharpening of the XRD peaks beyond this temperature is believed to be due to an increase in particle size.

From these results, it is concluded that for rapid preparation of bulk quantities of fine lanthanum strontium cuprate powder, the oxalate co-precipitation route is very convenient.

(v) Mist Pyrolysis

Electrode films of $\text{La}_{1.7}\text{Sr}_{.3}\text{CuO}_4$ on small plates of YSZ were prepared directly by the impact of sub-micron oxide spheres. A series of ultrasonic transducers operating at 1.6MHz were used to atomise an homogenous, stoichiometric solution of the metal acetates or nitrates. The resulting mist was carried in an air stream through two furnaces at 670K and 1100K , where the droplets were dried and calcined to spherical oxide particles. At the cold end of the system some of the particles deposited onto an orthogonally placed YSZ plate, while the remainder were trapped on a glass filter. The oxide layers obtained were sintered onto the YSZ substrates for approximately one hour at 1350K . Very strongly adherent and dense oxide films, $10\text{--}40\mu\text{m}$ thick, were obtained for deposition times of $45\text{mins--}4.5\text{hrs}$.

In this experiment, 1dm^3 of a 0.05M aqueous solution of the mixed nitrates gave spherical oxide particles with a mean diameter of $0.67\mu\text{m}$ ($\sigma=0.23\mu\text{m}$) (Figure 3). This is predictable and can be controlled, using the approximate relationship:

$$d^3 = (0.91 C M \gamma) / (V \rho \rho' f^2) \quad [\text{S.I. units}]$$

in which the particle diameter, d , is proportional to the cube root of its molecular weight, M , the solution concentration, C , and the surface tension of the solvent; and is inversely proportional to the cube root of its density, ρ , the density of the solvent, ρ' , the volume of the solution, V , and the square of the transducer frequency, f .

For lanthanum strontium cuprate, SEM micrographs of the cross-section of the electrode layers showed no pores and an apparently completely dense material, although an open structure of partially sintered particles was observed at the surface (Figures 4, 5). This is in contrast to similarly prepared oxide layers of lanthanum strontium manganite, which had a porous structure throughout. The required particle

sizes and firing conditions to produce adherent porous films of $\text{La}_{1-x}\text{Sr}_x\text{CuO}_4$ are yet to be determined, but, nevertheless, the mist pyrolysis route seems to offer considerable potential for SOFC electrode deposition.

(vi) Electrodes from Powder Slurries

All the routes described above can be used to prepare the oxide powder. A short series of experiments was carried out to determine whether the powders could easily be deposited as electrode films, using various solvents as powder dispersants. Samples of calcined oxide powder, prepared via the oxalate co-precipitation route, were ultrasonically dispersed in water, acetone, methanol, ethanol, heptanol and ethylene glycol. Films were spread across the surface of YSZ plates and dried in air, or under a heat lamp, before firing to around 1200K for two hours. By far the best results were obtained with water and ethanol which gave reasonably uniform, adherent, conductive, porous oxide layers. The more viscous solvents took several hours to dry and the oxide films were less adherent. The lighter solvents evaporated too rapidly to get a uniform coverage of the oxide powder. SEM micrographs of the water/ethanol-derived oxide electrodes showed them to consist of 1–5 μm oxide particles sintered together in an open structure, similar to that in Figure 5. EDAX measurements across the interface between the YSZ substrate and the electrode layer showed no evidence of reaction or diffusion of species between the two layers.

3. CHEMICAL STABILITY

The fact that adherent and conductive oxide layers could be produced from water slurries of the oxide powder was unexpected. The oxide doped with 7.5% strontium, investigated as a superconductor, is known to be moisture sensitive, and it had been observed that earlier prepared pellets of $\text{La}_{1-x}\text{Sr}_x\text{CuO}_4$ had degraded over the course of a few days in air to friable white hydroxides. However, none of the $\text{La}_{1-x}\text{Sr}_x\text{CuO}_4$ powders or electrode films showed any signs of degradation after exposure to air for several months, and their electrical conductivities and XRD patterns remained unchanged.

The apparent increase in stability of the oxide with a larger strontium doping was investigated further by thermogravimetric analysis (TGA). Earlier work by Michel and Raveau (7), for dopant levels up to 12.5% strontium, has shown that oxygen moves very readily into and out of the crystal lattice. In that work, weight loss was observed on heating in air between room temperature and 420K, followed by a weight gain up to 650K. This was mirrored by an order of magnitude fall and rise in electronic conductivity. Repeating these experiments on $\text{La}_{1-x}\text{Sr}_x\text{CuO}_4$ gave very different results. Between 330K and 1170K the oxide showed an approximately constant weight loss totalling to 1.6%. This was halted, but not reversed, on cooling. In an argon atmosphere the weight loss increased only slightly. Repeating the experiment on an identical oxide powder sample in oxygen gave a smaller total weight loss of 0.4%, suggesting that the weight loss in air was largely due to oxygen leaving the crystal lattice.

Further TGA studies, in air, showed that beyond 1270K weight loss increased substantially as the oxide began to volatilise. At 1450K the total weight loss amounted to around 12% with condensed deposits being observed on cooling. Powder samples,

annealed at 1470K for ten hours in air, were partially sintered and conducted electricity well. XRD on the shiny grey oxide showed a substantially changed structure containing a large percentage of La_2O_3 . Incongruent melting occurred between 1470K and 1570K, with gases being evolved.

It has been suggested in other work (14), that with 5–10% Sr-doping, oxide films can react with a zirconia substrate at temperatures as low as 1270K, after only ten minutes, possibly forming Sr_2ZrO_4 and $\text{La}_2\text{Zr}_2\text{O}_7$ (15). XRD showed no evidence of this for the 15% Sr-doped electrodes, following one hour anneals at 1270K and 1320K. However, a highly-conductive fused film, prepared at 1620K for thirty minutes, degraded over several days to powdery white hydroxides.

Collectively, these results suggest that the 15% Sr-doped oxide is considerably more stable than lower doped compositions. It appears that the non-stoichiometric structure of $\text{La}_{1.7}\text{Sr}_{.3}\text{CuO}_4$ will remain substantially stable with respect to hydrolysis, thermal decomposition and large changes in oxygen partial pressure, provided that processing temperatures are limited to 1300K.

4. THERMAL EXPANSION

The coefficient of thermal expansion, α , of $\text{La}_{1.7}\text{Sr}_{.3}\text{CuO}_4$, has been measured as approximately constant above 640K, at $8 \times 10^{-6}\text{K}^{-1}$. From 300K to 640K, expansion is variable averaging $3 \times 10^{-6}\text{K}^{-1}$. This is at the lower end of the range of α for yttria stabilised zirconia, which varies from around $7.5 \times 10^{-6}\text{K}^{-1}$ at room-temperature up to $12 \times 10^{-6}\text{K}^{-1}$ at 1170K.

Oxide films on 3%YSZ plates and 8%YSZ pellets were repeatedly cycled, between room-temperature and 1200K. Subsequent SEM analysis showed no evidence of cracking or loss of adherence of these electrodes.

5. ELECTRONIC CONDUCTIVITY

Very little high-temperature conductivity data for strontium-doped lanthanum cuprate have been reported in the literature. Most of the work done focuses on its superconducting properties and electronic conductivity below room-temperature. For dopant levels between 5%Sr and 20%Sr, room temperature conductivities are in the range 10^2 – $10^3 \cdot 3\text{Scm}^{-1}$, remaining approximately constant up to 600K. Work by Raveau and Smedskjaer (6,7,10) suggests that conductivity should reach a maximum close to 15%.

Four-point dc conductivity measurements were carried out on two rectangular section bars pressed from oxalate-derived oxide powder. The bars were fired for three hours at 1350K in air, giving densities of 89% with very little open porosity. In both cases, electronic conductivity in air decreased from around 280Scm^{-1} at room-temperature, to 60Scm^{-1} at 1170K, as expected for a metallic conductor (Fig.6). A proportion of this decline in conductivity can be attributed to the slight trend to lose oxygen from the structure, as temperature increases.

Similar conductivity measurements will be carried out for electrode films and

dense samples of the oxide at different partial pressures of oxygen, and with different strontium doping levels. It is anticipated that these will confirm that $\text{La}_{1.7}\text{Sr}_{0.3}\text{CuO}_4$ has the highest conductivity and the lowest sensitivity to changes in oxygen partial pressure, when compared to lower Sr-doped oxides.

6. IONIC CONDUCTIVITY

Oxygen self-diffusion measurements by Routbort (8) suggest that the ionic conductivity of 5% strontium-doped lanthanum cuprate is around 10^{-8}Scm^{-1} at 1000K, with an activation energy for ion motion of the order of 100kJmol^{-1} ($\sim 1\text{eV}$). With increasing levels of strontium doping (up to 10%Sr), it was reported that ionic conductivity decreased and activation energy increased. As described above, this is likely to be due to the immobilisation of oxygen ion vacancies (10).

Assuming, therefore, that the oxygen ion conductivity of $\text{La}_{1.7}\text{Sr}_{0.3}\text{CuO}_4$ is considerably lower than that of zirconia, two-point ionic conductivity measurements were carried out in which a polished pellet of the oxide was sandwiched between two YSZ blocking electrodes. The YSZ pellet electrodes were coated with platinum on their outside faces and connected to a constant current source. Measurements of the voltage across the electrode sandwich enabled the ionic conductivity of the material to be calculated from the geometry of the oxide pellet. Conductivity was found to increase exponentially with temperature, in air, from $4 \times 10^{-8}\text{Scm}^{-1}$ at room-temperature, to $1.2 \times 10^{-3}\text{Scm}^{-1}$ at 1070K (Figure 7). Activation energy for the conduction process was calculated as 107kJmol^{-1} (1.1eV).

The conductivity results are considerably higher than those indicated in the literature, and it was considered that electronic short-circuiting through the oxide might be occurring via reduction of gaseous oxygen at the oxide/YSZ interface on the anodic side, and oxidation of oxygen ions on the cathodic side of the electrode arrangement. Calculations of the flux of oxygen molecules impacting upon the interface area indicate that this was possible, and that the experiment might actually have measured a combination of the ionic conductivity of the zirconia pellets and the various contact resistances. This was confirmed by repeating the experiments using two pellets of yttrium barium cuprate of different thicknesses. In each case, the resistance of the pellet (in ohms), as a function of temperature, was calculated to be the same.

Clearly the experimental technique, as described, is inappropriate for electrocatalytic materials. However, the convenience of the method is such that alterations are being made to the electrode arrangement, which should shortly allow valid measurements of ionic conductivity in $\text{La}_{1.7}\text{Sr}_{0.3}\text{CuO}_4$ to be made easily.

7. CONCLUSIONS

A range of relevant theoretical considerations and experimental studies and observations have been discussed in the preceding sections. The paper was introduced with a comprehensive list of criteria required for a SOFC electrode, and all of those that have been considered, support $\text{La}_{1.7}\text{Sr}_{0.3}\text{CuO}_4$ as a potential cathode material.

TGA and XRD measurements indicate that in the high-temperature (up to 1170K)

oxidising environment of a SOFC, the non-stoichiometric defect structure of the oxide will remain substantially stable, over the long-term, with respect to the oxygen partial pressure and reaction with the YSZ electrolyte. Thermal expansion measurements and SEM analysis indicate that electrode integrity is unaffected by thermal cycling of the fuel cell.

Bulk electronic conductivity in air has been measured to be around 10^{-2}Scm^{-1} , of the same order as other cathode materials. It may be possible to enhance this by slight adjustments to the strontium level and by pre-annealing in oxygen.

The method used to measure ionic conductivity in $\text{La}_{1-x}\text{Sr}_x\text{CuO}_4$ appears to be unreliable, but indicates that the oxide may be an effective electrocatalyst. This will be investigated in future work on the catalytic activity of lanthanum strontium cuprate towards oxygen reduction.

Using Routbort's data suggests that an ionic conductivity of 10^{-6}Scm^{-1} would be too low for a dense electrode film, so that the layer would have to be porous. However, the same work also suggests that it may be possible to improve the conductivity substantially, by optimising the level of strontium doping. This will also be investigated.

Much of this paper has been concerned with techniques for the preparation of the oxide material and electrode deposition. The methods have been selected as being generally applicable to other mixed-metal oxide compounds, producing fine oxide powders from homogenous precursors at lower temperatures and in shorter times while avoiding possible contamination introduced through ball-milling. All of the techniques investigated have particular merits that may make them particularly appropriate for other oxide systems. However, for strontium-doped lanthanum cuprate, it is concluded that the bulk oxide powder is best prepared using the oxalate co-precipitation route in ethanol, although the relationship between particle size and solution concentration has not been studied. Electrode films can readily be deposited either from slurries of this oxide powder in ethanol, or by using the mist pyrolysis route. The latter method has the advantage that particle size can be controlled through changes in solution concentration, and electrode film thickness through the time allowed for powder deposition.

In summary, it is concluded that electrodes of 15% strontium-doped $\text{La}_{2-x}\text{Sr}_x\text{CuO}_{4-x/2+\delta}$ can readily be prepared on YSZ substrates, and satisfy all of the physical and chemical requirements for a SOFC. However, further study of its electrical and electrocatalytic properties is required in order to optimise the defect structure.

ACKNOWLEDGEMENTS

Funding for this work, at Imperial College, is being provided by British Gas plc, through a Research Scholarship in solid oxide fuel cells.

REFERENCES

- 1 B.L.Kuzin, A.N.Vlazon, Electrical and electrochemical characteristics of $\text{La}_{1-x}\text{Sr}_x\text{CoO}_3$ in contact with solid oxide electrolyte
Soviet Electrochemistry 20,[12],1510-1515,1984
- 2 Y.Ohno et al., Properties of oxides for high temperature solid electrolyte fuel cell
Solid State Ionics 9 & 10,1001-1008,1983
- 3 I.S.Shaplygin et al., Preparation and properties of the compounds Ln_2CuO_4 (Ln = La,Pr,Nd,Sm,Eu,Gd) and some of their solid solutions
Rus.J.Inorg.Chem. 24,[6],820-824,1979
- 4 J.G.Bednorz, Superconductivity at 40K in the oxygen defect perovskite $\text{La}_{2-x}\text{Sr}_x\text{CuO}_{4-y}$
Science 235,1372,1987
- 5 C.Michel et al., Introduction of bismuth into the high T_c superconductor $\text{La}_{2-x}\text{Sr}_x\text{CuO}_{4-y}$
Zeit.fur Physik.B-Condensed Matter 68,417,1987
- 6 N.Nguyen, B.Raveau et al., Oxygen defect K_2NiF_4 -type oxides: the compounds $\text{La}_{2-x}\text{Sr}_x\text{CuO}_{4-x/2+\delta}$
J.Sol.State Chem. 39,120-127,1981
- 7 C.Michel, B.Raveau, Oxygen intercalation in mixed valence copper oxides related to the perovskites
Revue de Chimie Minerale 21,[4],407,1984
- 8 J.L.Routbort et al., Oxygen diffusion in $\text{La}_{2-x}\text{Sr}_x\text{CuO}_{4-y}$
J.Mater.Res. 3,[1],116-121,1988
- 9 H.Takagi et al., The influence of oxygen deficiency on the electrical resistivity of high- T_c superconducting oxides $(\text{LaBa})_2\text{CuO}_{4-y}$
Jap.J.App.Phys. 26,[3],L218-L219,1987
- 10 L.C.Smedskjaer et al., Oxygen-vacancy behaviour in $\text{La}_{2-x}\text{Sr}_x\text{CuO}_{4-y}$ by positron annihilation and oxygen diffusion
Phys.Rev.B 36,[7],3903,1987
- 11 D.G.Gallacher, Nature and properties of some magnetic mixed oxides
PhD thesis, Dept.Chem.& Metallurgy, Glasgow Col.Tech. Feb.1986
- 12 P.H.Courty, H.Ajor, C.H.Marcilly, Mixed oxide in solid solution formed by thermal decomposition of amorphous precursors
Powder Technology 7,21-38,1973
- 13 G.M.Vest, S.Singaram, Synthesis of metallo-organic compounds for MOD powders and films
Proceedings of MRS Symposium L: defect properties and processing of hi-tec. non-metal materials, Boston, MA, 2-4/12/1985

- 14 H.Koinuma et al., Preparation of $(\text{La}_{1-x}\text{Sr}_x)_2\text{CuO}_{4-\delta}$ superconducting films by the screen printing method
Jap.J.App.Phys. 26,[4],L399-L401,1987
- 15 O.Yamamoto et al., Perovskite-type oxides as oxygen electrodes for high temperature oxide fuel cells
Solid State Ionics 22,241-246,1987

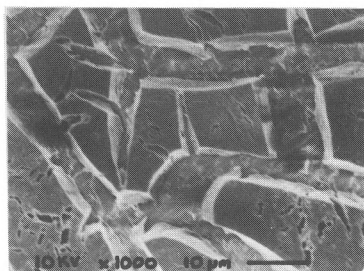


Figure 1
La_{1.7}Sr₃CuO₄ film on YSZ (from citrate-complex solution)

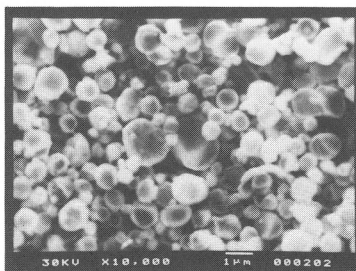


Figure 3
La_{1.7}Sr₃CuO₄ powder particles (mist pyrolysis)

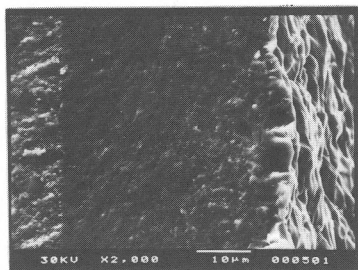


Figure 4
Cross-sectional fracture surface of La_{1.7}Sr₃CuO₄ film on YSZ (mist pyrolysis)

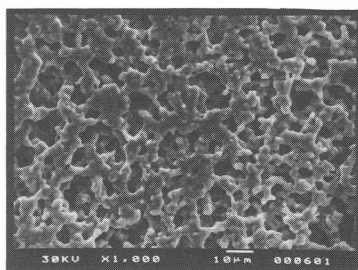


Figure 5
Porous surface structure of La_{1.7}Sr₃CuO₄ film on YSZ (mist pyrolysis)

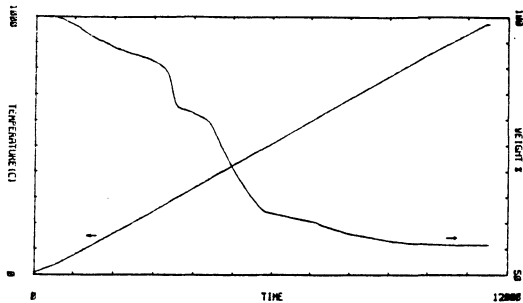


Figure 2
TGA decomposition of
 $\text{La}_{1.7}\text{Sr}_{.3}\text{Cu}$ -oxalate
powder in air

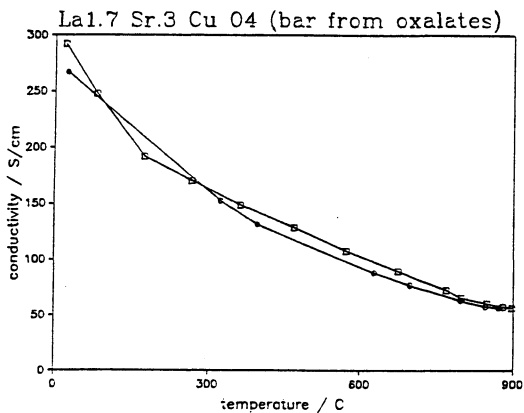


Figure 6
Bulk electronic conductivity
of $\text{La}_{1.7}\text{Sr}_{.3}\text{CuO}_4$, in air,
as a function of
temperature

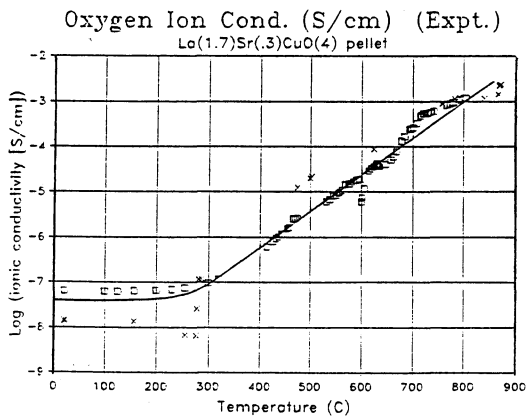


Figure 7
 O^{2-} conductivity of
 $\text{La}_{1.7}\text{Sr}_{.3}\text{CuO}_4$, as
measured using YSZ
electron blocking electrodes

SYNTHESIS OF AIR-SINTERABLE LANTHANUM CHROMITE POWDERS

L. A. Chick, J. L. Bates, L. R. Pederson and H. E. Kissinger
Pacific Northwest Laboratory^(a)
Richland, WA 99352

ABSTRACT

Lanthanum chromites, used as current interconnections in solid oxide fuel cells (SOFCs), have high electrical conductivity and are chemically stable. However, they are difficult to fabricate under conditions compatible with other SOFC components. A novel powder synthesis technique, the glycine/nitrate process, has been developed that produces chromite powders that can be sintered to near-full density in air at 1823 K. This paper describes the glycine/nitrate process for the synthesis and fabrication of lanthanum chromites. The sintering behavior and properties of a series of glycine/nitrate-produced lanthanum chromites are discussed. Some of the materials produced by this method match the thermal expansion of the electrolyte and maintain high electrical conductivity.

1. INTRODUCTION

Lanthanum chromites, as a class, comprise the state-of-the-art materials for use as current interconnects in solid oxide fuel cells (SOFCs) (1). LaCrO_3 has an ABO_3 -type perovskite structure. When alkaline-earth cations (Mg, Ca, Sr, or Ba) are substituted for a fraction of the La on the A lattice site, the electrical conductivity is greatly enhanced because of charge compensation transitions on the B lattice site (Cr^{3+} to Cr^{4+}) which create localized excess positive charges (small polarons) on an equal fraction of the Cr cations. These small polarons conduct by a hopping mechanism (2,3). Substitution of 16% of the La by Sr yields electrical conductivities near 30 mhos/cm at 1273 K, the nominal operating temperature of the SOFCs. The lanthanum chromites also have the required chemical stability in both air and in highly reducing atmospheres at SOFC operating temperatures.

However, thermal expansion coefficients for the Sr-substituted lanthanum chromites are reported to be almost 10% below that of the fully-stabilized ZrO_2 -(8.4M%) Y_2O_3 electrolyte (4). Also, the lanthanum chromites are difficult to sinter at temperatures required for SOFC

(a) Pacific Northwest Laboratory is operated by Battelle Memorial Institute for the U.S. Department of Energy under Contract DE-AC06-76RLO 1830.

fabrication to near-full density ceramics that are free of open porosity. Open porosity in the interconnect creates a direct diffusion path between the fuel and oxidant. Such oxygen diffusion lowers the efficiency of the cell.

Generally, the chromites sinter best at high temperatures (near 1900 K) in highly reducing atmospheres ($P[O_2]=10^{-10}$ to 10^{-12} atm.) (5). However, these conditions are not suitable for sintering the SOFCs as a unit because the lanthanum manganite air electrode material is unstable in reducing atmospheres. Sintering the lanthanum chromites in air, even at temperatures above 1900 K, results in low densities and substantial open porosity. These two SOFC materials appear incompatible from a fabrication standpoint if the entire fuel cell is to be sintered simultaneously as a unit.

The high sintering temperatures and low densities can be circumvented by using sintering additives in the chromites that lower the sintering temperature in air and increase densification rates. While the additives improve the final air-sintered density of the chromites, additive cations may diffuse from the chromite material into other SOFC components, causing degrading chemical interactions. The chromites may also be fabricated by completely different processes such as electrochemical vapor deposition (EVD), now used in state-of-the-art tubular SOFCs (6). The EVD process is complex, slow, expensive, and places limits on the chromite compositions that can be fabricated. EVD presently uses Mg (rather than Ca or Sr) as the alkaline-earth substitute for La. The Mg cation generally substitutes on the B sites for Cr as well as for the La on the A sites, and results in lower electrical conductivities (7).

A critical goal for the advancement of SOFC technology, therefore, is the development of Ca- or Sr-substituted lanthanum chromite powders that can be sintered in air to closed porosity without additives at temperatures less than 1823 K. In addition, these chromites must have thermal expansions close to those of the electrolyte and the electrodes.

Ideally, to achieve good sinterability, a ceramic powder should consist of dense, spherical or equiaxed particles with a narrow size distribution in the submicron range. Such powders can be formed into homogeneous green (unsintered) bodies with high green density, small pores, and a narrow pore-size distribution. It is especially important to avoid pores larger than the primary particle size. Such well-packed green bodies sinter to high density with closed porosity at minimum temperatures. In order to achieve these conditions, the particles should be discrete, rather than attached together in agglomerated clusters. Agglomerated particles pack to low green density and leave numerous large pores after sintering. These well-known ceramic processing principles are particularly germane to the chromites, which tend to be relatively non-reactive during sintering.

The current state-of-the-art powder synthesis technique for lanthanum chromites is the "Pechini" process (8). In this process, the appropriate proportions of the metal salts are dissolved in a water-ethylene glycol-citric acid solution. The mixture is evaporated and polymerized thermally to form viscous resins and eventually glassy polymers. The glassy resins are then calcined to oxidize and/or volatilize the organic components, leaving lanthanum chromites in the form of agglomerations of submicron particles. Because the particles are extensively clustered into hard agglomerates, vigorous crushing and grinding steps are required to reduce the agglomerate size prior to green-body consolidation and sintering. Settling may also be required to remove any remaining large agglomerates.

A novel powder synthesis technique, called the "glycine/nitrate" process,^(a) has been developed. This process can be used to synthesize a wide range of oxide ceramic powder compositions, including lanthanum chromites. Glycine/nitrate processing is fast and simple, and utilizes inexpensive, high-purity materials. Chromite powders synthesized by the glycine/nitrate process have demonstrated superior air-sinterability at low temperatures. This paper describes the glycine/nitrate process for the synthesis and fabrication of lanthanum chromites, and the sintering behavior and properties of a series of glycine/nitrate-produced lanthanum chromites.

2. GLYCINE/NITRATE SYNTHESIS AND PROCESSING OF LANTHANUM CHROMITES

The glycine/nitrate powder synthesis technique consists of two basic steps. First, metal nitrates and glycine or some other low molecular weight amino acid are dissolved in water. Second, the solution is boiled down until it thickens and ignites, producing ash that contains the oxide product. Subsequent processing for the production of laboratory samples includes calcination, sonication, and dry-pressing.

The glycine serves two purposes: first, it complexes the metal cations, increasing their solubility and preventing selective precipitation as the water evaporates; and secondly, it serves as fuel for combustion, being oxidized by the nitrate anions and by oxygen from the air. The glycine molecule has a carboxylic acid group at one end and an amine group at the other end. Alkali, alkaline-earth and possibly La cations are largely complexed by the carboxylic acid end of the molecule, as shown in Figure 1a. Transition metal cations are

(a) L. R. Pederson, L. A. Chick and G. J. Exharos, patents pending.

complexed by the amine group. As shown in Figure 1b, water molecules in the cation's coordination sphere are replaced by the amine-ends of the glycine molecules. Infrared spectroscopy has shown that the number of glycines which join the transition metal's coordination sphere is dependent upon the ratio of glycine to cations in the solution. Complexation prevents the metal salts from precipitating at water concentrations as low as a few weight percent. For the substituted lanthanum chromites, the solution can be boiled down until its viscosity increases to a honey-like consistency with no evidence of selective precipitation. The concentrated solution has an amorphous structure with the cations intimately mixed on a molecular scale.

As the last water is evaporated, the lanthanum chromite solution begins to swell, forming a viscous foam. The foam ignites spontaneously at a few hundred degrees Celsius. The generalized burn reaction is shown in Figure 2. The best results are usually obtained when the glycine-to-cation molar ratio is adjusted to yield the fastest burn. For the lanthanum chromites, this is a 2:1 glycine/cation mixture. Waste gas analysis by mass spectrometry showed the presence of CO, CO₂, NO, NO₂, and NO_x. Assuming that the CO/CO₂ and NO_x mixtures are dominated by CO and NO₂, calculations indicate that substantial atmospheric oxygen appears necessary to supplement the nitrates in their oxidizing role.

In laboratory-scale production, final evaporation of water and burning are accomplished using small batches of solution (appx. 15 mls) in 1000 ml beakers on a hot plate in a hood. A 40-mesh screen, fitted to the top of the beaker, serves to retain most of the ash. For especially active reactions which produce very fine ash, the ash is collected through a metal funnel that is placed over the beaker and connected to a vacuum cleaner.

At a 2:1 glycine/cation molar ratio, the lanthanum chromites produce ash consisting of irregularly shaped, generally oblong particles a few mm long and less than one mm wide. These ash particles have a foam-like morphology with very low bulk density, typically less than 0.02 g/cc. A scanning electron micrograph (SEM) of the ash is shown in Figure 3. In Figure 4, transmission electron microscopy (TEM) reveals that the ash is composed of very fine (25 to 100 nm diameter) lanthanum chromite particles linked together in chains. TEM brightfield and darkfield images indicate that the particles are individual crystals, joined at grain boundaries with no indication of an intervening amorphous phase.

These extremely fine, highly crystalline, equiaxed particles would comprise an ideal powder for sintering if they were not connected in chains. Like the Pechini process, the glycine/nitrate method results in agglomerates, not discrete particles. However, unlike the hard agglomerates produced by the Pechini technique, these are relatively "soft"; that is, they can be broken down into much smaller (generally submicron) agglomerates and discrete particles with minimal effort.

Calcination followed by sonication produces highly sinterable powders from the raw ash. Calcination in air for 5 h at 923 K results in growth of the primary particles to about 0.1 μm ; roughly eight or ten particles have sintered together to form each calcined particle. The agglomerates in the calcined powder are more easily broken down by sonication to submicron size than are those in the raw ash. The calcined material is suspended in hexanes using oxidized menhaden fish oil as a dispersant. The suspension is then pumped from a stirred flask through a high-intensity sonication device. The outlet from the sonicator feeds back into the stirred flask so that the suspension can be continuously sonicated for several hours. The resulting powder is compared to a powder of similar composition made by the Pechini process in Figure 5. The primary particles as well as the agglomerates are smaller and more uniform in size for the glycine/nitrate processed powder. The calcined and sonicated glycine/nitrate powders typically have BET surface areas near 20m²/g. If the particles were discrete, monodisperse spheres (which they are not, as seen in Figure 5), this specific surface area would correspond to a particle diameter of 45 nm.

Currently, powders are cold pressed and sintered to make laboratory samples for properties characterization. However, powders could be consolidated using colloidal techniques such as slip casting, tape casting, or calendaring.

All pressed samples were sintered at 1823 K in a resistance-heated furnace for 16 h in air. Samples were placed on crushed lanthanum chromite granules, supported by alumina plates. The heating and cooling rates were 100 and 300 K/h, respectively.

3. SINTERING CHARACTERISTICS OF GLYCINE/NITRATE-PRODUCED LANTHANUM CHROMITES

This paper discusses some of the recent studies of glycine/nitrate-produced lanthanum chromite sintering behavior. Sintering of the lanthanum chromites appears to be a complex process, apparently influenced by small amounts of secondary phases, by changes in composition caused by intentional adjustments to the batch solution and/or by selective volatility during sintering.

Recently, samples were prepared by the glycine/nitrate process in a series of compositions given by $\text{La}_{0.82}\text{Sr}_{0.15}\text{Cr}_{1-x}\text{Al}_x\text{O}_3$, where $x=0, 0.06, 0.10, 0.15, 0.20,$ and 0.29 . Aluminum was substituted for Cr on the B site to increase the thermal expansion coefficient while maintaining high electrical conductivity (9). Compositions were determined after sintering by sodium peroxide fusion followed by dissolution in nitric acid and analysis by inductively-coupled plasma atomic emission spectroscopy (ICP). Oxygen was not analyzed; the three oxygens per formula are an assumed concentration.

The sintering behavior of the no-Al ($x=0$) sample is compared to that of another sample, prepared by the same technique, that contains slightly more Sr and less La. This sample, hereafter referred to as Sr-rich, had the composition, $\text{La}_{.81}\text{Sr}_{.16}\text{CrO}_3$. The previously mentioned sample with no Al, $\text{La}_{.82}\text{Sr}_{.15}\text{CrO}_3$, is referred to as Sr-poor. These samples were analyzed on the same day, consecutively, decreasing the probability that the small difference in relative composition is accounted for by analysis error.

X-ray diffraction (XRD) patterns for the Sr-poor sample are shown in Figure 6. The patterns for the raw ash, before calcination, and for the sintered sample are shown in 6a and 6b, respectively. The reference pattern for $\text{La}_{.75}\text{Sr}_{.25}\text{CrO}_3$ is shown in 6c (10). Pure lanthanum chromite undergoes a symmetry change from orthorhombic at low temperatures to rhombohedral (hexagonal) above 560 K (11,12). The substitution of 16% of the La by Sr lowers the transition temperature to 190 K (3). Substitution of Al for Cr also lowers the transition temperature (13). Therefore, all of the materials in the present study exhibit the rhombohedral symmetry above ambient temperatures. The peaks are broadened for the ash because of the small particle size. Comparison of the sintered sample pattern to the reference pattern shows that positions are slightly shifted and the intensities of the doublets are sometimes reversed. These minor discrepancies are probably due to the difference in composition between the sintered sample and that used for generation of the file pattern. There is no evidence of minor secondary phases in either sample pattern. Patterns for the strontium-rich sample (ash and sintered) are essentially identical to those in Figure 6.

Although the Sr-rich sample contains only slightly more Sr than the Sr-poor sample, and although their ash- and sintered-XRD patterns are identical, significant differences were observed in the XRD patterns of the calcines (Figure 7) and in their sintering behavior. Several minor peaks in the Sr-rich calcine indicate the presence of between 3 and 5 mole% SrCrO_4 . The Sr-poor calcine contains a much lower level of strontium chromate, perhaps 1/2 to 1 mole%, as well as a third phase, believed to be La_2CrO_6 at a concentration of about 1 to 2 mole%. Concentration estimates are based on relative peak intensities and can be considered semi-quantitative at best.

Figure 8 shows optical micrographs of the sintered Sr-rich and Sr-poor chromite samples. It is apparent that the Sr-rich sample contains significantly less porosity than the Sr-poor sample. Immersion density measurements yield 6.3 g/cc for the Sr-rich sample and 5.3 g/cc for the Sr-poor sample. Theoretical density for these compositions containing no Al is 6.59 g/cc.

The sintered samples containing Al all yield XRD patterns similar to Figure 6b, with slight shifts in peak position indicating shrinkage of the unit cell as Al concentration is increased (see Figure 9).

Although the unit cell shrinks as Al is added, the lower atomic weight of Al compared to Cr results in a decreasing theoretical density from 6.59 g/cc for $x=0$ to 6.51 g/cc for $x=0.3$.

Figure 10 is a plot of open porosity and percent of theoretical density attained during sintering versus degree of Al substitution. The data were determined on the sintered samples by immersion tests in cyclohexanone. The effect of Al in decreasing open porosity and increasing overall sintered density is dramatic. At $x=0.1$, open porosity is essentially zero. Addition of Al above $x=0.2$ appears to degrade sintered density and causes the return of open porosity.

The porosity in these samples is not uniformly distributed. Optical micrographs, taken near the surfaces of the samples with $x=0$ and $x=0.15$, are shown in Figure 11. The surface visible in Figure 11a was the lower surface of the $x=0$ pellet that rested on the lanthanum chromite grains during sintering. This sample warped during sintering such that the lower surface, that was in contact with the lanthanum chromite grains, is concave and porous. The upper surface of the $x=0$ sample appears identical to the interior (left edge of Figure 11a). The $x=0.15$ sample did not warp during sintering. All of its surfaces are identical to that near the right edge of Figure 11b. It is apparent that, with no aluminum present, the porosity of the sintered material increases markedly near the surface. In contrast, the substitution of 15% of the chromium by aluminum ($x=0.15$) results in a dense near-surface region containing fewer, larger pores, and showing evidence of substantial grain-growth. This dense band is over 100 μm thick and is present on all sides of the sample. The density of the surface region is obviously higher than that of the bulk; probably approaching about 97% of theoretical. It is apparent from the micrograph that the material within about 10 μm of the surface of the $x=0.15$ sample is nearly free of pores.

4. DISCUSSION

The enhancement of sintering in the Sr-rich, aluminum-free chromite, demonstrated in Figure 8, can be attributed to the greater concentration of SrCrO_4 that is present prior to sintering (Figure 7a). The phase diagram presented by Negas and Roth (14) shows SrCrO_4 in air melts incongruently at 1524 K to form Cr_2O_3 , liquid, and oxygen. The liquid may distribute at the grain boundaries, promoting liquid-phase sintering. Meadowcroft (15) demonstrated that the sintered density of $\text{La}_{0.84}\text{Sr}_{0.16}\text{CrO}_3$ increased when excess strontium was added in the form of SrCO_3 before pressing and sintering. The maximum beneficial effect occurred when between 4 and 6 mole% SrCO_3 was added. Very little increase in sintered density was observed until more than 1 mole% SrCO_3 was added. It seems possible that the enhanced sintering observed by Meadowcroft may have been due to the formation of SrCrO_4 at intermediate temperatures followed by melting and liquid-phase sintering. Berjoan (16) reports that La_2CrO_6 decomposes at 1513 K, presumably to

LaCrO_3 , La_2O_3 , and oxygen. The high-temperature crystalline and liquid products of the minor phases present in both calcines may become partially incorporated into the major Sr-substituted lanthanum chromite phase during sintering, explaining the absence of minor phases in the XRD patterns of the sintered samples (Figure 6b).

The enhancement of sintering in the sample surfaces of the materials containing Al (Figure 11) is difficult to explain based on current information. Anderson et al. (13) have reported that substitution of Al for Cr in Mg-substituted lanthanum chromites reduces the volatility of chromium at 2013 K as determined by weight-loss measurements. The composition of the volatile components was not reported. We have performed X-ray energy dispersive spectroscopy (EDS), using an SEM, on polished cross-sections of the recent $x=0$ and $x=0.15$ samples. Compositions were measured at various distances from the surfaces shown in Figure 11. The outer 100 μm of the porous surface in the $x=0$ sample (Figure 11a) appears to be depleted in Cr and enriched in Sr, relative to the bulk. The outer 10 μm of the dense surface in the $x=0.15$ sample (Figure 11b) appears to be enriched in strontium with no significant change in Cr, La, or Al relative to the bulk. It might be concluded that Al retards the volatility of lanthanum chromite from the surface during sintering, preventing the enlargement of pores and promoting sintering.

However, this does not explain why the surfaces of the samples containing Al are more dense than the interiors. Furthermore, it is not known why the lower surface of the $x=0$ sample was extremely porous relative to the upper surface. Recall that the lower surface rested on lanthanum chromite grains supported by an alumina disk while the upper surface was directly exposed to the air. Because this sample became warped, concave upward, during sintering, it is evident that enhanced sintering (shrinkage) of the upper surface caused the warpage. Therefore, the porosity in the lower surface is mainly due to retarded sintering rather than to mass-loss from volatility, even though it is evident that volatility does occur.

Previous experience with sintering of similar Al-free samples, which had been placed directly on alumina disks with no intervening lanthanum chromite grains, indicates that direct contact with alumina retards sintering, results in very porous lower surfaces (Figure 11a), and in upward concavity. Any alumina surfaces that are located within a few centimeters of chromite samples during sintering turn pink, indicating the presence of Cr. It is possible that intervening lanthanum chromite grains do not provide enough separation from the alumina surfaces to prevent enhanced volatility.

In other previous experiments, glycine/nitrate-produced lanthanum chromite calcines that were ball milled, using an aluminum oxide mill and media, exhibited low sintered densities. Although not confirmed, this could have been due to contamination of the green body by minute aluminum oxide particles from the milling media.

In summary, incorporation of Al into the lanthanum chromite structure during synthesis results in markedly enhanced sintering near all of the sample surfaces, while proximity of Al-free samples to aluminum oxide surfaces retards sintering near the surface. Aluminum oxide particulate inclusion may also retard chromite sintering. The processes underlying these phenomena are, as yet, unexplained, but probably involve the retardation of volatility by incorporated Al and the enhancement of volatility by proximity to aluminum oxide. These processes may be further complicated by the effects of incorporated Al on minor crystalline or liquid phases at the grain boundaries or on the oxidation state of the lanthanum chromite near the surface.

In any case, the sintering behavior of the samples with Al substituted for 10 to 20% of the Cr is promising. SOFC interconnects need only be several tens of microns thick for state-of-the-art tubular designs (6), well under the thickness of the dense, near-surface regions in the air-sintered laboratory samples. It is reasonable to expect that films of the necessary thickness would sinter to the point of closed porosity throughout. In addition, Al substitution decreases the electrical conductivity only moderately, but increases the thermal expansion. The direct-current conductivity of the $x=0.15$ sample is only 16% lower at 1273 K than that of the $x=0$ sample. The thermal expansion coefficient for Al substitution of $x=0.15$ between 373 and 1323 K is $10.64 \times 10^{-6}/K$. This value is only 1% lower than that for yttria-stabilized zirconia, measured on the same device.

5. CONCLUSIONS

- 1) The glycine/nitrate powder synthesis method provides a simple, fast technique for producing a wide range of oxide ceramic powder compositions. The technique uses inexpensive, and high-purity chemicals.
- 2) The glycine/nitrate method produces lanthanum chromite powders that contain smaller primary particles and smaller, softer agglomerates than powders produced by the current state-of-the-art technique.
- 3) Several substituted lanthanum chromite powders have been produced by the glycine/nitrate method that are highly reactive, sintering to near-full density, with closed porosity, at 1823 K in air.
- 4) When the composition of the glycine/nitrate-produced, Sr-substituted lanthanum chromite powders is adjusted such that the calcined powder contains 3 to 5 mole% $SrCrO_4$, densification in air at 1823 K is enhanced. This enhancement of sintering is probably due to the presence of a liquid phase at the sintering temperature.

5) Incorporation of Al into the Sr-substituted lanthanum chromite structure, as a substitute for a fraction of the chromium, results in enhanced sintering and closed porosity near the surface. The reason for this effect is unknown, but it may be related to inhibition of volatility.

6) The glycine/nitrate-produced material with composition $\text{La}_{.82}\text{Sr}_{.15}\text{Cr}_{.85}\text{Al}_{.15}\text{O}_3$ shows promise for use as the SOFC interconnect material. Layers up to about 100 μm thick sinter in air to near-full density with closed porosity after 16 h at 1823 K. This material has a high electrical conductivity and a thermal expansion that very closely matches that of yttria-stabilized zirconia.

6. ACKNOWLEDGMENTS

The authors gratefully acknowledge the U.S. Department of Energy for sponsorship of this work. We also wish to thank J. E. Gardner, K. H. Bliss, J. E. Coleman, R. W. Stephens, and N. T. Saenz for technical assistance and D. K. Hilliard for editorial assistance.

REFERENCES

1. K. Kinoshita, F. R. McLarnon and E. J. Cairns, "Fuel Cells Handbook", DOE/METC-88/6096, U.S. Department of Energy, Morgantown Energy Technology Center, Morgantown, WV (1988)
2. J. B. Webb, M. Sayer, and A. Mansingh, "Polaronic Conduction in Lanthanum Strontium Chromite", Can. J. Phys., Vol. 55 (1977) p. 1725.
3. D. P. Karim and A. T. Aldred, "Localized Level Hopping Transport in $\text{La}(\text{Sr})\text{CrO}_3$ ", Phys. Rev. B, Vol. 20 (1979) p. 2255.
4. J. Jacobs, K. M. Castelliz, W. Manuel and H. W. King, "The Electrical Conductivity and Thermal Expansion of Potential MHD Electrodes Based on Mixed Perovskites of Lanthanum Strontium Chromite and Strontium Zirconate", in Conference on High-Temperature Sciences Related to Open-Cycle, Coal-Fired MDH Systems, ANL-77-21, Argonne National Laboratory, Argonne, IL (1977) p. 148.
5. J. W. Halloran and H. U. Anderson, "Influence of O_2 Partial Pressure on Initial Sintering of Alpha Cr_2O_3 ", J. Amer. Cer. Soc., Vol. 57 (1974) p. 150.
6. S. C. Singhal, R. J. Ruka and S. Sinharoy, "Interconnection Materials Development for Solid Oxide Fuel Cells," DOE/MC/21184-1, Westinghouse R&D Center, Pittsburgh, PA (1985).

7. B. K. Flandermeyer, M. M. Nasrallah, D. H. Sparlin, and H. U. Anderson, "Thermogravimetric and Electrical Conductivity Studies of Mg-Doped LaCrO_3 and Ln-Doped SrTiO_3 ," in Transport in Nonstoichiometric Compounds, (G. Simkovich and V. S. Stubican, eds.), Plenum Press, NY (1984) p. 17.
8. M. P. Pechini, "Method of Preparing Lead and Alkaline Earth Titanates and Niobates and Coating Method Using the Same to Form a Capacitor", U. S. Patent 3330697 (1967).
9. H. U. Anderson, "Fabrication and Property Control of LaCrO_3 -Based Oxides," in Processing of Crystalline Ceramics, (H. Palmour, R. F. Davis, and T. M. Hare, eds.), Plenum Press, New York (1978) p. 469.
10. JCPDS card file no. 32-1240, International Center for Diffraction Data, Swarthmore, PA.
11. E. M. Levin and H. F. McMurdie, Phase Diagrams for Ceramists, 1975 Supplement, (M. K. Reser, ed.), American Ceramic Society, Columbus, Ohio (1975) Figs. 4397 and 4402.
12. J. S. Ruiz, A. M. Anthony, and M. Foex, "On the Semiconducting Properties of Lanthanum Chromite", C. R. Hebd. Seances Acad. Sci., Ser. B, Vol 264 (1967) p. 1271.
13. H. U. Anderson, R. Murphy, A. K. Fox, B. Rossing, and A. Aldred, "Compositional Dependence of Thermal Expansion, Lattice parameters, Volatilization Rate and Electrical Conductivity of LaCrO_3 Based on Oxides", in Proceedings of Workshop on High-Temperature Solid Oxide Fuel Cells BNL-50756 (H. S. Isaacs, S. Srinivasan, and I. L. Harry eds.), Brookhaven National Laboratory, Upton, NY (1977) p. 41.
14. T. Negas and R. S. Roth, J. Res. Nat Bur. Stand. Sect. A, Vol. 3, (1969) p. 433.
15. D. B. Meadowcroft, "Some Properties of Strontium-doped Lanthanum Chromite", Brit. J. Appl. Phys., Vol. 2 (1969) p. 1225.
16. R. Berjoan, Rev. Int. Hautes Temp. Refract, Vol. 13 (1976) p. 119.

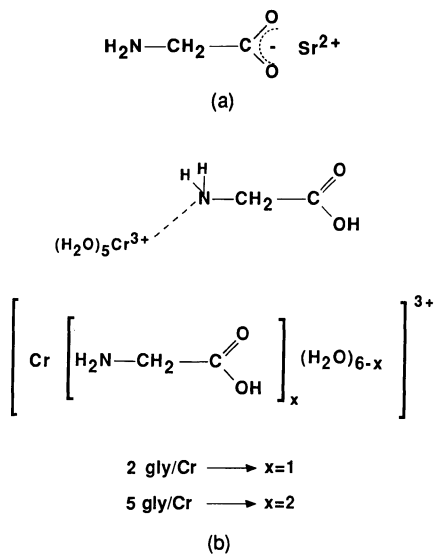


FIGURE 1. Complexation of metal cations by glycine in aqueous solution: (a) complexation of alkali or alkaline-earth cations by the carboxylic acid; (b) complexation of transition-metal or rare-earth cations by the amine.

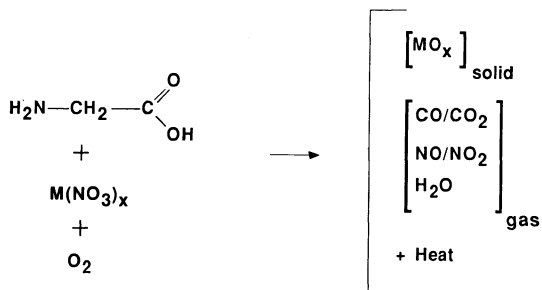


FIGURE 2. Generalized glycine/nitrate burn reaction.

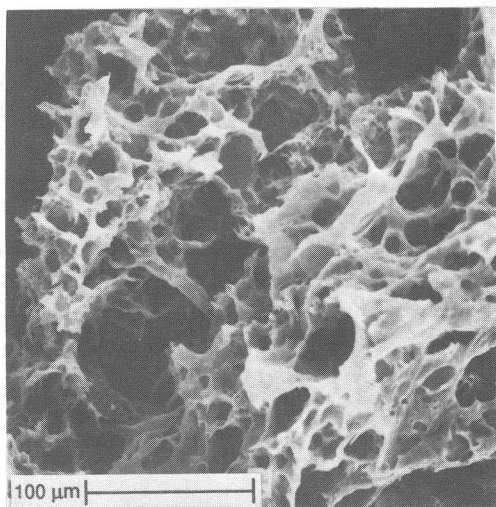


FIGURE 3. Scanning electron micrograph of glycine/nitrate-produced lanthanum chromite ash.

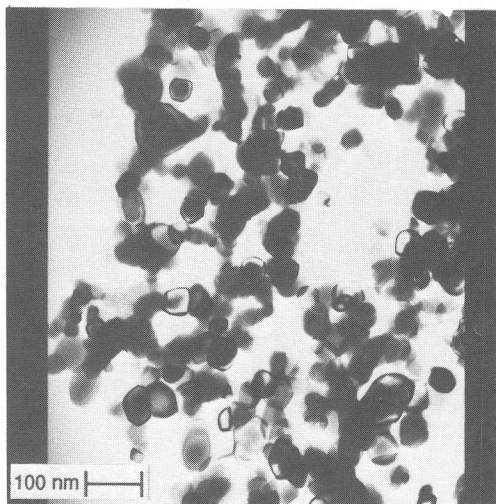
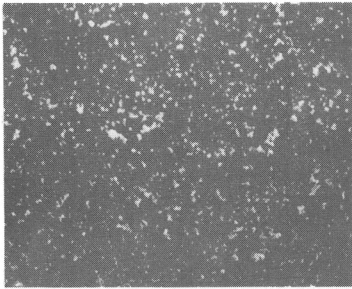
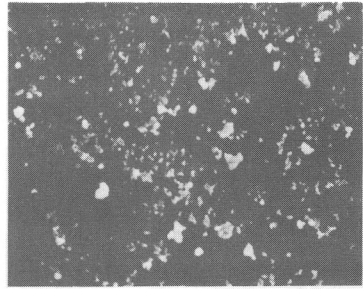


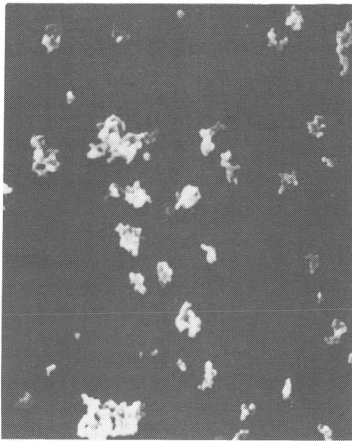
FIGURE 4. Transmission electron micrograph of glycine/nitrate-produced lanthanum chromite ash.



10 μm \longleftrightarrow

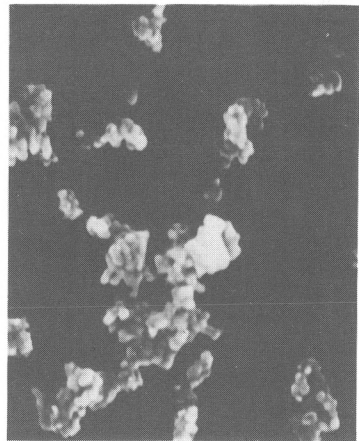


10 μm \longleftrightarrow



1 μm \longleftrightarrow

(a)



1 μm \longleftrightarrow

(b)

FIGURE 5. Chromite powders. (a) Glycine/nitrate-produced $\text{La}(\text{Sr})\text{CrO}_3$. (b) $\text{Y}(\text{Sr})\text{CrO}_3$ produced by Pechini process.

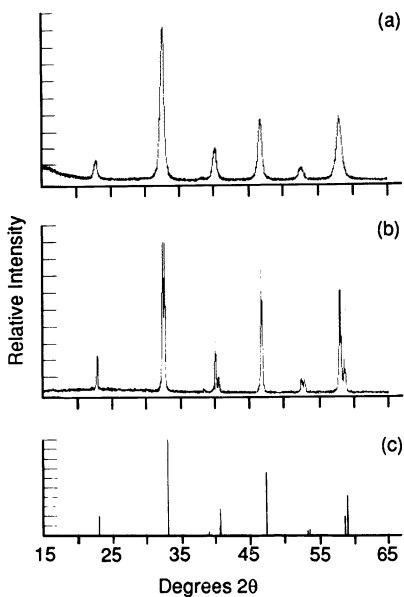


FIGURE 6. XRD patterns for $\text{La}_{0.82}\text{Sr}_{0.15}\text{CrO}_3$: (a) ash, as synthesized by glycine/nitrate process, (b) sintered sample, (c) JCPDS file # 32-1240 (9) for $\text{La}_{0.75}\text{Sr}_{0.25}\text{CrO}_3$.

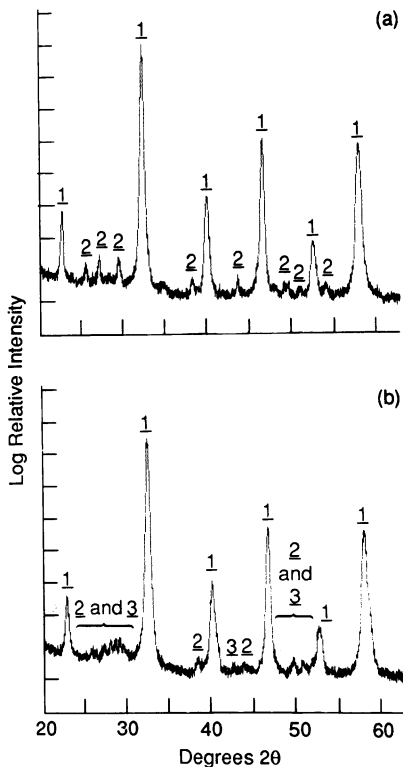
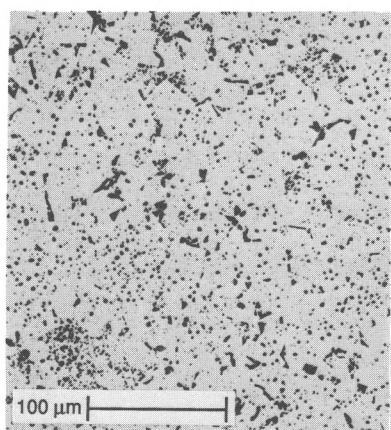
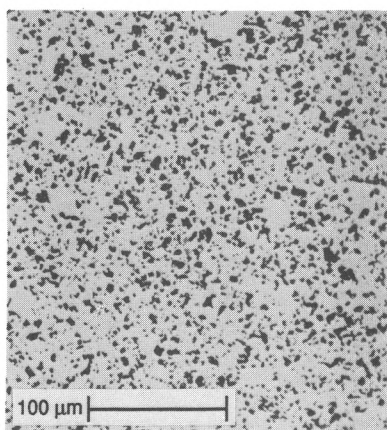


FIGURE 7. XRD of calcined ash. Phase 1 is $\text{La}(\text{Sr})\text{CrO}_3$. Phase 2 is SrCrO_4 . Phase 3 is La_2CrO_6 : (a) Strontium-rich sample, $\text{La}_{0.81}\text{Sr}_{0.16}\text{CrO}_3$, (b) Strontium-poor sample, $\text{La}_{0.82}\text{Sr}_{0.15}\text{CrO}_3$.



(a)



(b)

FIGURE 8. Optical micrographs of polished sections of air-sintered, strontium-substituted lanthanum chromites: (a) from calcine containing appx. 3 to 5 mole% SrCrO_4 , (b) from calcine containing appx. 1 to 1/2 mole % SrCrO_4 .

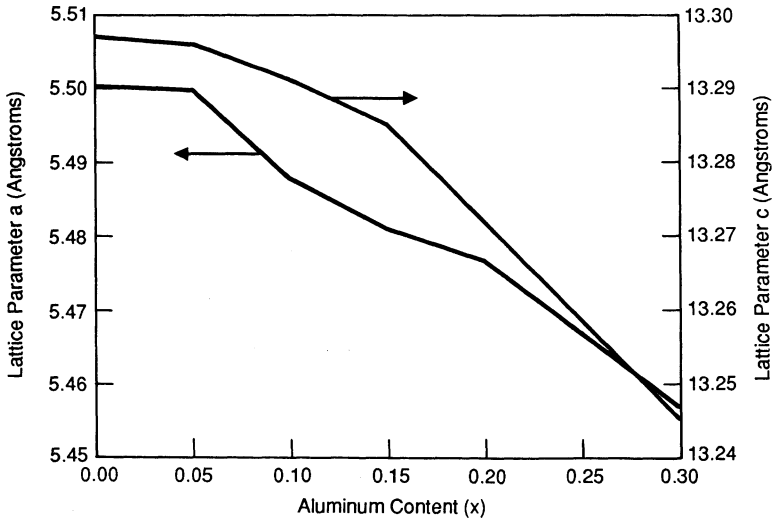


FIGURE 9. Variation of lattice parameters measured by X-ray diffraction for the series, $\text{La}_{.82}\text{Sr}_{.15}\text{Cr}_{1-x}\text{Al}_x\text{O}_3$. ($\text{Cu K}\alpha$, $\lambda = 1.54059$.) Rhombohedral cell referred to hexagonal axes.

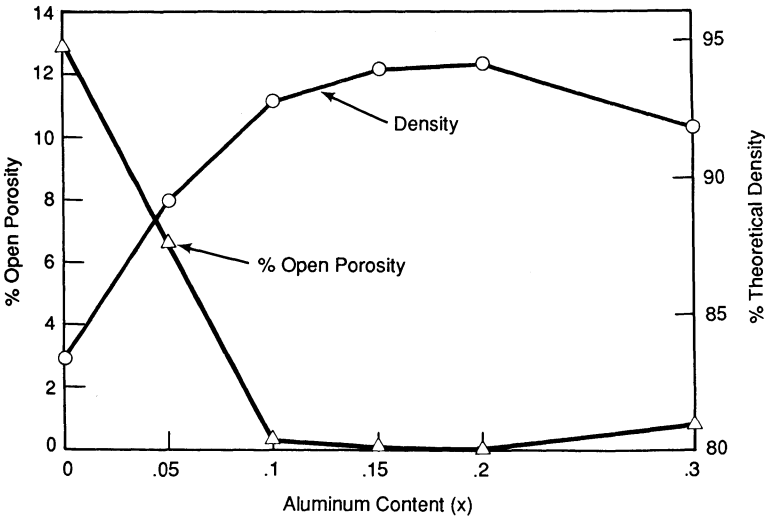
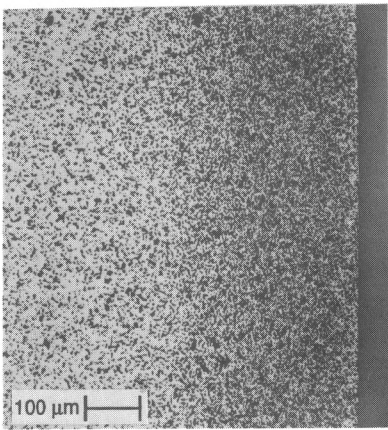
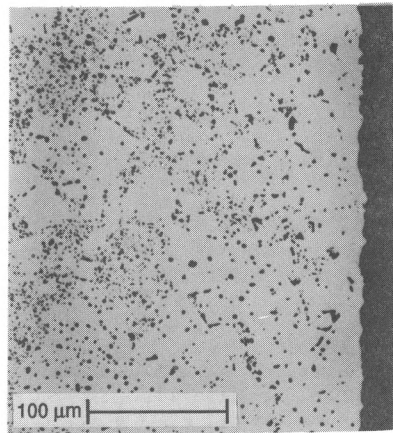


FIGURE 10. Percent open porosity and percent of theoretical density of air-sintered samples versus aluminum content. Analyzed compositions are $\text{La}_{.82}\text{Sr}_{.15}\text{Cr}_{1-x}\text{Al}_x\text{O}_3$.



(a)



(b)

FIGURE 11. Optical micrographs near edges of air-sintered samples. (a) $\text{La}_{.82}\text{Sr}_{.15}\text{CrO}_3$. (b) $\text{La}_{.82}\text{Sr}_{.15}\text{Cr}_{.85}\text{Al}_{.15}\text{O}_3$.

PREPARATION OF LaMnO_3 THIN FILM ELECTRODE FOR SOLID
OXIDE FUEL CELLS BY VACUUM EVAPORATION

H. Michibata, H. Tenmei, T. Namikawa and Y. Yamazaki
Tokyo Institute of Technology at Nagatsuta, 4259
Nagatsuta Midori-ku, Yokohama, Japan

ABSTRACT

The preparation process of a thin film zirconia fuel cell by means of vacuum evaporation technique has been studied. The thin film cell is composed of a partially stabilized zirconia (PSZ) thin film, porous nickel anode and thin film oxide cathode. LaMnO_3 and LaCoO_3 were selected as the cathode material. The cathode layer was prepared on a PSZ electrolyte film by evaporating a sintered mixed oxide of La_2O_3 and MnO_2 or CoO , and by annealing the film in air at 800°C for 1h.² The electrolyte film was synthesized by oxidizing a multi-layered film of Zr and Y which had been prepared by electron beam evaporation. The electrolyte film was formed on a Ni foil substrate. A release of thermal stresses in the electrolyte film was experienced when the substrate was changed from a Ni plate to a Ni foil which was supported with a frame made of Kovar. The open circuit voltage of a cell prepared on a Ni plate was 0.8V at 700°C . The maximum current and the maximum power output were 0.7mA and 0.14mW, respectively. The results of the test with the nickel foil cells are also presented.

1. INTRODUCTION

It is expected that compact and highly efficient electric generators can be built by using solid oxide fuel cells(1). For this purpose, it is important to increase the conversion efficiency and performance of the cell at high temperatures. In practice, reducing electric resistances of electrolyte, electrode and interconnector is the primary target in the development of the cell. We have proposed thin film cell structures (2-4) which have planar metal substrate or support. The electrolyte and electrodes were prepared on the substrate using vacuum evaporation techniques(5,6). The planar structure is suitable for lowering the electric resistances, and the metal support is preferable to ceramic supports in assembling a cell stack. In this paper, we first report on the preparation process of a thin film cathode and then describe the fabrication process of the electrolyte layer on nickel foil substrate placed on a metal frame.

2. ELECTRODE PREPARATION

A large number of materials have been tested for the cathode of YSZ cells and it was found that several oxides having perovskite structure fairly satisfied the requirements of the cathode. In particular, LaMnO_3 and LaCoO_3 are expected to support the further development of SOFC. The thin films of the oxides were prepared as follows. La_2O_3 and MnO_2 (99.9% pure), or CoO for LaCoO_3 , powders were mechanically mixed; then calcined at 1100°C for 12h. The product was crushed and pressed in the form of a pellet with a pressure of 5000kgcm^{-2} . The evaporation source was prepared by sintering the pellet at 1100°C for 12h. The molar ratio of La to Mn(or Co) of the evaporation source was adjusted to 2.0 because of the reduction in La content during the evaporation. The evaporation condition is shown in Table I. The films were deposited on PSZ electrolyte films. Because the as-deposited films were amorphous, they were annealed in air at 800°C for 1h. The phases of the annealed films were examined by X-ray diffraction analysis. The thickness and the diameter of the prepared cathode of the test cell were $0.4\mu\text{m}$ and 3mm, respectively.

In general, the composition of vacuum evaporated films deviates from that of the source material because of the difference in vapor pressures of the elements or compounds. Therefore the prepared oxide films were examined using EDX analysis and X-ray diffraction analysis. The X-ray diffraction patterns of the films are shown in Figure 1. When the evaporation was carried out with a source having a composition of $\text{La}/\text{Mn}=1.0$, the film contained an excess of MnO_2 phase with a small amount of LaMnO_3 phase. When the film was deposited with the source composition of $\text{La}/\text{Mn}=4.0$, the most part of the film was La_2O_3 and the rest was LaMnO_3 . These data led to the result that homogeneous LaMnO_3 films are formed with the evaporation source having the composition ratio near $\text{La}/\text{Mn}=2.0$.

The preparation process of LaCoO_3 cathode was similar to that of LaMnO_3 . When the evaporation was conducted with the source composition of $\text{La}/\text{Co}=1$, the most part of the deposited film was Co_3O_4 (7).

3. ELECTROLYTE PREPARATION

The preparation procedure of the electrolyte film on a nickel plate was as follows. A nickel plate(25 X 25mm, 1mm thick, 99.6% pure) was polished and heated in air at 900°C for 1h to form nickel oxide layer on the surface (see Figure 2a). The thickness of the oxide layer was about $10\mu\text{m}$. PSZ film was prepared on the oxide layer. First zirconium was deposited for 500\AA and Y and Zr were alternately deposited in a vacuum of $3 \times 10^{-4}\text{Pa}$ with a substrate temperature of 250°C as shown in Figure 2b. Then the multilayered film was annealed in air at 900°C for 1h. These evaporation and oxidation processes were repeated 5 times to form a $5\mu\text{m}$ thick fine PSZ film. The nickel oxide layer under the electrolyte film converts to porous nickel when the cell is exposed to fuel gas, which then acts as the anode.

The X-ray analysis of the electrolyte film showed that the most part of the film was tetragonal phase and the rest was monoclinic phase. The tetragonal peak height increased as the evaporation and oxidation processes were repeated. No traces of cracks or pores were observed in the cross section of the electrolyte films. It is believed that the repetition of the evaporation of Zr and Y heals the defects in the electrode films being prepared. Increasing the annealing temperature to 1000°C causes a separation of the PSZ and nickel oxide layer from the nickel substrate. Homogeneity of the elements in the PSZ film was examined using EDX analysis. The concentration of yttrium was constant through the film within the limit of experimental error. Y and Zr were not detected in the nickel oxide layer on the substrate.

4. SUBSTRATE AND SUPPORT

In order to release the thermal stresses accumulated in the boundary between the electrolyte and the metal substrate, a thin film cell was prepared on a thin Ni foil which was supported with an alloy frame, and the system was tested. A low thermal expansion coefficient alloy composed of Fe, Ni and Co was selected for the support material. The alloy is known as Kovar and is used as the connection between metal and ceramics because of good thermal expansion matching.

First the center of a Kovar sheet (25 X 25mm, 1mm thick) was machined and a 3mm diameter hole was opened. After the surface cleaning, a Ni foil (99.7%, 10 μ m thick) was pressed on the alloy sheet using a ceramic holder and heated to 700°C for 1h. Then the Ni foil with Kovar support was heated in air at 700°C for 3h to convert the Ni foil to a nickel oxide film. The electrolyte layer was prepared on the nickel oxide film using the previously described method and a cathode was formed onto the layer by evaporating 0.1 μ m thick platinum. The Ni foil, Ni plate and Kovar plate were purchased from The Japan Lamp Industries Co.,Ltd..

5. CELL TEST

The prepared thin film cells were tested using a high temperature cell test apparatus (3); it is designed to minimize cell damage during test at high temperature. Hydrogen and air were used as the fuel and oxidizing gas, respectively.

In the test of the 0.4 μ m thick LaMnO₃ cathode, cell voltage was observed from 300°C ; at 700°C , the OCV of 0.8V was obtained. As shown in Figure 3, a linear relationship between cell voltage and current was observed at various temperatures. The maximum current and the maximum output power at 700°C were 0.7mA and 0.14mW, respectively. The cell test was continued for 20h at 700°C , and no deterioration was detected in the cell characteristics.

In the case of the LaCoO_3 cathode with the same thickness, cell voltage was observed from 400°C , however, the cell failed at 450°C . The electrode thickness had to be reduced to $0.1\mu\text{m}$ to continue cell test at high temperature. The maximum current of 0.15mA and the maximum output power of 0.03mW were obtained at 700°C . The failure of the cell is believed to be due to irregular thermal expansion of LaCoO_3 near test temperature.

In the test of the Ni foil substrate cell with the Pt cathode, the cell voltage was observed from 350°C ; at 700°C , the OCV of 0.9V was obtained. The relationship between cell voltage and current is shown in Figure 4. The maximum current and the maximum output power were 0.23mA and 0.05mW , respectively. The Ni foil cell was cycled 3 times between 700°C and room temperature, and no apparent damage was observed in the cycled cell. When the surface of the Ni foil was previously polished, the OCV at 700°C increased to 1.1V . The reduced current density in the data is attributed to the point contacts between the surface of the cathode and the current collector of the test equipment.

6. CONCLUSIONS

Planar thin film solid oxide fuel cells were prepared on nickel substrates, surfaces of which were previously oxidized. The PSZ electrolyte and oxide cathodes were prepared by vacuum evaporation methods. The adherence of the cathode to the electrolyte film was compared between LaMnO_3 and LaCoO_3 . It was found that LaMnO_3 is superior to LaCoO_3 for the cathode of PSZ thin film cells.

The synthesized PSZ thin film was suitable for the electrolyte of high temperature thin film cells, because the OCV of 1.1V was recorded at 700°C with a vacuum evaporated Pt cathode. It was found that the thermal stresses in the electrolyte layer could be reduced by using a nickel foil substrate instead of bulk substrates. This combination of electrolyte and substrate has proven effective in extending the cycle life of thin film solid oxide fuel cells.

It was also demonstrated that a conductive thin film anode could be prepared from an oxide layer on the surface of Ni sheet or foil.

REFERENCES

1. A. O. Isenberg, W. A. Pabst, E. F. Sverdrup, and D. H. Archer, Proc. Biennial Fuel Cell Symp., 6th, New York (1969).
2. Y. Yamazaki and T. Namikawa, Abstract 340, p514, The Electrochemical Society Extended Abstracts, Vol. 85-2, Las Vegas, Nevada, Oct. 13-18, 1985.

3. T. Namikawa, Y. Yamazaki, I. Saitoh, T. Kanai, S. Sumiya, and M. Satou, DENKI KAGAKU, Vol. 52, No. 10, 714 (1984).
4. T. Ando, T. Namikawa, and Y. Yamazaki, DENKI KAGAKU, Vol. 54, No.7, 614 (1986).
5. H. Michibata, T. Namikawa, and Y. Yamazaki, Abstracts, p268, The Electrochemical Society Extended Abstracts, Vol. 87-2, Honolulu, Hawaii, Oct. 18-23, 1987.
6. T. Namikawa, T. Ando, H. Michibata, and Y. Yamazaki, DENKI KAGAKU, Vol. 55, No. 9, 712 (1987).
7. H. Michibata, T. Namikawa, and Y. Yamazaki, DENKI KAGAKU, Vol. 57, No. 3, 255 (1989).

TABLE I

Evaporation condition for the preparation
of LaMO_3 (M=Mn,Co) film

Source material	La_2O_3	MnO_2 (CoO)
Purity (%)	99.99	99.9
Content (mol%)	66.6	33.3
Substrate temperature ($^{\circ}\text{C}$)	250	
Deposition rate ($\text{\AA}/\text{min}$)	400	
Chamber pressure (Pa)	3×10^{-4}	
Emission current (mA)	100	

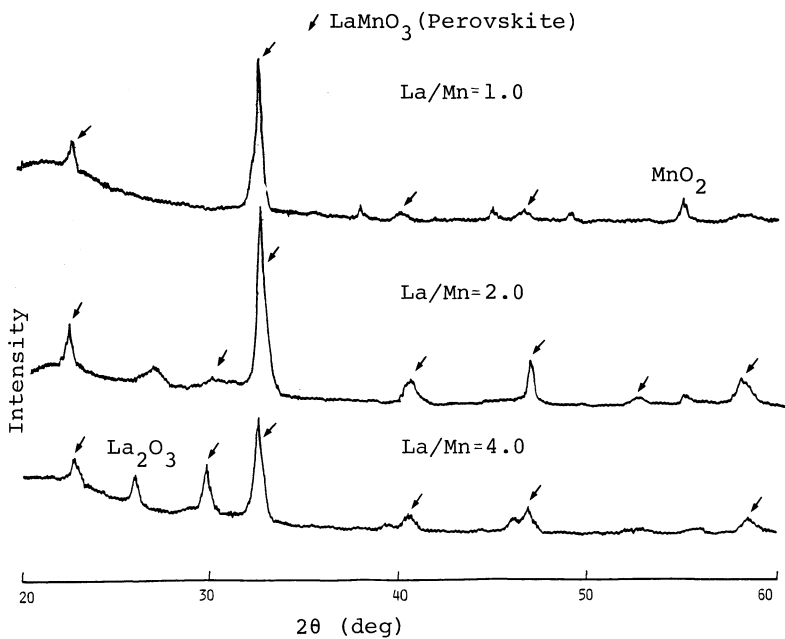


Fig. 1 X-ray diffraction patterns of cathode films prepared from targets with different compositions

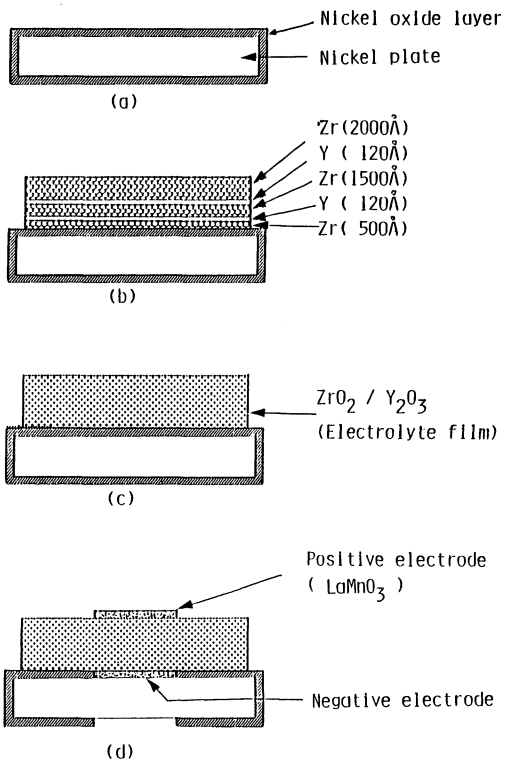


Fig. 2 Preparation process of a thin film cell:
processes (b) and (c) were repeated.

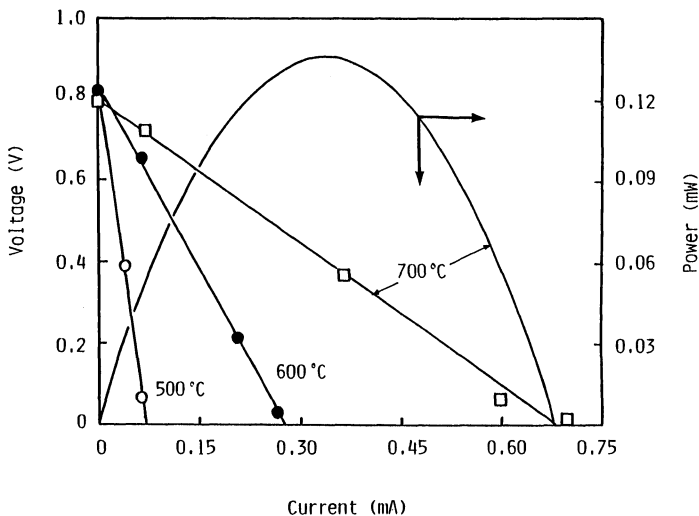


Fig. 3 Cell voltage vs. current for various temperatures measured with LaMnO_3 electrode and Ni plate substrate.

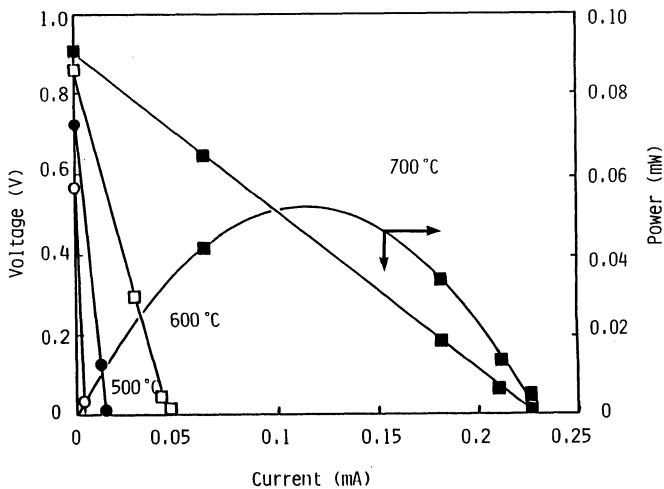


Fig. 4 Cell voltage vs. current measured with Pt electrode and Ni foil substrate.

DEPOSITION AND ELECTRICAL PROPERTIES OF THIN POROUS CERAMIC ELECTRODE LAYERS

L.G.J. de Haart, R.A. Kuipers, K.J. de Vries
and A.J. Burggraaf
Laboratory of Inorganic Chemistry, Materials Science
and Catalysis, University of Twente, P.O.Box 217
7500 AE Enschede, The Netherlands

ABSTRACT

Investigations have been performed on the influence of the morphology on the electrical properties and polarization behaviour of thin porous ceramic electrode layers used in SOFC. Thin layers (2 - 4 μm) of the cathode material $\text{Sr}_{0.15}\text{La}_{0.85}\text{MnO}_3$ (15SLM) were filmcoated on YSZ substrates from classified suspensions. The porosity and pore-size distribution of the filmcoated layers are affected by the particle-size distribution in the suspension. Accordingly, the specific conductivity of the layers decreases significantly with increasing porosity and mean pore-size. A specific conductivity of 109 S.cm^{-1} was obtained at 1000°C for a $2.9 \mu\text{m}$ thick layer from a suspension with particles of $0.10 - 0.25 \mu\text{m}$.

1 INTRODUCTION

In the development of SOFC based on yttria-stabilized zirconia (YSZ) solid electrolytes, one of the state-of-the-art cathode materials is Sr-doped LaMnO_3 . This perovskite-type material exhibits a high electronic conductivity of around 100 S.cm^{-1} at 1000°C . Its thermal expansion coefficient matches the one of YSZ and the material is stable at the operating temperature of the SOFC (i.e. 1000°C) (1).

One of today's most advanced SOFC stack designs is the tubular configuration introduced by Westinghouse around 1980 (1-3). On the outer wall of a porous Ca-stabilized zirconia support tube a layer of the Sr-doped LaMnO_3 cathode material is deposited. A gas tight YSZ electrolyte layer covers the air electrode. Finally the porous Ni-zirconia cermet fuel electrode is deposited on the electrolyte layer. Adjacent tubes, i.e. single cells are interconnected via strips of the interconnection material Mg-doped LaCrO_3 and of ductile nickel felt (1,2). Unfortunately the tubular SOFC design has the disadvantage of a long electron current path through the electrode layers. This causes, especially in the cathode layer, large ohmic voltage drops. The resistivity of the Sr-doped LaMnO_3 layer is still too high for this type of configuration (1). The thickness of the cathode layer can be increased in order to decrease the ohmic resistance, but this can increase the concentration polarization losses arising from a reduced gaseous oxygen flux through the pores of the thick cathode layer. As stressed by Steele (1), this undesirable feature emphasises the important role of design.

In the monolithic-type configuration first proposed by the Argonne National Laboratory (1,4) and the planar configurations which recently have gained much more interest (5), the electron current path through the electrode layer is considerably shorter,

thus substantially decreasing the ohmic polarization losses in these types of configurations. Unfortunately the low electrocatalytic activity of the Sr-doped LaMnO_3 cathode material towards the oxygen reduction reaction still causes severe non-ohmic polarization losses. This low electrocatalytic activity compels the existence of three-phase boundaries electrolyte/electrode/gaseous oxygen for the oxygen reduction reaction to occur. That is, the cathode layer must have a certain porosity, which in turn affects the conductivity of the electrode layer.

The important role the morphology of the electrode layer, i.e. the porosity and the pore-size distribution, thus plays, is not considered well in literature. Therefore we have investigated the influence of the morphology of thin porous ceramic electrode layers on their electrical properties and polarization behaviour.

2 EXPERIMENTAL

Powders with the composition $\text{Sr}_{0.15}\text{La}_{0.85}\text{MnO}_3$ (15SLM) were prepared via a citrate synthesis route (6) and calcined for 16 hours at 1000 °C in air. After wet ball-milling, the powder was classified by centrifuging suspensions of the powder in isopropyl-alcohol (IPA). The collected fractions of the classified powder were again suspended in IPA (40 % of solid material by weight) with 0.5-1.0 wt% addition of an organic stabilizing agent.

Substrates used for layer deposition were disks (diameter 12 mm, thickness 1 mm) of YSZ (12 wt% Y_2O_3) and alumina plates (12 x 6 x 1 mm). Both kind of substrates were polished single-sided with diamond paste down to a $R_a \leq 0.05 \mu\text{m}$. Prior to the layer deposition the substrates were ultrasonically cleaned in isopropyl-alcohol and degreased in boiling hexane.

Layers were deposited by immersing the substrates in the 15SLM suspensions and withdrawing them at a constant speed. Layer thicknesses obtained could be controlled by varying the withdrawal speed (0.125 - 1.25 mm/sec) and the number of repeated dips. In the latter case, the samples were dried in air between subsequent dips. After this filmcoating procedure the samples were finally given a heat treatment for 2 hours at 1100 °C in air.

Layer thicknesses were determined using a DEKTAK surface probe. A JEOL Scanning Electron Microscope type 35CF was used to study the morphology of the deposited layers. Layer resistivity measurements were performed with a 4-point DC technique using Pt point electrodes. Current-overvoltage measurements were performed using a three electrode cell as described in ref.(7). Annular shaped working and counter electrodes of Pt and Pt point shaped reference electrode were used.

3 RESULTS AND DISCUSSION

The XRD pattern of a 15SLM powder sample indicated the formation of a single-phase perovskite-type material. The pattern is very similar to the pattern reported for $\text{Sr}_{0.1}\text{La}_{0.9}\text{MnO}_3$ by Hammouche et al. (8) and the one for $\text{Sr}_{0.1}\text{La}_{0.9}\text{CoO}_3$ reported by Ohbayashi et al. (9). The pattern could be perfectly indexed in the hexagonal-rhombohedral system.

A BET surface area of $4.7 \text{ m}^2/\text{g}$ was determined for the calcined powder by Ar gas adsorption measurements at 77 K. Assuming spherically shaped particles, a mean particle size of $0.2\text{-}0.3 \text{ }\mu\text{m}$ can be calculated from S_{BET} . For the classification of the powder centrifuging speeds and times were estimated using Stoke's law for sedimentation (10) for several particle size ranges. These are given in Table I. Classified suspensions were analyzed with SEM; these results are shown also in Table I. The latter data show, that a systematic error occurs in the estimation using Stoke's law. These data also show, that centrifuging resulted more in narrowing the particle-size distribution going from R1 to R5, than in the actually aimed fractionating in distinct particle-size ranges. This result is due to the classification procedure, which causes the collected fractions to have a large tail on the small particle-size end as discussed by Parish and Bowen (11).

In Figure 1 SEM photographs are shown of sintered layers filmcoated on YSZ from the suspensions R1, R3 and R5 respectively. Although the mean particle-size in the three suspensions does not differ that much, remarkable differences are observed in the deposited layers. The layer dipcoated from R5 shows a close packed structure of only small grains sintered together (Figure 1c). This layer has a very homogeneous porosity and pore-size distribution. Due to however the slightly larger particles and relatively big agglomerates in the suspensions R3 and R1 pore-sizes and porosity increase remarkably in these layers. The large agglomerates in the suspension R1 cause the pore-size distribution in the layer to be less homogeneous. Layer thicknesses as determined by DEKTAK surface probe ranged between 2.0 and $4.0 \text{ }\mu\text{m}$. These layer thicknesses were obtained after repeated (10 to 15) times dipping, where samples were dried in air in between. Figure 1d shows a SEM photograph of a cross-section of a dipcoated sample. It clearly shows the 15SLM layer on top of the dense YSZ substrate. The layer thickness is very constant as is the porosity throughout the layer.

The annealing of the samples for 2 hours at $1100 \text{ }^\circ\text{C}$ in air provided the layers good adherence to the substrate. A prolonged annealing time at $1100 \text{ }^\circ\text{C}$ or higher temperatures like $1200 \text{ }^\circ\text{C}$ causes the 15SLM layer to react with the YSZ substrate. On samples fired at $1200 \text{ }^\circ\text{C}$ for 16 hours the thin perovskite layers had reacted completely with the YSZ substrate. After prolonged heating (upto 100 hours) at $1000 \text{ }^\circ\text{C}$ however no reactivity of the thin 15SLM layer with the YSZ was observed. The 15SLM layer thickness remained the same and with SEM no changes in the morphology were observed.

Figure 2 shows the specific conductivity ($\log \sigma T$) as a function of the reciprocal temperature of the layers dipcoated on alumina from the suspensions R1, R3 and R5 respectively. Straight lines are observed over the whole temperature range, consistent with a small-polaron conduction mechanism model (12). Activation energies calculated from the slopes are 16.0 kJ/mol for the R1 sample, 13.1 kJ/mol (R3) and 13.8 kJ/mol (R5). These values are all slightly higher than the value of 9.6 kJ/mol reported by Kertesz et al. (13) for ceramic samples with composition $\text{Sr}_{0.16}\text{La}_{0.84}\text{MnO}_3$, having an apparent density of 80%. Grain boundary conductivity may account for the higher value of the activation energy that was observed in the porous ($> 50\%$) and relatively thin ($2\text{-}4 \text{ }\mu\text{m}$) 15SLM layers.

Specific conductivity values for the R5 sample are one order of magnitude higher than the ones measured for the R1 sample. The R3 sample lies in between these two, showing the effect that the porosity and pore-size distribution, observed in Figure 1, have

on the specific conductivity. The specific conductivity of the R5 sample amounts to 109 S.cm^{-1} at 1000°C , which is adequate for a planar type SOFC. The value mentioned is also rather close to the value of 133 S.cm^{-1} reported by Kertesz et al. (13) for the conductivity of the 80% dense sintered sample. It also compares well with the conductivity Takeda et al. (14) measured for thin sputtered layers with the composition $\text{Sr}_{0.3}\text{La}_{0.7}\text{MnO}_3$.

The influence of the morphology of the filmcoated layers on the polarization behaviour of these cathodes is presently being investigated.

4 CONCLUSIONS

It has been shown that the morphology of thin porous ceramic electrode layers can be controlled by using classified suspensions for the filmcoating procedure. Specific conductivities can be reached, which are adequate for a planar type SOFC. Further conclusions as for the influence of the morphology on the polarization behaviour are at this moment premature.

ACKNOWLEDGEMENT

The investigations were performed under contract with the Commission of the European Communities (CEC) within the Non-Nuclear Energy R and D Programme (contracts no. EN3E-167-E and EN3E-168-P).

REFERENCES

- (1) B.C.H. Steele, Ceramic Electrochemical Reactors, Current Status and Application, Ceramionics, Surrey (UK) (1987).
- (2) J.T. Brown, *Energy* **11** (1986) 209
- (3) E.F. Sverdrup, C.J. Warde and A.D. Glasser, in: 'From Electrocatalysis to Fuel Cells' (G. Sandstede, ed.), Univ. of Washington Press, Seattle 1972, p. 255
- (4) S.E. Dorris et al., 1988 Fuel Cell Seminar Abstracts, Long Beach CA, Oct 23-26, 1988, p. 29
- (5) M. Hsu, *ibid.*, p.33
- (6) M.A.C.G. van de Graaf et al., *Science of Ceramics* **9** (1977) 75; D.H.A. Blank, H. Kruidhof and J. Flokstra, *J. Phys. D: Appl. Phys.* **21** (1988) 226
- (7) B.A. Boukamp et al., *Solid State Ionics* **28-30** (1988) 1187
I.C. Vinke et al., *Solid State Ionics* **28-30** (1988) 1201
- (8) A. Hammouche, E. Siebert and A. Hammou, *Mat. Res. Bull.* **24** (1989) 367
- (9) H. Ohbayashi, T. Kudo and T. Gejo, *Jap. J. Appl. Phys.* **13** (1974) 1
- (10) See e.g. Th.F. Tadros, in: Solid/Liquid Dispersions (Th.F. Tadros, ed.), Academic Press, London 1987, Ch.11, p.225
- (11) M. Parish and H.K. Bowen, *Ceramics Internat.* **10** (1984) 75
- (12) S.P. Mitoff, *Progr. Ceram. Sci.* **4** (1966) 217
- (13) M. Kertesz et al., *J. Solid State Chem.* **42** (1982) 125
- (14) Y. Takeda et al., *J. Electrochem. Soc.* **134** (1987) 2656

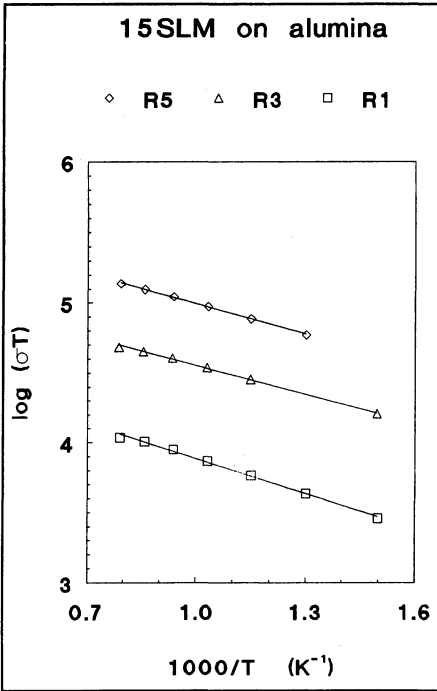


FIGURE 1
(next pages)

SEM photographs of the filmcoated 15SLM layers
 (a) from the suspension R1
 (b) from the suspension R3
 (c) from the suspension R5
 Magnification is 10.000x .
 (d) cross-section
 Magnification is 4000x .

FIGURE 2

Specific conductivities ($\log \sigma T$) of the 15SLM layers filmcoated from the suspensions R1, R3 and R5 respectively as a function of the temperature ($1000/T$).

Table I			
Particle and Agglomerate Sizes			
in the 15SLM Suspensions used for Filmcoating			
suspension no.	Stoke's law estimated particle-size range	SEM analysis	
		observed particle-size range	agglomerates observed upto
R1	2.0 μm	0.2 - 0.5 μm	5 μm
R3	1.1 - 1.5 μm	0.15 - 0.40 μm	1.2 μm
R5	0.3 - 0.7 μm	0.10 - 0.25 μm	0.4 μm

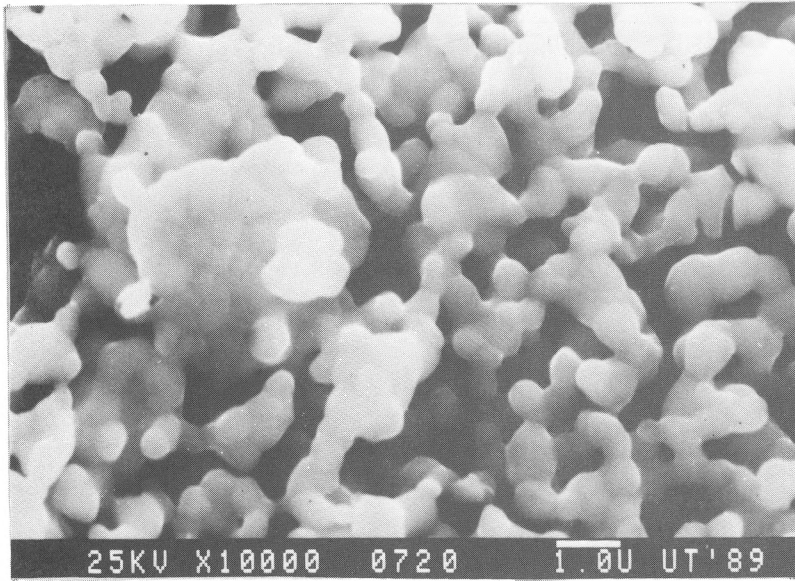
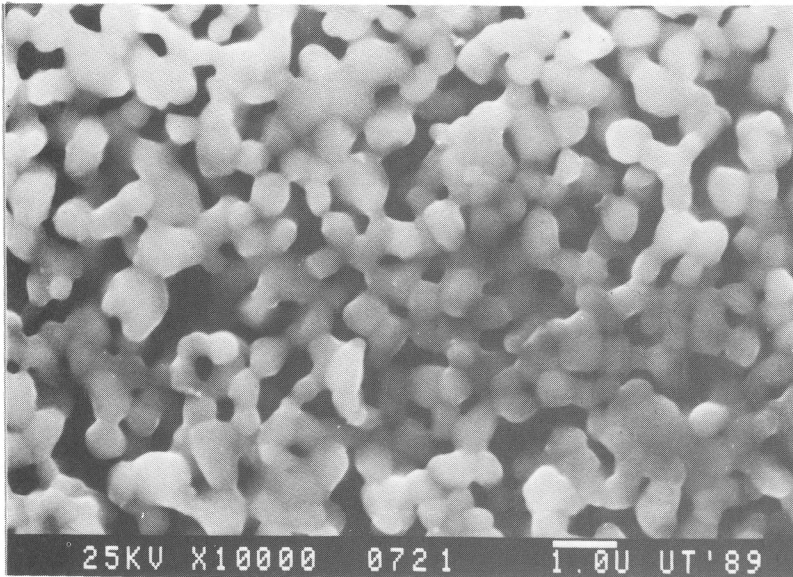


FIGURE 1a (above)

FIGURE 1b (below)



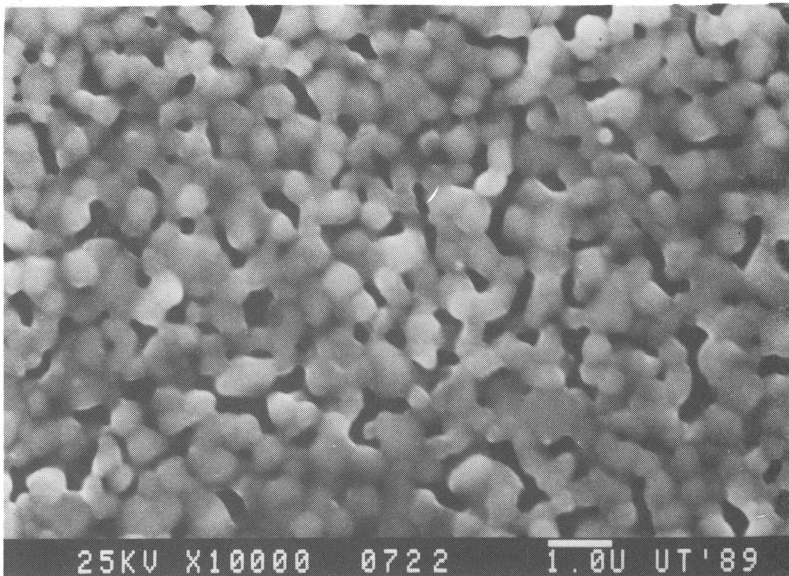
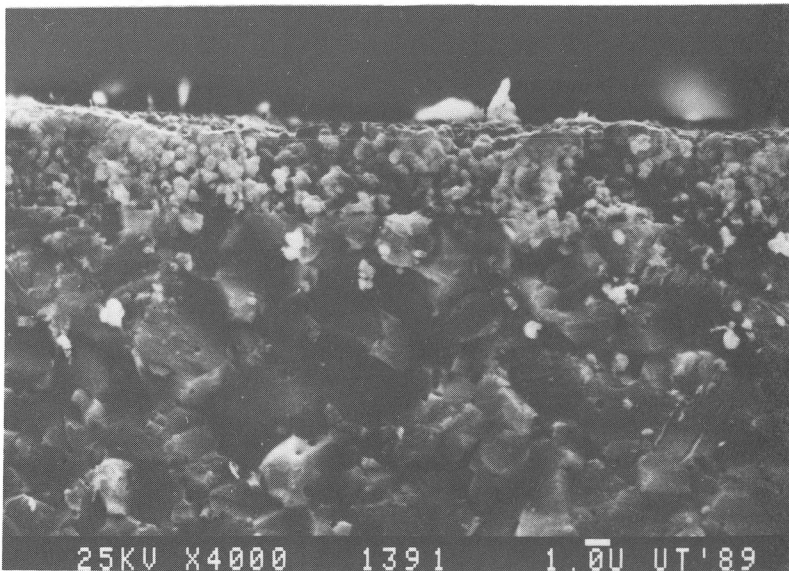


FIGURE 1c (above)

FIGURE 1d (below)



EFFECT OF Pt ADDITIONS ON THE RESISTANCE OF $\text{La}_{0.9}\text{Sr}_{0.1}\text{MnO}_3$ CATHODE

A. Tsumoda, T. Yoshida and S. Sakurada
Corporate Research and Development Laboratory
Toa Nenryo Kogyo K.K.
3-1 Nishi-tsurugaoka 1-Chome, Ohi-machi
Iruma-gun, Saitama-ken, Japan 354

ABSTRACT

The effect of platinum additions to $\text{La}_{0.9}\text{Sr}_{0.1}\text{MnO}_3$ on the electrical conductivity and cathodic properties were studied with a view to reduce ohmic polarization loss of SOFC. The electrical conductivity at 1000°C rose from 5.3 Scm^{-1} to 12 Scm^{-1} by increasing platinum content from 0 vol% to 41.8 vol%. Platinum additions reduced the ohmic polarization of SOFC from 1.1 ohm to 0.8 ohm and the current density of SOFC rose from 0.48 A/cm^2 to 0.63 A/cm^2 at 0.5 V. Other results suggested that this improvement is attributed to not only increasing the electrical conductivity of cathode but also reducing the contact resistance between cathode and electrical collector.

1. INTRODUCTION

Recently, solid oxide fuel cells (SOFC) have attracted much attention. The 3kW pilot plant of tubular type cell made by Westinghouse Electric Corporation has been running for more than 3000 hours in Osaka Gas Co.,Ltd.(1). Many other solid oxide fuel cell configurations, for example monolithic, honeycomb and planar, have also been proposed.

On account of high operating temperature, selection of materials for SOFC is restricted. $\text{La}_{0.9}\text{Sr}_{0.1}\text{MnO}_3$ has been used as a cathode for Westinghouse tubular cell(2) and Argonne National Laboratory monolithic cell(3). A perovskite oxide, especially Sr doped LaMnO_3 , is used as a cathode for SOFC nowadays(4). These materials have high catalytic activity for dissociation of oxygen molecules, relatively high electrical conductivity, and thermal and chemical stability. The cathodic properties of LaMO_3 (M=Mn,Co) have been examined(5,6). The electrical conductivity and its temperature dependence of perovskite oxides have also been studied (7,8,9). According to these studies the electrical conductivity of Sr doped LaMnO_3 at 1000°C reaches more than 100

Scm^{-1} , and is sufficient for cathode of a SOFC. However, the electrical conductivity of an actual perovskite cathode is expected to be much lower than such values because of its porosity and pore shape(10). Therefore, ohmic polarization loss of cathode forms a large part of total ohmic polarization loss of a SOFC(11). It is, therefore, important to improve the electrical conductivity of porous perovskite cathode. On the other hand, platinum has less activity for dissociation of oxygen molecules but high electrical conductivity compared with those of perovskite oxides. In this paper, the effect of platinum additions on the electrical conductivity and the cathodic properties of $\text{La}_{0.9}\text{Sr}_{0.1}\text{MnO}_3$ were studied with a view to reduce ohmic polarization loss of SOFC.

2. EXPERIMENTAL

Powders of the composition $\text{La}_{0.9}\text{Sr}_{0.1}\text{MnO}_3$ and platinum were mixed in an agate mortar and dispersed in a binder solution. These slurries were painted on 1cm wide alumina substrates for the electrical conductivity measurements. Four platinum wires were put on each specimen as probes for four probe D.C. method, and the slurries were painted on the four platinum wires again. After that, specimens were dried in an oven at 90°C. The distance between two potential probes was 1cm and the thicknesses of the cermets were 0.35-0.45mm. The samples were heated in a tubular furnace in flowing oxygen gas and the electrical conductivities were measured with a HOKUTO DENKO potentiostat/galvanostat.

The morphologies of these specimens were observed by a JEOL JSM-820 scanning electron microscope and the X-ray mapping images of all elements were obtained by an energy dispersive X-ray microscopy(EDX), KEVEX DELTA CLASS ANALYZER. The crystalline structures were analyzed and identified by a PHILIPS PW-1700 XRD system. The porosities of cermets were measured by a mercury penetration method with a MICROMERITICS porosimeter, AUTO PORE 9200.

The cathodic properties of the $\text{La}_{0.9}\text{Sr}_{0.1}\text{MnO}_3$ /platinum cermets were examined. 3 mol% yttria doped PSZ sheets from NIPPON SHOKUBAI KAGAKU were used as the solid oxide electrolyte. The thickness of the PSZ sheets is about 0.2mm. Ni/ZrO₂=10/1 cermet was used as an anode. The cathode and anode were painted on the PSZ sheets with a square active area of 1.0cm². Platinum mesh for the electrical collector covered the anode. The electrical collector on the cathode was a platinum wire for clarifying the effect of the electrical conductivity of cathode. This PSZ sheet was put between alumina tubes. The gas seal between the alumina tube and the PSZ sheet was made with a TEMPAX glass ring gasket. The cell was heated in air at a rate of 10°C/min and the

temperature was held at 1000°C. As feed gas, oxygen was supplied to the cathodic side of the cell and hydrogen to the anodic side, respectively. Voltage-current characteristics and the non ohmic polarization properties were measured with the potentiostatic and the current interrupter method, respectively. SOLATRON 1286 ELECTROCHEMICAL INTERFACE was used for these measurements. The difference between the overall voltage-current characteristics and the non ohmic polarization loss measured by the current interrupter method is thought to be an ohmic polarization loss.

3. RESULTS AND DISCUSSION

By the SEM image of the platinum powder used in this study, platinum grains looked spherical and the diameter of each grain was about 0.5 μm . The surface of platinum after calcining at 1000°C was much sintered, though no significant change was observed for that of $\text{La}_{0.9}\text{Sr}_{0.1}\text{MnO}_3$ of which grains were about 5 μm in size.

SEM image and X-ray mapping image by EDX of $\text{La}_{0.9}\text{Sr}_{0.1}\text{MnO}_3/\text{platinum}=76.5/23.5$ vol% cermet after calcining at 1000°C, shown in Figs.1 and 2, revealed that platinum grains were sintered to larger grains. Some small grains of platinum were found between $\text{La}_{0.9}\text{Sr}_{0.1}\text{MnO}_3$ grains, and large platinum grains were unconnected with each other. Consequently, the electrical conduction mechanism of this sample was presumed not to be that of a metal. From the XRD pattern of this cermet, no reaction compound of $\text{La}_{0.9}\text{Sr}_{0.1}\text{MnO}_3$ and platinum was found.

In Fig.3, the electrical conductivities of painted $\text{La}_{0.9}\text{Sr}_{0.1}\text{MnO}_3/\text{platinum}$ cermets at 1000°C are shown as a function of platinum content. The electrical conductivity of $\text{La}_{0.9}\text{Sr}_{0.1}\text{MnO}_3$ was 5.3 Scm^{-1} . This value was about two orders of magnitude lower than that of other study, 133 Scm^{-1} (8). It is considered that the difference of the electrical conductivities of painted $\text{La}_{0.9}\text{Sr}_{0.1}\text{MnO}_3$ from that of bulk $\text{La}_{0.9}\text{Sr}_{0.1}\text{MnO}_3$ depends on its porosity. The porosity of painted $\text{La}_{0.9}\text{Sr}_{0.1}\text{MnO}_3$ was very large as shown in Fig.4. The platinum additions improved the electrical conductivities of cermets and reduced the porosities. Drastic change was not observed for the electrical conductivities. This is different from the case of Ni/ZrO₂ cermet used as an anode of SOFC(12). Though the threshold of Ni content has been reported 30 vol% Ni, no threshold was found in $\text{La}_{0.9}\text{Sr}_{0.1}\text{MnO}_3/\text{platinum}$ cermet up to 41.8 vol% platinum. Platinum grains used in this study are supposed to easily migrate and grow larger due to small diameter. The platinum grains were, therefore, dispersed in $\text{La}_{0.9}\text{Sr}_{0.1}\text{MnO}_3$ grains and were unable to make connections with each other as shown in Fig.2.

Fig.5 shows the temperature dependence of the electrical conductivities of

La_{0.9}Sr_{0.1}MnO₃/platinum cermets. The ln(σ T) versus 1/T curves of La_{0.9}Sr_{0.1}MnO₃/platinum cermets were almost straight. All curves were nearly parallel. As mentioned above, the temperature dependence of the electrical conductivity of these cermets was not that of metal. It has been reported that the electrical conduction mechanism of La_{1-x}Sr_xMnO₃ is small-polaron conduction mechanism because the ln(σ T) versus 1/T curve is straight line(7,8). Accordingly, it is thought that the conduction mechanism of these cermets is also governed by that of La_{0.9}Sr_{0.1}MnO₃. The electrical conductivity of perovskite oxides is said to decrease with increasing porosity(6). The cermets shrank by sintering of platinum grains and the porosities of the cermets decreased as shown in Fig.4. It is possible that the electrical conductivities of these cermets improved without changing the conduction mechanism. This is thought to be one of the effects of platinum additions.

Fig.6 shows the effect of platinum additions on current density of SOFC. The current density rose from 0.48 A/cm² to 0.63 A/cm² at 0.5 V with increasing platinum content up to 23.5 vol% but drastically decreased in the case of the cathode involving 41.8 vol% platinum. In Fig.7, the effects of platinum additions on non ohmic and ohmic polarization are shown. The non ohmic polarization did not change with increasing platinum content. Using the cathode with 41.8 vol% platinum, it was observed that the surface of the cathode peeled off from the electrical collector after experiment. This is probably due to shrinkage of this cermet. Much ohmic polarization of this cell is attributed to this phenomenon.

The resistance of 3 mol% yttria doped PSZ sheet which is 0.2mm thick and 1.0cm² large is about 0.5 ohm. The electrical conductivity of the cermet involving 23.5 vol% platinum could not explain clearly a drastic decrease of ohmic polarization eliminating the resistance of PSZ sheet. It is suggested that a contact resistance exists between electrolyte and electrodes, or electrodes and electrical collectors. To confirm this, following experiment was carried out. After painting La_{0.9}Sr_{0.1}MnO₃ as cathode, a platinum wire was placed on it as the electrical collector and the cermet with 23.5 vol% platinum was painted around the platinum wire. Cell performance was measured. As shown in Table 1, the ohmic polarization decreased from 1.1 ohm to 1.0 ohm and the current density improved from 0.48 A/cm² to 0.53 A/cm². This result suggests that one of the effects of platinum additions is a reduction in the contact resistance between the cathode and the electrical collector. It is speculated that the apparent contact area of the electrical collector to the La_{0.9}Sr_{0.1}MnO₃ grains increased because of many platinum grains contact to the electrical collector. Generally, the resistances of an electrolyte and electrodes are reduced with increasing active area of cell. However, the contact resistances do not change. Consequently, the effect of platinum

additions is thought to be more important for the scale up of SOFC.

4. CONCLUSIONS

- ①. The platinum grains used in this study sintered at 1000°C but $\text{La}_{0.9}\text{Sr}_{0.1}\text{MnO}_3$ was little sintered at this temperature.
- ②. The electrical conductivity at 1000°C of painted $\text{La}_{0.9}\text{Sr}_{0.1}\text{MnO}_3$ improved by platinum additions. It is speculated that this improvement is due to reduced porosity of the cermet by platinum sintering.
- ③. The ohmic polarization of SOFC consisted of ohmic resistances of materials and contact resistances.
- ④. Platinum additions reduced the contact resistance between the cathode and the electrical collector and increased the current density of SOFC. This effect is thought to be more important for the scale up of SOFC.

ACKNOWLEDGEMENTS

This work was supported by the Petroleum Energy Center which was subsidized by MITI.

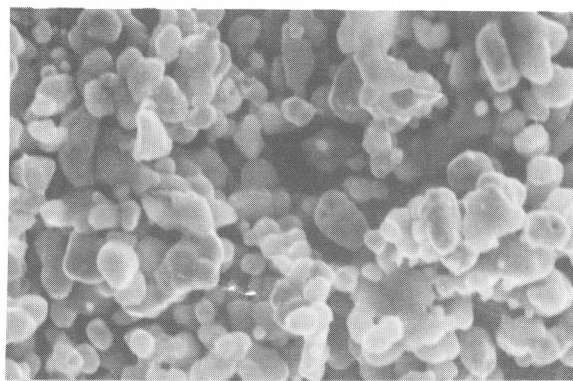
REFERENCES

1. M. Harada and Y. Mori: Abstracts of 1988 Fuel Cell Seminar, Long Beach, California, October 23-26, 1988, 18.
2. A.O. Isenberg: Proceedings of the Conference on High Temperature Solid Oxide Electrolyte, Brookhaven National Laboratory, August 16-17, 1983, 1, 4.
3. T.E. Easler, B.K. Flandermeier, T.D. Clear, D.E. Busch, R.J. Fousek, J.J. Picciolo and R.B. Poeppel: Abstracts of 1986 Fuel Cell Seminar, Tucson, Arizona, October 26-29, 1986, 72.
4. T. Yoshida, T. Hoshina, I. Mukaizawa and S. Sakurada: to be published in J. Electrochem. Soc.
5. Y. Takeda, R. Kanno, M. Noda, Y. Tomida and O. Yamamoto: J. Electrochem. Soc., 134, (11), 2656 (1987)

6. J.Mizusaki, H.Tagawa, K.Tsuneyoshi, K.Mori and A.Sawata: J.Chem.Soc.Japan, (9), 1623 (1988)
7. D.P.Karim and A.T.Aldred: Phys.Rev., B20, 2255 (1979)
8. M.Kertesz, I.Riess and D.S.Tannhauser: J.Solid State Ionics, 42, 125 (1982)
9. O.Yamamoto, Y.Takeda, R.Kanno and M.Noda: Solid State Ionics, 22, 241 (1987)
10. W.D.Kingery, H.K.Bowen and D.R.Uhlmann: "Introduction to Ceramics", 2nd ed., 518, 617, Wiley, New York (1976)
11. D.C.Fee, S.A.Zwick and Ackerman: in Ref.2, 27
12. D.W.Dees, T.D.Claar, T.E.Easler, D.C.Fee and F.C.Mrazek: J.Electrochem. Soc., 134, 9, 2141 (1987)

Table 1 Effect of $\text{La}_{0.9}\text{Sr}_{0.1}\text{MnO}_3$ /platinum cermet painted around the electrical collector on the ohmic polarization and the current density of SOFC.

	Ohmic polarization (ohm)	Current density (A/cm ²)
$\text{La}_{0.9}\text{Sr}_{0.1}\text{MnO}_3$ cathode	1.1	0.48
$\text{La}_{0.9}\text{Sr}_{0.1}\text{MnO}_3$ cathode with the cermet containing 23.5 vol% platinum around the electrical collector	1.0	0.53



↔ 1 μ m

Fig.1 Scanning electron micrograph of $\text{La}_{0.9}\text{Sr}_{0.1}\text{MnO}_3$ /platinum=76.5/23.5 vol% cermet after calcination at 1000 $^{\circ}$ C.



Fig.2 Energy dispersive X-ray micrograph of platinum in $\text{La}_{0.9}\text{Sr}_{0.1}\text{MnO}_3$ /platinum=76.5/23.5 vol% cermet after calcination at 1000 $^{\circ}$ C.

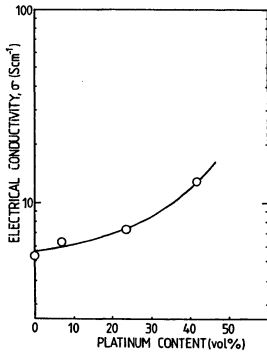


Fig.3 Relation between the electrical conductivities at 1000°C for painted $\text{La}_{0.9}\text{Sr}_{0.1}\text{MnO}_3$ /platinum cermets and those platinum content.

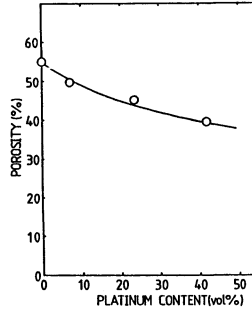


Fig.4 Relation between the porosities of painted $\text{La}_{0.9}\text{Sr}_{0.1}\text{MnO}_3$ /platinum cermets and those platinum content.

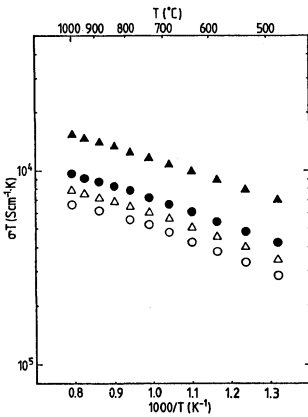


Fig.5 Temperature dependence of the electrical conductivities of painted $\text{La}_{0.9}\text{Sr}_{0.1}\text{MnO}_3$ /platinum cermets. Platinum content (vol%): (○)0, (△)7.1, (●)23.5, (▲)41.8

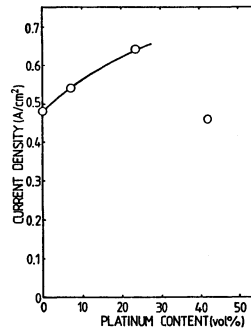


Fig.6 Effect of platinum additions to $\text{La}_{0.9}\text{Sr}_{0.1}\text{MnO}_3$ on the current densities at 0.5 volt of SOFC.

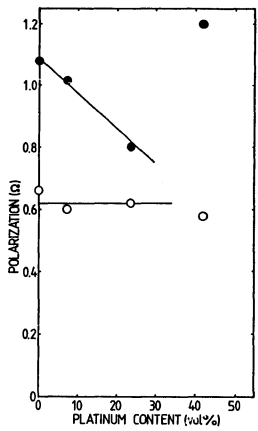


Fig.7 Effect of platinum additions to $\text{La}_{0.9}\text{Sr}_{0.1}\text{MnO}_3$ on the polarization properties of SOFC: (○)non ohmic polarization, (●)ohmic polarization.

MEASUREMENT OF THE CHEMICAL DIFFUSION COEFFICIENT OF OXYGEN IN $(\text{La}_{0.79}\text{Sr}_{0.20})\text{MnO}_{3-\delta}$

A. Belzner, T. M. Gür and R. A. Huggins
Department of Materials Science and Engineering,
Stanford University, Stanford, CA 94305-2205

ABSTRACT

Oxide perovskites of the general formula $(\text{La}_{1-x}\text{Sr}_x)\text{MnO}_{3-\delta}$ are being used as air electrodes in high temperature solid oxide fuel cells. The chemical diffusion coefficient of oxygen in $(\text{La}_{0.79}\text{Sr}_{0.20})\text{MnO}_{3-\delta}$ was measured using the potentiostatic step method. This solid state ionic technique involved the use of a stabilized zirconia oxide electrolyte. The diffusion coefficient of oxygen in this mixed-conducting perovskite was found to be of the order of 10^{-7} cm²/sec at temperatures between 700°C and 860°C and at oxygen partial pressures between 0.21 atm and 10^{-8} atm.

INTRODUCTION

Perovskite type oxides of transition metals are interesting materials for oxygen electrodes and oxidation catalysts [1]. The general formula is $(\text{Re}_{1-x}\text{M}_x)\text{TmO}_{3-\delta}$, where Re is a rare earth metal, typically lanthanum, M is an alkali earth metal (Ca or Sr), and Tm denotes a first row transition metal (Cr, Mn, Fe, Co, Ni). Members of the series $(\text{La}_{1-x}\text{Sr}_x)\text{MnO}_{3-\delta}$ are, in particular, being used as air electrodes in high temperature solid oxide fuel cells. All these oxides are mixed conductors in which the transport of oxide ions plays a major role in the oxygen electrode reaction. The knowledge of the transport parameters for oxygen will help in the characterization and selection of materials for special purposes as well as in understanding the reaction mechanisms involved. In this work a solid state electrochemical method was used to measure the chemical diffusion coefficient of oxygen in the mixed-conducting oxide $(\text{La}_{0.79}\text{Sr}_{0.20})\text{MnO}_{3-\delta}$.

THEORETICAL CONSIDERATIONS

The experimental arrangement is shown in Figure 1. It can be represented as:

(+) oxygen reference electrode / solid oxide electrolyte / mixed conducting sample (-)

The activity of oxygen in the sample at the sample/electrolyte interface can be calculated from the open circuit voltage, "OCV", of the cell using the Nernst equation. Conversely, the oxygen activity at the sample/electrolyte interface can be controlled by imposing a voltage across the cell.

It is assumed that initially the activity a^0 of the electroactive species is uniform throughout the sample. In a potentiostatic step experiment the activity $a_{x=0}$ at the interface is set to a different value a' at time $t=0$ by imposing a voltage step on top of the OCV. The volume of the sample is allowed to reequilibrate with the interface by a diffusional process. The rate of transport of the oxygen addition or deletion from the sample by solid state diffusion is

monitored by measuring the cell current as a function of time. It has been shown elsewhere, that the solution to the current-time behaviour under these conditions has two approximations relating to short or long times [2,3].

According to the short time approximation the cell current is a linear function of $t^{-1/2}$. The chemical diffusion coefficient D of the electroactive species in the sample material is obtained from the slope S of the cell current, plotted as a function of $t^{-1/2}$, as follows :

$$D = [S * (V_m \pi^{1/2}) * 1/(AzF) * ((\delta E/\delta y)/\Delta E)]^2 \quad (1)$$

Here, V_m is the molar volume of the sample substance, A is the geometrical contact area between the sample and the electrolyte, z is the charge number of the electroactive species, and F is the Faraday constant. ΔE is the applied potential step. $\delta E/\delta y$ is the slope of the open circuit voltage as a function of the stoichiometric number y of the electroactive species, i.e. the local slope of the coulometric titration curve. (In this case : $y = 3 - \delta$) Assuming that the slope is constant within the composition range of an experiment, $1/\Delta y$ can be substituted for $((\delta E/\delta y)/\Delta E)$. Δy is calculated from the total charge flux per experiment.

The long time approximation is given by :

$$\ln(I) = \ln\{ (2azF) * 1/(LV_m) * (\Delta E/(\delta E/\delta y)) * D \} - (1.071/L^2) * D * t \quad (2)$$

The chemical diffusion coefficient may be determined from either the intercept or the slope of $\ln(I)$ plotted as a function of time. In the latter case only the sample thickness L is needed as an additional parameter to obtain D .

By carrying out the potentiostatic step experiment until equilibrium is attained, and repeating it at stepwise increasing or decreasing voltages, the diffusion coefficient can be obtained as a function of the oxygen activity in the sample. At the same time a point of the equilibrium coulometric titration curve is obtained during each experiment. The slope of the coulometric titration curve can be used to calculate the "thermodynamic enhancement factor" $\delta \ln(a)/\delta \ln(c)$ [2] :

$$\delta \ln(a)/\delta \ln(c) = (zqy/kT) * (\delta E/\delta y) \quad (3)$$

By this factor the diffusion is enhanced if a composition gradient is present in the sample.

EXPERIMENTAL

A single crystal slab of 10 m% Y_2O_3 stabilized zirconia of about 12 mm in diameter and 0.6 mm in thickness was used as solid oxide electrolyte. Both faces of the zirconia slab were polished to mirror shine using 1 micron diamond paste. A porous platinum electrode layer was deposited on one face using Hanovia platinum paste.

The sample was a sintered pellet of $(\text{La}_{0.79}\text{Sr}_{0.20})\text{MnO}_{3.8}$. The mass of the pellet was 0.2 g, the thickness L was 1.7 mm and the cross sectional area, which equals the geometrical contact area between the pellet and the zirconia slab, was 0.2 cm^2 . One face of the pellet was polished by using 6 micron diamond paste.

All the other external surfaces of the pellet were covered by a layer of gold using Hanovia paste which was subsequently fired at 850°C in air. The uncoated surface of the pellet was then pressed by a spring mechanism on to the bare face of the zirconia slab. A platinum foil electrode 12 mm in diameter was pressed against the gold coated back side of the pellet.

The gold layer was intended to act as a diffusion barrier for oxygen. In order to provide further sealing of the sample volume and to prevent air from leaking into the zirconia/sample interface, the volume remaining around the sample between the Pt foil and the zirconia slab was filled with Pyrex powder. The setup was then fired in air at 850°C in order to consolidate the Pyrex and kept at temperatures of 700°C and above during the subsequent diffusion measurements.

Diffusion measurements were carried out at temperatures between 700°C and 860°C . Voltage steps of typically 100mV were applied to the cell. The sample was kept at negative potentials versus the Pt/air electrode - i.e. at oxygen activities below 0.21 atm. The maximum voltage applied was 400mV, corresponding to oxygen partial pressures of 3×10^{-9} atm and 1.5×10^{-8} atm at 760°C and 860°C , respectively. Usually oxygen was depleted from the sample. For some experiments the cell was shortcircuited and the sample thus replenished with oxygen to reach equilibrium with the atmospheric oxygen pressure again. A summary of the experimental conditions and results is given in Table 1.

RESULTS AND DISCUSSION

The validity range of the short time approximation given by equation (1) was determined from log/log plots of the current/time behaviour. A dependence of the form $I = x \cdot t^{-1/2}$ was found for time intervals of roughly 2000 to 20,000 sec at 700°C , varying to about 300 to 3000 sec at 860°C . An exponential current decay according to equation (2) was found at times $t \geq 30,000$ sec (8h) at 700°C and $t \geq 10,000$ sec (3h) at 860°C . The diffusion coefficients for "long times" given in Table 1 were calculated from the slope of the $\ln(I)/t$ plot.

The diffusion coefficient for oxygen in $(\text{La}_{0.79}\text{Sr}_{0.20})\text{MnO}_{3.8}$ is of the order of 10^{-7} cm^2/sec at 700°C and reaches values of 10^{-6} cm^2/sec at 860°C . It increases by a factor of 5 (short-time results) to 9 (long time results) in that temperature range. This corresponds to an activation energy of 1.0 to 1.3 eV (22 to 30 kcal/mole) for the diffusion of oxygen in this material. It should be noted that the diffusion coefficient also depends strongly on the oxygen partial pressure, generally decreasing as the oxygen partial pressure decreases. It was observed that its value varies considerably within a voltage step of 100 mV. This may account partially for the observed scatter in the diffusion data in an Arrhenius plot. Measurements using voltage steps smaller than 100mV should yield the activation energy with less scatter.

The diffusion coefficients obtained from the short time behaviour are systematically smaller than those obtained from the long time behaviour. This may be due to the contact resistance between the sample and the electrolyte. A high contact resistance will cause an ohmic voltage drop at the interface and thus lower the effective activity step. This, however, affects only the short time behaviour. In any case, the results from the short and the long time behaviour are of the same order of magnitude and show the same trends as functions of temperature and oxygen partial pressure.

The thermodynamic enhancement factor for the chemical diffusion of oxygen is of the order of 10^4 . This is a comparatively high number. Enhancement factors of this order of magnitude were observed earlier for the diffusion of Li in Li_3Sb and for the diffusion of Cu in Cu_2S and Ag in Ag_2S [4].

ACKNOWLEDGEMENTS

The authors would like to thank Dr. H. U. Anderson from the University of Missouri at Rolla for providing the samples used in these experiments.

Financial support from the Gas Research Institute is gratefully acknowledged.

One of us (A. Belzner) also received partial support from the Alexander von Humboldt-Stiftung, Bonn, West Germany, in the form of a Feodor Lynen Fellowship.

REFERENCES

1. J. O. Bockris and T. Otagawa, *J. Electrochem Soc.* **131**, 290-302 (1984).
2. W. Weppner and R. A. Huggins, *Annual Review of Materials Science* **8**, 269-311 (1978).
3. C. J. Wen, C. Ho, B. A. Boukamp, I. D. Raistrick, W. Weppner and R. A. Huggins, *International Metal Reviews* **2**, 253-268 (1981).
4. W. Weppner, *Solid State Ionics* **3/4**, 1-6 (1981).

Table 1: Diffusion coefficients and enhancement factors for oxygen in $(\text{La}_{0.79}\text{Sr}_{0.20})\text{MnO}_{3-\delta}$

T [°C]	ΔE [V]	$D_{\text{short times}}$ [cm ² /sec], * 10 ⁷	$D_{\text{long times}}$	dE/dy [V]	dln(a)/dln(c)
700	42.5 -> 140	1.0	3.5	444	32,000
	140 -> 240	3.8	7.4	1140	81,000
760	0 -> 100	2.5	8.8	249	17,000
	100 -> 200	5.5	15	339	23,000
	200 -> 300	3.3	9.8	307	21,000
	300 -> 400	2.2	5.3	280	19,000
780	21.3 -> 0	6.8	10	257	17,000
815	24 -> 0	7.5	8.1	202	13,000
	0 -> 100	3.8	0.96	142	9,100
	100 -> 200	1.4	3.1	114	7,300
860	0 -> 100	12	17	139	8,600
	100 -> 200	4.3	13	94	5,800
	200 -> 300	1.8	8.8	84	5,200
	300 -> 400	0.28	4.5	47	2,900

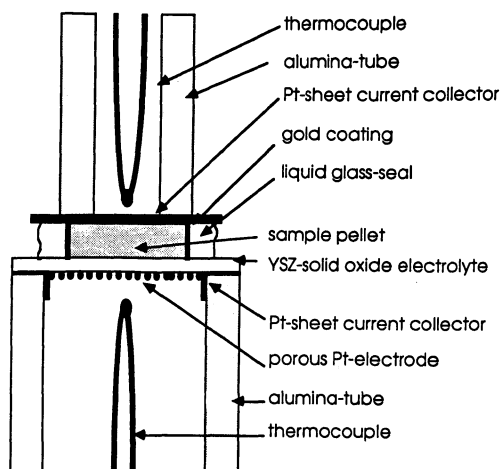


Fig. 1 Assembly of the solid state electrochemical cell

STRUCTURAL, SINTERING AND ELECTRICAL
PROPERTIES OF THE PEROVSKITE-TYPE
(La, Sr) (Cr, Mn) O₃

Rasit Koc, Harlan U. Anderson and Scott A. Howard
Department of Ceramic Engineering
Don M. Sparlin
Department of Physics
University of Missouri-Rolla, MO, 65401

ABSTRACT

The $LaCr_{1-x}Mn_xO_3$ system has been investigated to determine the best composition for high temperature electrode and fuel cell interconnector applications. Structural studies were made using a Rietveld pattern-fitting structure-refinement algorithm with X-ray powder diffraction data. The pattern fitting nature of this technique aided in the identification of phases and allowed for precise determination of the lattice parameters for the component phases. For compositions annealed at temperatures below 1200°C a single orthorhombic phase was found for $x < 0.55$ while a single rhombohedral phase existed for $x > 0.60$. A mixture of the two phases existed for intermediate compositions. Lattice parameters were shown to vary smoothly as a function of atomic substitution.

Sintering studies were done in air at temperatures below 1500°C. Significant improvement in densification was observed with substitution of 50% Mn for Cr. A density of 95% theoretical was achieved with the substitution of 70% Mn for Cr.

Electrical conductivity (d.c.) measurements were made as a function of temperature and oxygen activity. At 1000°C and 1 atm. O₂ the electrical conductivity measurements ranged from 2.2 S/cm to 20 S/cm for the compounds $LaCr_{0.6}Mn_{0.4}O_3$ and $La_{0.9}Sr_{0.1}Cr_{0.2}Mn_{0.8}O_3$, respectively. The conductivity showed thermal activation for all compositions. The activation energy increased as Mn was substituted for Cr in $LaCrO_3$ to a maximum at 20% Mn, and then decreased to its original value as the Mn content increased beyond 30%. The concentration of carriers was directly proportional to the Sr and Mn content under oxidizing conditions. A sharp decrease in the conductivity occurred for oxygen activity of less than approximately 10⁻¹³ at 1000°C. A positive sign Seebeck coefficient was observed for all the compositions indicating p-type conductivity. The Seebeck coefficient was nearly

temperature independent and decreased linearly with substitution of Mn for Cr. Calculated carrier mobilities indicated that the substitution of Mn for Cr significantly decreased the carrier mobility. The substitution of Sr for La did not significantly increase the carrier concentration, but did increase the carrier mobility.

I. INTRODUCTION

Over the past decade, because of promising applications as electrode materials for high temperature devices, the perovskite type oxides $LaMnO_3$ and $LaCrO_3$ have received a great deal of attention. The main use of $LaMnO_3$ and $LaCrO_3$ has been as an electrode and interconnector material for MHD power generation and high temperature fuel cells, respectively. However, $LaCrO_3$ with dopants (such as Mg, Sr, Al, and Ni) is difficult to densify even at temperatures as high as $1800^\circ C$ and has relatively low electrical conductivity (less than 1 S/cm at $1000^\circ C$ and oxygen activity of 10^{-16}) (1). $LaMnO_3$ doped with Sr has been used as cathode for fuel cells (2). The electrical conductivity of Sr-doped $LaMnO_3$ in an oxidizing atmosphere is very high (190 S/cm at $1000^\circ C$) (3), however, it dissociates at $1000^\circ C$ and an oxygen activity of 10^{-15} . Other perovskite structure oxides such as $LaNiO_3$ and $LaCoO_3$ have also been investigated as high temperature electrodes but, at $1000^\circ C$ and in reducing conditions these oxides are also unstable to dissociation (4). The addition of Cr to those oxides has been suggested as a method of increasing the stability of those oxides towards reduction. However, the addition of Cr has two negative effects; the electrical conductivity is decreased and the ability to sinter such oxides diminishes as the Cr content increases. However, it has also been seen that stability against reducing is improved at high Cr content ($La_{0.8}Sr_{0.2}Cr_{0.8}Ni_{0.2}O_3$) (5).

In this study the substitution of Mn for Cr was investigated to see if both electrical conductivity and sinterability of $LaCrO_3$ could be improved without the deterioration of the stability under reducing condition. The purpose of this work was to develop an interconnector for solid oxide fuel cells by combining the desirable properties of $LaCrO_3$ and $LaMnO_3$, and to gain an understanding of the effect of different cation substitutions on the properties.

II. EXPERIMENTAL PROCEDURE

A number of compositions of $LaCrO_3$ - $LaMnO_3$ based powders were prepared using the liquid-mix process (6). Each composition was prepared by dissolving predetermined amounts of La carbonate, Mn carbonate, Sr carbonate, and a Cr containing solution in citric acid and ethylene glycol. The mixtures were heated on a hot plate at about $95^\circ C$ until polymerization occurred. Subsequent heating at higher temperatures resulted in the decomposition of the polymer resin and allowed conversion into the desired oxide. Final calcination was done at $850^\circ C$ for 8 hours. To insure that the synthesis was correct, each composition was subjected to X-ray diffraction

analysis using a General Electric XRD-700 X-ray diffractometer scanned at a rate $1^\circ 2\theta$ /min. In order to improve the X-ray diffraction patterns, a number of the compositions were reheated to 1200°C for 4 hours. This treatment increased both the crystallinity and the grain size of the powders (grain size increased from $0.1\ \mu\text{m}$ to $1.0\ \mu\text{m}$). X-ray diffraction patterns from these powders were subjected to the Rietveld structural refinement procedure in order to determine lattice parameters and phases. For the electrical conductivity and sintering studies, some of the powders were pressed into bars with the aid of a PVA and water binder. A compaction pressure of $1075\ \text{kg}/\text{cm}^2$ yielded $1.0 \times 0.6 \times 1.5\ \text{cm}^3$ bars with a green density about 40% of theoretical. Densification was carried out at 1475°C for 11 to 48 hours in a SiC heated box furnace. Bulk densities were measured using xylene as a saturating liquid. Scanning electron micrographs of the polished surface of sintered compounds were taken with a model JEOLCO JSM -35 CF scanning electron microscope.

Electrical conductivity (d.c) and the Seebeck coefficient measurements were measured on $(0.3 \times 0.3 \times 1.5\ \text{cm}^3)$ rectangular shaped specimens which were electroded with Pt paste. The specimens were then mounted between two platinum blocks. Platinum- 10% Rh/Pt thermocouples were used to measure the temperature at the both ends of the specimens. A Pt wire heater was wound on the lower end of the holder in order to generate a temperature gradient along the vertical direction. Three sets of specimens and holders were inserted into a MoSi_2 furnace in which atmospheric control was achieved by using flowing gas mixtures composed of either O_2 - N_2 or CO_2 - forming gas (10% H_2 - 90 N_2). A stabilized zirconia oxygen sensor was used to monitor the oxygen partial pressure of the gas mixture. The Seebeck coefficients were determined by measuring temperature gradients and thermal emf's through the common leads of the thermocouples. Electrical conductivity measurements were made using a two-probe, four-wire Kelvin technique in which two leads carry the current (1mA) and the other two measure the voltage drop. The measurements were made using a data logger, (A Hewlett Packard 3497A data acquisition/control unit) which employs a HP-85 computer both as a control and readout device. More details on this apparatus are available in Ref. 18.

III. RESULTS AND DISCUSSION

A. STRUCTURAL STUDIES (RIETVELD REFINEMENT)

The Rietveld technique (7,8) of pattern-fitting-structure-refinement was used to determine precise values of the lattice parameters and assay the phase/composition of selected specimens. This technique is based on the ability to calculate an X-ray powder diffraction pattern when the structural parameters for respective phases are known. Figure 1 shows the phase/composition relationship obtained using this refinement procedure. Results showed the existence of a single orthorhombic phase when the system has Mn content (x) less than 0.55 moles while a single rhombohedral phase existed when the Mn content (x) was greater than 0.60 moles. A mixture of the two phases was found for intermediate compositions.

The parameters obtained for the orthorhombic and rhombohedral phases examined in this study exhibit a large number of overlapping and otherwise unresolved diffraction lines. For this type of overlapping the Rietveld technique has two major advantages. The first advantage is that it generates the correct number of lines to fit the observed diffraction patterns and constrains their positions based on the values of the lattice parameters for the respective phase. The second advantage in using this technique arises from the number of data points (observations) used in refining the variables of interest. Estimates of the lattice parameters are obtained using all the information available over the region of the scan; this includes overlapping lines. Using this procedure, the lattice parameters were calculated for each composition and are plotted in Figures 2 and 3 for each region. $LaCrO_3$ was found to consist of a single orthorhombic phase with lattice parameters $a = 5.5206(4) \text{ \AA}$, $b = 5.4861(4) \text{ \AA}$ and $c = 7.7742(8) \text{ \AA}$, in excellent agreement with published values (9). Lattice parameters are shown to vary smoothly as a function of Mn substitution for Cr. The lattice parameters of some compositions calculated from the Rietveld program are also listed in Table I. The end member $LaMnO_3$ had a rhombohedral structure with lattice parameters $a = 5.4724(1) \text{ \AA}$ and a rhombohedral angle 60.582° (1) in agreement with published values (10).

B. SINTERING STUDIES

The densification of the various compositions was studied as function of Mn content and time at 1475°C in air. The results are listed in Table II and illustrated in Figure 4. It was clear that substitution of Mn for Cr improved the sinterability of all compositions. At the present time there are no data to determine which mass transport mechanism is dominating the densification mechanism in the compounds. However, it is certain that Mn substitution for Cr in $LaCrO_3$ increases the sintered density. The microstructures indicated that when Sr was added as an acceptor to improve electrical conductivity, it also enhanced the sinterability. Significant improvement in densification was observed with substitution of 50% Mn for Cr, and 95% theoretical density was achieved with substitution of 70% Mn for Cr. Sintered compounds from the rhombohedral region were ground and subjected to X-ray analysis to investigate their crystal structures. It was found that they had orthorhombic structure at room temperature. This indicated a structural phase transition from rhombohedral to orthorhombic structure during the sintering. The cell volume change during this transition was from about 117.4° to 234.4° which might slightly enhance the densification through the Hedval effect (11). However, clarification of the mechanism will have to be deferred to future studies.

C. ELECTRICAL CONDUCTIVITY STUDIES

1. TEMPERATURE DEPENDENCE

D.C. electrical conductivity measurements were made in air over the

temperature range from 25 to 1200°C. Previous studies on $(La, Sr)CrO_3$ (12) and $(La, Sr)MnO_3$ (10) have shown that they have intrinsic p-type conductivity due to the formation of cation vacancies with charge being carried by holes via the small polaron mechanism.

For the small polaron mechanism, the electrical conductivity (13), can be expressed as;

$$\sigma = (C/T) \exp (-E/kT) \text{ ----- (1)}$$

where C is both a charge carrier concentration and material constant, T is the absolute temperature, E is the activation energy, and k is Boltzmann's constant. Therefore, for materials which obey the small polaron mechanism, a plot of $\log (\sigma T)$ versus $1/T$ gives a straight line whose slope is proportional to the activation energy.

The electrical conductivity data for $LaCr_{1-x}Mn_xO_3$ and $La_{0.9}Sr_{0.1}Cr_{1-x}Mn_xO_3$ are shown in Figures 5 and 6, respectively, as $\log (\sigma)$ versus reciprocal temperature. (dotted lines are taken from Ref. 14 for $x=0.0$ and Ref. 10 for $x=1.0$) The data were similar in both systems with an order of magnitude drop in the conductivity when a small amount of Mn was substituted for Cr. The electrical conductivity values lie between those of $LaCrO_3$ and $LaMnO_3$ when about 40% Cr was substituted by Mn in $LaCr_{1-x}Mn_xO_3$. Figures 7 and 8 are typical Arrhenius plots of $\log (\sigma T)$ versus reciprocal temperature. These plots are in excellent agreement with the linear behavior predicted by Eq.1. The activation energies for motion of charge carriers determined from Figures 7 and 8 are plotted in Figure 9 as a function of Mn content. The activation energy increased with Mn content to a maximum at 20% Mn (conductivity is minimum) and then decreased to its original value as the Mn content was increased to above 30%. The activation energies for conduction in $LaCr_{1-x}Mn_xO_3$ were calculated to be 0.48, 0.34, 0.27, 0.21 eV for $x=0.2$, $x=0.3$, $x=0.4$ and $x=0.6$, respectively. Additional Sr content beyond 10% did not significantly alter the activation energies.

Seebeck measurements were made to determine the type and concentration of charge carriers. Figures 10 and 11 are the Seebeck coefficients versus temperature for $LaCr_{1-x}Mn_xO_3$ and $La_{0.9}Sr_{0.1}Cr_{1-x}Mn_xO_3$. In both systems, the substitution of Mn for Cr significantly decreased the Seebeck coefficients. A substitution of 20% Mn for Cr in both systems changed the temperature dependence to a nonlinear behavior. As the Mn substitution for Cr was increased further, the Seebeck coefficients exhibited a temperature independent behavior, indicating that the carrier mobility, rather than the carrier concentration, was thermally activated. According to the Heikes formula this type of behavior indicates a small polaron conduction mechanism which agrees with the electrical conductivity measurements. Using the assumption that only one electron is allowed on a given site and both spin and orbital degeneracy are negligible yields an expression for the Seebeck coefficient (15);

$$Q = (k/e) \{ \ln ((1-x) / x) + S^* / k \} \text{ ----- (2)}$$

where k is Boltzmann's constant, e is the unit charge, x is the fraction of hopping sites which are occupied and S^* is the vibrational entropy associated with the ions surrounding a polaron on a given site. This equation leads to a temperature independent Seebeck coefficient. Usually, the entropy S^* is small enough to be negligible, therefore, the Seebeck coefficient depends only on the concentration term. Using the Seebeck data and Heikes formula, the fraction of hopping sites at 1000°C were calculated as a function of Mn content (Figure 12). As can be seen the occupied fraction of hopping sites increased as Mn content increased, indicating that conduction was taking place in the partially filled Mn^{3+} conduction band. If this was not the case, an increase in conductivity should be expected as Mn content increased. This supposition is supported from the results obtained from the activation energy variation as a function of Mn content (Figure 9). It has been shown that the activation energy for hopping polarons is inversely proportional to the separation distance between polaron sites (16). At low Mn content, the activation energy increased as a result of the large separation between Mn ions. When the Mn content increased the activation energy decreased due to the decrease in separation distance between Mn ions. The observed weak temperature dependence of the Seebeck coefficient implies that the carrier concentration is not a strong function of temperature. Therefore, the temperature dependence of electrical conductivity would be largely dependent on the mobility of charge carriers. Additional Sr substitution for La in $LaCr_{1-x}Mn_xO_3$ compounds did not alter either the temperature dependence or the Seebeck coefficients of these compounds. However, according to the concept of controlled valence theory, the increase of acceptor concentration in p-type materials will create increased charge carrier concentration. Seebeck coefficients measured in the high temperature region for Sr-doped compounds were found to be close to those of undoped ones. It may be concluded that additional Sr substitution for La in the Mn doped compounds does not create additional charge carriers as expected from the theory. Therefore, the electrical conductivity of these perovskite-type oxides is dominated by the mobility rather than the carrier concentration.

2.OXYGEN ACTIVITY DEPENDENCE

The d.c. electrical conductivity measurements for $LaCr_{0.4}Mn_{0.6}O_3$, $La_{0.9}Sr_{0.1}Cr_{0.4}Mn_{0.6}O_3$ and $La_{0.9}Sr_{0.1}Cr_{0.6}Mn_{0.4}O_3$ were made as a function of oxygen activity at 1000°C . The results are shown in Figure 13. In Figure 13, $La_{0.9}Sr_{0.1}MnO_3$ and $LaCr_{0.95}Mg_{0.05}O_3$ data are included for comparison. They are taken from Ref.10 and Ref.14, respectively. Seebeck measurements were also made as a function of oxygen activity at 1000°C for some compositions. It was found that the Seebeck coefficients were always positive even after the compounds decomposed. At 1000°C with decreasing oxygen activity, the Seebeck coefficients increased to a maximum then started decreasing as a result of structural decomposition. The critical oxygen activity for compounds were observed to be close to those for $LaMnO_3$ (About 10^{-15} atm. at 1000°C). An initial drop in the electrical conductivity of compounds was observed as oxygen activity was decreased. This must be due to the reduction in the number of

charge carriers as oxygen vacancies were introduced. This was confirmed by the oxygen activity dependence of the Seebeck coefficient at 1000°C. Figure 14 shows the experimental evidence of such a relationship between conductivity and Seebeck coefficient for $La_{0.9}Sr_{0.1}Cr_{0.6}Mn_{0.4}O_3$. As can be seen in Figure 14, the Seebeck coefficient increased and the electrical conductivity decreased with decreasing oxygen activity. This was true until decomposition occurred.

3. MOBILITY OF CHARGE CARRIERS

The mobility of charge carriers can be determined by combining the Seebeck and electrical conductivity data. Since the Seebeck coefficients were positive, the electrical conductivity is assumed to be due to holes only. The electrical conductivity for holes is given by;

$$\sigma = (A_v/V_M)pe\mu \text{ ----- (3)}$$

where A_v is Avogadro number, V_M is the molar volume, p is the molar fraction of holes, e is the unit charge and μ is the hole mobility. The Seebeck coefficient for holes can be represented by;

$$Q = (k/e) \{ \ln (N_v V_M / A_v p) \} \text{ ----- (4)}$$

where k is Boltzmann constant and N_v is the density of states. Assuming that S^* is negligible, combining Eq. 3 and 4 and rearranging yields a mobility term;

$$\mu = (\sigma / N_v e) \exp (Qe/k) \text{ ----- (5)}$$

Using the information obtained from a structural refinement procedure (Table I), the density of states was calculated for each composition. Using these values for the density of states and the experimental data, the mobility of charge carriers for compounds were calculated from Eq. 5 as function of temperature and Mn content. The results from these calculations are shown in Figures 15 and 16. The mobilities of charge carriers are tabulated in Table III. These results indicate that the mobility was significantly decreased by Mn substitution for Cr and increased by the substitution of Sr for La. Electrical conductivity and Seebeck results indicate that the electrical conductivity in these compounds ($La,Sr)(Cr,Mn)O_3$ is dominated by the mobility of charge carriers rather than by the carrier concentration.

Note that the mobility of charge carriers for these perovskites are only approximate, since the Heikes formula which assumed that both spin and orbital degeneracy were negligible was involved in the calculation. The real situation may be more complicated than that described by Heikes formula. However, these small mobility values are consistent with the criteria given by Goodenough (17). For the small polaron mechanism, the mobility can be expressed as;

$$\mu = (A/T) \exp(-W_H/kT) \text{ ----- (6)}$$

where A is the pre-exponential factor depending on the fraction of hopping sites, T is the absolute temperature, k is the Boltzmann constant and W_H is the activation energy for hopping. A straight line is expected in a $\ln(\mu T)$ versus reciprocal temperature plot if conduction obeys the small polaron mechanism. Figures 17 and 18 show the data for compounds plotted according to Eq. 6. Using these plots, the activation energy for carrier hopping in $(LaCr_{1-x}Mn_xO_3)$ were calculated as 0.63, 0.30 and 0.21 eV for $x=0.2$, $x=0.4$, $x=0.6$, respectively. From the Seebeck and conductivity data, it can be concluded that carrier mobility rather than the carrier concentration is thermally activated, and the activation energies for hopping obtained from the mobility data increases with Mn content, rises to maximum where the mobility is minimum, and then decreases back to its original value as Mn content increased above 30%. This behavior was similar to that observed from the electrical conductivity data. Note that within the accuracy of the measurements these activation energies for hopping are the same as those calculated from the electrical conductivity which is given in Figure 9. Data obtained from both mobility and electrical conductivity data is shown in Figure 19 for comparison.

IV. CONCLUSION

The $LaCrO_3$ - $LaMnO_3$ system forms a solid solution. A single orthorhombic phase was found for substitution of less than 55% Mn for Cr, a single rhombohedral phase existed for substitution of greater than 60% Mn for Cr, and a mixture of two phases for the intermediate compositions. Lattice parameters were shown to vary smoothly as a function of substitution. Mn substitution for Cr significantly improved the sinterability. Densities above 95% TD were achieved at 1475°C for the composition $La_{0.9}Sr_{0.1}Cr_{0.3}Mn_{0.7}O_3$. The electrical conductivity and Seebeck data were interpreted by a small polaron mechanism. The carrier mobility rather than carrier concentration is thermally activated. Electronic conduction occurs in the Mn^{3+} conduction band when there is as much as 20% Mn substitution for Cr. Substitution of Mn for Cr significantly decreased the carrier mobility. Additional Sr substitution for La did not result in an increase in the carrier concentration, but in the carrier mobility of the resulting ceramics.

ACKNOWLEDGEMENT

The authors wish to gratefully acknowledge the technical assistance of George Carini on the electrical conductivity measurements. This research was sponsored by the Department of Energy, Basic Science Division.

REFERENCES

1. S. Rainer, "Méthod for Preparation of an Electronically Conducting Oxidic Material Free of Noble Metals for Applications at High Temperatures and in a Broad Oxygen Partial Pressure Domain" , German Patent No: 2824408, May 1982.
2. S. Isaacs, Symposium Proceedings Fuel Cells Technology and Application. November 16-18, 1981.
3. K. Kamata, T. Nakajima, T. Nakamura, "Electrical Conductivities of $LaMnO_3$ and $SmMnO_3$ ", *Yogyo-Kyokai-Shi* 11, 63-64, 1980.
4. T. Nakamura, G. Petzow, L.J. Gauckler, "Stability of the Perovskite Phase $LaBO_3$ (B = V,Cr,Mn,Fe,Co,Ni) in Reducing Atmosphere", *Mat. Res. Bull.* Vol. 14, pp. 649-659, 1979.
5. W. Baukal, W. Kuhn, H. Kleinschmager, F. J. Rohr, *Power Sources*, Vol. 1., pp. 203, 1976-77.
6. M. Pechini, U.S.A Patent No: 3330697, July 1967.
7. H. M. Rietveld, "A Profile Refinement Method for Nuclear and Magnetic Structures", *J. Appl. Cryst.* 2, pp. 64-71, 1969.
8. D. B. Wiles and R. A. Young, "A New Computer Program for Rietveld Analysis of X-Ray Powder Diffraction Patterns", *J. Appl. Cryst.* 14, pp. 149-151, 1981.
9. C.P.Khattak and D.E.Cox, "Structural Studies of the Lanthanum Chromite", *Mat. Res. Bull.* Vol. 12, pp. 463-472, 1977.
10. J.H.Kuo, Ph.D. Thesis, University of Missouri-Rolla, 1987.
11. W.D. Kingery, H.K. Bowen, D.R. Uhlmann, "Introduction to Ceramics", Second Ed., New York, John Wiley & Sons, 1976.
12. D.P.Karim and A.T.Aldred, "Localized Level Hopping Transport in $La(Sr)CrO_3$ ", *Phys. Rev. B.* 20, 6, pp. 2255-63, 1979.
13. J.P.Goodenough, "Localized vs. Collective d Electrons and Neel Temperatures", *Phys. Rev.*, 164, 785, 1967.
14. B. K. Flandermeyer, Ph.D. Thesis, University of Missouri-Rolla, 1984.
15. A. F. Joffe, "Physics of Semiconductors", Academic Press, New York, 1960.
16. J.B. Webb, M. Sayer, and A. Mansingh, "Polaronic Conduction in Lanthanum Strontium Chromite.", *Can. J. Phys.*, 55, 1725, 1977.
17. J. B. Goodenough, "Metallic Oxides ", *Prog. in Solid State Chem.*, 5, 238, 1971.
18. G. Carini, M.S. Thesis, University of Missouri-Rolla, 1988.

TABLE I

LATTICE PARAMETERS OF COMPOSITIONS IN THE SYSTEM LaCrO_3 - LaMnO_3 CALCULATED FROM RIETVELD PROGRAM

Composition	a (Å)	b (Å)	c (Å)	Angle °	Structure	Theoretical Density g/cc
LaCrO_3	5.5206 (4)	5.4861 (4)	7.7742 (8)		Orthorhom.	6.74
$\text{LaCr}_{.7}\text{Mn}_{.3}$	5.5153 (7)	5.4808 (7)	7.7674 (14)		" "	6.78
$\text{La}_{.89}\text{Sr}_{.1}\text{Cr}_{.7}\text{Mn}_{.3}$	5.5150 (5)	5.4782 (5)	7.7708 (9)		" "	6.62
$\text{LaCr}_{.6}\text{Mn}_{.4}$	5.5176 (6)	5.4800 (7)	7.7830 (11)		" "	6.78
$\text{LaCr}_{.5}\text{Mn}_{.5}$	5.5229 (2)	5.4806 (2)	7.7657 (3)		" "	6.79
$\text{La}_{.89}\text{Sr}_{.1}\text{Cr}_{.5}\text{Mn}_{.5}$	5.5153 (6)	5.4700 (6)	7.7885 (12)		" "	6.62
$\text{LaCr}_{.45}\text{Mn}_{.55}$	5.5235 (4)	5.4821 (4)	7.7687 (7)		44 %orth +	6.79
$\text{LaCr}_{.45}\text{Mn}_{.55}$	5.4655 (1)	-	-	60.6850(34)	56 %Rhom.	6.82
$\text{LaCr}_{.4}\text{Mn}_{.6}$	5.5251 (6)	5.4852 (5)	7.7770 (10)		43 %orth +	6.78
$\text{LaCr}_{.4}\text{Mn}_{.6}$	5.4653 (8)	-	-	60.6840(19)	57 %Rhom.	6.82
$\text{LaCr}_{.3}\text{Mn}_{.7}$	5.4628 (4)	-	-	60.6834(8)	Rhombohed.	6.83
$\text{La}_{.89}\text{Sr}_{.1}\text{Cr}_{.3}\text{Mn}_{.7}$	5.4680 (1)	-	-	60.5876(17)	" "	6.67
$\text{LaCr}_{.2}\text{Mn}_{.8}$	5.4704 (1)	-	-	60.6375(20)	" "	6.83
$\text{LaCr}_{.1}\text{Mn}_{.9}$	5.4679 (1)	-	-	60.5821(21)	" "	6.85
LaMnO_3	5.4724 (1)	-	-	60.5829(21)	" "	6.84

* Numbers in parenthesis refer to standard deviation for parameters.

For example; a=5.5206, S.D.=0.0004 shown as a=5.5206 (4)

TABLE II
SINTERING PROPERTIES OF COMPOUNDS

Compound	Sinter.Temp. (°C)	Sinter.Time (Hour)	Green Density (g/cm ³)	Bulk Density (g/cm ³)	% T.D.	% Porosity (open)
La Cr _{0.7} Mn _{0.3} O ₃	1475	11	2.89	4.06	60	39
		24	2.81	4.20	62	34
		48	2.68	4.35	64	33
La .9Sr .1Cr .7Mn .3O ₃	1475	11	3.17	4.51	68	35
		24	3.22	4.54	68.5	29
		48	3.11	4.71	71	26
La Cr _{0.5} Mn _{0.5} O ₃	1475	11	2.73	4.70	69	29
		24	2.74	5.04	74	19
		48	3.02	5.27	77.7	13
La .9Sr .1Cr .5Mn .5O ₃	1475	11	3.15	5.28	80	18
		24	2.93	5.40	81.5	11
		48	3.14	5.55	84	10
La Cr _{0.3} Mn _{0.7} O ₃	1475	11	3.19	6.01	88	1
		24	3.16	6.26	92	1
		48	2.99	6.41	94	1
La .9Sr .1Cr .3Mn .7O ₃	1475	11	3.19	6.08	91	1
		24	3.10	6.27	94	1
		48	2.98	6.35	95.5	1

TABLE III
 AT 1000 °C THE CALCULATED CARRIER MOBILITY FOR
 COMPOUNDS (La,Sr) Cr_{1-x}Mn_xO₃

Compound	Mobility(0% Sr) cm ² /V.sec	Mobility(10% Sr) cm ² /V.sec
X = 0.0	0.07	0.12*
X = 0.2	0.0013	0.0044
X = 0.4	0.0024	0.0048
X = 0.6	0.0072	0.0073
X = 1.0	0.045	0.058**

* From Ref. 15

**From Ref. 10

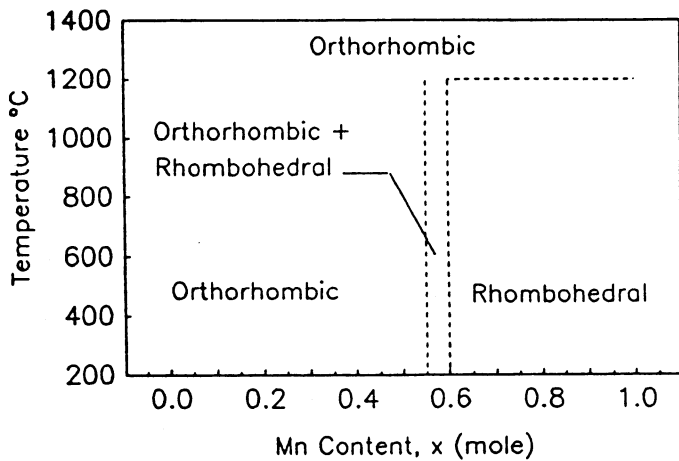


Figure 1. The phase/composition relationship obtained using the refinement procedure.

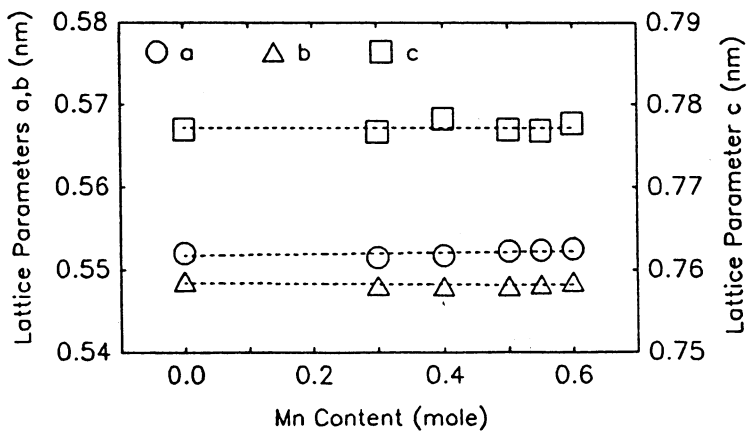


Figure 2. Lattice Parameters in the orthorhombic region.

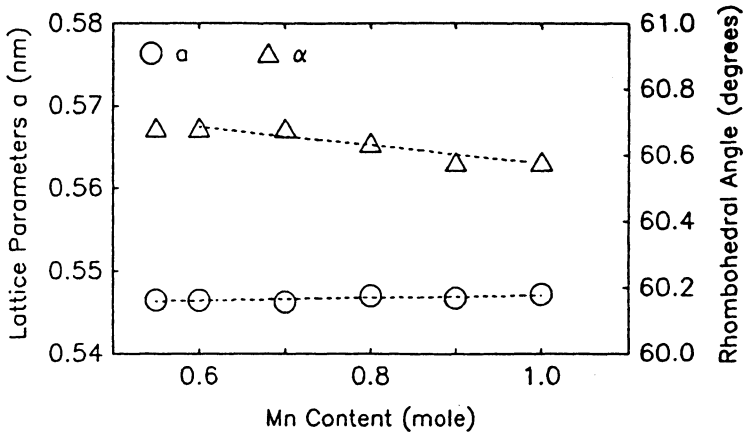


Figure 3. Lattice parameter in the rhombohedral region.

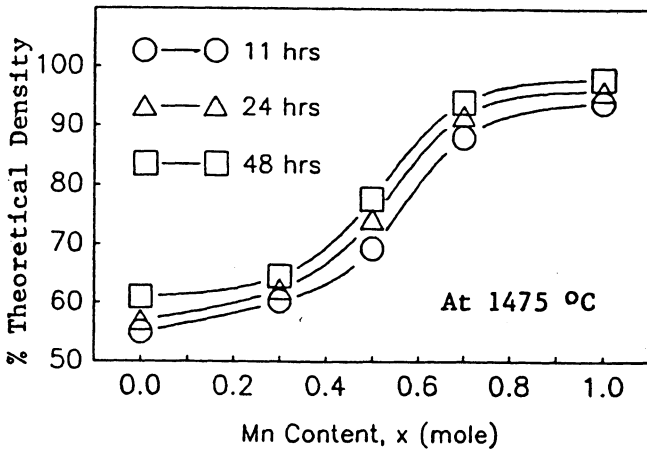


Figure 4. Sintering behavior of the compounds as a function of Mn content.

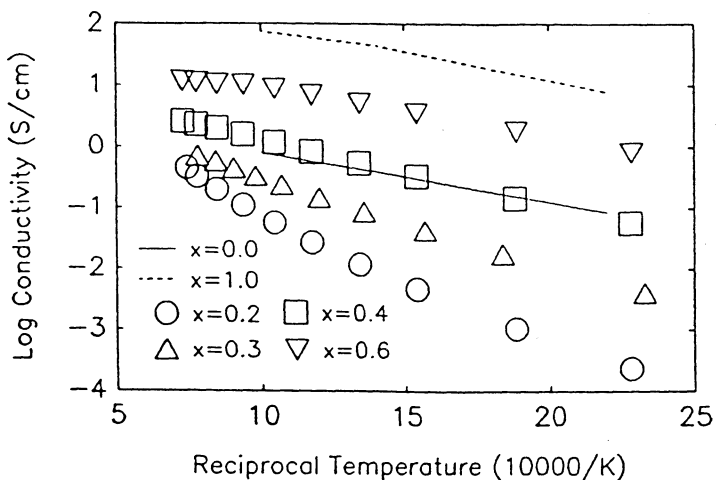


Figure 5. The electrical conductivity of compounds $\text{LaCr}_{1-x}\text{Mn}_x\text{O}_3$ as a function of temperature.

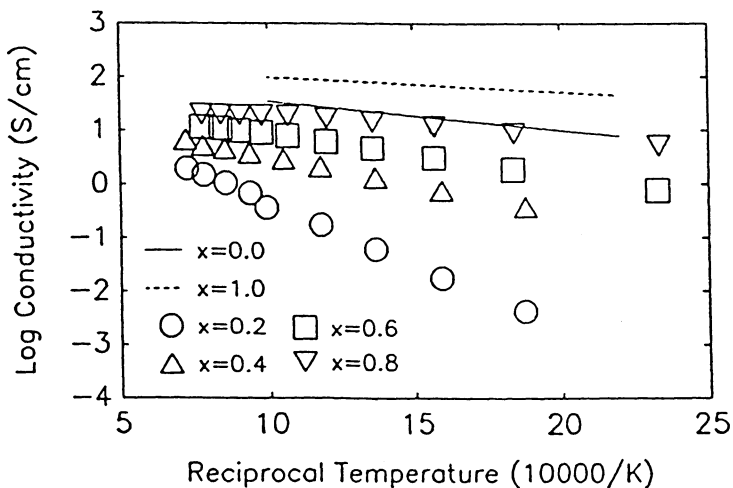


Figure 6. The electrical conductivity of compounds $\text{La}_{0.9}\text{Sr}_{0.1}\text{Cr}_{1-x}\text{Mn}_x\text{O}_3$ as a function of temperature.

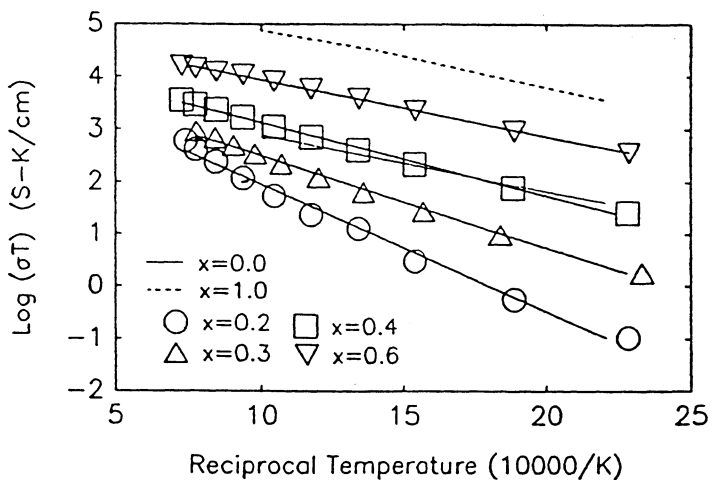


Figure 7. $\text{Log}(\sigma T)$ vs. $1/T$ for compositions $(\text{LaCr}_{1-x}\text{Mn}_x\text{O}_3)$.

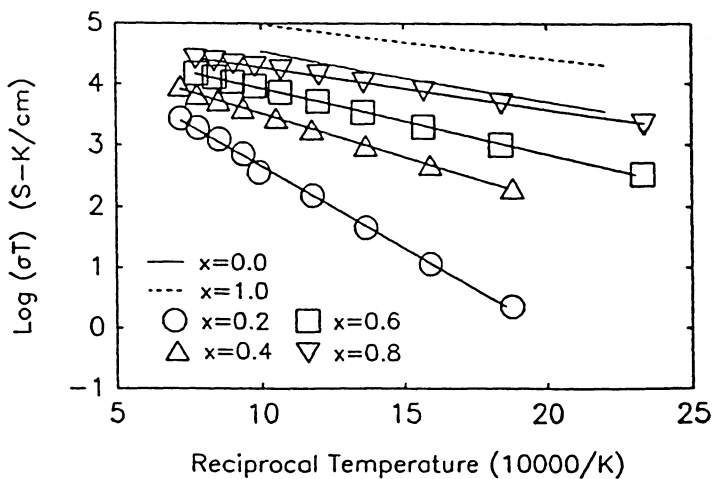


Figure 8. $\text{Log}(\sigma T)$ vs. $1/T$ for compositions $(\text{La}_{0.9}\text{Sr}_{0.1}\text{Cr}_{1-x}\text{Mn}_x\text{O}_3)$.

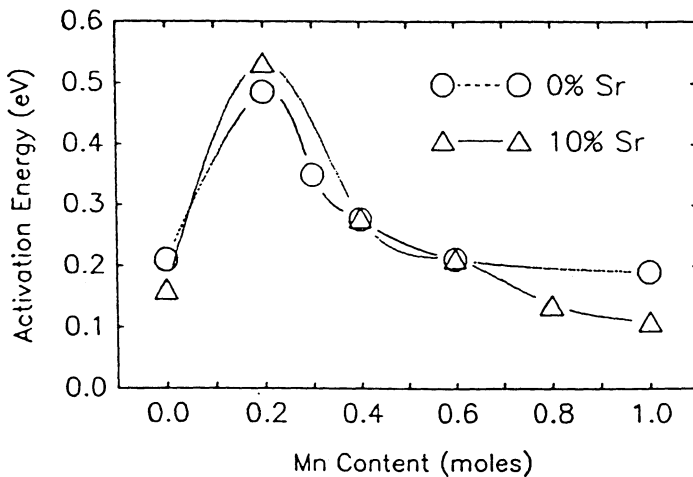


Figure 9. Activation energy for conductivity vs. Mn content ($(\text{La,Sr})\text{Cr}_{1-x}\text{Mn}_x\text{O}_3$ (calculated from conductivity data).

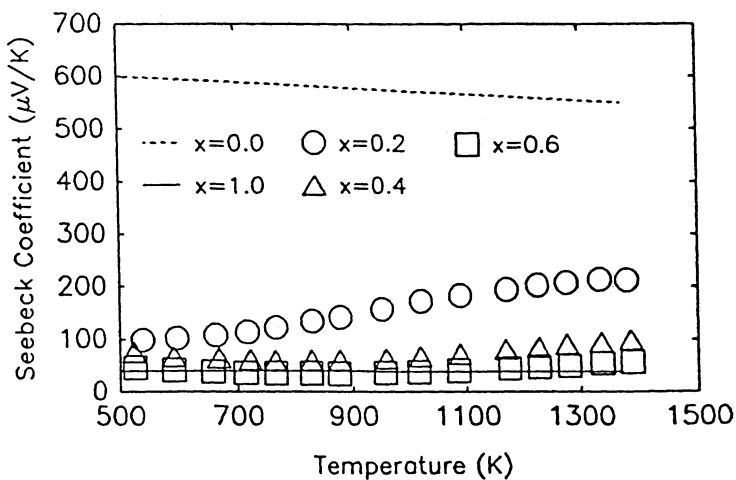


Figure 10. Seebeck coefficient of compounds as a function of temperature ($\text{LaCr}_{1-x}\text{Mn}_x\text{O}_3$).

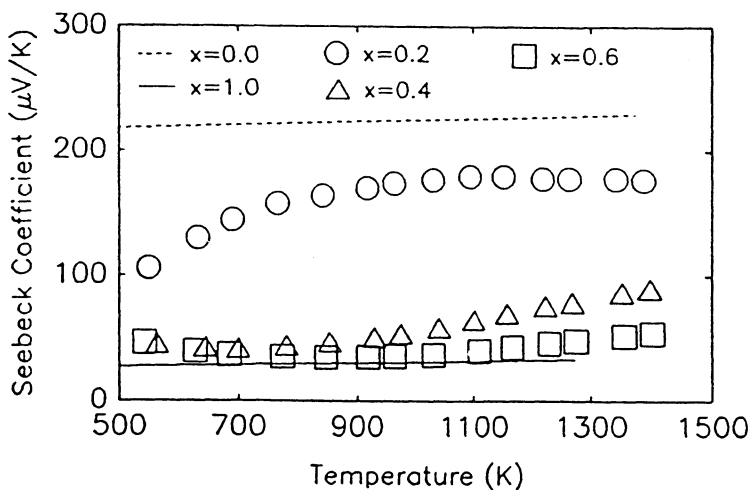


Figure 11. Seebeck coefficient of compounds as a function of temperature ($\text{La}_{0.9}\text{Sr}_{0.1}\text{Cr}_{1-x}\text{Mn}_x\text{O}_3$).

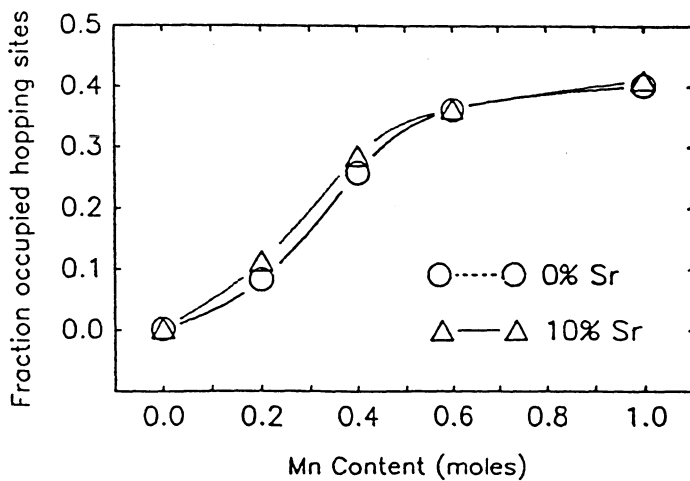


Figure 12. Calculated fraction of hopping sites (occupied) as a function of Mn content at 1000°C ($(\text{La,Sr})\text{Cr}_{1-x}\text{Mn}_x\text{O}_3$).

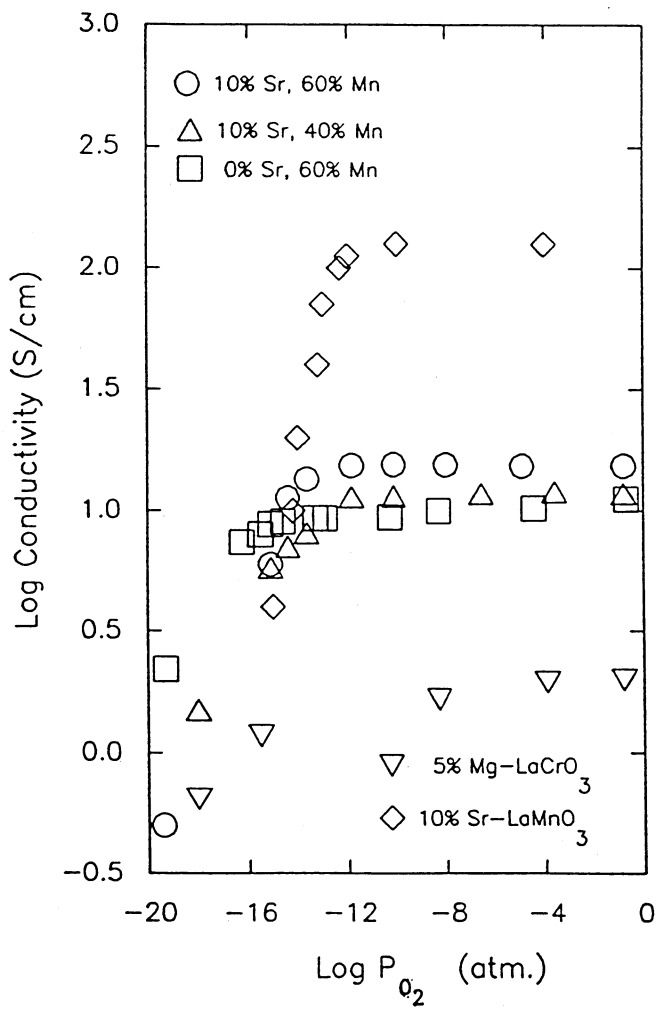


Figure 13. Log Conductivity vs. Log Oxygen activity for compounds at 1000°C.

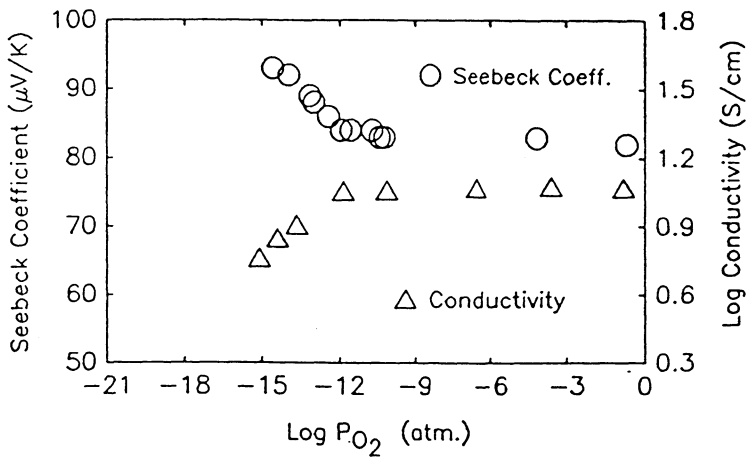


Figure 14. Seebeck coefficient and Log conductivity as a function of oxygen activity for $\text{La}_{0.9}\text{Sr}_{0.1}\text{Cr}_{0.6}\text{Mn}_{0.4}\text{O}_3$ at 1000°C .

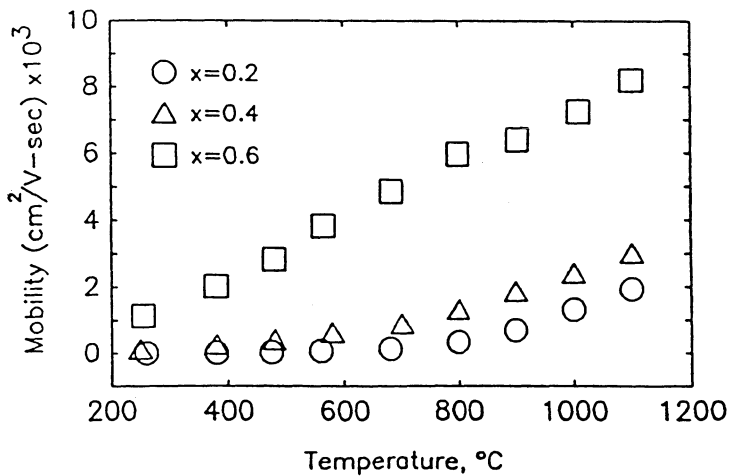


Figure 15. Mobility of compounds as a function of temperature ($\text{LaCr}_{1-x}\text{Mn}_x\text{O}_3$).

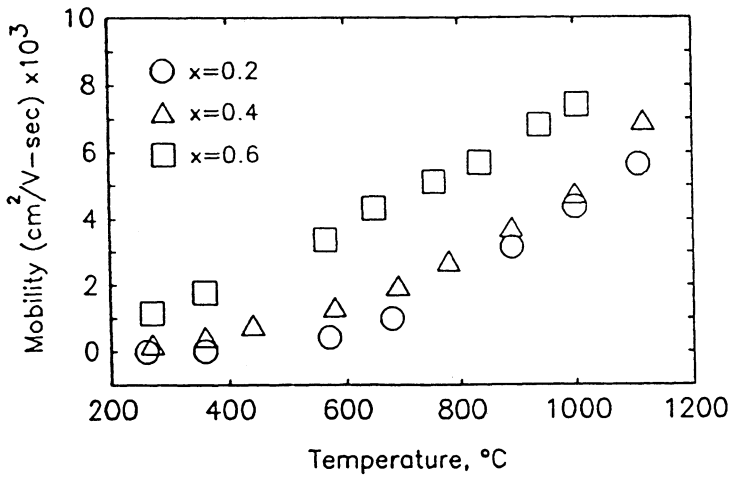


Figure 16. Mobility of compounds as a function of temperature ($\text{La}_{0.9}\text{Sr}_{0.1}\text{Cr}_{1-x}\text{Mn}_x\text{O}_3$).

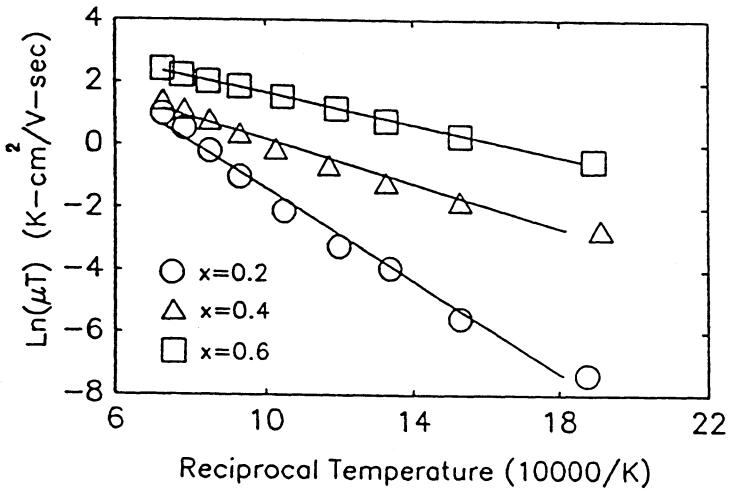


Figure 17. $\text{Ln}(\mu T)$ vs. reciprocal temperature for $\text{LaCr}_{1-x}\text{Mn}_x\text{O}_3$.

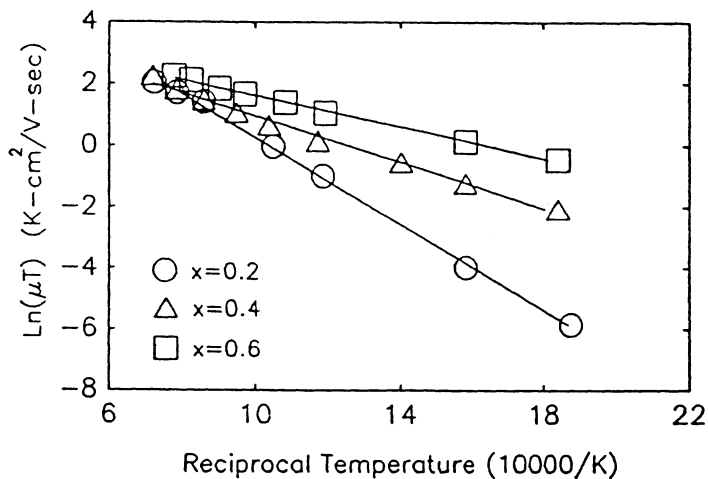


Figure 18. $\ln(\mu T)$ vs. reciprocal temperature for $\text{La}_{0.9}\text{Sr}_{0.1}\text{Cr}_{1-x}\text{Mn}_x\text{O}_3$.

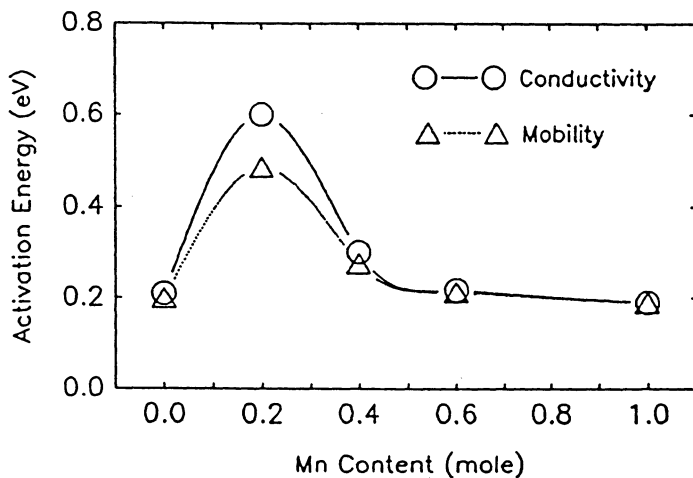


Figure 19. Activation energy for compounds as a function of Mn content ($\text{LaCr}_{1-x}\text{Mn}_x\text{O}_3$). (Calculated from both mobility and conductivity data).

STABILITY OF PEROVSKITE OXIDE ELECTRODE
WITH STABILIZED ZIRCONIA

O. Yamamoto, Y. Takeda, R. Kanno and T. Kojima
Department of Chemistry, Faculty of Engineering
Mie University
Tsu, 514 Japan

ABSTRACT

High temperature interactions between yttria-stabilized zirconia and lanthanum manganite, which are the prime candidates for the electrolyte and the air electrode material for solid oxide fuel cells, respectively, have been investigated. The pellets prepared by pressing a powder mixture of ZrO_2 with 8 mole % Y_2O_3 (8YSZ) and $(La,Sr)_{1-x}MnO_3$ were allowed to react in open air at 1200-1350 °C and analyzed by X-ray diffraction to examine the reaction products. At 1200 °C, stoichiometric $LaMnO_3$ reacted with 8YSZ and produced $La_2Zr_2O_7$ with the reaction time of 24h. On the other hand, no reaction product was observed for the mixture of La deficient $La_{0.8}MnO_3$ and 8YSZ for 192h at 1200 °C. At a much higher temperature of 1300 °C, $La_2Zr_2O_7$ was observed in all the mixtures of $(La,Sr)_{1-x}MnO_3$ ($x=0-0.2$) and 8YSZ for 50h, but the reaction kinetics for the La deficient $La_{1-x}MnO_3$ and 8YSZ was slower.

1. INTRODUCTION

High temperature solid oxide fuel cells (SOFC) have exceptional potential for electric power generation because of the simplicity of system design and the availability of high quality by-product heat. However, there are many material problems remaining to be solved to obtain a high performance fuel cell, arising from the high operating temperature of 1000 °C. The most significant material limitation at present is imposed by the cathode and the cathode leads because of the high corrosion effect of oxygen at working temperature. The complex oxides in the perovskite family have been extensively examined as the cathode for SOFC(1-3). After more than twenty years investigation, the favoured cathode material for SOFC

system with Y_2O_3 stabilized zirconia (YSZ), which is the best candidate as the electrolyte at present stage, is strontium-doped lanthanum manganite $La_{1-x}Sr_xMnO_3$, because of the high electrical conductivity, the good compatibility with YSZ, and the catalytic activity for the dissociation of oxygen molecules (4-5). Although $La_{1-x}Sr_xMnO_3$ is widely used today, cathode materials with improved reactivity with YSZ are still required. In a previous paper (6), the interactions between 8YSZ and the perovskite-type oxides $La_{1-x}Sr_xMO_3$ ($M=Cr, Mn, Fe, Co$) sputtered on it were examined, and the reaction products of $La_2Zr_2O_7$ and Sr_2ZrO_4 were observed for the samples annealed at $1100^\circ C$ for 15h in open air. The cathodic polarization (polarization for oxygen reduction) of the $La_{1-x}Sr_xMO_3$ electrodes in air varied depending on the pre-annealing temperature and period. In the case of the $La_{0.7}Sr_{0.3}MnO_3$ electrode, the overpotential for the oxygen reduction at $800^\circ C$ was not affected significantly with the annealing process at $1000^\circ C$, and increased rapidly with annealing period at the annealing temperature of $1100^\circ C$. Lau and Singhal reported the reactivity of $La_{0.9}Sr_{0.1}MnO_3$ with ZrO_2 -10 mole % Y_2O_3 (10YSZ) (7). At $1000^\circ C$ for 1728 h, a compound $La_2Zr_2O_7$ was observed as minor phase and a quaternary $ZrO_2 \cdot Y_2O_3 \cdot MnO_3 \cdot LaO_y$ solid solution as the major one, and at $1400^\circ C$, $La_2Zr_2O_7$ was found as the major phase. More recently, Dokiya et al. have proposed that reactivity of lanthanum deficient $(La,Sr)_{1-x}MnO_3$ with 8YSZ could be lower compared with that of the stoichiometric $(La,Sr)MnO_3$ with 8YSZ (8). In this study, the reactivity of $(La,Sr)_{1-x}MnO_3$ ($x=0-0.2$) with 8YSZ has been examined in more detail with the help of X-ray diffraction analysis.

2. EXPERIMENTAL

The perovskite-type oxides $(La,Sr)_{1-x}MnO_3$ ($x=0-0.2$) were prepared from La_2O_3 (chemical grade), $SrCO_3$ (chemical grade), and Mn_2O_{3+x} (chemical grade). To avoid water contamination, commercially available La_2O_3 was first heated up to $1000^\circ C$ before quenching to room temperature. The oxygen content of the starting material Mn_2O_{3+x} was determined by chemical method to be 3.01. The mixtures of La_2O_3 , $SrCO_3$ and Mn_2O_{3+x} were ground and fired in open air at $1300^\circ C$ for 12 h. The reaction products were then ground thoroughly. The BET specific surface area was $0.2-0.3 \text{ m}^2/\text{g}$. Yttria-stabilized zirconia containing 8 mole % Y_2O_3 was obtained from Tosoh, Japan. The powder of 8YSZ was heated at $1450^\circ C$ for 3 h before the reactivity study. The BET specific surface area was $0.26 \text{ m}^2/\text{g}$. The specimens for

reactivity studies were prepared by first mixing the 8YSZ and $(\text{La,Sr})_{1-x}\text{MnO}_3$ powders thoroughly and then pressing the powder mixture into 1.2cm diameter pellet under a pressure of 2,500kg/cm². These pellets were allowed to react in air at 1200-1350 °C. After reaction the specimens were analyzed with the help of x-ray diffraction analysis using Rigaku RAD diffractometer to identify the reaction products. The content of $\text{La}_2\text{Zr}_2\text{O}_7$, which was a reaction product, was determined by the intensity ratio of x-ray diffraction lines of the (222) plane of $\text{La}_2\text{Zr}_2\text{O}_7$ and the (111) plane of 8YSZ which correspond to the highest diffraction lines of $\text{La}_2\text{Zr}_2\text{O}_7$ and 8YSZ, respectively. The calibration was determined by the diffraction intensity ratio of the mixtures of 8YSZ and $\text{La}_2\text{Zr}_2\text{O}_7$ powders. A good linearity between the content of $\text{La}_2\text{Zr}_2\text{O}_7$ and the intensity ratio was obtained in the range of 0-30 mole % $\text{La}_2\text{Zr}_2\text{O}_7$. $\text{La}_2\text{Zr}_2\text{O}_7$ was obtained by heating a mixture of La_2O_3 and ZrO_2 in air at 1500°C for 7 h.

The electrical conductivity of $\text{La}_2\text{Zr}_2\text{O}_7$ was measured using a frequency response analyzer (Solartron FRA-1250) over the frequency range 10^{-1} to 6.5×10^4 Hz and the temperature range of 600 to 1000 C with platinum paint electrodes. The pellet of $\text{La}_2\text{Zr}_2\text{O}_7$ with 1.0cm diameter was prepared by pressing under a pressure of 2500kg/cm², and was annealed at 1500 °C for 3 h.

3. RESULTS AND DISCUSSION

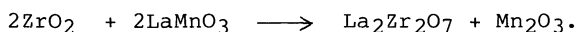
Lanthanum manganite has the perovskite-type structure, which is a modified cubic structure. Stoichiometric LaMnO_3 , prepared from the constituent oxides by firing in N_2 at 1300 °C, is a perovskite with orthorhombic distortion (9). According to Wollan and Koehler (10) and Yakel (11), LaMnO_3 has a monoclinic cell with $a=c=3.99\text{Å}$, $b=3.85\text{Å}$ and $\beta=92.7^\circ$. On addition of CaMnO_3 this monoclinic distortion decreases. The rhombohedral structure has also been found by Harwood(12). In the LaMnO_3 - SrMnO_3 system, the cubic structure was found at lower Mn^{4+} concentration (12% to 19%). At higher Mn^{4+} concentration at first a rhombohedral distortion developed but disappeared at 35-45% Mn^{4+} (13). Our results are shown in Fig. 1. The observed x-ray diffraction lines of the stoichiometric composition LaMnO_3 were indexed by the monoclinic structure. On the other hand, the La-deficient $\text{La}_{1-x}\text{MnO}_3$, where the Mn^{4+} content is increased, was found to be the hexagonal structure with $a=5.539$ and $c=13.353$ for $\text{La}_{0.95}\text{MnO}_3$ and with $a=5.538$ and $c=13.370$ for $\text{La}_{0.90}\text{MnO}_3$. In

order to compare the lattice parameters between monoclinic and hexagonal distortion, the parameters of the hexagonal structure were transformed to those of the rhombohedral structure. As shown in this figure, the unit cell volume decreases with increasing x up to $x=0.10$. Generally, orthoferrite type perovskite LnMO_3 , where Ln and M stand for the lanthanide and transition metals, also shows oxygen nonstoichiometry, which depends on the preparation method, and the structure changes with the content of oxygen. We are presently studying the effect of the oxygen content. $\text{La}_{0.9}\text{Sr}_{0.1}\text{MnO}_3$ and $\text{La}_{0.75}\text{Sr}_{0.1}\text{MnO}_3$ showed the hexagonal structure. The crystal structures and the lattice parameters for $(\text{La,Sr})_{1-x}\text{MnO}_3$ are summarized in Table I.

The reactivity tests of the $\text{La}_{1-x}\text{MnO}_3$ ($x=0, 0.05, 0.10, 0.15, 0.20$) with 8YSZ and the $\text{La}_{0.9-x}\text{Sr}_{0.1}\text{MnO}_3$ ($x=0, 0.15$) with 8YSZ were carried out at 1200, 1250, 1300 and 1350 °C with various reaction times. The typical results at 1200 and 1300 °C are shown in Fig. 2 and Fig. 3, respectively. The observed phases after reactivity tests were $\text{La}_2\text{Zr}_2\text{O}_7$ and a solid solution of YSZ and La_2O_3 and / or MnO_x which was confirmed by the change in the lattice parameter of YSZ. At 1200 °C, the stoichiometric LaMnO_3 reacted with 8YSZ to produce $\text{La}_2\text{Zr}_2\text{O}_7$ with reaction time of 24 h. The amount of the reaction product $\text{La}_2\text{Zr}_2\text{O}_7$ increases with the reaction time. In the cases of $\text{La}_{0.85}\text{MnO}_3$ and $\text{La}_{0.80}\text{MnO}_3$, $\text{La}_2\text{Zr}_2\text{O}_7$ was not observed with reaction time of 192 h. Strontium-doped lanthanum manganite, $\text{La}_{0.9}\text{Sr}_{0.1}\text{MnO}_3$, also reacts with 8YSZ to produce $\text{La}_2\text{Zr}_2\text{O}_7$. However, the amount of the reaction product $\text{La}_2\text{Zr}_2\text{O}_7$ with the same reaction time was diminished with the substitution of Sr for La. At a much higher temperature of 1300 °C, about 4 mole % of $\text{La}_2\text{Zr}_2\text{O}_7$ was observed with the reaction time of 24 h for the couple LaMnO_3 and 8YSZ, the amount of which is around two times larger than that at 1200 °C. In the case of the couple $\text{La}_{0.8}\text{MnO}_3$ and 8YSZ, no reaction product was found with the reaction time of 48 h. After 72 h, about 0.7 mole % of $\text{La}_2\text{Zr}_2\text{O}_7$ is observed, and the amount of it increases with further reaction time.

The lattice parameter of the cubic zirconia 8YSZ heated with LaMnO_3 at 1300 °C for 24 h, changed to 5.144Å from the original 5.134Å and with further reaction time no change in the parameter was found. The lattice parameter of the system 10YSZ and $\text{La}_{0.9}\text{Sr}_{0.1}\text{MnO}_3$ at 1400 °C was found by Lau and Singhal to be in the range of 5.1540Å (145h) to 5.1545Å (1098h) (7). The original lattice parameter of 10YSZ is 5.1444Å. The insertion of La ions into the cubic ZrO_2 lattice was found to have a net effect of

expanding the lattice. On the other hand, the lattice parameters of 8YSZ with $\text{La}_{0.85}\text{MnO}_3$ and $\text{La}_{0.8}\text{MnO}_3$ heated at 1300°C were observed to be in the range of 5.137Å (24 h) and 5.141Å (192h). The solid solution formation rate of 8YSZ with the La deficient $\text{La}_{1-x}\text{MnO}_3$ is lower than that with the stoichiometric LaMnO_3 . From our and Lau's results, we could assume that $\text{La}_{1-x}\text{MnO}_3$ reacts with the cubic zirconia to produce the solid solution and then the solid solution reacts with $\text{La}_{1-x}\text{MnO}_3$ to produce $\text{La}_2\text{Zr}_2\text{O}_7$ according to the following reaction ;



The continuous solid-state reaction proceeds by the diffusion of ions through the reaction products. In this case, the rate determining process may be the diffusion of La^{3+} or Zr^{4+} through $\text{La}_2\text{Zr}_2\text{O}_7$. The solid state reaction kinetics with diffusion control in the ideal condition obeys the following parabolic growth law ;

$$x^2 = 2\bar{k}t,$$

where x is the thickness of the reaction product layer, t the reaction time and k the practical reaction rate constant. The mole fraction of $\text{La}_2\text{Zr}_2\text{O}_7$ vs. $t^{1/2}$ curves at 1250°C and 1350°C are shown in Fig. 4 and Fig. 5, respectively. LaMnO_3 and $\text{La}_{0.9}\text{Sr}_{0.1}\text{MnO}_3$ show a good linearity, and $\text{La}_{0.9}\text{MnO}_3$ and $\text{La}_{0.8}\text{MnO}_3$ also show a good linearity after an induction period. From the slopes of these curves, \bar{k} at various temperatures were calculated. The temperature dependences of \bar{k} are shown in Fig. 6. The activation energy calculated from $\log \bar{k}$ vs. $1/T$ curves could be attributed to the activation energy for diffusion of the rate determining mobile ion(13). As shown in Fig. 6, the slopes are almost the same for all the systems $(\text{La,Sr})_{1-x}\text{MnO}_3$. The activation energy is calculated to be about 25 KJ/mole. This activation energy may correspond to that for the diffusion of La^{3+} or Zr^{4+} in $\text{La}_2\text{Zr}_2\text{O}_7$. We cannot directly compare this value with any other reported value, because no diffusion data in $\text{La}_2\text{Zr}_2\text{O}_7$ is available; however, in similar systems such as Zr^{4+} in $(\text{Zr,Ca})\text{O}_2$, the activation energy is also about 25 KJ/mole (14). The difference in reaction activity between the stoichiometric LaMnO_3 and the La-deficient $\text{La}_{0.8}\text{MnO}_3$, especially in the initial stages, may be explained by the slow diffusion of La and Mn ions in $\text{La}_{0.8}\text{MnO}_3$ than that in LaMnO_3 . Lau and Singhal reported that Mn and La diffused from $\text{La}_{0.9}\text{Sr}_{0.1}\text{MnO}_3$ into ZrO_2 (Y_2O_3) whereas the diffusion of Zr and Y into $\text{La}_{0.9}\text{Sr}_{0.1}\text{MnO}_3$ was found to be negligible. The

slow diffusion of La and Mn ions in $\text{La}_{0.8}\text{MnO}_3$ could be explained by the much denser structure of $\text{La}_{0.8}\text{MnO}_3$ than that of LaMnO_3 as shown in Fig. 1.

In a previous paper, we reported that the cathodic overpotential for the sputtered $\text{La}_{1-x}\text{Sr}_x\text{MO}_3$ ($\text{M}=\text{Cr}, \text{Mn}, \text{Fe}, \text{Co}$) as oxygen electrode increased with the annealing period at 1000°C or higher (6). This decline in the electrode performance can be explained by the chemical reaction of 8YSZ and $\text{La}_{1-x}\text{Sr}_x\text{MO}_3$. In Fig 7, the electrical conductivity of the main reaction product $\text{La}_2\text{Zr}_2\text{O}_7$ is shown. The conductivity is about two and a half orders of magnitude lower than that of 8YSZ. The charge carrier in $\text{La}_2\text{Zr}_2\text{O}_7$ may be oxide ions similar to that in the pyrochlore-type structure $\text{Gd}_2\text{Zr}_2\text{O}_7$ (15). The high cathodic polarization of the $\text{La}_{1-x}\text{Sr}_x\text{MnO}_3$ electrode pre-annealed at 1000°C or higher could be explained by the formation of the low conductivity phase $\text{La}_2\text{Zr}_2\text{O}_7$.

4. CONCLUSIONS

From the reactivity studies of the pellets of the mixture of $(\text{La}, \text{Sr})_{1-x}\text{MnO}_3$ and cubic zirconia with 8 mole % Y_2O_3 , it can be concluded that $(\text{La}, \text{Sr})_{1-x}\text{MnO}_3$ reacts with zirconia to form a solid solution of the cubic zirconia with La_2O_3 and/or MnO_x and then the solid solution reacts with $(\text{La}, \text{Sr})_{1-x}\text{MnO}_3$ to form compound $\text{La}_2\text{Zr}_2\text{O}_7$. The reaction kinetics is dependent on the $(\text{La}+\text{Sr})/\text{Mn}$ ratio, and the La deficient lanthanum manganite is less reactive than the stoichiometric one. For practical application as the cathode material of SOFC, $(\text{La}, \text{Sr})_{1-x}\text{MnO}_3$ ($x=0.1-0.2$) is the most suitable electrode material, because of its chemical stability with YSZ and high electrical conductivity.

REFERENCES

1. C. S. Tedmon, Jr., H. S. Spacil and S. P. Mitoff, J. Electrochem. Soc., 116, 1170 (1969).
2. R. Steiner, F. J. Rohr and W. Fischer, in 4th Proc. Int. Symp. Fuel Cells (Antwerpen, 1972).

3. A. O. Isenberg, National Fuel cell Seminar Abst. (Newport Beach, 1982) pp. 154.
4. W. Feduska and A. O. Isenberg, J. Power Sources, 10, 89 (1983)
5. D. C. Fee et al. in 1986 Fuel cell seminar Abs., Tucson, U. S. A. (1986) p40.
6. O. Yamamoto, Y. Takeda, R. Kanno and M. Noda, Solid State Ionics, 22, 241 (1987).
7. S. K. Lau and S. C. Singhal, Proc. Corrosion 85, Boston, March (1985).
8. M. Dokiya, H. Yokogawa, T. Kawada, N. Sakai, T. Iwata and M. Mori, Proc. IECEC 89, Washington D, C, (1989).
9. A. Wold and R. J. Amott, J. Phys. Chem. Solids, 9, 176 (1959).
10. E. O. Wollan and W. C. Koehler, Phys Rev., 100, 545 (1955).
11. H. L. Yorkel, Acta Cryst., 8, 394 (1955).
12. M. G. Harwood, Proc. Phys. Soc., 68B, 586 (1955).
13. H. Schmalzried, Angeus, Chem. Int. Ed., 2, 251 (1963).
14. W. H. Rhodes, R. E. Carter, J. Am. Ceram. Soc., 49, 244 (1966).
15. P. K. Moon and H. L. Tuller, Solid State Ionics, 28/30, 470 (1988).

Table I Crystal structures and lattice parameters
of $(\text{La,Sr})_{1-x}\text{MnO}_3$.

Compound	Crystal structure	lattice parameter			β
		a	b	c	
LaMnO_3	monoclinic	3.888 (2)	3.894 (2)	3.909 (3)	90.64 (6)
$\text{La}_{0.95}\text{MnO}_3$	hexgonal	5.599 (8)		13.354 (3)	
$\text{La}_{0.9}\text{MnO}_3$	hexgonal	5.539 (7)		13.370 (2)	
$\text{La}_{0.85}\text{MnO}_3$	hexgonal	5.539 (7)		13.370 (2)	
$\text{La}_{0.8}\text{MnO}_3$	hexgonal	5.539 (5)		13.369 (2)	
$\text{La}_{0.9}\text{Sr}_{0.1}\text{MnO}_3$	hexgonal	5.533 (1)		13.362 (2)	
$\text{La}_{0.75}\text{Sr}_{0.1}\text{MnO}_3$	hexgonal	5.538 (1)		13.375 (2)	

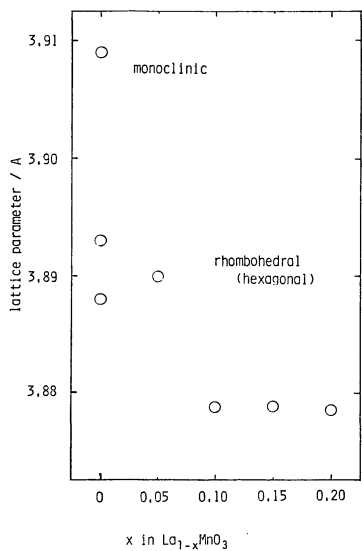


Fig.1 Lattice parameters vs x in $\text{La}_{1-x}\text{MnO}_3$.

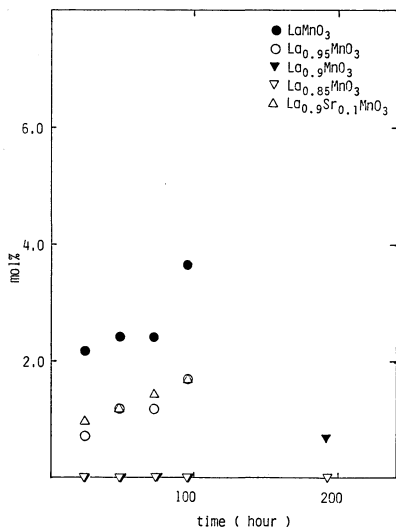


Fig.2 Mole fraction of $\text{La}_2\text{Zr}_2\text{O}_7$ produced in the $\text{La}_{1-x}\text{MnO}_3$ and 8YSZ interface at 1200°C .

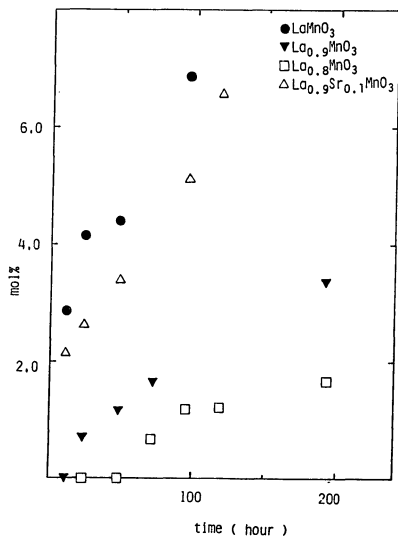


Fig.3 Mole fraction of $\text{La}_2\text{Zr}_2\text{O}_7$ produced in the $\text{La}_{1-x}\text{MnO}_3$ and 8YSZ interface at 1300 °C.

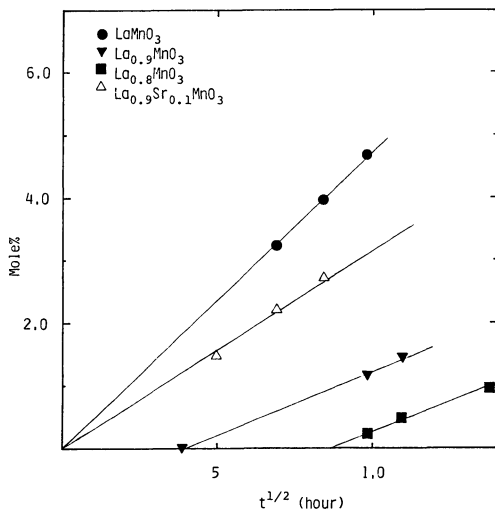


Fig.4 Mole fraction of $\text{La}_2\text{Zr}_2\text{O}_7$ produced in the $\text{La}_{1-x}\text{MnO}_3$ and 8YSZ interface at 1250 °C.

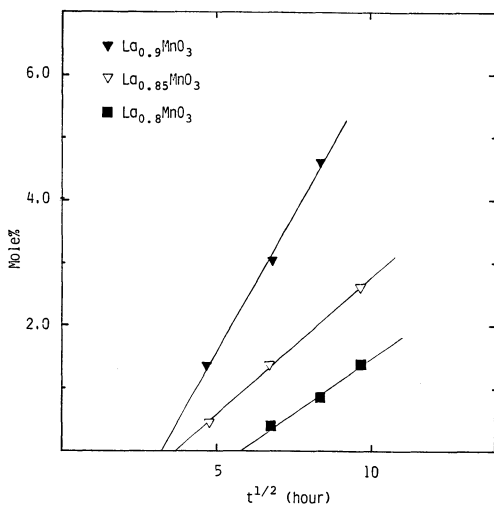


Fig.5 Mole fraction of $\text{La}_2\text{Zr}_2\text{O}_7$ produced in the $\text{La}_{1-x}\text{MnO}_3$ and 8YSZ interface at 1350 °C.

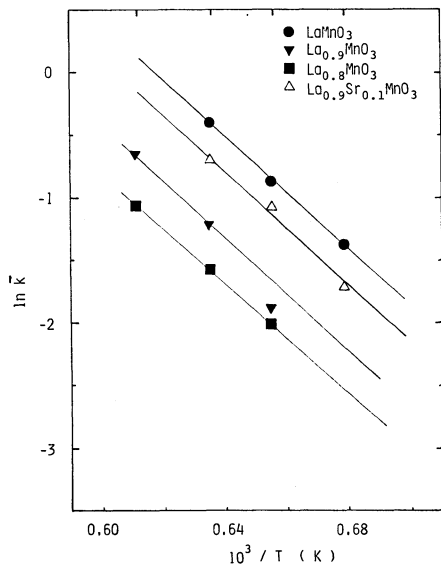


Fig.6 Temperature dependence of \bar{k} for $(\text{La,Sr})_{1-x}\text{MnO}_3$.

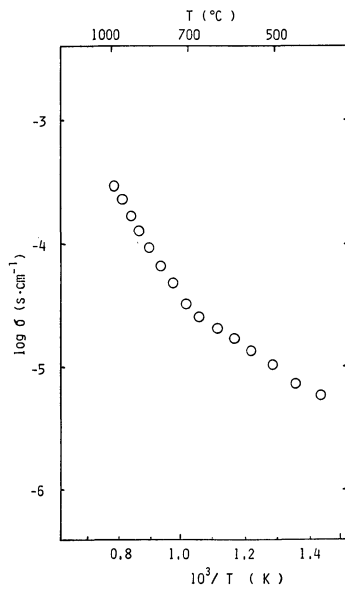


Fig. 7 Temperature dependence of the electrical conductivity of $\text{La}_2\text{Zr}_2\text{O}_7$.

REACTION KINETICS AND MICROSTRUCTURE OF
 $\text{La}_{0.6}\text{Ca}_{0.4}\text{MnO}_3/\text{YSZ}$ AIR ELECTRODE

Junichiro Mizusaki and Hiroaki Tagawa
Institute of Environmental Science and Technology,
Yokohama National University,
156 Tokiwadai, Hodogaya-ku, Yokohama 240, Japan

Kikuji Tsuneyoshi and Akihiro Sawata
Advanced Technology Research Center,
Mitsubishi Heavy Industries, Ltd.,
1-8-1 Sachiura, Kanazawa-ku, Yokohama 236, Japan

Abstract

By complex-impedance and cathodic polarization measurements and SEM observation, studies were made on the relationships between microstructure of the porous oxide layer and electrochemical properties of SOFC air electrodes, air / $\text{La}_{0.6}\text{Ca}_{0.4}\text{MnO}_3/\text{YSZ}$. It was shown that the reaction rate was essentially determined by the microstructure of the oxide layer at the air/ $\text{La}_{0.6}\text{Ca}_{0.4}\text{MnO}_3/\text{YSZ}$ triple phase boundary. The electrode interface conductivity and cathodic current at the air electrode increase with increase in the air / oxide layer / YSZ triple phase boundary. However, the kinetics of the rate determining reaction was essentially the same irrespective of the different morphology of the oxide layer.

1. INTRODUCTION

To reduce environmental impacts caused by the use of fossil fuels, such as green house effect by CO_2 emission, acid rain by SO_2 , and waste heat pollutions, it is urgent to develop high efficiency systems for fossil energy conversion. We consider SOFC as one of the more desirable systems and have started basic research on the electrode reactions in SOFC (1,2).

In a previous paper (1), we prepared perovskite-type oxides, $\text{La}_{0.6}\text{Ca}_{0.4}\text{MO}_3$ (M=Mn, Co), by a ceramic method, and studied the relationships between the thickness of porous oxide-electrode layer and the electrode properties of the air electrode system, air / $\text{La}_{0.6}\text{Ca}_{0.4}\text{MO}_3$ (M=Mn, Co) / YSZ. It was shown that the electrochemical properties are essentially independent of the thickness of oxide layer. From the results, it was concluded that the rate of electrode reaction is determined by the reaction at the air / electrode oxides / YSZ triple phase boundaries. Thus, close relationships were expected between the electrode properties and the microstructure of the porous oxide layer / YSZ interface.

In the present paper, our interest is focused on the relationships between the microstructure of porous oxide layer and electrochemical properties of the SOFC air electrode, air / $\text{La}_{0.6}\text{Ca}_{0.4}\text{MnO}_3$ / YSZ. To obtain the porous electrodes of different morphology, we synthesized $\text{La}_{0.6}\text{Ca}_{0.4}\text{MnO}_3$ by different procedures and prepared electrode / YSZ interfaces at different firing temperatures.

2. EXPERIMENTAL

Materials. $\text{La}_{0.6}\text{Ca}_{0.4}\text{MnO}_3$ were prepared by two methods, a ceramic method and a 'drip pyrolysis' method. In the ceramic method, we used carbonates of La, Ca, and Mn as starting materials. They were mixed together in the desired ratio by a ball mill for 24 hr, baked at 1200°C for 20 hr, crushed into powders of $< 100 \mu\text{m}$ in diameter, recalined at 1200°C for 20 hr and again crushed into powders. The powders consisted of chunks of irregular shapes and sizes, most of them 1-3 μm in size.

In the 'drip pyrolysis' method, we used nitrates of La, Ca and Mn as starting materials. Aqueous solutions of these nitrates, about 0.1M in concentrations, were mixed together in a proper metallic ratio. The solutions were introduced into capillary at a rate of about $0.5\text{cm}^3\text{min}^{-1}$, and then dripped from the tip of the capillary into a quartz tube with air flow. The tube was placed in a furnace kept at $600\pm 10^\circ\text{C}$. The drops were splashed upon the heated quartz-tube wall, abruptly dried and oxidized into perovskite-type oxides. The powders consisted of polycrystalline particles of 0.1-0.5 μm in diameter.

Powder X-ray analysis revealed that the oxides thus formed showed no other peaks than the single series of the perovskite-type.

For the electrolyte, sintered YSZ ($\text{ZrO}_2\text{-}8\text{m}/\text{oY}_2\text{O}_3$) pellets were used. YSZ powders supplied by Tosoh Co. Ltd. were pressed and sintered in air at 1400°C into pellets of 10mm in diameter and 1-3mm in thickness with relative density of more than 95%.

Preparation of Electrodes with Different Morphology The oxides were mixed with turpentine oil and painted on one side of the YSZ pellet. The electrodes with oxides by the ceramic method were fired at either 1000, 1100 or 1200 °C for 2-4 hr. The electrodes with oxides prepared by drip pyrolysis were fired at 1100 or 1200 °C for 4hr. The thickness of the porous oxide-electrode layer was calculated by the weight change of the pellet before and after the electrode mounting. As a counter and a reference electrode, Pt paste was mounted on the other side of the pellet.

Electrochemical Measurements The complex impedance measurements were made over the frequency range of 100kHz-1mHz using three terminal method. Steady-state cathodic polarization was measured using a current interruption method. Measurements were made in air at temperatures 900

and 1000°C.

3. RESULTS AND DISCUSSION

Electrode Morphology Figures 1 and 2 show typical SEM images of $\text{La}_{0.6}\text{Ca}_{0.4}\text{MnO}_3/\text{YSZ}$ interfaces. In Fig. 1, comparison is made between the electrodes fired at 1100°C and 1200°C with $\text{La}_{0.6}\text{Ca}_{0.4}\text{MnO}_3$ prepared by the ceramic method. When the electrode was fired at 1100°C, the oxide particles still showed irregular edges and were connected with each other by narrow bottleneck-type bridges. The contact area between YSZ and the oxide particles was small and most of the contacts were rather close to a point contact. When the firing temperature was 1200°C, the surface of the oxide particles became smooth and the contacts between the particles were thick. The contact between the oxide particles and YSZ surface was also thick, and each contact between a particle and YSZ was face-to-face type. The area of closely contacted interface of oxide electrode / YSZ increased considerably and the three phase boundary of air / oxide electrode / YSZ increased slightly with increase in firing temperature.

Figure 2 shows the change with firing temperature in the oxide electrode / YSZ interface for the electrode prepared by the drip pyrolysis method. When fired at 1100°C, the microstructure is finer than that of the electrode prepared by the ceramic method and, in contrast to the oxides prepared by the ceramic method, the oxide by the drip pyrolysis method has smooth surface and the particles contact each other with thick necking. At the electrode / YSZ interface, each oxide particles contacted with YSZ in face-to-face. When fired at 1200°C, oxide particles grew remarkably. Due to this growth, the area of closely contacted interface increased, some of the pores in the electrode were closed from the outer gas phase, and the triple phase boundary at the interface decreased.

Electrode Interface Conductivity and Capacitance From the impedance arcs obtained by complex impedance measurements, we determined the electrode interface conductivity, σ_E and apparent capacitance, C_E by the equations,

$$\sigma_E = 1/AR_E \quad (1)$$

and

$$C_E = \sigma_E/2\pi f_T \quad (2)$$

where A is the apparent area of YSZ surface on which $\text{La}_{0.6}\text{Ca}_{0.4}\text{MnO}_3$ was mounted, R_E is the electrode interface resistance obtained from the impedance arc and f_T is the frequency corresponding the top of the impedance arc. In this analysis, we assumed that the electrode interface impedance can be expressed by a RC parallel equivalent circuit (3).

Figure 3 shows the dependence of σ_E and C_E on the thickness of the porous electrode layer, d , for the electrodes fired at 1100°C. The upper scale shows the thickness in μm calculated using the theoretical density of $\text{La}_{0.6}\text{Ca}_{0.4}\text{MnO}_3$. Because the oxide electrode is porous, the actual thickness is about 1.6-1.7 times the calculated one. σ_E and C_E for the electrode prepared by drip pyrolysis are much larger than that of the electrode prepared by the ceramic method. They are essentially constant irrespective of the electrode thickness.

Figure 4 shows the dependence of σ_E and C_E at 1000°C on the firing temperatures of the electrode. For the electrodes prepared by the ceramic method, σ_E and C_E increase with temperature. For the electrode prepared by drip pyrolysis, σ_E decreases while C_E increases with increase in temperature.

In the studies of the Ar-O₂(g), Pt / YSZ electrode (4,5) and the SOFC electrode using the oxide prepared by a ceramic method (1), the authors and co-workers have proposed a model of electrode reaction. According to this model, σ_E is proportional to the length of the triple phase boundary of gas / electrode / YSZ, and C_E is proportional to the area of micro-closed pores left at the closely contacted electrode / YSZ interface. Based on this model, we can explain the relationships obtained in this work between the results on σ_E and C_E and the electrode morphology by SEM observations. From the SEM observation in the present study, the triple phase boundary is maximum for the electrode prepared by drip pyrolysis and fired at 1100°C. For this electrode, the maximum σ_E was observed. For the electrodes with oxide by the ceramic method, both the triple phase boundary by SEM observation and σ_E increased with temperature. For the electrodes with oxide by drip pyrolysis, the triple phase boundary decreases with temperature due to grain-growth, and σ_E also decreased.

The closely contacted area of electrode / YSZ interface is larger for the electrodes by drip pyrolysis than those by the ceramic method, and becomes larger with increasing firing temperature. The largest area is observed for the electrode prepared by drip pyrolysis and fired at 1200°C. The direction of changes in C_E with the change in the preparation procedure and firing temperature is the same with that of the changes in the closely contacted area at the electrode / YSZ interface.

Steady-State Cathodic Polarization Current Figure 5 shows typical cathodic steady-state polarization current at 1000°C. Apparently, the current is not affected by the thickness of the porous oxide layer. The largest current is observed for the electrode with $\text{La}_{0.6}\text{Ca}_{0.4}\text{MnO}_3$ layer by drip pyrolysis and fired at 1100°C. In Fig. 6, comparison is made for the cathodic polarization curves at 900°C for the electrode fired at different temperatures with $\text{La}_{0.6}\text{Ca}_{0.4}\text{MnO}_3$ by the ceramic method. Comparing the morphology and polarization curves, we find that the steady state polarization current is larger for the electrode with longer triple phase boundary.

Relationships between Kinetics and Morphology Because σ_E is proportional to the exchange current (4), we normalized the steady state current by σ_E of each electrode, so that we can examine if the reaction kinetics changes with the electrode morphology. Figure 7 shows the plot of I/σ_E vs. overpotential, η , at 1000°C; all the data fall on one curve, suggesting that the reaction kinetics is essentially the same independent of the electrode thickness and microstructure.

In a previous paper (2), we reported σ_E and steady-state polarization current as a function of temperature and oxygen partial pressure, $P(O_2)$, using Ar-O₂, La_{0.6}Ca_{0.4}MnO₃ / YSZ electrodes fired at 1100°C with La_{0.6}Ca_{0.4}MnO₃ prepared by drip pyrolysis. For the conditions of small overpotential, the reaction rate was summarized into empirical equations

$$\sigma_E = (4Fk/RT)P(O_2)^{1/2} \quad (3)$$

$$i = k[a_0 - P(O_2)a_0^{-1}] \quad (4)$$

$$2\eta F = RT \ln [a_0/P(O_2)^{1/2}] \quad (5)$$

where k is a rate constant, $P(O_2)$ is oxygen partial pressure in the gas phase, and a_0 is the oxygen activity at the electrode / YSZ interface. Under large cathodic overpotential, limiting current appeared which was proportional to $P(O_2)$.

From Eqs. (3)-(5), i/σ_E is calculated as

$$i/\sigma_E = RT/4F[\exp(2\eta F/RT) - \exp(-2\eta F/RT)] \quad (6)$$

The solid curve in Fig. 7 shows the relationship of Eq. (6). The results of the present work essentially agree with Eq. (6), suggesting the rate equations holds for the La_{0.6}Ca_{0.4}MnO₃ / YSZ electrodes of different morphology.

Figure 8 shows i/σ_E vs. η at 900°C for the electrodes fired at different temperatures with La_{0.6}Ca_{0.4}MnO₃ prepared by the ceramic method. Under low overpotential, the i/σ_E vs. η relationships obey Eq. (8). However, for larger overpotential, limiting current was observed. The limiting current depends on the electrode firing temperature, and therefore on the electrode morphology. At present, the details of relationships between the limiting current and morphology are not yet clear.

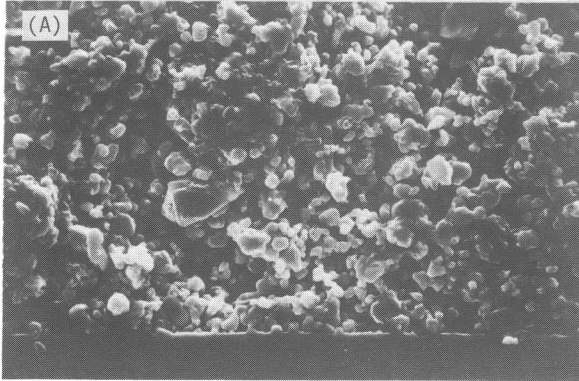
4. CONCLUSIONS

Close relationships between the microstructure of the porous oxide layer and electrochemical properties of electrodes were shown using air / La_{0.6}Ca_{0.4}MnO₃ / YSZ electrode systems. The electrochemical properties are essentially determined by the microstructure of air /

porous oxide layer / YSZ triple phase boundary, and the reaction rate increases with increase in the length of the triple phase boundary.

REFERENCES

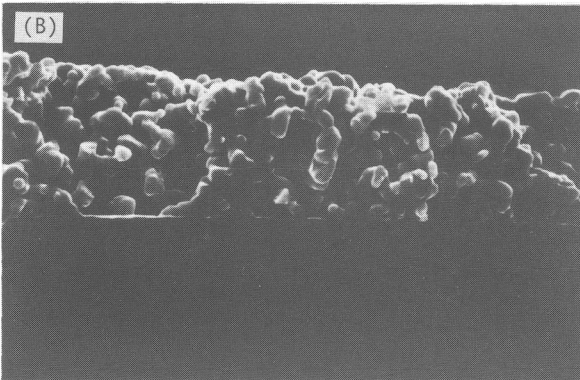
- (1) J. Mizusaki, H. Tagawa, K. Tsuneyoshi, K. Mori, and A. Sawata, Nippon Kagaku Kaishi, 1623 (1988).
- (2) K. Tsuneyoshi, K. Mori, A. Sawata, J. Mizusaki, and H. Tagawa, Solid State Ionics, in press.
- (3) J. Sasaki, J. Mizusaki, S. Yamauchi, and K. Fueki, Bull. Chem. Soc. Jpn., 54 1688 (1981).
- (4) J. Mizusaki, K. Amano, S. Yamauchi, and K. Fueki, Nippon Kagaku Kaishi, 1160 (1985).
- (5) J. Mizusaki, K. Amano, S. Yamauchi, and K. Fueki, Solid State Ionics, 22 313 (1987).



$\text{La}_{0.6}\text{Ca}_{0.4}\text{MnO}_3$

YSZ

10µm

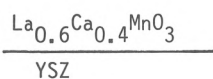
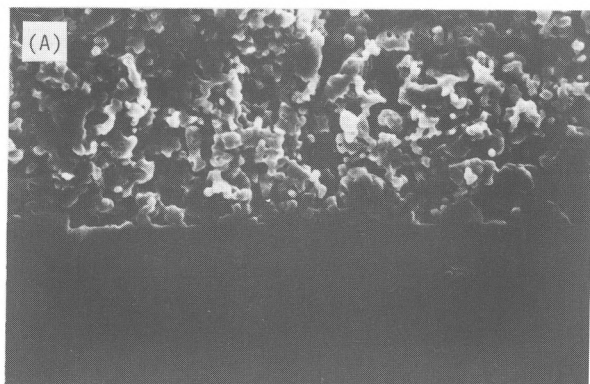


$\text{La}_{0.6}\text{Ca}_{0.4}\text{MnO}_3$

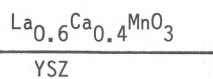
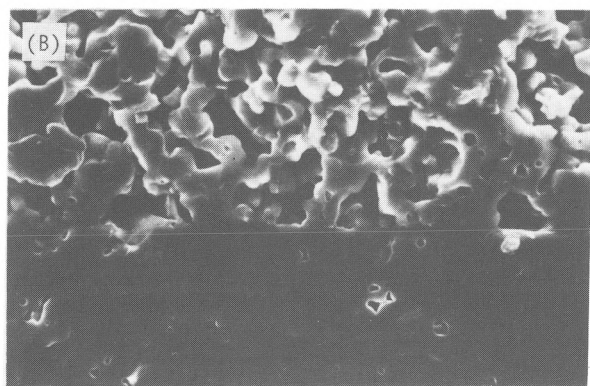
YSZ

10µm

Fig. 1. SEM images of $\text{La}_{0.6}\text{Ca}_{0.4}\text{MnO}_3$ / YSZ interface. $\text{La}_{0.6}\text{Ca}_{0.4}\text{MnO}_3$ was prepared by the ceramic method. (A): fired at 1100°, (B): fired at 1200°C.



10 μm



10 μm

Fig. 2. SEM images of $\text{La}_{0.6}\text{Ca}_{0.4}\text{MnO}_3$ / YSZ interface. $\text{La}_{0.6}\text{Ca}_{0.4}\text{MnO}_3$ was prepared by the drip pyrolysis method. (A): fired at 1100° , (B): fired at 1200°C .

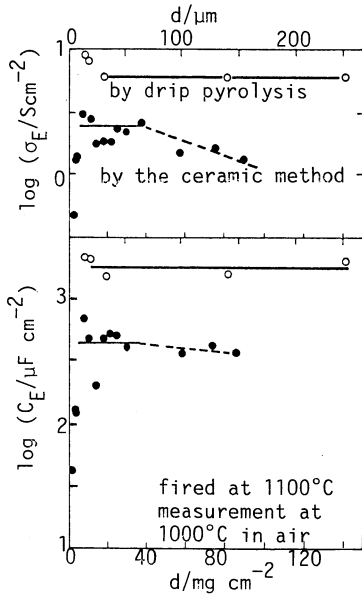


Fig. 3. σ_E and C_E at 1000°C in air as a function of the thickness of $\text{La}_{0.6}\text{Ca}_{0.4}\text{MnO}_3$ layer, d . Electrodes were fired at 1100°C. The upper scale shows the thickness calculated using the theoretical density of the oxide. Actual thickness is about 1.6-1.7 times the theoretical one. Closed symbols: $\text{La}_{0.6}\text{Ca}_{0.4}\text{MnO}_3$ prepared by the ceramic method, open symbols: prepared by drip pyrolysis.

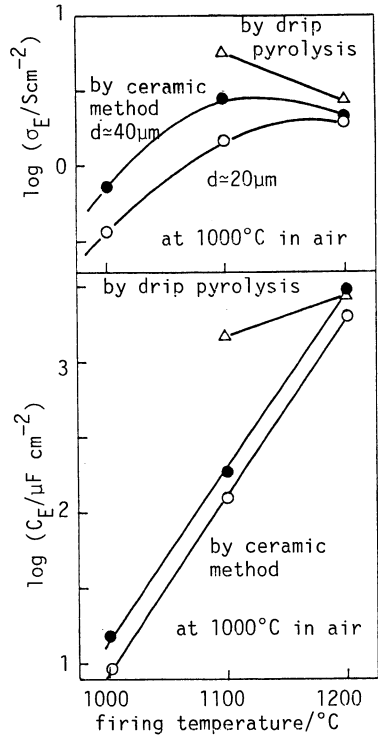


Fig. 4. σ_E and C_E at 1000°C in air as a function of the electrode firing temperature for $\text{La}_{0.6}\text{Ca}_{0.4}\text{MnO}_3 / \text{YSZ}$. Δ : prepared by drip pyrolysis, \circ, \bullet : prepared by the ceramic method.

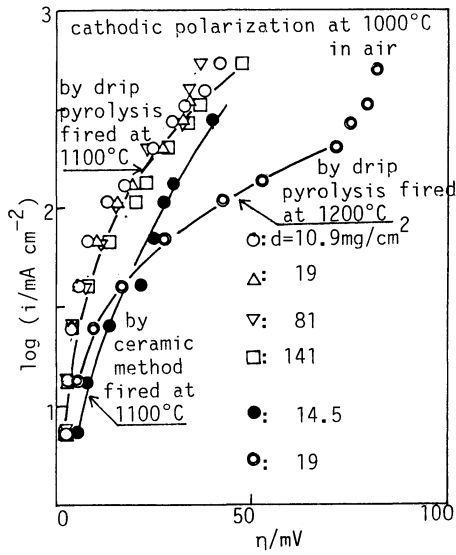


Fig. 5. Steady-state cathodic polarization current at 1000°C in air for $\text{La}_{0.6}\text{Ca}_{0.4}\text{MnO}_3 / \text{YSZ}$ prepared by different processes.

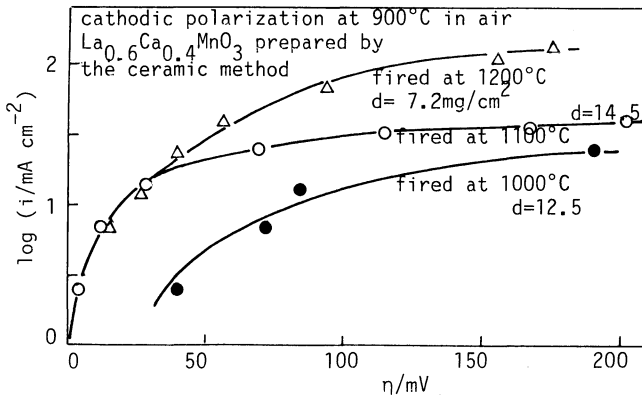


Fig. 6. Steady-state cathodic polarization current at 900°C in air for $\text{La}_{0.6}\text{Ca}_{0.4}\text{MnO}_3 / \text{YSZ}$. $\text{La}_{0.6}\text{Ca}_{0.4}\text{MnO}_3$ was prepared by the ceramic method. Electrode firing temperature is different.

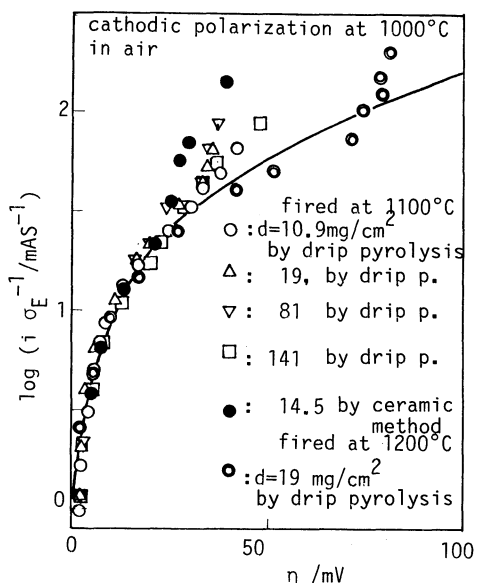


Fig. 7. Steady-state cathodic polarization current at 1000°C in air normalized by σ_E for $\text{La}_{0.6}\text{Ca}_{0.4}\text{MnO}_3$ / YSZ prepared by different processes. The solid curve was calculated from Eq. (6).

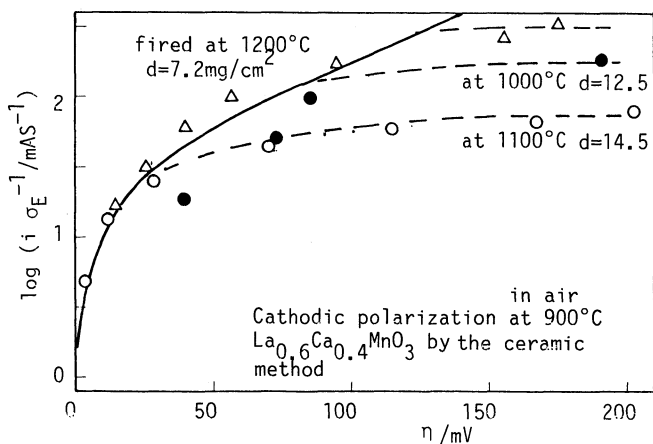


Fig. 8. Steady-state cathodic polarization current at 900°C in air normalized by σ_E for $\text{La}_{0.6}\text{Ca}_{0.4}\text{MnO}_3$ / YSZ. $\text{La}_{0.6}\text{Ca}_{0.4}\text{MnO}_3$ was prepared by the ceramic method. Electrode firing temperature is different. The solid curve was calculated from Eq. (6).

OXYGEN REDUCTION AT THE $\text{La}_{1-x}\text{Sr}_x\text{MnO}_3$ /ZIRCONIA ELECTRODE

A. Hammouche, E. Siebert, M. Kleitz and A. Hammou
ENSEEG - LIESG
B.P. 75
38402 Saint Martin d'Hères (France)

ABSTRACT

The kinetics of oxygen reduction at the $\text{ZrO}_2\text{-Y}_2\text{O}_3/\text{La}_{1-x}\text{Sr}_x\text{MnO}_3$ electrode ($0 \leq x \leq 0.5$) has been studied by steady-state polarization and transient measurements. The electrode behavior is similar to that of conventional metal electrodes for low cathodic polarization. At high polarization, a sudden increase of the electrode kinetics is observed. This can be related to the creation of oxygen vacancies in $\text{La}_{1-x}\text{Sr}_x\text{MnO}_3$, as demonstrated by redox potentiometric measurements. The strontium content in the electrode is a determining parameter for this property. The experimental results suggest two different reaction pathways under low and high cathodic polarization. Rapid oxygen diffusion through the electrode material is the main characteristic of the newly observed behavior.

1. INTRODUCTION

The choice of cathode material in a solid electrolyte fuel cell is of great importance since the cell efficiency is mainly governed by the cathodic process. Besides obvious conditions to be fulfilled such as phase stability, low vapor pressure at 1000°C, chemical compatibility, matching expansion coefficient and good adherence with the solid electrolyte, other important characteristics include high electronic conductivity and high electroactivity for the oxygen reduction.

Oxides having the perovskite structure have been proposed as alternatives to platinum (1-4). Among them, lanthanum manganite has been reported to be the best candidate (5,6). Pure LaMnO_3 is not sufficiently conducting. When a fraction of La^{3+} is replaced by divalent cations such as Sr^{2+} , the charge deficit is compensated by a valence change on manganese ions from Mn^{3+} to Mn^{4+} and, under certain experimental conditions, the formation of oxygen vacancies. This increases the conductivity up to several hundred $\Omega^{-1}\text{cm}^{-1}$ depending on the dopant concentration. An oxide ion conduction may also be expected, due to the presence of oxygen vacancies (1).

Few kinetics studies on the oxygen reduction mechanism have been reported on these compounds at high temperature. Takeda et al. (4,7) have studied the cathodic polarization of $\text{La}_{1-x}\text{Sr}_x\text{MO}_3$, where $M = \text{Fe}, \text{Mn}, \text{Cr}$ or Co , sputtered on yttria stabilized zirconia, at 800°C in air in the potential range 0-400 mV. The best performances, in the case of $\text{La}_{1-x}\text{Sr}_x\text{MnO}_3$, were

obtained for $x = 0.5$. A dependence of the current density on the electrode thickness showed that the optimum is obtained for $2 \mu\text{m}$. The observed high electroactivity was attributed to its high catalytic activity and to the large effective reaction area due to the high oxide diffusion in the material. In a previous study, Hammouche et al.(8) have compared the electrocatalytic activity of pin-shaped electrodes. This kind of electrode was used to overcome difficulties in separating the effect of morphology from the effects of the electrode composition itself. The best results were also obtained for the composition $x = 0.5$ within the same potential range. In aqueous electrolyte, a similar behavior was demonstrated a few years ago (9) and correlated with the electronic structure of the compound.

Here we will report on the oxygen reduction kinetics of the system $\text{La}_{1-x}\text{Sr}_x\text{MnO}_3/\text{ZrO}_2\text{-Y}_2\text{O}_3$ (9 mol %) over a wide electrode potential range as a function of the oxygen pressure P and strontium doping x . A conventional platinum electrode will be used for comparison.

2. EXPERIMENTAL

Yttria stabilized zirconia (9 mol %) noted YSZ was used as the electrolyte. It was prepared from a mixture of Y_2O_3 and ZrO_2 powders calcined at 1050°C . After grinding, the product was compacted into pellets and then sintered at 1850°C for 2 hours. The final density was greater than 95%.

The perovskites were also synthesized by high temperature solid state reactions. The starting materials were La_2O_3 , SrCO_3 and MnCO_3 with high purity. Compositions ranging from 0 to $x \leq 0.5$ were prepared by mixing the appropriate amounts of reagents. The mixed powders were calcined at 1200°C for 20 hours, ground, pressed under $2\text{t}/\text{cm}^2$ and sintered at 1500°C in air for 2 hours. Chemical analysis, microscopic investigation and X ray diffraction patterns were made for each sample to confirm the composition. All the compounds were found to be single phased and had the selected composition and the right crystalline structure. The results of this microscopic investigation and of the study of structural, electrical and thermal properties have been reported in detail (8,10). The compounds crystallize in the hexagonal-rhombohedral structure. The thermal expansion coefficient diverges by no more than 2.6×10^{-6} deg.⁻¹ with respect to that of YSZ. The electrodes behave as p type semi-conductors with conductivities of the order of $100 \Omega^{-1} \text{cm}^{-1}$ at 950°C .

The electrochemical experiments were carried out on a three electrode cell similar to that assembled by Schouler (11) and illustrated in Fig. 1. The electrolyte was a thin pellet of YSZ (20 mm in diameter and 1.5mm thick). Two platinum-pasted electrodes (Degussa 308A) were applied on its upper-side. One of the electrodes measured about 1cm^2 and was used as a counter-electrode. The other one, with a smaller area, acted as a reference electrode. The single-point contact working electrode was made of a pin-shaped sample of the investigated perovskite oxide. The electrode-electrolyte contact area was small ($\approx 10^{-3} \text{cm}^2$). Three working electrodes could be simultaneously tested under the same operating conditions. For comparison, a single-point electrode made of a

pure platinum ball, produced by melting the end of a wire in an acetylene/oxygen flame, was also tested. The oxygen pressure in the surrounding atmosphere was controlled by an electrochemical oxygen pump coupled to an oxygen gauge (12). Pure argon was used as the vector gas. The working temperature was maintained at 960°C.

To compare the characteristics of the investigated electrodes, we measured their contact area with the electrolyte according to Newman's formula (13), recommended by Isaacs et al. (2) :

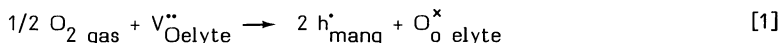
$$r = 1/4\sigma R$$

where r is the surface contact radius, R the electric resistance of the electrolyte and σ its conductivity under the measurement conditions. The resistance R was measured by impedance spectroscopy.

The electrochemical studies were carried out by steady-state I (E) polarization curve analysis. The ohmic drops were determined by impedance spectroscopy. The transient behavior of the electrode was also measured under different experimental conditions. A Solartron Electrochemical Interface 1186 coupled with a Solartron 1250 Frequency Response Analyser was used for this study.

3. RESULTS AND DISCUSSION

The overall oxygen reduction reaction can be written :



(Kroger notation is used.)

The subscript mang (respectively elyte) means that the species is located in $La_{1-x}Sr_xMnO_3$ (respectively YSZ). Previous studies on single point platinum electrodes (14) have shown that under high polarization, the current reaches a limiting value which is commonly attributed to a limitation by the oxygen supply process to the electrode reaction zone. It has been demonstrated on different metal electrodes that the general shape of the steady-state I(E) curve depends neither on the texture nor on the nature of the metal.

A typical example of a steady-state current-potential curve obtained with $La_{1-x}Sr_xMnO_3$ under 10^{-3} atm is shown in Fig. 2. For comparison, the curve obtained with a Pt electrode of similar contact area, under the same experimental conditions, is also plotted on the figure. The essential difference between the two curves is that in the case of the manganite electrode, two regions noted I and II on the figure can easily be distinguished :

Low cathodic potential region (I) - Here, the I(E) curve is similar to that of a platinum electrode. The catalytic activity for oxygen reduction is of the same order of magnitude. It has already been reported that in this potential range the electrode activity increases as the degree of strontium substitution increases. Fig. 3 shows for example the current densities per length of the

electrode contact perimeter recorded under -100 mV polarization. The best performances are obtained for $x = 0.5$ for which the manganite appears to be better than Pt.

High cathodic potential region (II) - Under high cathodic polarization, a sharp transition is observed. The current markedly increases as shown in Fig. 2. After this transition, the $I(E)$ curve also shows a limiting current I_l plateau at higher cathodic potential. It is much greater than that measured on platinum. A detailed investigation as a function of the oxygen pressure, showed that I_l obeys a square root dependence on the oxygen partial pressure in the range 10^{-4} - 10^{-2} atm. As a consequence, in this potential region the performance characteristics of $\text{La}_{1-x}\text{Sr}_x\text{MnO}_3$ are markedly higher than that of Pt.

We checked that this sudden increase of the electrode kinetics could not be attributed to the sole electrochemical reduction of the electrode material. A calculation shows that the complete reduction of the electrode according to reaction [2] can account for only 1% of the quantity of electricity which crosses the cell during the electrode polarization study. The current increase can neither be attributed to the electrolyte reduction which would only occur at overpotentials more cathodic than -1.3V. We must therefore conclude that after the transition, the main electrode process is still an oxygen electrode reaction. Moreover, the definite dependence of the limiting current on the oxygen pressure confirms this statement.

On the $I(E)$ curve, a rather accurate transition electrode potential E_T can be determined (cf Fig.2). It depends on x as shown in Table I. The higher the strontium content, the easier the transition occurs (the lower the overpotential magnitude $|E_T|$). In this respect, the $x = 0.5$ compound also appears to be the best in terms of electrode kinetics.

Our assumption is that a change in the electrode reaction mechanism occurs at E_T leading to the onset of an important electrocatalytic effect.

This point is confirmed by the analysis of the voltammograms and the transient responses of the electrode to a current or a potential step. A typical voltammogram obtained for a scan rate of 1mV/s is given in Fig. 4. The starting potential is 0mV. As usually observed, a hysteresis loop is present. However, in contrast to the response of a classical redox system, the current is larger during the backwards scan and the hysteresis becomes increasingly important as the scan rate decreases. Consistently with that, the steady-state curve shows current magnitudes much larger than those observed on the voltammogram plotted under the same experimental conditions. This behavior indicates that the enhancement of the electrode kinetics is due to a slow modification of the electrode material.

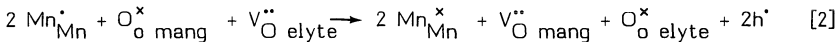
A typical response of the electrode to a current or a potential step corresponding to region II is shown in Fig. 5. At the beginning the response is similar to the usual transient behavior observed when a concentration supply overpotential is the rate determining step (15). More precisely, the variation of the transient current obeys with a good accuracy the classical Cottrell-type linear relationship as a function of $t^{-1/2}$. This relationship is checked in

Fig. 6. After a certain time, noted τ on the figure, the electrode process is characterized by a depolarization phenomenon. The $E(t)$ curve shows an overshoot while the $I(t)$ curve shows a net current enhancement. This behavior is consistent with the voltammogram analysis and confirms that a modification in the electrode material occurs at the transition leading to a new reaction mechanism which favors oxygen reduction.

After polarization in region II, the open circuit electrode potential relaxes as shown in Fig. 7. It shows a typical plateau at a redox potential noted E_w . A second small inflexion point located at -330 mV/air was also noticed. As this potential does not depend either on the electrode composition or on the oxygen partial pressure in the gas, it was attributed to the reoxidation of an impurity. Because of the small amplitude of this phenomenon, it will not be taken into consideration in what follows and only the principal wave will be examined. A study as a function of the electrode composition and of the oxygen pressure was performed. The E_w values are highly dependent on the degree of strontium doping x in the electrode. The higher the x values, the lower the magnitude of $|E_w|$ (cf. Table I). The variation is parallel to that observed for $|E_{\bar{r}}|$. No significant influence of the oxygen partial pressure on E_w was detected. The parameter E_w is therefore characteristic of the electrode material.

The basic principle of this kind of transient measurement has been described in detail by Fabry et al. who used this experimental technique for the measurement of thermodynamic data on oxides (16) and for the determination of the redox potential of point defects dissolved in solid electrolytes (17). According to the arguments developed in these papers, it can be concluded, in our case, that:

- When a cathodic current flows through the cell, the electrode material is partly reduced. The following reaction can be proposed :



Such a reduction will result in a marked increase of the oxide vacancy concentration in the electrode material

- As soon as the current is interrupted, the electrode is reoxidized by the oxygen present in the surrounding gas. The potential plateau can be interpreted by assuming that the reoxidation proceeds according to the following equation :

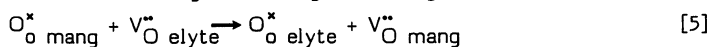
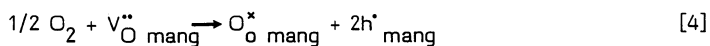


and by assuming that the oxygen flux is constant throughout the reoxidation process. The related electrode potential variation can be calculated with the assumption that the component activities are equal to their concentrations. The theoretical curve also presents a wave whose potential at the inflexion point increases as the strontium content increases.

All the observations converge to the same conclusion : under high cathodic polarization ($E < E_T$) the electrode is partly reduced and oxygen vacancies are created. The electrode is no longer mainly an electronic conductor. A mixed conductivity has been generated resulting in a new reaction mechanism. This change of mechanism is schematically depicted in the Fig. 8.

In region I, the electrode is regarded as an electronic conductor (diagram a in the figure). The behavior of the electrode is typical of a conventional metal electrode for which the reaction zone is concentrated around the triple contact line. A concentration overpotential is clearly identified as rate determining (18). The marked influence of the strontium doping on the electrode kinetics in region I can be explained in two ways, i.e. either by the effect of the variation of the electronic Fermi level in the electrode on the electrode parameters or by assuming that Mn^{4+} are active adsorption sites on the electrode surface. This second assumption supposes that the electrode surface plays a determining role in the oxygen supply to the triple contact line. In order to explain the enhancement of the electrocatalytic activity as a function of x , Matsumoto et al. (9) proposed to establish a parallelism between the Mn-O interactions in the bulk of the material and those existing at the surface between the Mn cation and the oxygen molecule. The former determines the magnitude of the resistivity of the oxide, the latter determines its catalytic activity for oxygen reduction. The adsorbed oxygen molecules are viewed as completing the octahedral coordination polyhedra of the Mn cations on the electrode surface. The degree of the overlap integral between their orbitals seems to be reflected by that of the overlap integral between the corresponding orbitals of the cation and oxygen ion in the oxide bulk. This parameter increases as the dopant content increases leading to an improved electronic exchange in the bulk and on the surface of the electrode (20). We also observed a parallel increase in the conductivity and the catalytic activity of these electrodes.

In region II, the electrode is a mixed electronic-ionic conductor (diagram b with figure 3). The oxygen reduction pathway is modified. The drastic increase in the reaction rate can be related to the sudden increase in the oxygen vacancy concentration inside the electrode. The actual oxygen reduction therefore occurs on the manganite surface. The oxide ions produced during this reduction diffuse to the electrode-electrolyte interface where a simple ionic transfer occurs. This reaction scheme can be written as :



The catalytic effect of the reduced manganite can be attributed to the simultaneous presence of the two electroactive species h^{\bullet} and $V_{O}^{\bullet\bullet}$ in this phase. The same conclusion has already been proposed by Schouler regarding the surface of the electrolyte (11).

More recently, a detailed analysis of the impedance diagrams plotted at different overpotentials of the steady-state polarization curve (21) has confirmed the mechanism proposed for oxygen reduction on the $\text{La}_{1-x}\text{Sr}_x\text{MnO}_3$ /YSZ electrode. In region II, the diagram shape indicates a limited diffusion process confirming the mechanism proposed above. The overall process would be partly limited by the oxygen vacancy diffusion in the manganite. A corresponding diffusion coefficient has been calculated to be approximately $4 \times 10^{-8} \text{ cm}^2 \text{ s}^{-1}$ at 960°C for oxygen in reduced manganite.

ACKNOWLEDGEMENTS

This work was initiated by Dr E. Schouler who passed away in December 87. It has been supported by the Commission of the European Communities.

REFERENCES

1. T. Takahashi and H. Iwahara, "High Temperature Solid Electrolyte Fuel Cells", in Research on Effective Use of Energy, V. 3, Japan, Jan.1982, p.727
2. H. S. Isaacs and L. J. Olmer, "Comparison of Materials as Oxygen Catalytic Electrodes on Zirconia Electrolyte", J. Electrochem. Soc., 129, (1982), 436
3. T. Kenjo, T. Maruyama, T. Yoshida, Y. Kouno and Y. Saito, "Strontium Oxide-doped Lanthanum Iron Oxides as Air Electrodes for High Temperature Solid Electrolyte Fuel Cells", in Report of the Research Laboratory of Engineering Materials, Tokyo, 11, (1986), 17
4. O. Yamamoto, Y. Takeda, R. Kanno and M. Noda, "Perovskite-type Oxides as Oxygen Electrodes for High Temperature Oxide Fuel Cells", Solid State Ionics, 22, (1987), 241
5. F. J. Rohr, "High-Temperature Fuel Cells", in Solid Electrolytes, P. Hagenmuller and W. Van Gool Ed., (1978), 431
6. B. C. H. Steele, I. Kelly, H. Middleton and R. Rudkin, "Oxidation of Methane in Solid State Electrochemical Reactors", Solid State Ionics, 28-30, (1988), 1547
7. Y. Takeda, R. Kanno, M. Noda, Y. Tomida and O. Yamamoto, "Cathodic Polarization Phenomena of Perovskite Oxide Electrodes with Stabilized Zirconia", J. Electrochem. Soc., 134, (1987), 2656
8. A. Hammouche, E. Siebert and A. Hammou, "Crystallographic, Thermal and Electrochemical Properties of the System $\text{La}_{1-x}\text{Sr}_x\text{MnO}_3$ for High Temperature Fuel Cells", Mat. Res. Bull., 24, (1989), 367
9. Y. Matsumoto, H. Yoneyama and H. Tamura, "Dependence of the exchange Current Density of Oxygen Reduction on the Resistivities of $\text{La}_{1-x}\text{Sr}_x\text{MnO}_3$ and $\text{LaNi}_{1-x}\text{M}_x\text{O}_3$ Electrodes", J. Electroanal. Chem., 83, (1977), 245

10. A. Hammouche, E. J. L. Schouler and M. Henault, "Electrical and Thermal Properties of Sr-Doped Lanthanum Manganites", *Solid State Ionics*, 28-30, (1988), 1205
11. E. J. L. Schouler and M. Kleitz, "Electrocatalysis and Inductive Effects at the Gas, Pt / Stabilized Zirconia Interface", *J. Electrochem. Soc.*, 134, (1987), 1045
12. J. Fouletier, G. Vitter and M. Kleitz, "Measurement and Regulation of Oxygen Content in Gases Using Solid Electrolyte Cells. III. Oxygen Pump-Gauge", *J. App. Electrochem.*, 5, (1975), 111
13. J. Newman, "Resistance for Flow of Current to a Disk", *J. Electrochem. Soc.*, 113, (1966), 501
14. P. Fabry and M. Kleitz, "Influence of the Metal and the Electrolyte Compositions on the Characteristics of the Oxygen Electrode Reaction on Solid Oxide Electrolyte", *Electroanal. Chem. and Interf. Electrochem.*, 57, (1974), 165
15. L. J. Olmer, "The Oxygen Electrode Reaction on Zirconia Electrolytes", Thesis, New York, (1980)
16. P. Fabry, M. Kleitz and C. Déportes, "Sur l'Utilisation d'une Electrode Ponctuelle dans les Cellules à Oxyde Electrolyte Solide. I. Application aux Mesures Thermodynamiques et à la Détermination du Nombre de Transport Electronique de l'Electrolyte", *J. Solid State Chem.*, 5, (1972), 1
17. P. Fabry, M. Kleitz and C. Déportes, "Sur l'Utilisation d'une Electrode Ponctuelle dans les Cellules à Oxyde Electrolyte Solide. II. Application à la Détermination des Tensions d'Oxydoréduction des Défauts Ponctuels dans l'Electrolyte", *J. Solid State Chem.*, 6, (1973), 230
18. E. J. L. Schouler, "Relation Between Solid Oxide Electrolyte Surface Properties and Electrode Reaction Kinetics", *Solid State Ionics*, 9-10, (1983), 945
19. Y. Matsumoto, H. Yoneyama and H. Tamura, "Influence of the Nature of the Conduction Band of Transition Metal Oxides on Catalytic Activity for Oxygen Reduction", *J. Electroanal. Chem.*, 83, (1977), 237
20. A. Hammouche, "Contribution à l'Etude de $\text{La}_{1-x}\text{Sr}_x\text{MnO}_3$ Comme Matériau d'Electrode à Oxygène à Haute Température", Thesis, Grenoble, (1989)
21. A. Hammouche, E. Siebert, M. Kleitz and A. Hammou, "Oxygen Electrode Reaction on $\text{La}_{1-x}\text{Sr}_x\text{MnO}_3$ Oxides in High Temperature Solid Electrolyte Cells", Ext. Abs. in First International Symposium on Electrochemical Impedance Spectroscopy, May 22-26, (1989), Bombannes (France)

x	E_{τ} , mV/air determined at 0.2 atm	E_w , mV/air ³ determined at 10 ⁻³ atm
0.00	-	-516
0.10	-160	-730
0.19	-158	-591
0.30	-110	-547
0.37	-	-498
0.50	-94	-405

Table I. Influence of the strontium concentration in $\text{La}_{1-x}\text{Sr}_x\text{MnO}_3$ on E_{τ} and E_w .

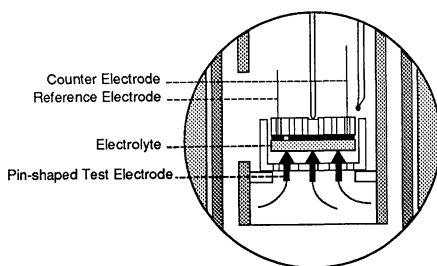


Fig. 1 - Polarization cell diagram

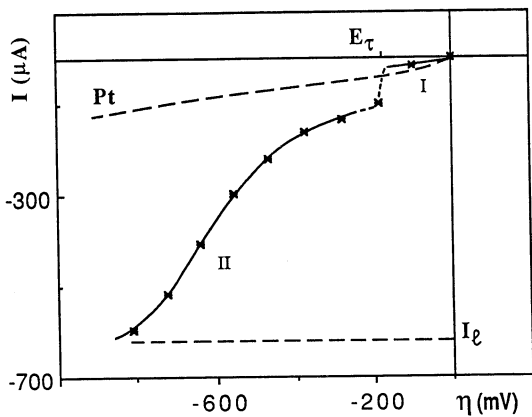


Fig. 2 - Steady-state $I(\eta)$ characteristics of a Pt and a $\text{La}_{1-x}\text{Sr}_x\text{MnO}_3$ electrode. E_τ is the transition potential. $P = 10^{-3}\text{atm}$, $T = 960^\circ\text{C}$, $x = 0.3$.

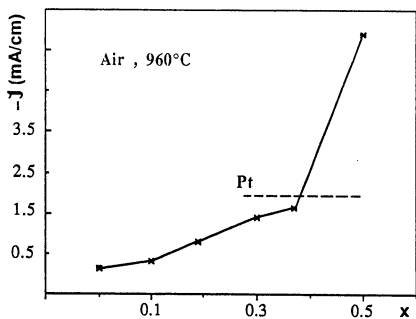


Fig. 3 - Dependence of the current density on electrode composition for $\text{La}_{1-x}\text{Sr}_x\text{MnO}_3$ at -100mV overpotential.

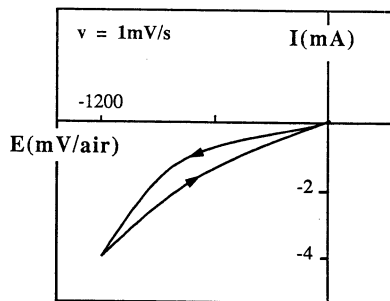


Fig. 4 - Typical voltammogram for the reduction of O_2 . $x = 0.4$, $P = 0.2\text{atm}$.

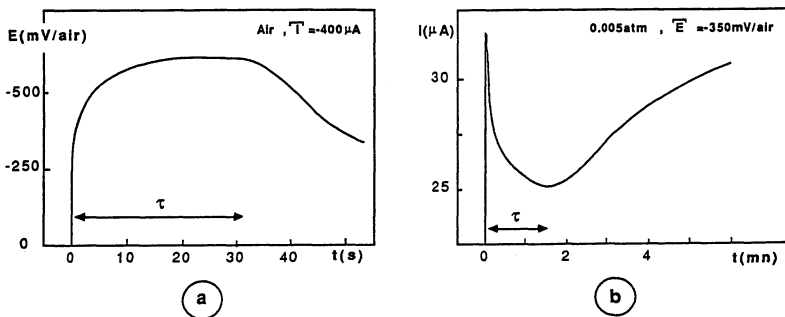


Fig. 5 - Typical transient responses of an electrode to: a) a current step and b) a potential step, located in region II ($x = 0.1$).

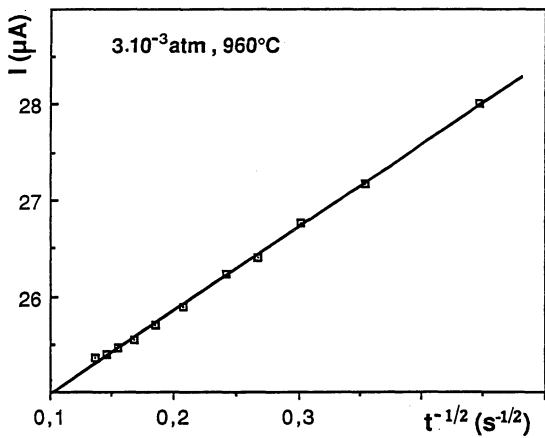


Fig. 6 - $I(t^{-1/2})$ plot of the data shown in Fig.5-b for $t < \tau$.

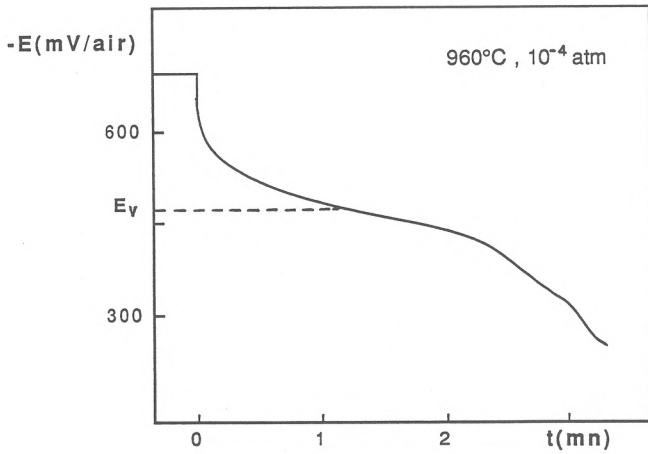


Fig. 7 - Relaxation of the electrode under open circuit, after polarization in region II, $x = 0.4$.

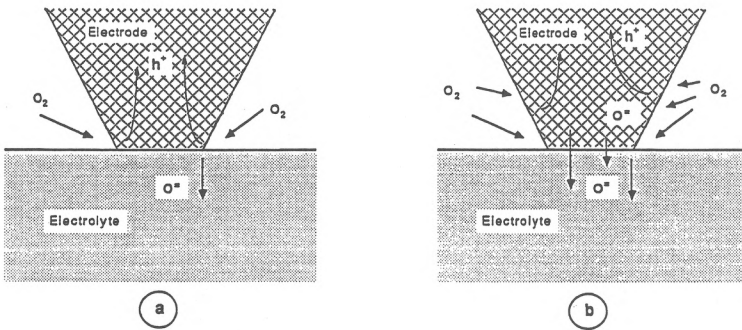


Fig. 8 - Diagram of the oxygen reduction in a solid oxide electrolyte cell with:
 a) a pure electronic conductor b) a mixed (electronic and ionic) conductor.

**TUBULAR
SOLID OXIDE FUEL CELLS**

DESIGN AND PERFORMANCE OF TUBULAR
SOLID OXIDE FUEL CELLS

N. J. Maskalick
Westinghouse Electric Corporation
Research and Development Center
Pittsburgh, PA 15235

ABSTRACT

Single solid oxide fuel cells which, when series-parallel interconnected, combine to form multi-kW modules, are examined in detail to quantify processes affecting available running power. These processes involve power losses across internal resistances, most of which are accounted for by the geometry and known resistivities of the materials employed. Other major power losses are due to diffusion of gases through the electrodes and porous support tube of the cell. The experimental methods employed to determine these quantities are described, along with examples describing the effect of temperature and of current density.

BACKGROUND

High-temperature solid oxide electrolyte cells are the product of much theoretical and experimental work extending from 1900, when Nernst (1) observed the electrolytic evolution of oxygen from a rod of $(ZrO_2)_{0.85}(Y_2O_3)_{0.15}$. Solid electrolytes were studied in oxygen concentration cells by Haber and Moser (2) in 1905.

The transference number of the oxygen ion in $(ZrO_2)_{0.85}(CaO)_{0.15}$ electrolyte is near unity as demonstrated by Kingery, et al. (3). The same electrolyte was used in a cell by Weissbart and Ruka (4) to measure near-theoretical voltages for the hydrogen-oxygen reaction. Archer (5), et al., constructed multi-cell batteries using stabilized zirconia electrolyte and platinum electrodes.

The electrolyte employed by Archer was in a self-supported "bell-and-spigot" geometry. To decrease internal resistance as much as possible, the active cell region of the electrolyte was machined to a minimum practical thickness of approximately 400μ . The machined electrolyte was a comparatively thick structure, wasteful of power due to excessive voltage drop across the large internal resistance.

Electrolyte having considerably less thickness was needed to decrease internal resistance and also to minimize the cost of dense zirconia, particularly where yttria rather than calcia is the stabilizing agent. Isenberg, et al. (6) evaluated a cell with an approximately 30μ thick zirconia-yttria electrolyte, formed by chemical vapor deposition (CVD); which developed near-theoretical open-circuit voltage.

Isenberg (7) also evaluated a 7-cell, series-interconnected unit with 12 cm^2 active cell area. The 40μ thick air electrode was a composite oxide type with porous and partially electronically conducting stabilized zirconia backed by a CVD tin-doped indium oxide current collector. A 30μ electrochemically vapor deposited (EVD) yttria-stabilized zirconia electrolyte and a 30μ sintered cobalt-zirconia cermet completed the cell structure. Interconnection of cells was accomplished with EVD-deposited, magnesium-doped lanthanum chromite. Support for the cells in this design was provided by a porous, calcia-stabilized zirconia tube on the inner (fuel electrode) surface of the 7-cell unit. Such cells were capable of operation at an average power density of $0.24\text{ w}/(\text{cm}^2\text{- electrode area})$ at 1000°C . More than 5000h of operation was achieved with the 7-cell stack using simulated coal gas as fuel. With this data base, the high-temperature solid oxide fuel cell design was then developed into the present type, which is envisioned as best for electrical generator configurations.

This paper describes one part of a multi-phase program to pursue the high-temperature SOFC (Solid Oxide Fuel Cell) technology toward its use in the commercial generation of electrical power. The objective is to establish baseline performance capability under a variety of test conditions for specific sources of fuel such as natural gas. The technology is based on materials, processes and designs developed for technical and economic feasibility.

EXPERIMENTAL

The new cell structure and method of cell interconnection, according to Isenberg (8), is as follows:

The tubular, single-cell design employs a strontium-modified lanthanum manganite cathode, an yttria-stabilized zirconia electrolyte and a nickel cermet anode (Figure 1). The cell component layers are supported on a porous, calcia-stabilized zirconia tube. The anode (outermost layer) of the cell is contacted directly by nickel felt. The cathode (innermost layer) of the cell is contacted by a sealed interconnection (IC) material, which is stable both in oxygen and in fuel/ H_2O gas mixtures. The IC then contacts nickel felt on the exterior surface of the cell. The design thus establishes both cathodic and anodic electrical terminals in the fuel (reducing) atmosphere.

The experimental apparatus is shown schematically in Figure 2. It comprises an alumina muffle tube which contains the test cell in such a way that fuel gas flows upward over the cell exterior while air is admitted to the cell interior. The air is pre-heated within an alumina air feed tube; initially contacts the cell air electrode at the closed, or lower end; then reverses direction and flows toward the open end, where partially spent air and partially spent fuel mix and combust. Typical cell operation is at 85% fuel utilization and 25% air utilization, followed by direct combustion of the remaining gases. The fuel cell produces both electrical and thermal energy.

The apparatus employs nickel bus bars for current leads to a controlled-resistance external load. Platinum leads measure cell potentials directly at the cell anode and cathode. The muffle tube housing is contained within a 3-zone furnace. Cell temperatures are measured within the air chamber with a Pt, Pt, 10% Rh thermocouple. Control over the fuel/H₂O ratio fed to the cell is accomplished by bubbling hydrogen through water which is thermostatically controlled at a temperature corresponding to the desired water partial pressure.

Mixtures of fuel and H₂O are admitted to the cell (anode) at flow rates designed to keep fuel utilization at a constant value, e.g. 85%, during changes in cell operating current. Similarly, air flow matches any cell current to provide for constant air utilization, e.g., 25%.

Experimental values of total cell resistance, R, were obtained by measurement of the virtually instantaneous voltage drop observed by oscilloscope upon interruption of a known current through the cell. These experimental values are in reasonable agreement with calculation based upon the dimensions of the cell, the known resistivity of the electrolyte, and estimates of electrode resistivities.

Since cell construction employs nickel bus bars comprising an equipotential along the entire length of the cell, the working cell voltage, V_T, is constant along the length of the cell, even though fuel/H₂O ratios vary. When current passes through the cell, the terminal voltage is given by:

$$V_T = E - IR - \eta_i \quad (1)$$

where

- V_T = the working voltage of the cell, volts.
- E = the reversible voltage of the cell, volts.
- I = the current passing through the cell, amps.
- R = the electrical resistance of electrodes and electrolyte, and contacts, ohms.
- η_i = the polarization voltage losses associated with irreversibilities in electrode processes, volts.

In general, E , I and η , are nonlinear functions of position along the length of the cell. These parameters are subject to the condition that their sum, at any specific set of operating conditions is equal to, V_T , as in Equation [1]. Thus, each are some mean or weighted average of their local values.

Total voltage losses at the cathode are basically derived by comparison of loaded cell voltage for the cathode in air vs. the cathode in pure oxygen. Within this total cathodic voltage loss, η_d , that portion due to N_2-O_2 counter diffusion in macro pores, is estimated by measurement of the difference of loaded cell voltages in air versus He - 21% O_2 . The difference between total cathodic voltage loss, and η_d is attributed mainly to Knudsen flow in very fine capillaries and is labelled η_x .

Anodic voltage losses, η_f , are estimated by reference to a performance model for the fuel electrode. The model estimates that the observed voltage loss when the fuel gas is diluted with nitrogen, 1:1, volumetrically, is approximately equal to fuel electrode H_2-H_2O counterdiffusion losses in macro pores.

Values of IR-free voltage losses were plotted by adding the applicable IR value to data for the terminal voltage, V_T , versus current, I . η_d , η_x and η_f are similarly added to generate cumulative η_d -free, η_x -free and η_f -free curves which illustrate the individual contributions of each of these voltage-loss components as a function of current density.

RESULTS AND DISCUSSION

Upon connecting the cells to an external load, reproducible V-I curves are obtained. Figure 3, the case of 950°C operation up to 450 mA/cm², shows that virtually all of the voltage drop at 150 mA/cm² is due to IR (ohmic) voltage losses. At 450 mA/cm², diffusion losses, η_d , η_x , η_f have greatly increased, and constitute approximately 50% of the total voltage drop. The topmost curve represents idealized operation with zero voltage loss. Other activated processes, such as charge transfer, comprise negligible contributions to cell power losses.

Figure 4, the case of 1025°C operation up to 450 mA/cm², shows a similar, decreasing voltage loss due to diffusion effects except that, at 450 mA/cm², diffusion-type losses account for only approximately 30%, with η_x -type losses virtually absent. In general, diffusion voltage losses decrease rapidly with increasing temperature so that fuel cell operation is most efficient at higher temperatures.

Cell performance stability is illustrated by output voltage, under constant running parameters, over a period of time. Figure 5 illustrates the loaded voltage of a cell as a function of time at 950°C, 250 mA/cm², 85% H₂ fuel utilization and 25% air utilization. Another aspect of performance stability is the voltage drop due to electrical resistance of the cell. As previously mentioned, IR drop constitutes the major voltage loss in the cell over current densities of practical interest. Figure 5 also shows resistance levels for this test cell during time on test.

SUMMARY

The results of the high temperature cell tests have provided insights with respect to specific voltage losses, and performance stability for tubular solid oxide fuel cell. V_T , the working cell voltage, is affected by four voltage loss components. IR, the material/geometry-based voltage loss due to resistance, constitutes the major inefficiency over current densities of interest. The electrical resistance of the cell is the sum of its parts, metallic and semiconducting. The overall result of increasing operating temperature is to lower cell resistance moderately, resulting in a second-order effect on overall performance, compared to diffusion mechanisms.

Cathode voltage losses derive from N₂-O₂ counterdiffusion through the pores of the cathode structure and also through the porous support tube. Another, lesser cathodic loss is measured which is attributed to Knudsen flow of N₂-O₂ through very small capillaries or grain boundaries.

Anode voltage losses due to counter diffusion of H₂-H₂O are minor and play less of a role in affecting fuel cell performance. In all cases of diffusion limitation, however, increasing operating temperature helps to lower voltage losses and increase performance.

ACKNOWLEDGMENTS

This work was sponsored by the Westinghouse Electric Corporation, and the Morgantown Energy Technology Center, U.S. Department of Energy under Contract #DE-AC21-80ET17089.

REFERENCES

1. W. Nernst, "Über die electrolytische Leitung fester Körper bei sehr hohen Temperaturen," Z. Electrochem. 6, 41, (1900).

2. F. Haber and A. Moser, "Das Generatorgas und das Kohlenelement," Z. Elektrochem. Angew. Physik. Chem., 11, 593, (1905).
3. W. D. Kingery, J. Pappis, M. E. Doty, and H. C. Hill, "Oxygen Ion Mobility in Cubic, $Zr_{0.85}Ca_{0.15}O_{1.85}$," J. Am Ceram. Soc., 42, (8), 393-98, (1959).
4. J. Weissbart and R. Ruka, "A Solid Electrolyte Fuel Cell," J. Electrochem. Soc. 109, (8), 723-726, (1962).
5. D. H. Archer, R. L. Zahradnik, E. F. Sverdrup, W. A. English, L. Elikan, J. J. Alles, "Solid Electrolyte Batteries," Proc. 18th Ann. Power Sources Conf., 36, (1964).
6. A. O. Isenberg, W. A. Pabst, E. F. Sverdrup and D. H. Archer, "A Thin-Film solid Electrolyte Fuel Cell," Division of Fuel Chemistry, Paper No. 24, 158th ACS National Meeting, New York, NY, September 8-11, (1969).
7. A. O. Isenberg, "Energy Conversion via Solid Oxide Electrolyte Electrochemical Cells at High Temperatures," Sol. St. Ionics, 3/4, 431-437 (1981).
8. A. O. Isenberg, "Recent Advancements in Solid Electrolyte Fuel Cell Technology," Abstract, National Fuel Cell Seminar, Newport Beach, CA, 154-156, Nov. 14-18, (1982).

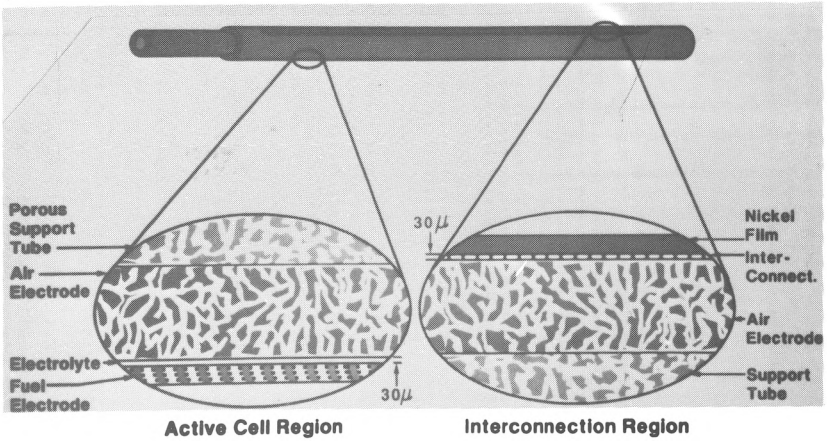


Fig. 1 - Tubular fuel cell in cross-section.

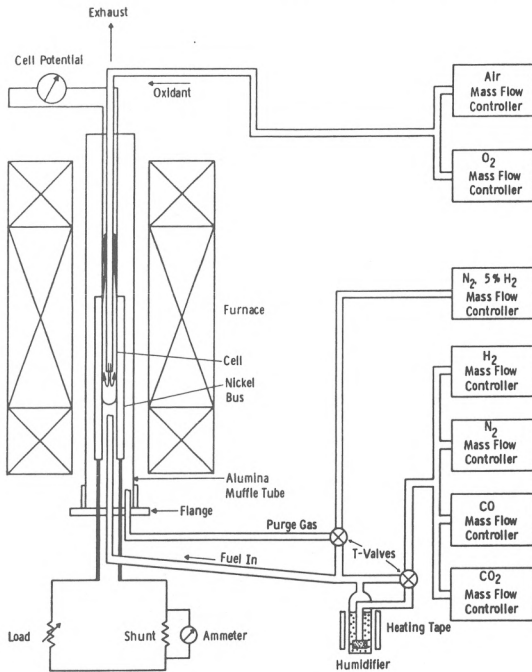


Fig. 2 - Fuel cell test stand schematic.

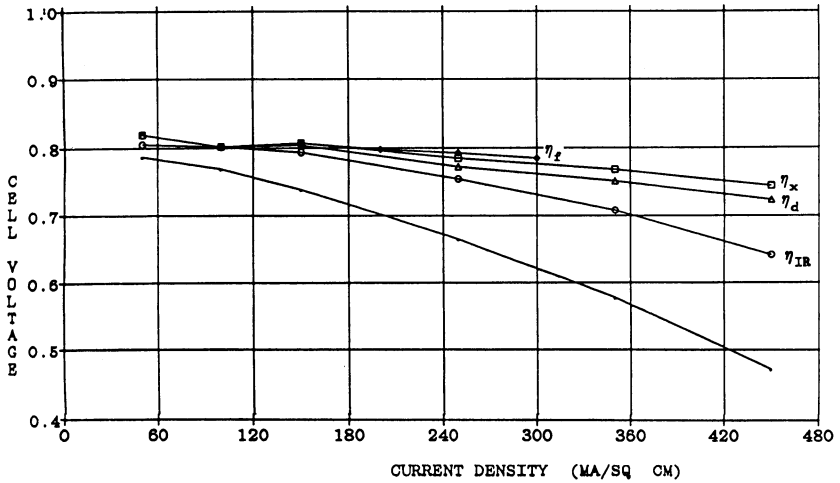


Fig. 3 - The influence of η_{IR} , η_d , η_x , and η_f on tubular fuel cell performance at 950°C, 85% H₂ fuel utilization and 25% air utilization.

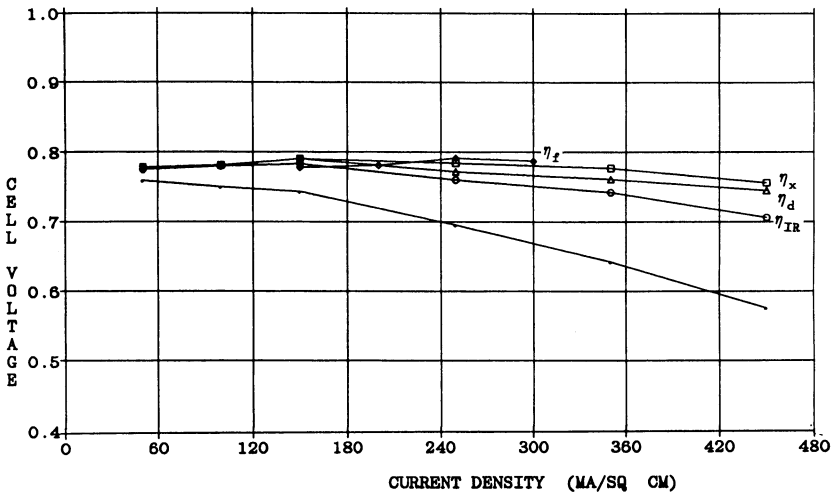


Fig. 4 - The influence of η_{IR} , η_d , η_x and η_f on tubular fuel cell performance at 1025°C, 85% H₂ fuel utilization and 25% air utilization.

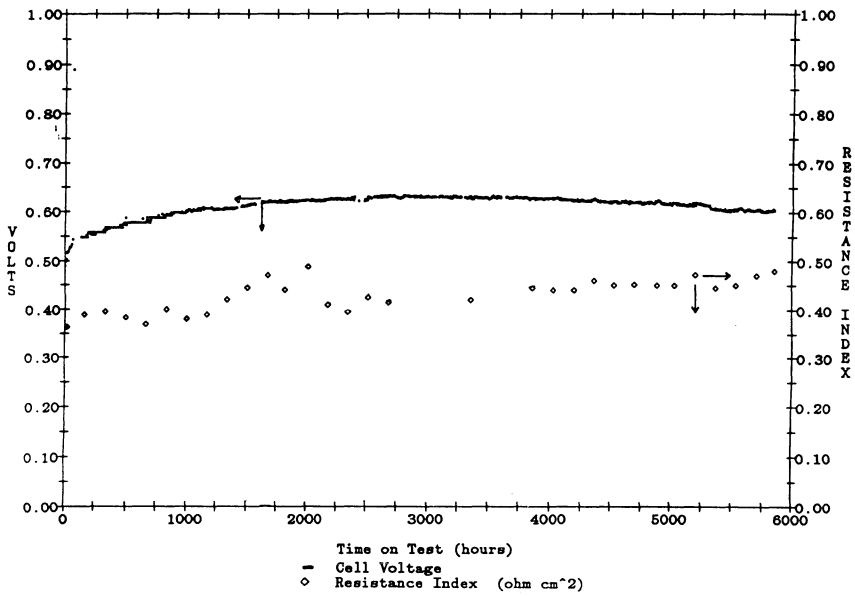


Fig. 5 - Fuel cell voltage versus time on test at 950°C, 250 mA/cm², 85% H₂ fuel utilization and 25% air utilization.

THIN FILM SOLID OXIDE FUEL CELLS WITH
ZrO₂- AND CeO₂-BASED ELECTROLYTES

H. Arai, K. Eguchi, T. Setoguchi
H. Itoh, and T. Inoue

Department of Materials Science and
Technology, Graduated School of
Engineering Sciences, Kyushu University 39
6-1 Kasugakoen, Kasuga-shi, Fukuoka 816,
Japan

Abstract

Thin film solid oxide fuel cells (SOFC) were fabricated using plasma spraying and RF-ion plating methods. The NiO electrode and stabilized zirconia (YSZ) films were plasma-sprayed onto a porous alumina substrate. The open circuit voltage (OCV) and maximum power were 0.9 V and 260 mW·cm⁻² for a single cell, respectively. The fuel cell with a ceria-based electrolyte exhibited higher output power than that with a YSZ electrolyte. The open circuit voltage of ceria-based SOFC could be improved by coating YSZ thin film on the electrolyte at the fuel side, since the reduction of ceria with H₂ was suppressed.

1. Introduction

Development of fabrication techniques for thin film electrolytes and porous film electrodes have been increasingly requested for the practical uses of SOFC to attain high output power. Not only development of thin film technology, but also use of high conductivity materials such as cation doped ceria as an electrolyte is one of the solutions for enhancing the cell performance. In this study, we fabricated SOFC with ZrO₂- or CeO₂-based solid electrolytes by plasma spraying method or RF-ion plating method and measured the current-voltage (I-V) and the current-power (I-P) characteristics of the hydrogen-oxygen fuel cell.

2. Experimental

Figure 1 illustrates the design of tubular SOFC

fabricated by plasma spraying. Porous fuel electrode (ca. 60 μm thick NiO) and yttria-stabilized zirconia (YSZ) (ca. 200 μm thick) were sprayed in sequence onto a porous alumina support tube by using Onoda Cement, APS-7000 equipment. Pt paste was applied on the electrolyte surface as an air electrode and fired at 800 °C. A thin film of YSZ was coated on samaria-doped ceria disk by RF-ion plating technique. I-V and I-P characteristics of $\text{H}_2 + \text{H}_2\text{O} - \text{O}_2$ fuel cell were measured in a flowing system.

3. Results and Discussion

3.1 SOFC with plasma-sprayed YSZ thin film

I-V and I-P characteristics of plasma-sprayed hydrogen-oxygen fuel cell were measured at 800-1000 °C in a flowing system. The open circuit voltage of the single cell (0.9 V) was lower than the theoretical value (1.1 V). Maximum power of the fuel cell was about 14 $\text{mW}\cdot\text{cm}^{-2}$ for the initial type cell. The reasons for low OCV and power are a) gas leakage from electrolyte-alumina interface, b) oxidation of fuel electrode and electric lead, and c) dense microstructure of the fuel electrode. Gas permeation through the electrode was minimized by the control of spraying condition and film thickness to $5.0 \times 10^{-6} \text{ cm}^4\cdot\text{g}^{-1}\cdot\text{sec}^{-1}$ at room temperature. All the NiO part exposed to oxygen was sealed by alumina gas tight film which was plasma-sprayed. The porosity of the electrode was found to change with spraying angle to the substrate. The permeation coefficient of N_2 at room temperature became larger when the plasma spraying torch was set at a smaller angle to the substrate. Under optimized conditions, we fabricated the cell stacks by plasma spraying and measured their performance. The open circuit voltage and maximum power were 0.91 V and 260 $\text{mW}\cdot\text{cm}^{-2}$ for a single cell and 3.5 V and 0.82 $\text{W}\cdot\text{cm}^{-2}$ for a four-cell stack (Fig.2).

3.2 SOFC with CeO_2 -based solid electrolyte coated with YSZ thin film

The ceria-based oxides generally have higher ionic conductivity than stabilized zirconia. Samaria-doped ceria, $(\text{CeO}_2)_{0.8}(\text{SmO}_2)_{0.2}$ (SDC), has the highest ionic conductivity of ceria-based oxides as reported previously(1). However, the open circuit voltage of fuel cell with ceria-based oxide was smaller than the theoretical value which is estimated from the partial

pressure of H_2 , H_2O , and O_2 (Fig.3), because of partial reduction of the ceria-based oxide at the fuel side. We attempted to suppress the reduction of electrolyte by coating thin film of stabilized zirconia by RF-ion plating method on the fuel side of the electrolyte(2). The film quality was optimized by controlling RF-power, bias voltage, and substrate temperature during ion plating process. The open circuit voltage of the fuel cell with YSZ coated SDC approached that of the cell with YSZ and was very stable during operation for 20 h. The voltage drop in the I-V curve of the cell partially resulted from the large anodic overpotential at the YSZ-anode interface, whereas the anodic overpotential was quite small for non-coated SDC-anode interface. Of various metals examined as anode, the power of the fuel cell with Fe or Ni anode was higher than that with Pt anode, because the overpotentials of Fe and Ni anode were smaller than that of Pt anode.

4. Conclusions

- (1) A single SOFC fabricated by plasma spraying method showed the OCV of 0.9 V.
- (2) The porosity of the electrode was controlled by changing the spraying angle to substrate ; the permeation coefficient of N_2 was large for the film sprayed from the small angle.
- (3) SDC has high ionic conductivity, but the reduction at the fuel side deteriorate OCV. With coating YSZ thin film by RF-ion plating method on the fuel side of the SDC, the open circuit voltage approached the theoretical OCV and was stable during the operation.
- (4) The overpotentials of Fe and Ni anode were smaller than that of Pt.

Acknowledgment

The authors wish to express their thanks to Onoda Cement Co.,Ltd. for their experimental support with the fabrication of SOFC stacks by plasma spraying method.

References

- (1) H.Yahiro, Y.Eguchi, K.Eguchi, and H.Arai, J.Appl. Electrochem., 18 (1988) 527-31.
- (2) H.Yahiro, Y.Baba, K.Eguchi, and H.Arai, J.Electrochem. Soc., 135 (1988) 2077-80.

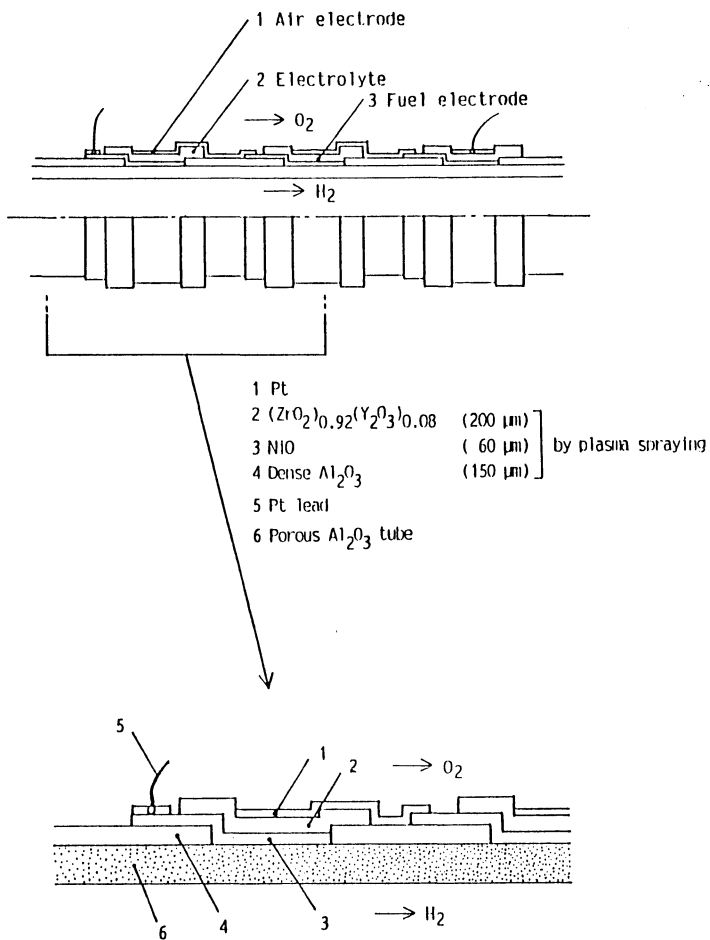


Fig.1 Schematic views of the tubular solid oxide fuel cell.

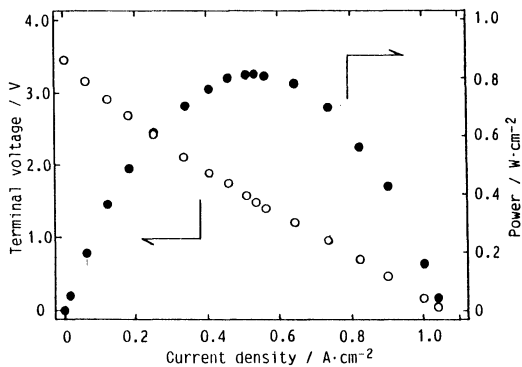


Fig. 2 I-V and I-P characteristics of 4-cells stack at 1002.5 °C.
 H_2 , Ni | 8 mol% YSZ | Pt, O_2

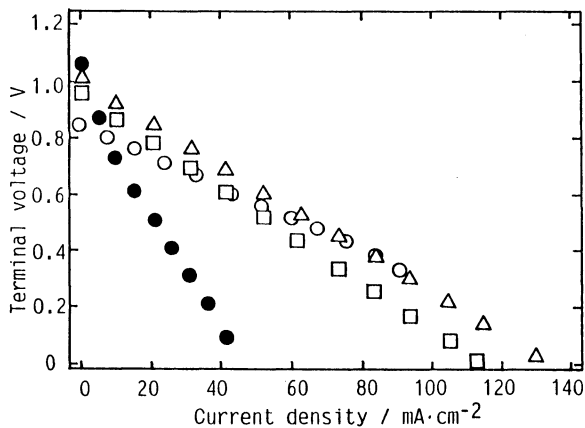


Fig. 3 I-V characteristics of fuel cell at 800 °C.
 □ H_2 , Pt | $(\text{ZrO}_2)_{0.85}(\text{YO}_{1.5})_{0.15}$ coated
 $(\text{CeO}_2)_{0.8}(\text{SmO}_{1.5})_{0.2}$ | M, O_2
 △ H_2 , Fe | $(\text{ZrO}_2)_{0.85}(\text{YO}_{1.5})_{0.15}$ coated
 $(\text{CeO}_2)_{0.8}(\text{SmO}_{1.5})_{0.2}$ | M, O_2
 ○ H_2 , Pt | $(\text{CeO}_2)_{0.8}(\text{SmO}_{1.5})_{0.2}$ | M, O_2
 ● H_2 , Pt | $(\text{ZrO}_2)_{0.85}(\text{YO}_{1.5})_{0.15}$ | M, O_2
 M : $\text{La}_{0.6}\text{Sr}_{0.4}\text{Co}_3$

TEMPERATURE DISTRIBUTION IN TUBULAR SOLID
OXIDE FUEL CELL

Kiyoshi Kanamura, Shoji Yoshioka, Zen-ichiro Takehara
Department of Industrial Chemistry, Faculty of Engineering,
Kyoto University, Yoshida-hommachi, Sakyo-ku, Kyoto 606, Japan

ABSTRACT

The temperature distribution in tubular solid oxide fuel cell (SOFC) was calculated by using finite element method. In order to estimate the temperature distribution, the current distribution and the partial pressure distributions of hydrogen, water, and oxygen were obtained. From the temperature distribution in the tubular SOFC, it can be seen that the heat generated in SOFC flows from the electrolyte region to the porous yttria stabilized zirconia substrate and the hydrogen electrode. The half of heat generated in SOFC was transported to hydrogen gas chamber. If such heat is utilized for the reforming reaction of a hydrocarbon to hydrogen, the total energy conversion efficiency is improved from 70% to 90%. Therefore, the internal reforming fuel cell is attractive.

1. INTRODUCTION

Solid oxide fuel cells (SOFC) have been investigated and developed, because of their high energy conversion efficiency. These researches concentrated on the development of materials for electrodes and electrolytes and the construction of the cell [1]. Recently, the excellent design of SOFC has been achieved by using Electrochemical Vapor Deposition (EVD) [2]. In such a SOFC, the thin electrolyte was deposited on the conductive oxide cathode which was deposited on the porous calcia stabilized zirconia. In this study, the temperature distribution in such a solid oxide fuel cell was calculated by finite element method in order to offer the fundamental data for the development of the high energy conversion SOFC.

The maximum work generated by SOFC corresponds to ΔG of the hydrogen combustion. The energy of $T\Delta S$ cannot be utilized as electric energy in SOFC. Moreover, additional work caused by the overpotentials of hydrogen and oxygen electrodes and the ohmic loss of the electrolyte cannot be utilized as electric energy. In order to minimize such unutilized work, the thickness of electrolyte must be decreased and excellent oxygen and hydrogen electrodes must be developed.

On the other hand, the heat generated in SOFC may be utilized for

the reforming reaction of a hydrocarbon. The calculation of the temperature distribution in SOFC is important to determine the practical operation conditions.

2. CURRENT AND PARTIAL PRESSURES DISTRIBUTIONS
IN TUBULAR SOFC

In this calculation, the heat generation elements and the heat absorption elements were considered as follows. In the case of the tubular solid oxide fuel cell, the heat is generated or absorbed by the following factors;

- (1) Overpotentials of hydrogen and oxygen electrodes.
- (2) Ohmic resistance of yttria stabilized zirconia.
- (3) Ohmic resistance of electrodes.
- (4) Entropy changes of hydrogen and oxygen electrodes.

The overpotentials of hydrogen and oxygen electrodes are dependent on the current. The relationship between the overpotentials and the current has been examined and suggested by many researchers [3,4,5]. In this study, the model cell was constructed by using LaCoO₃ as a cathode, Ni cermet as an anode, and yttria stabilized zirconia as an electrolyte. The following equations were adopted in the calculation of the heat generation from the overpotentials [3]. The electrochemical parameters are listed in Table 1.

For hydrogen electrode, the overpotential (η_{i_a}) is

$$\eta_{i_a} = \frac{RT}{\alpha nF} \ln\left(\frac{I}{I_0}\right) \quad (1)$$

where I is current and I₀ is exchange current.

For oxygen electrode, if the activation and diffusion overpotential is assumed to be negligible, the overpotential (η_{i_c}) is

$$\eta_{i_c} = 0 \quad (2)$$

The heat generation from the ohmic resistance of yttria stabilized zirconia is also dependent on the current. The ohmic resistance of electrodes is negligibly small. The relationship between the voltage loss in the electrolyte (ΔV) and the current (I) obeys Ohm's law.

$$\Delta V = I \times R \quad (3)$$

where R is the resistance of yttria stabilized zirconia. It can be measured by using the impedance method [6].

The heat generation from the thermodynamic entropy change

becomes larger with increasing temperature. The heat of TAS has to be taken into account for the calculation of the temperature distribution. The total reaction in SOFC is the hydrogen combustion. TAS is easily estimated from the thermodynamic consideration. However, in the electrochemical system, the total reaction is separated into cathode and anode reactions. The entropy change is also separated.

$$TAS = TAS_{\text{cathode}} + TAS_{\text{anode}} \quad (4)$$

The entropy changes at cathode and anode can be estimated from Seebeck coefficients of oxygen and hydrogen electrode reaction as reported in [7]. The entropy change of oxygen electrode reaction was estimated to be $-81.6 \text{ J K}^{-1} \text{ mol}^{-1}$ per two electrons under 0.21 atm oxygen partial pressure. The dependence of entropy change on partial pressure can be represented by the following equations.

Total reaction



For hydrogen electrode,

$$\Delta S_{\text{anode}} = (S_{\text{H}_2\text{O}} - R \int_1^{P_{\text{H}_2\text{O}}} d \ln P) - (S_{\text{H}_2} - R \int_1^{P_{\text{H}_2}} d \ln P) - S_{\text{O}_2}^* \quad (6)$$

For oxygen electrode,

$$\Delta S_{\text{cathode}} = S_{\text{O}_2}^* - \frac{1}{2} (S_{\text{O}_2} - R \int_1^{P_{\text{O}_2}} d \ln P) \quad (7)$$

where $S_{\text{O}_2}^*$ is transported entropy of O^{2-} ion. The entropy changes of hydrogen and oxygen electrodes under various partial pressures can be calculated from equations (6) and (7).

Thus $\Delta S_{\text{cathode}}$ changes with the partial pressure of oxygen and ΔS_{anode} changes with the partial pressure of hydrogen and water in solid oxide fuel cell. In other words, the heat generation depends on the partial pressure of hydrogen, water and oxygen. Therefore, the partial pressure distribution has to be estimated in order to calculate the temperature distribution in the tubular SOFC.

The current distribution was calculated by using a model, as shown in Fig.1. The SOFC was divided into n elements. The current passed through each element is represented by I_n . The total current (I) is given by the sum of each element current (I_n).

$$I = I_1 + I_2 + \dots + I_i + \dots + I_n \quad (8)$$

If the electrode or bus bars have excellent electronic conductivities, the cell voltage of each element is equal to total cell voltage (V).

$$V = V_1 = V_2 = \dots = V_n \quad (9)$$

For element 1, the relationship between V_1 and I_1 is represented by the following equation,

$$V_1 = E_e - \eta_i - RI_1 \quad (10)$$

where η_i is given by equation (11) and E_e is determined from the partial pressures of hydrogen, water, and oxygen according to the Nernst equation.

$$\eta_i = \eta_{i_a} + \eta_{i_c} \quad (11)$$

$$E_e = E_0 - \left(\frac{RT}{nF}\right) \ln\left(\frac{P_{O_2}}{P_{O_2} P_{H_2O}^2}\right) \quad (12)$$

For other elements, the same relationship can be established. The hydrogen and air flow horizontally through the chambers in the cell at constant rate, where the flow rate of air is the same as that of hydrogen. The partial pressures of oxygen and hydrogen at the entrances of chambers are higher than that at the exits, because oxygen and hydrogen are consumed by the electrode reactions. The partial pressure in element 2 is given by the following equation,

$$P_{H_2,2} = \frac{I_1}{U_{H_2,1} - \frac{I_1}{2F}}}{U_{H_2,1} + U_{H_2O,1}} \quad (13)$$

The air and water partial pressures are given by similar equations.

$$P_{O_2,2} = \frac{I_1}{0.21U_{air,1} - \frac{I_1}{4F}}}{U_{air,1} - \frac{I_1}{4F}} \quad (14)$$

$$P_{H_2O,2} = \frac{\frac{I_1}{2F} + U_{H_2O,1}}{U_{H_2O,1} + U_{H_2,1}} \quad (15)$$

where $U_{i,1}$ is the molar flux of species i at the entrance of SOFC (mol s^{-1}) and is calculated from the flow rate. In this way, the partial pressures in element 2 can be obtained. As a result, E_e can also be determined. From E_e and V , I_2 can be calculated by using equation (10). Such a procedure is repeated n times. Finally, the current distribution and the partial pressure distribution can be calculated.

Fig.4 shows the current distribution in SOFC at various flow rates of hydrogen. The average current density is 200 mA cm^{-2} . The partial current near the entrance of SOFC is larger than that near the exit. The distribution depends on the flow rate and current. The distribution becomes larger with decreasing flow rate. Fig.5 shows the partial pressure distributions in SOFC at 5 cm s^{-1} ($0.0376 \text{ mol s}^{-1}$) flow rate of hydrogen and air. The hydrogen partial pressure gradually decreases along the Z axis from the entrance to the exit. Under these conditions, 90% of hydrogen introduced in SOFC is consumed by the electrode reaction. The oxygen partial pressure also decreases. The partial pressure distribution of hydrogen is larger than that of oxygen. Thus the flow rate influences the distributions of current and the partial pressures.

In this way, the partial pressure distributions of hydrogen, oxygen, and water and the current distribution in SOFC were obtained. From these results, the heat generation at each element can be estimated. The temperature distribution in SOFC can be calculated by using finite element method.

3. TEMPERATURE DISTRIBUTION IN TUBULAR SOFC

Fig.6 shows the model of the tubular SOFC and the initial and boundary conditions of the calculation. At the interface between the oxygen chamber and the porous yttria stabilized zirconia, the thermal boundary is assumed. Thermal conductivity at the interface is calculated from ρ (density), μ (viscosity), C_p (heat capacity), k (heat conductivity), u (velocity), and D (diameter or length), as summarized in Table 2. The hydrogen and oxygen flow along the Z axis from the entrance to the exit. The hydrogen electrode is made from nickel cermet and its thickness is $500 \mu\text{m}$. The oxygen electrode is made from LaCoO_3 and its thickness is $500 \mu\text{m}$. The electrolyte is yttria stabilized zirconia and its thickness is $500 \mu\text{m}$. Thermal conductivities of these materials are listed in Table 3.

Thus, all parameters used in the calculation of the temperature distribution in the tubular SOFC can be estimated. Therefore the calculation by finite element method was carried out. Fig.7 shows the temperature distribution in the electrolyte along the Z axis. The temperature at the entrance is lower than that at the exit. From the current distribution, it is expected that the heat generated at the entrance is larger than that at the exit. This fact indicates that the heat generated near the entrance of SOFC is transported to the hydrogen gas and oxygen gas and the temperatures in hydrogen and oxygen chambers increase. As a result, the temperature in electrolyte near the exit also increases. The temperature distribution in SOFC strongly depends on the flow rate, and the uniform temperature distribution can be obtained at 30 cm s^{-1} , where the flow rate of air is the same as that of hydrogen gas. With increasing flow rate, the amount of heat transported to gas decreases; as a result the temperature difference between the entrance and the exit becomes small.

Fig.8 shows the temperature distribution along the R axis near the entrance of SOFC. The highest temperature is observed at the cathode region. The temperatures at the porous yttria stabilized zirconia and the nickel cermet electrode are lower than that at the electrolyte. The heat is transported from the electrolyte to hydrogen gas and oxygen gas. The temperature gradient is largest at the electrolyte region.

ACKNOWLEDGMENTS

This work was supported by a Grant-in-Aid for Scientific Research from the Ministry of Education, Science and Culuture of Japanese Government (No.62603016).

REFERENCES

- [1] H.S.Isaacs and L.J.Olmer, J.Electrochem.Soc., 129, 436 (1982).
- [2] W.Feduska and A.Isenberg, J.Power Sources, 10, 89 (1983).
- [3] N.J.Maskalick and D.K.Mclain, J.Electrochem.Soc., 135, 6 (1988).
- [4] N.Nakagawa and M.Ishida, Ind.Eng.Chem.Res., 127, 1181 (1988).
- [5] E.J.Schouler and H.S.Isaacs, Solid State Ionics, 5, 555 (1981).
- [6] A.E.McHale and H.L.Tuller, Solid State Ionics, 5, 515 (1981).
- [7] Z.Takehara, K.Kanamura, and S.Yoshioka, J.Electrochem.Soc., to be published.
- [8] N.J.Maskalick and D.K.Maclain, J.Electrochem.Soc., 135, 6 (1988).

Table 1 Electrochemical Parameters used in the calculation of the current distribution.

Electrochemical parameters	
I_0	9.8 A m ⁻²
αn	1.8*
σ^{**}	0.1 S cm ⁻¹

*:from reference [8].

**: $R=(1/\sigma)(L/S)$; L:thickness of YSZ element, S:surface area of YSZ element.

Table 2 Physical parameters of hydrogen and air at 1273 K.

	$\rho/g\text{ cm}^{-3}$	$\mu/g\text{ cm}^{-1}\text{ s}^{-1}$	$C_p/J\text{ g}^{-1}\text{ K}^{-1}$	$k/J\text{ cm}^{-1}\text{ s}^{-1}\text{ K}^{-1}$
Air	0.276	6×10^{-5}	1.1×10^3	0.2
H ₂	0.019	3×10^{-5}	1.4×10^4	0.1

Table 3 Heat conductivities of the materials in SOFC.

material	$k/J\text{ cm}^{-1}\text{ s}^{-1}\text{ K}^{-1}$
YSZ	0.027
porous YSZ	0.011
LaCoO ₃	0.022
Ni cermet	0.11

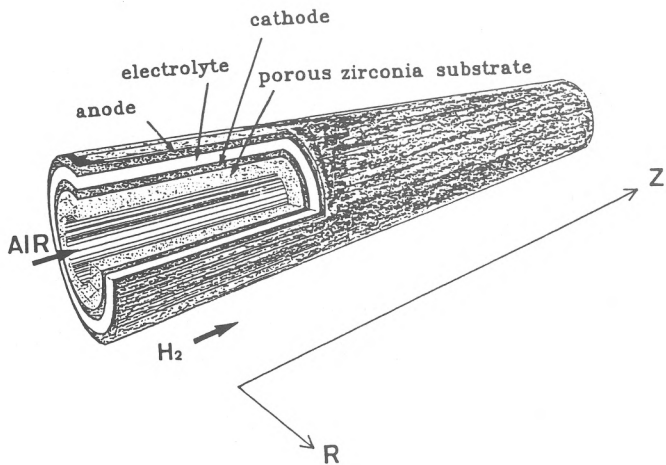


Fig.1 Schematic illustration of tubular SOFC.

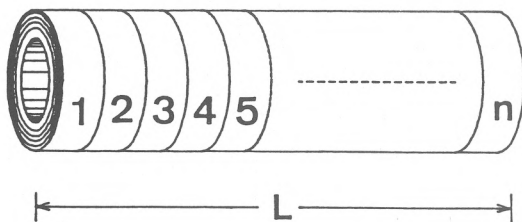


Fig.2 Model for calculation of current and partial pressure distributions.

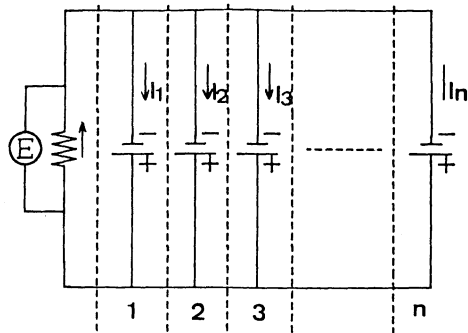


Fig.3 Equivalent circuit of model in Fig.2.

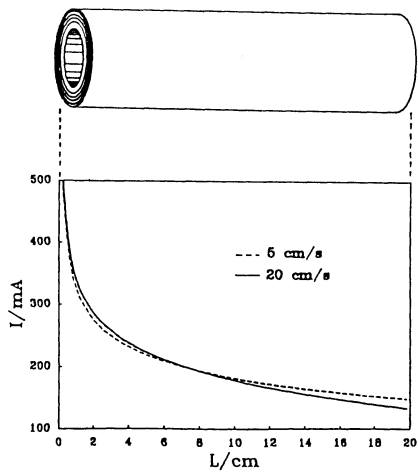


Fig.4 Current distribution in tubular SOFC.

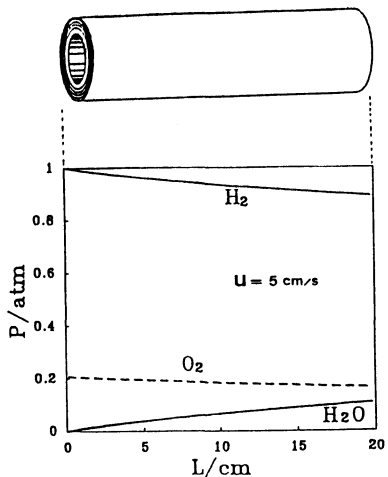


Fig. 5 Partial pressure distribution in tubular SOFC.

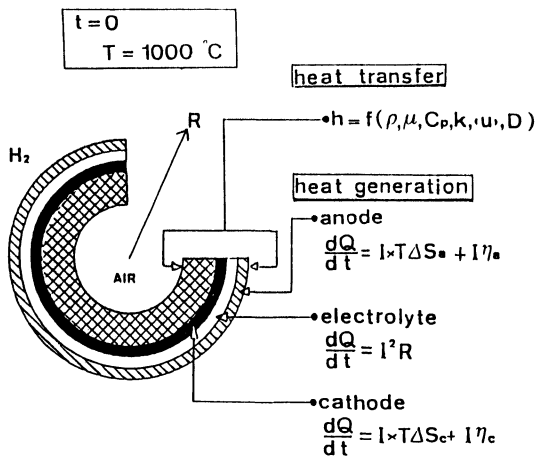


Fig. 6 Model for calculation of temperature distribution and initial and boundary conditions.

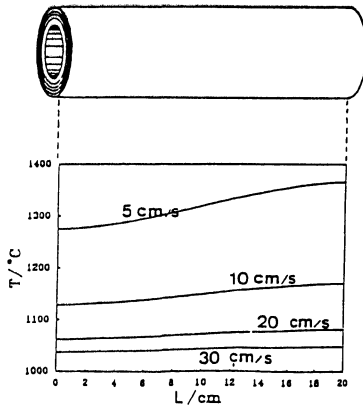


Fig.7 Temperature distribution in YSZ along the Z axis at various flow rates.

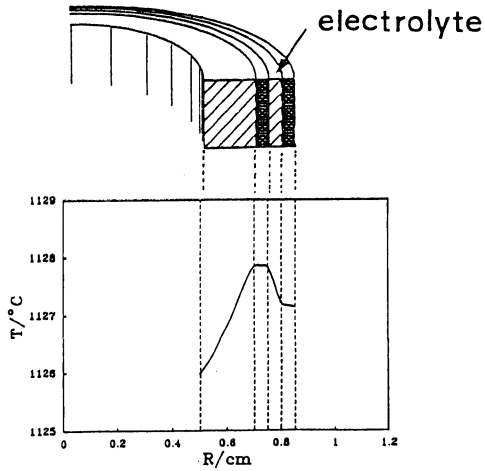


Fig.8 Temperature distribution along the R axis near the entrance of SOFC at 10 cm s^{-1} .

**MONOLITHIC
SOLID OXIDE FUEL CELLS**

FORMING AND PROCESSING OF MONOLITHIC SOLID OXIDE FUEL CELLS

Nguyen Q. Minh, Craig R. Horne, Felix Liu, Paul R. Staszak,
Thomas L. Stillwagon, and James J. Van Ackeren

Allied Signal Aerospace Company
AiResearch Los Angeles Division
2525 West 190th Street
Torrance, California 90504-6099

ABSTRACT

The principal technical challenge in the development of the monolithic solid oxide fuel cell (MSOFC) is fabrication of the intricate structure. Fabrication of the MSOFC requires incorporation of four thin fuel cell layers (anode, electrolyte, cathode, and interconnect) into a self-supporting structure. At present, the MSOFC is fabricated by forming the fuel cell as a green body and cofiring the cell at elevated temperatures to form a sintered monolithic structure. Forming the MSOFC involves fabricating thin tapes, laminating, corrugating, and bonding the various layers into the required structure. Cofiring the fuel cell involves sintering the green body at selected processing conditions. Parameters of the forming and processing steps must be tailored and controlled to produce MSOFC structures with desired properties and free of defects. This paper presents and discusses the results obtained on forming and processing the MSOFC using a fabrication sequence based on the calendaring technique.

1. INTRODUCTION

The monolithic solid oxide fuel cell (MSOFC) is a design concept that places the thin ceramic components of a solid oxide fuel cell in a lightweight, compact structure (1) and so achieves high efficiency, excellent performance, and extraordinarily high power density. In the coflow version of the MSOFC, the fuel cell consists of a honeycomb-like array of adjacent fuel and oxidant channels that resemble corrugated paperboard (Figure 1). The walls of the channels are formed from multilayer laminates of the cell components. As can be seen from Figure 1, the coflow MSOFC is made of two types of laminated structures, each composed of three ceramics -- anode/electrolyte/cathode (A/E/C) and anode/interconnect/cathode (A/I/C). The A/E/C composite is appropriately corrugated and is stacked alternately between flat A/I/C composites. Typical thickness of cell components in the coflow MSOFC is 25 to 100 microns, and the distance from cell to cell is 1 to 2 mm. In the crossflow version of the MSOFC, fuel and oxidant channels are formed from corrugated anode and cathode layers,

respectively (Figure 2). Fuel and oxidant flows are at right angles to each other. The A/E/C and A/I/C composites are flat and stacked alternately between the corrugated anode and cathode layers (2).

One of the major technical challenges in developing the MSOFC is fabricating the intricate structure. Fabrication of the MSOFC involves forming four thin fuel cell layers, incorporating them into the monolithic structure, and cofiring the structure at elevated temperatures to form the required sintered structure. A critical aspect in the fabrication of the MSOFC is to tailor and control forming and processing conditions to produce MSOFC structures with desired properties and free of defects. This paper presents and discusses the results obtained on forming and processing the MSOFC using a fabrication sequence based on the calendaring technique.

2. FABRICATION PROCESS

The materials currently used for the MSOFC are Y_2O_3 -stabilized ZrO_2 for electrolytes, Ni/Y_2O_3 - ZrO_2 cermet for anodes, Sr-doped $LaMnO_3$ for cathodes, and Sr- or Mg-doped $LaCrO_3$ for interconnects. Fabrication of these materials into the monolithic structure must yield: (i) dense electrolyte and interconnect along with porous anode and cathode layers, (ii) good interfacial bonding between adjacent layers, (iii) insignificant reaction and interdiffusion between neighboring layers, and (iv) reliable and crack-free structures. The MSOFC fabrication work reported in this paper is based on the calendaring technique for forming the thin ceramic layers. The calendaring technique has been used for making ceramic tapes (3) and has been developed for preparing electrolyte support structures ($LiAlO_2$) in molten carbonate fuel cells (4,5).

TAPE CALENDERING

The tape calendaring process consists of dispersing the ceramic powder in a thermoplastic organic vehicle system to form a plastic mass. The mass is then sheeted into thin tape using a two-roll mill.

Organic vehicle systems used in calendered ceramic tapes are almost exclusively composed of two components: binders and plasticizers. The binder is a thermoplastic resin and qualitatively, the binder should possess the following properties:

- Confer plasticity upon the ceramic powder sufficient for rolling.
- Wet the powder to aid dispersion and minimize entrapped gas.
- Show stability under mixing and rolling conditions.
- Impart adequate tear strength to the body during forming and sufficient rigidity during the initial stage of binder burn-out.
- Leave a minimal amount of residue after burn-out.
- Have an adequate storage life.

The plasticizer is a minor organic additive the function of which is to increase the plasticity (fluidity) of the ceramic-binder mixture. The plasticizer should have the following properties:

- **Compatibility with the binder:** It should not react but form a softened mixture with the binder, thereby increasing flexibility of the ceramic-binder mixture.
- **Low volatility:** This ensures the retention of the plasticizer during forming operations which is necessary for consistent rheology and moldability.

The criteria for the selection of an organic vehicle system for ceramic tape calendaring is that it will tolerate a high solid volume fraction, provide good tear strength, impart proper rheological properties to the ceramic-binder mixture during rolling, and provide easy removal of the tape from the rolls and molds.

The ceramic-binder mixture must be prepared prior to tape calendaring and, therefore, dispersive mixing of the ceramic powder in the organic vehicle is an important initial step. High-intensity mixers are often used to soften the binder through heat of friction and to achieve uniform dispersion. Additional mixing is promoted by the shear resulting from passage of the plasticized mass between two rolls travelling at different speeds. Final passes through the mill are made with the rolls travelling at approximately the same speeds to achieve high-quality, tear-free tape surfaces. The important factors in tape rolling are roll speed, roll temperature, and number of passes. Good temperature control of the roll surface and a high number of passes are essential for producing tapes of uniform thickness. The tape temperature rise during calendaring must be carefully controlled to prevent binder and plasticizer loss. Organic material loss may cause formation of gas bubbles and may result in brittle tape that is susceptible to cracking during forming.

FABRICATION PROCESS FOR MONOLITHIC SOLID OXIDE FUEL CELLS

The fabrication scheme for the MSOFC based on the calendaring technique is shown in Figure 3 (6). In this fabrication process, ceramic powder, binder, and plasticizer are first blended in a jar mill. The blended materials are then mixed in a high-intensity Banbury mixer to form a plastic mass. The mass is calendared into a thin flat tape using a Farrel two-roll mill. The Farrel mill has two counter-rotating chromium-plated stainless steel rolls with independent variable speed control. The temperature of the two rolls is regulated by independently controlled circulating oil baths, and the separation between the counter-rotating rolls is also adjustable. Tape thickness is controlled by the spacing of the two rolls.

Multilayer composites are fabricated by laminating individual tapes in a second rolling operation. The mechanical force from this second rolling operation bonds the layers of the composite. Two types of composites, A/E/C and A/I/C, are required for the MSOFC. To form coflow MSOFC stacks, for example, the A/E/C composites are corrugated. These corrugated layers are then bonded between flat A/I/C tapes. The MSOFC stack is then processed to remove the binder and plasticizer and sintered into rigid structures.

During processing, the integrity of the fuel cell stack depends upon several factors. First, the individual cell materials must have acceptably close coefficients of thermal expansion to minimize thermal expansion mismatch stresses during cofiring. In addition, the sintering characteristics of the individual layers should match in linear shrinkage rates so that the multilayer composites do not crack or delaminate during firing. In general, there are two stages of shrinkage during firing of a ceramic tape. An example of a typical shrinkage plot of an electrolyte tape during firing as a function of temperature is given in Figure 4. At low temperatures, a small percent of shrinkage of the tape is observed as the organic components are extracted and the ceramic grains are drawn closer together. This amount of shrinkage is directly dependent on the binder and plasticizer loading relative to the surface area of the ceramic powder. At high temperatures, a large percent of shrinkage occurs due to sintering of the ceramic particles. The shrinkage due to high-temperature sintering is directly dependent on the ceramic particle size, surface area, and volume loading. In firing the laminated structures of the MSOFC, it is critical to match the shrinkage profile for all of the components. Any mismatch in the shrinkage profile can cause stress in the fired bodies, resulting in cracking. Cracks through the electrolyte and interconnect layers of the MSOFC will permit cross-leakage of fuel and oxidant. Thus, matching the shrinkage over the temperature range of binder burn-out and sintering is vital to successfully firing the MSOFC stacks.

3. FORMING AND PROCESSING MONOLITHIC SOLID OXIDE FUEL CELLS

Individual cell components, A/E/C and A/I/C composites, and coflow MSOFC stacks have been formed by the fabrication process described above and have been processed at elevated temperatures.

CELL COMPONENTS

Electrolyte: The electrolyte fabricated in this work is made from Tosoh yttria-stabilized zirconia (8 mol% yttria). Thin electrolyte tapes made by calendaring have been sintered to above 94% of theoretical density at 1400°C.

Anode: The anode is made from yttria-stabilized zirconia and nickel oxide powder (The NiO will be reduced to nickel metal when exposed to the fuel in the fuel cell). Porous anodes (up to 23% porosity before hydrogen reduction) have been fabricated. Due to the nickel content, the anode has the highest thermal expansion among the MSOFC components (7,8); therefore, anode raw materials have been tailored to obtain a good coefficient of thermal expansion match with the other components.

Cathode: The cathode is made from HUA Associates strontium-doped lanthanum manganite. Cathode layers of up to 25% porosity have been produced in this work. The properties (specifically, sintering shrinkage and porosity) of the cathode are tailored by varying the starting powder characteristics. Pore formers are also used to increase cathode porosity.

Interconnect: The interconnect used in this work is made from strontium- or magnesium-doped lanthanum chromite. Because of the high volatility of chromium in oxidizing atmospheres, it is difficult to sinter LaCrO₃ to full density in air at temperatures below 1400°C (9,10). Sintering

aids (fluxes) have been used to improve the sinterability of LaCrO_3 . Densities of up to 100 percent of theoretical have been attained by adding certain sintering aids to the LaCrO_3 .

COMPOSITES

Anode/electrolyte/cathode composite: Single cells or A/E/C composites have been fabricated using the calendaring technique. Figure 5 shows the cross-section of a single cell in green state. Green single cells have been fired successfully at 1400°C . Figure 6 shows a scanning electron micrograph of a fracture surface of a sintered single cell. Figures 7A and 7B are high-magnification photographs showing the porous microstructures of the anode and cathode layers, respectively. As can be seen from Figure 6, the electrolyte is dense, while the anode and cathode layers are porous. The single cell has no cracks and displays good bonding between layers.

Anode/interconnect/cathode composite: Fluxed interconnects have been incorporated into A/I/C composites. Figure 8 is a scanning electron micrograph of a polished cross-section of an A/I/C composite. The porous layer at the top is the Sr-doped LaMnO_3 cathode. The middle layer is the high-density interconnect, and the porous layer at the bottom is the $\text{NiO}/\text{Y}_2\text{O}_3\text{-ZrO}_2$ anode. The micrograph shows that the composite can be cofired to yield a porous anode and cathode along with a dense interconnect.

STACKS

Coflow MSOFC stacks of various sizes have been built in this work to demonstrate fabricability of the monolithic structure. Stack fabrication has concentrated on forming corrugations, bonding the composites together, and processing the stack at high temperatures. The corrugation method currently used in stack fabrication is based on compression molding. The A/E/C composite is corrugated using a heated press and a mold that consists of a rubber top and a metal bottom. The corrugations of the mold have right angle peak and valley edges with a side slope of 45 degrees. Uniform corrugations have been formed by this technique. Corrugated A/E/C layers have been bonded between flat A/I/C layers to form coflow stacks (Figure 9). Green stacks have been sintered at 1400°C , and Figure 10 shows a stack after firing. The fired stack exhibits minimum cracking and delamination.

ACKNOWLEDGMENTS

This work is supported in part by Gas Research Institute and Southern California Edison. The authors would like to thank C. Gonzalez and R. Kumar for their assistance in the experimental work.

REFERENCES

1. D. C. Fee, R. K. Steunenberg, T. D. Claar, R. B. Poeppel, and J. P. Ackerman, 1983 Fuel Cell Seminar, Courtesy Associates, Washington, D. C., 1983, p. 74.
2. C. C. McPheeters, D. C. Fee, R. B. Poeppel, T. D. Claar, D. E. Busch, B. K. Flandermeyer, T. E. Easler, J. T. Dusek, and J. J. Picciolo, 1986 Fuel Cell Seminar, Courtesy Associates, Washington, D. C., 1986, p. 44.
3. B. R. Schat and H. J. Engel, Proc. Brit. Ceram. Soc., No. 18, 1970, p. 281.
4. General Electric Company, "Development of Molten Carbonate Fuel Cell Power Plant," Final Report DOE/ET/17019-20(Vol. 2), March 1985.
5. C. D. Iacovangelo and W. D. Pasco, J. Electrochem. Soc., 135, 221 (1988).
6. N. Minh, F. Liu, P. Staszak, T. Stillwagon, and J. Van Ackeren, 1988 Fuel Cell Seminar, Courtesy Associates, Washington, D.C., 1988, p. 105.
7. S. Majumdar, T. Claar, and B. Flandermeyer, J. Am. Ceram. Soc., 69, 628 (1986).
8. D. W. Dees, T. D. Claar, T. E. Easler, D. C. Fee, and F. C. Mrazek, J. Electrochem. Soc., 134, 2141 (1987).
9. D. B. Meadowcroft, Brit. J. Appl. Phys., 2, 1225 (1969).
10. G. Group and H. U. Anderson, J. Am. Ceram. Soc., 59, 449 (1976).

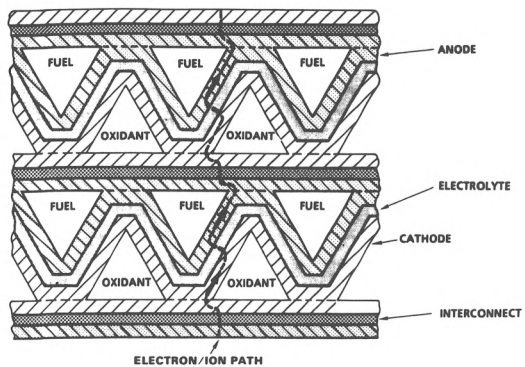


Figure 1. Coflow Monolithic Solid Oxide Fuel Cell.

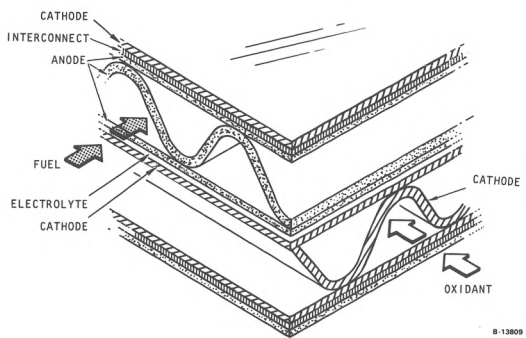


Figure 2. Crossflow Monolithic Solid Oxide Fuel Cell.

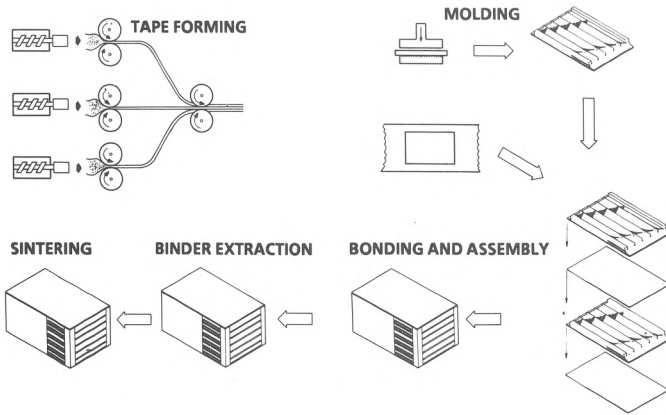


Figure 3. Fabrication Process Based on Calendaring Technique.

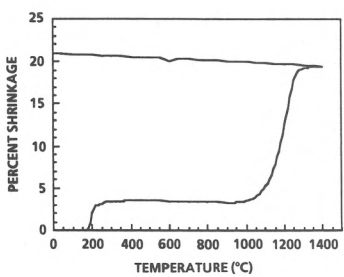


Figure 4. Shrinkage Profile of Electrolyte.

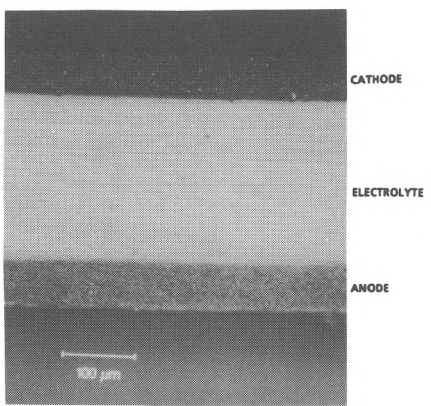


Figure 5. Cross-Section of Green Single Cell.

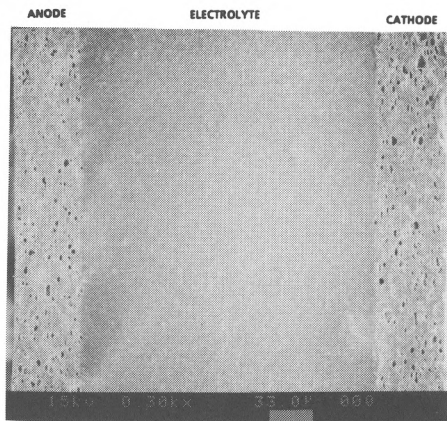


Figure 6. Scanning Electron Micrograph of Fracture Surface of Single Cell.

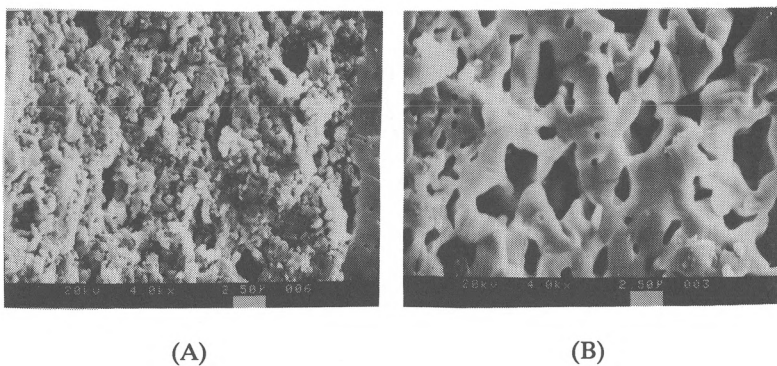


Figure 7. Scanning Electron Micrograph of
(A) Anode
(B) Cathode

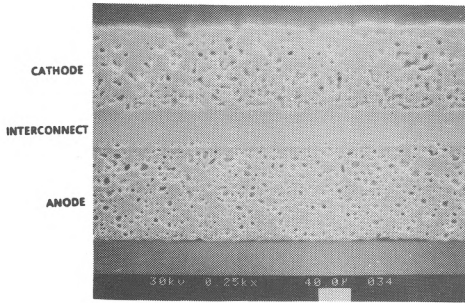


Figure 8. Scanning Electron Micrograph of Polished Cross-Section of A/I/C Composite.

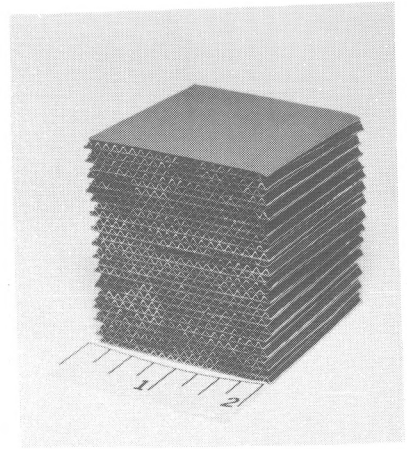


Figure 9. A Green Coflow MSOFC Stack.

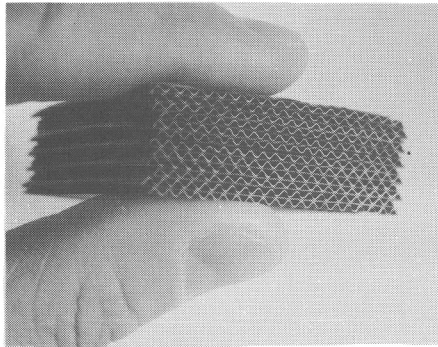


Figure 10. A Sintered MSOFC Stack Made from Calendered Multilayer Tapes.

INTERFACIAL EFFECTS IN MONOLITHIC SOLID OXIDE FUEL CELLS

Dennis W. Dees, Uthamalingam Balachandran, Stephen E. Dorris,
John J. Heiberger, Charles C. McPheeters, and John J. Picciolo

Argonne National Laboratory,
Chemical Technology Division and
Materials and Components Technology Division,
Argonne, Illinois 60439

ABSTRACT

The interfacial resistance of thin three-layer ceramic solid oxide fuel cell composites was studied at 1000°C using AC impedance techniques. The anode interfacial resistance was found to increase dramatically when the H₂O content decreased below 0.03 atm in a H₂/H₂O fuel system. Increases in the anode interfacial resistance were also observed in the presence of H₂S. Significant decreases in the anode interfacial resistance were accomplished by tailoring the electrode's microstructure.

INTRODUCTION

The Monolithic Solid Oxide Fuel Cell (MSOFC) under development at Argonne National Laboratory is an oxide-ceramic structure in which appropriate electronic and ionic conductors are fabricated in a "honeycomb" shape similar to a block of corrugated paperboard (1). The fundamental building block for the structure is an individual fuel cell made of a thin three-layer ceramic composite. The composite is a yttria-stabilized zirconia (YSZ) electrolyte sandwiched between a nickel-YSZ cermet anode and a strontium-doped lanthanum manganite cathode, shown in Figure 1. The fuel cell is operated at 1000°C. The electrochemical performance of the three layer composite is limited by the bulk resistance of the electrolyte and interfacial resistances of each of the electrode-electrolyte interfaces. Reduction of these interfacial resistances is important to obtaining high power densities with the MSOFC.

AC impedance studies are used to examine the fuel cell's electrochemical performance and to separate the bulk resistance from the interfacial resistances (2). A reference electrode is used to separate the interfacial resistance into the anode/electrolyte component and the cathode/electrode component. Anode/electrolyte and cathode/electrolyte interfacial resistances of less than 0.1 Ω cm² have been obtained. In order to determine the interfacial impedance information more accurately, symmetric anode/electrolyte/anode and cathode/electrolyte/cathode composites are fabricated and examined. While both the anode/electrolyte and cathode/electrolyte interfaces

have been examined extensively, the anode/electrolyte interfacial resistance studies are discussed here in detail.

RESULTS

A complex impedance plot of an anode/electrolyte/anode composite is given in Figure 2. The high frequency limit of the real impedance axis is used to determine the bulk resistance of the composite, and the interfacial resistance of the composite is determined by the difference between the low and high frequency limits. Two circular arcs are clearly visible in the complex impedance plot, neither of which is a semi-circle. Circular arcs that do not have true semi-circular shapes are quite common in solid oxide systems and are generally attributed to the distribution of interfacial properties (3). Both circular arcs can be associated with the electrode/electrolyte interfaces and they have a local maximum at approximately 10 and 500 Hz.

The effect of changing the concentration of H_2 and H_2O in the fuel was examined. Generally changing the concentration of H_2 between a few mole percent and pure hydrogen has only a small effect on the interfacial resistance of the electrode. Likewise diluting the fuel with He does little to change the interfacial resistance. Conversely, the partial pressure of H_2O has a significant influence on the interfacial resistance of the electrode. An order of magnitude reduction in the partial pressure of H_2O from 0.03 atm increases the interfacial resistance by approximately a factor of five, with most of this increase occurring in the low frequency circular arc. The decrease in interfacial resistance with increasing H_2O content is not significant once the H_2O content reaches a few percent. It was also observed that changes in interfacial resistance resulting from variation of H_2O partial pressure were found to be totally reversible.

Evidence indicates that H_2O is not the critical component, but oxygen-containing molecules are important. An example of this is the fact that CO/ CO_2 systems perform as well as H_2/H_2O fuels. The effect of H_2O partial pressure on the interfacial resistance has been observed by other researchers in similar systems (4).

The effect of sulfur on the anode/electrolyte interfacial resistance was examined by adding H_2S to the H_2/H_2O fuel. While there was some increase in interfacial resistance the loss in performance of the electrode was not devastating. This is true even at H_2S concentrations in excess of 100 PPM. At concentrations significantly higher than 100 PPM H_2S the nickel is not thermodynamically stable. It should be noted that these tests were relatively short term in that the criteria for a steady interfacial resistance was on an hourly basis. The change in the complex impedance plot for a composite between 0 and 105 PPM H_2S is given in Figure 3. The interfacial resistance increases from 0.271 to 0.446 Ω cm^2 . The interesting aspect is that the chief change in the interfacial resistance is in the high frequency circular

arc. Post test examination of the composites after the sulfur tests reveal that all the electrolyte was discolored (darkened). The discoloration could be a result of sulfur incorporation or oxygen depletion of the electrolyte. Sulfur being incorporated into the electrolyte could explain why the sulfur effects were not reversible.

The microstructure of the interface has a strong effect on the interfacial resistance. Clearly increasing the three-phase (gas, nickel, and YSZ) electrochemically-active area should reduce the interfacial resistance. An example of this is the effect of nickel particle separation on the interfacial resistance. The results of ten different fuel cell tests is given in Figure 4. Generally, reduction in the average nickel particle separation was accomplished by reducing the nickel particle size rather than by increasing the nickel content. One can conclude that significant reduction in the interfacial resistance can be obtained by reducing the nickel particle separation.

CONCLUSIONS

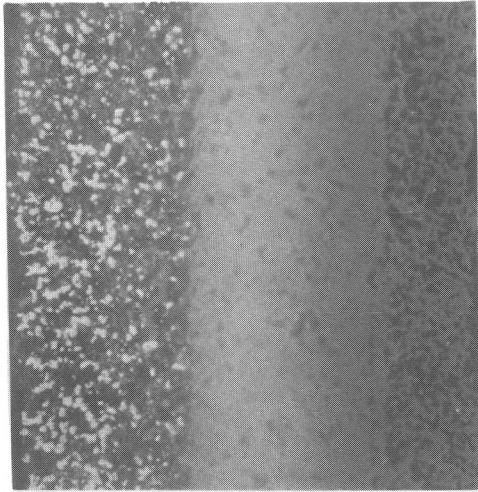
The interfacial resistance of the anode in the MSOFC is influenced by gas composition and electrode microstructure. H_2 fuel should contain at least a few percent H_2O in order to minimize the interfacial resistance of the anode/electrolyte interface. Significant decreases in the interfacial resistance are possible by tailoring the electrode's microstructure.

ACKNOWLEDGEMENTS

This work was sponsored by the Defense Advanced Research Projects Agency of the U.S. Department of Defense under ARPA Order No. 4850. Argonne National Laboratory is operated for the U.S. Department of Energy under contract No. W-31-109-Eng-38.

REFERENCES

1. C. C. McPheeters et al., pp. 29-32, Abstracts of the 1988 Fuel Cell Seminar, Long Beach, CA, October 23-26, 1988.
2. J.R.Macdonald, "Impedance Spectroscopy," John Wiley & Sons Inc., New York (1987).
3. M.Kleitz, H.Benard, E.Fernandez, and E.Schouler, Advances in Ceramics, 3, 310 (1980).
4. E.J.L.Schouler and M.Kleitz, Journal of the Electrochemical Society, 134, 1045 (1987).



10 μm

Figure 1. Optical micrograph of a typical anode/electrolyte/cathode composite

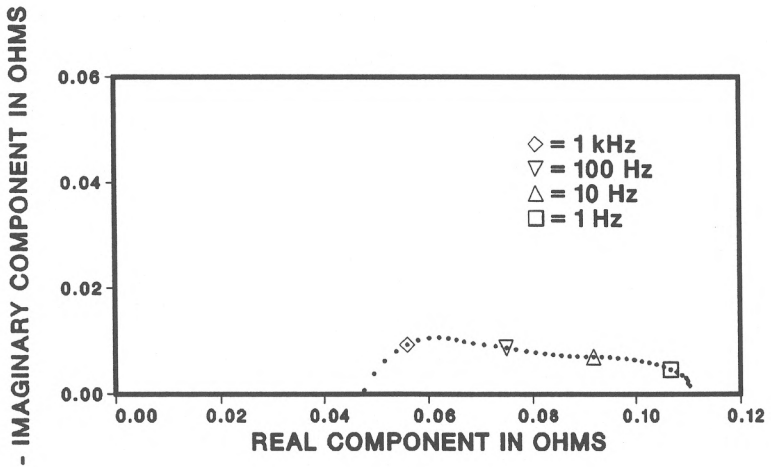


Figure 2. Complex impedance plot of anode/electrolyte/anode composite at 1000°C with $\text{H}_2/\text{H}_2\text{O} = 97/3$ (Area = 6.8 cm^2)

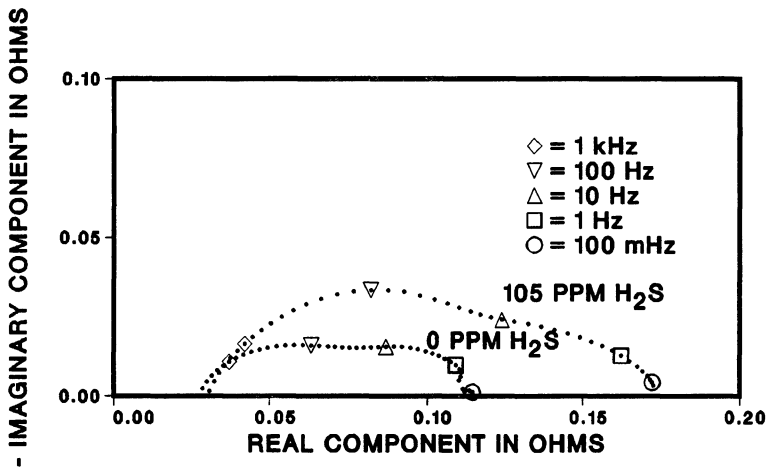


Figure 3. Complex impedance plots of anode/electrolyte/anode composite at 1000°C with H₂/H₂O = 97/3 (Area = 6.4 cm²)

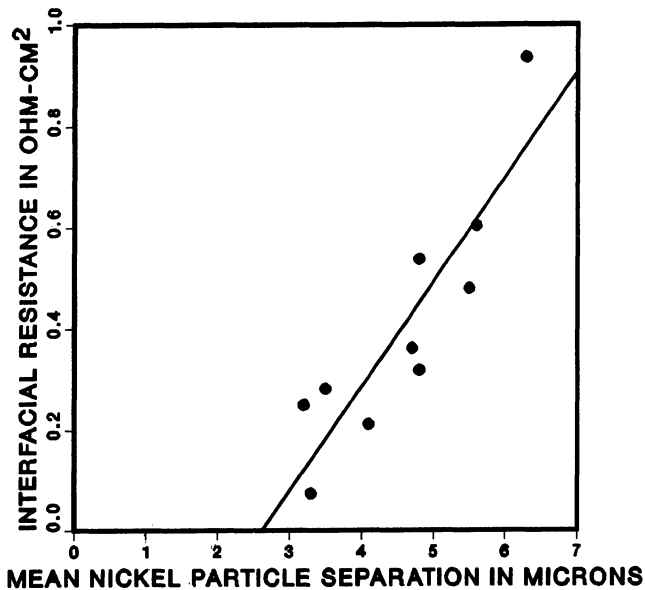


Figure 4. MSOFC anode interfacial resistance vs. mean nickel particle separation

**PLANAR
SOLID OXIDE FUEL CELLS**

OVERVIEW OF PLANAR SOFC DEVELOPMENT AT NCLI

Masayuki Dokiya, Natsuko Sakai, Tatsuya Kawada, Harumi Yokokawa
Tomoo Iwata*, and Masashi Mori**
National Chemical Laboratory for Industry
1-1 Higashi, Tsukuba, Ibaraki, 305 Japan
* Fuji Electric Corporate Research and Development, Ltd.
2-2-1 Nagasaka, Yokosuka, 240-01 Japan
** Central Research Institute for Electric Power Industry
2-11-1 Iwato-kita, Komae, Tokyo, 201 Japan

Abstract

This paper summarizes the present status of investigation on solid oxide fuel cell (SOFC) at National Chemical Laboratory for Industry (NCLI). The main target of the investigation is to clarify the possibility of a large planar SOFC, which is suitable for on-site power generation (10 - 100 MW). Emphases were placed on the following points.

- (1) Thermodynamical study on the compatibility among materials;
- (2) Development of a highly active nickel anode;
- (3) Development of new lanthanum chromites for separator material and ill-sinterable lanthanum manganites for cathode material;
- (4) Development of a method of fabricating a planar SOFC by cheap tape casting and co-firing.

1. Introduction

Planar solid oxide fuel cell (SOFC) will be more suitable than tubular SOFC as far as relatively large scale (10 - 100 MW) on-site power plants are concerned, because (1) the internal ohmic resistance of tubular cells will be larger than that of planar cells[1] and (2) the tubular cells require a large number of cell tubes. Our target is to fabricate, using cheap tape casting process, cells which have effective electrode area as large as 1000 cm² or even much larger, if possible. The possibility of a large scale planar cell is, however, suspected from two reasons; (1) difficulties associated with the fabrication process and (2) cell destruction by thermal stress[2].

Difficulties in fabrication arise mainly from the fragility of fully yttria stabilized zirconia (FSZ). A large sintered plate of FSZ will be too fragile to be handled by hands. Two methods have been investigated in the present study to overcome this fragility of FSZ; (1) attaching borders to a FSZ plates and (2) co-firing green cell components as one piece.

The co-firing method requires compatibility of constituent materials during sintering. It is well known that a separator material, lanthanum chromite, cannot be sintered to a gas-tight

dense plate in air. It was found that a cathode material, lanthanum manganite, also cannot be fired and joined to a FSZ plate above 1470 K because it loses activity as an electrode. Therefore, new materials have been investigated for a separator and a cathode to make the co-firing process feasible.

2. New materials

2.1 Sinterable lanthanum chromite; $(La_{1-x}Ca_x)(Cr_{1-y}Ca_y)O_3$

A dense gas-tight separator (interconnector) is an indispensable component of SOFC, both for tubular and planar cells. Thermodynamical study suggested that lanthanum chromite is the only one perovskite which is stable in hydrogen as well as in air as shown in Fig.1. It is also chemically compatible with the FSZ electrolyte, the Ni anode, and the lanthanum manganite perovskite cathode. Technological difficulty arises from the ill-sinterable nature of this compound. High sintering temperatures make chromium trioxide evaporate very rapidly.

We found that chromium deficient lanthanum calcium chromite can be sintered in air to gas-tight dense plates. The composition region of this perovskite is shown in Fig.2. For convenience, this compound is expressed as $(La_{1-x}Ca_x)(Cr_{1-y}Ca_y)O_3$, although it has not been yet confirmed whether calcium really substitutes B site or not. The width of chromium deficit "y" seems to be small (about 1 - 3 %). The precise determination of chromium deficit "y" is now under progress. The vapor pressures of chromium trioxide gas shown in Fig.2 have been estimated using "CTC/SOLGASMIX" system[3]. The estimated vapor pressure of chromium trioxide suggests that the low vapor pressure of chromium deficient perovskite helps the sintering of this compound. As shown in Fig.3, this new chromite has high electrical conductivity, sufficient enough for separator materials. Fig.4 shows that this perovskite was sintered to more than 90 % of theoretical density in air.

2.2 New air electrode material; $(La_{1-x}Sr_x)(Mn_{1-y}Cr_y)O_3$

Thermodynamics predicted that perovskite of cobalt or nickel will react with zirconia as shown in Fig.5. Lanthanum manganite, cathode material, has almost the same thermal expansion coefficient as FSZ. Feduska et al[4], Mizusaki et al[5], and Okuyama et al.[6], found that this manganite degraded its electrode activity and in some conditions reacted with FSZ yielding $SrZrO_3$ or $La_2Zr_2O_7$, after being fired with FSZ electrolyte above 1470 K. We found that 10 % manganese excess perovskite, $(La_{1-x}Sr_x)_{0.9}MnO_3$, is relatively stable. The sinterability, however, is promoted by excess manganese. We have investigated the chemical stability of this compound thermodynamically[7]. Fig. 6 shows the thermodynamically predicted relationship between A-site deficit(1-y), O^{2-} deficit (δ), and valence of manganese(n). The shaded area in Fig.6 shows the region in which lanthanum manganite can exist stably but can

react with zirconia (between A1 and A3). The perovskite in the lower region (between A2 and A3) can make stable contact with FSZ at 1573 K. The chemical stability can be summarized as follows: (1) This perovskite is a non-stoichiometric compound; (2) the chemical stability with FSZ depends on the extent of manganese excess, and (3) the deficiency of manganese will promote the reaction with FSZ.

These results indicate that the stabilization of lanthanum manganite is indispensable for co-firing process. We have tried to stabilize lanthanum manganite by mixing lanthanum chromite with an aim of preventing sintering and reaction with FSZ. It was found that $\text{La}(\text{Sr})\text{Mn}(\text{Cr})\text{O}_3$ has ill-sinterable nature compared to $\text{La}(\text{Sr})\text{MnO}_3$ and can be mounted on FSZ at a temperature as high as 1720 K. The activity is, however, relatively low compared to the corresponding manganite mounted at 1420 K. Further improvement is now being attempted.

2.3 Ni-FSZ cermet anode

Fig.7 shows a single cell performance with a 0.17 mm thick FSZ plate. Anodic polarization was the largest irreversible loss. It was found that fine dispersion of Ni is required to obtain high electrode activity from X-ray micro probe analysis. It was also found that pre-sintering of Ni-FSZ cermet is also required to obtain high electrode activity as shown in Fig.8. Reaction resistances increased at the initial stage of cell operation using Ni-FSZ cermet anodes which were prepared at lower pre-sintering temperatures. This result suggested a possibility of Ni particle migration during cell operation. Electrodes prepared from three different raw materials showed almost the same activity as shown in Fig.9. It will be required to add some promoters or to regulate electrode texture to obtain higher electrode activity.

3. Cell Fabrication

3.1 Bordered cell and its performance

Borders were attached to an electrolyte plate in order to reinforce fragile electrolyte plate and also to furnish gas inlet and outlet: fuel gas holes opened onto the top surface of electrolyte and closed at the bottom, and vice versa for air holes. Green films of FSZ were prepared by a doctor blade method, layered at borders, and then co-fired. The central part of electrolyte plate thus prepared was still too fragile to fabricate large cells. A lanthanum chromite separator plate was also prepared by sintering of a doctor blade film. The single cell performances are shown in Fig.10. Results of a very small cell (0.3 cm^2) showed fairly high latent potentiality of planar SOFC, whereas those of enlarged cells (7 cm^2) were worse than the small cell, though improvement was achieved step by step as shown in Fig.10. This was achieved mainly by improving current collection. Stacked cells were fabricated with these

electrolytes and separators. A performance test is now under progress with the stacked cells.

3.2. Co-firing process

A co-firing method was investigated on the following three combinations of green films and ceramic foam membranes:

- (A) distributor/anode/electrolyte/cathode/distributor
- (B) distributor/binding film/separator/binding film/distributor
- (C) (A) + (B)

Ceramic foam membranes were adopted as distributor in an attempt to reduce thermal stress during co-firing and cell operation. Materials for distributor were FSZ, lanthanum chromite, lanthanum manganite, Ni-FSZ cermet, or mixtures of them. Green ceramic foam membranes were prepared by dipping poly-urethane foam membranes in slurries of ceramic powders and organic binders. Very porous (80 - 90 % porosity) ceramic foam membranes were obtained on burning organic binder and then sintering.

Good adhesion is the most important factor to co-fire composite plates without cracks. Use of binding films cannot be avoided to ensure good adhesion between films and ceramic foam membranes. It should be noted that pin holes were detected especially when solvents were used to attain good adhesion between films and ceramic foam membranes. It was observed that solvents destroyed uniform texture of green films. Green composite plates were sintered to flat plates when the same kinds of raw materials were used, whereas composite plates waved when different kinds of materials were combined. In the case of combination (C), almost all samples separated between films and ceramic foam membranes. Stacked cells can be fabricated piling composite plates (A) and (B) alternately. Several attempts were made to combine the "bordering" and the "co-firing" methods to furnish gas inlet and outlet on the composite plate in order to furnish an internal gas manifold. Holes were furnished successfully whereas borders produced cracks in some cases. The merit of piling composite plates (A) and (B) is easy sealing of gas holes, because we can use adhesive or filler agents to help gas sealing of holes. We think that such a fabrication method will be more suitable for a large planar cell than fabricating a cell as one piece. The largest composite plates obtained was about 80 mm square which was the limit of size producible by our electric furnace.

4. Conclusions

New materials were found for a sinterable separator and an ill-sinterable cathode; $(La_{1-x}Ca_x)(Cr_{1-y}Ca_y)O_3$ and $(La_{1-x}Sr_x)(Mn_{1-y}Cr_y)O_3$. These two materials made the co-firing fabrication of a planar SOFC feasible. A distributor which has ceramic foam structure was found to be an effective material to reduce thermal stress during co-firing. Fragile electrolyte plates can be reinforced by supporting with this distributors of ceramic foam membranes. This method will be applied to

fabrication of a large planar cell.

References

- (1) D. C. Fee, S. A. Zwick, and J. P. Ackerman, "Solid Oxide Fuel Cell Performance" in Proc. of the Conference on High Temperature Solid Oxide Electrolytes-1983, (compiled by F. J. Salzano), BNL 51728 (1983), vol.1, p.29
- (2) C. Lu and T. M. Maloney, "Mathematical Modeling of Solid Oxide Fuel Cells", in Abstract of National Fuel Cell Seminar-1988, vol.1, p.78 (1988)
- (3) H. Yokokawa, M. Fujishige, S. Ujiie, and M. Dokiya, "CTC: Chemical Thermodynamic Computation System", Journal of the National Chemical Laboratory for Industry, vol.83 (special issue) (1988)
- (4) W. Feduska, A. O. Isenberg, D. Q. Hoover, J. E. Bauerle, J. G. Cleary, L. J. Ceschini, R. E. Grimble, R. R. Jensen, S. K. Lau, B. R. Rossing, R. J. Ruka, S. C. Singhal, C. J. Spengler, and G. E. Zymboly, "High-temperature Solid Oxide Electrolyte Fuel Cell Power Generation System", DOE/ET/17089-18, Westinghouse Electric Corporation R&D Center (1984)
- (5) J. Mizusaki, H. Tagawa, K. Tsuneyoshi, K. Mori, and A. Sawada, to be published in Solid State Ionics
- (6) R. Okuyama, private communication
- (7) H. Yokokawa, N. Sakai, T. Kawada, and M. Dokiya, to be published in Denikagaku
- (8) B. F. Flandermeier, M. M. Nasrallah, D. M. Spalin, and H. U. Anderson, High temperature science, 259, 20 (1985)

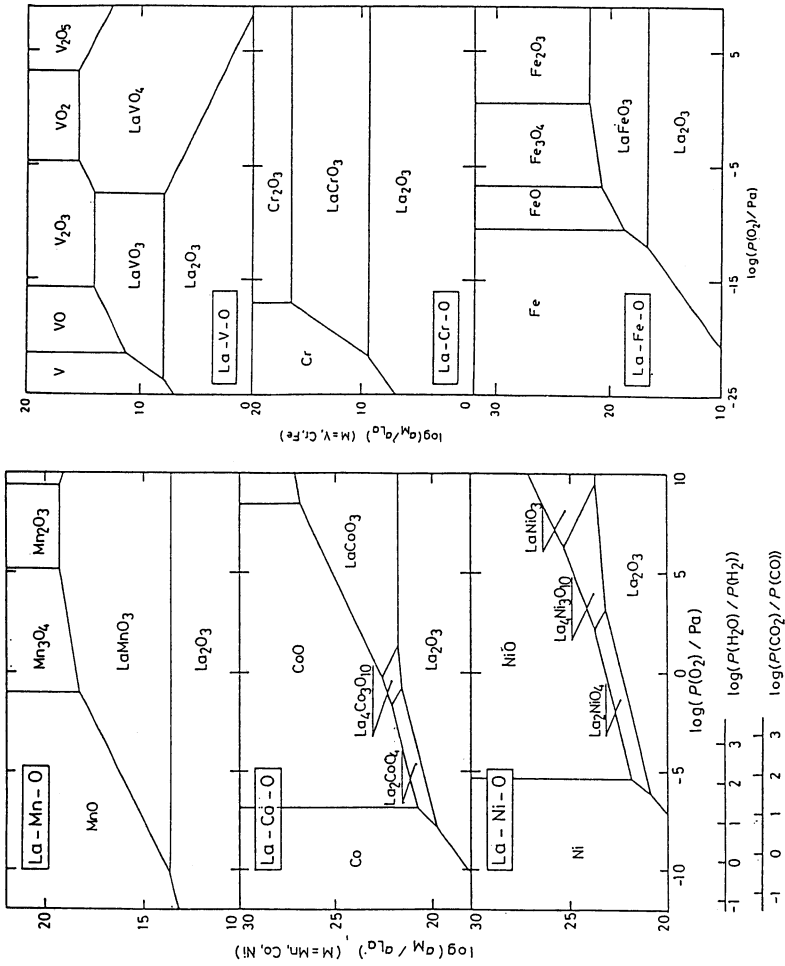


Fig.1 Stability of Perovskites at Oxygen Partial Pressures.

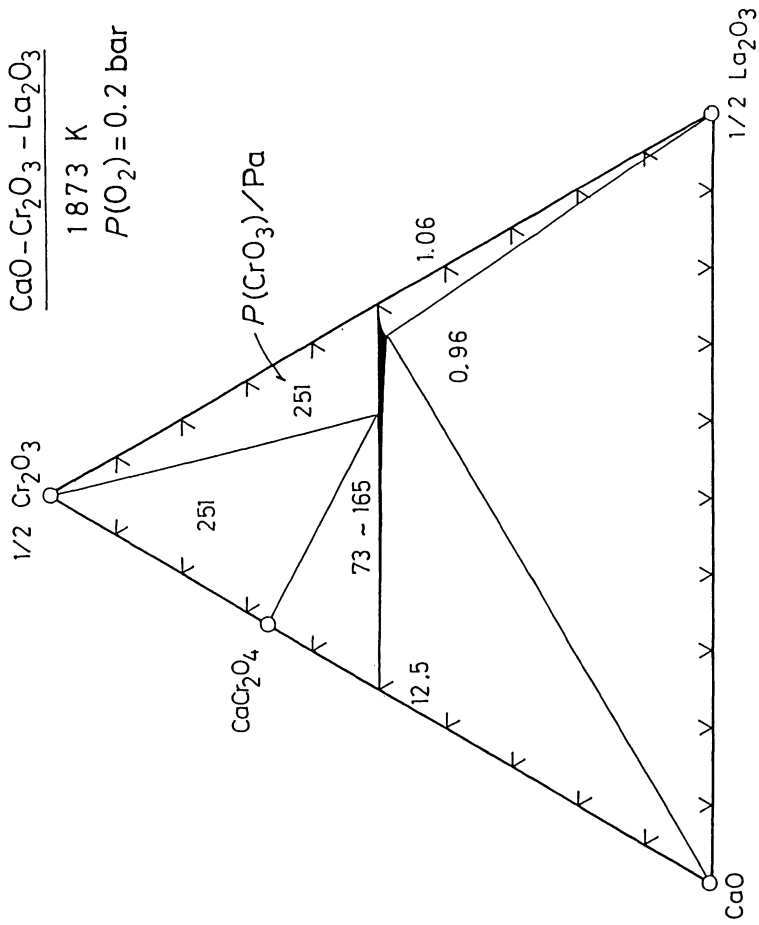


Fig. 2 Phase Diagram and Vapor Pressure of CrO_3

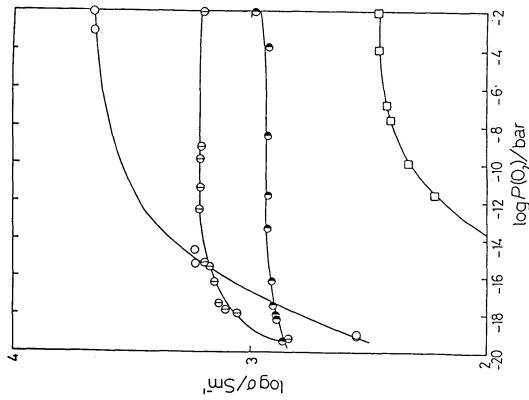


Fig.3 Oxygen Partial Pressure Dependence of Electrical Conductivity of $(La_{1-x}Ca_x)(Cr_{1-y}Ca_y)O_3$ at 1193 K.
 ○ : $(La_{0.70}Ca_{0.30})(Cr_{1-y}Ca_y)O_3$
 ○● : $(La_{0.92}Ca_{0.08})(Cr_{1-y}Ca_y)O_3$
 ● : $(La_{0.97}Ca_{0.03})(Cr_{0.97}Ca_{0.03})O_3$
 □ : $La(Cr_{0.9}Mg_{0.1})O_3$
 (Flandermeier et al. [8])

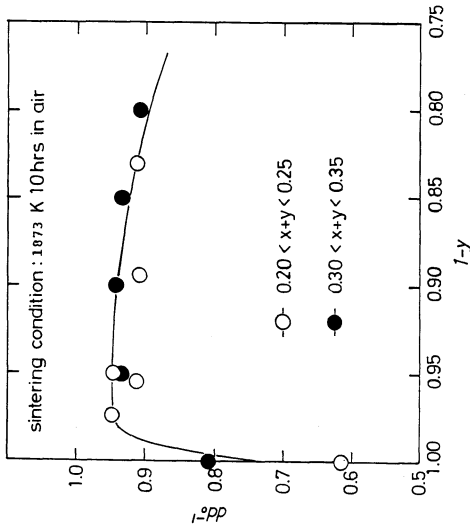


Fig.4 Effect of Chromium Deficit on Relative Density for $(La_{1-x}Ca_x)(Cr_{1-y}Ca_y)O_3$: The data are classified by content of Calcium (X + Y).

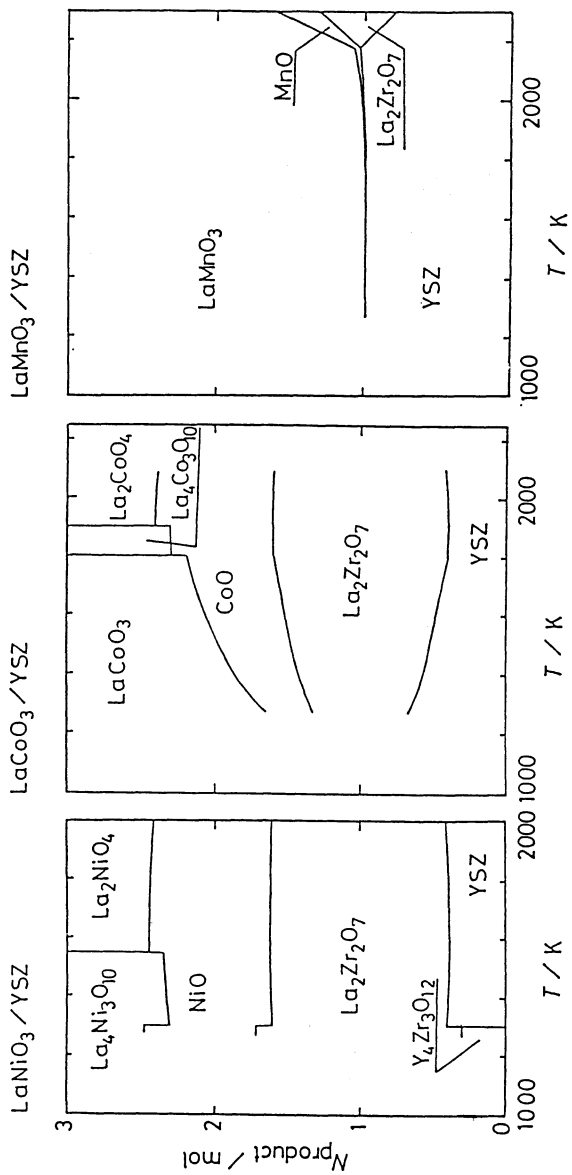


Fig.5 Reactivity of Perovskites with ZrO₂ at Different Temperatures.

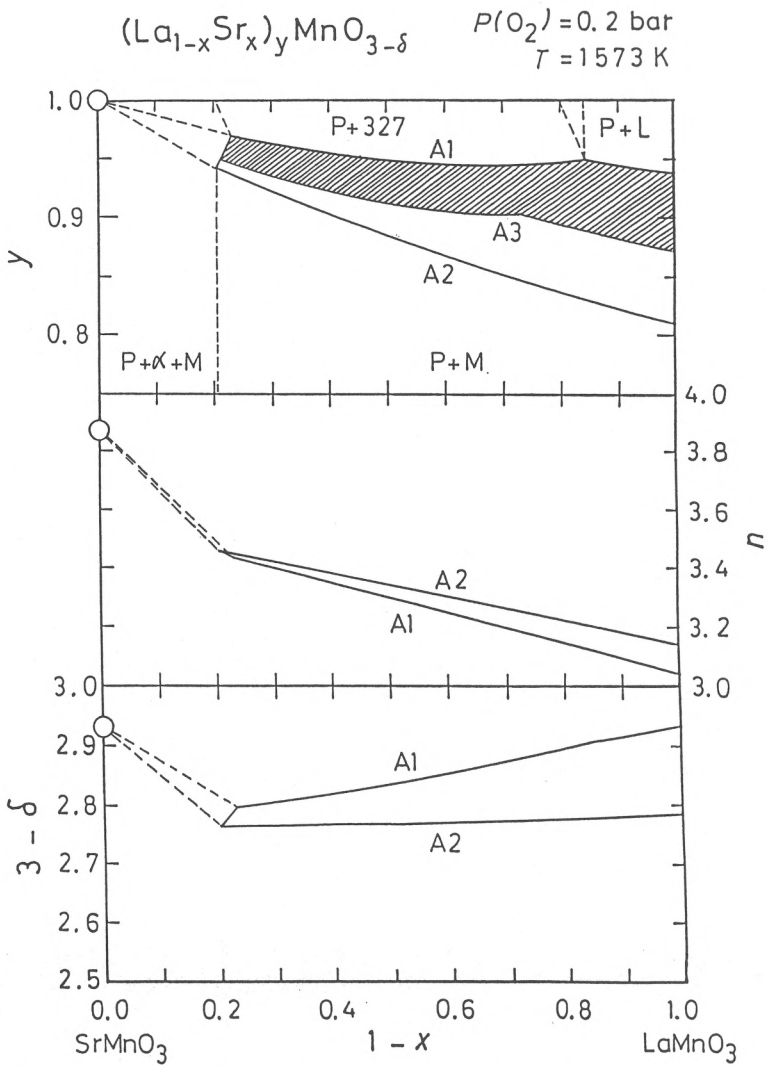


Fig.6 Stability of $\text{La}(\text{Sr})\text{MnO}_3$ in Relation with A-site Deficit ($1-y$), O Deficit (δ), and Average Valence of Mn (n): Shaded region between A1 and A3 is unstable against the reaction with YSZ and the region between A2 and A3 is stable at 1573 K.

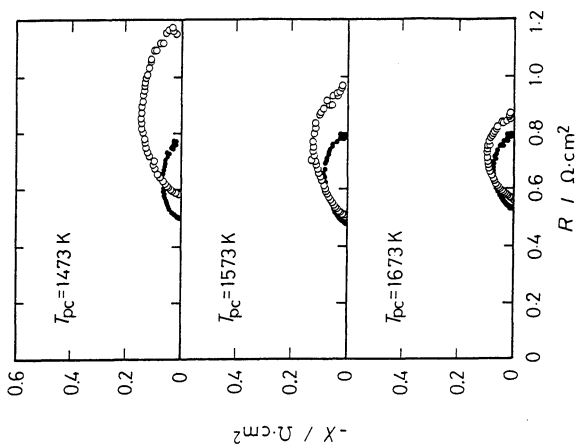


Fig.8 Effect of Pre-sintering Temperatures: (T_{pc}) at 1273 K with $H_2/H_2O = 97/3$; Ni (40 %) -FSZ was sintered at 1773 K.

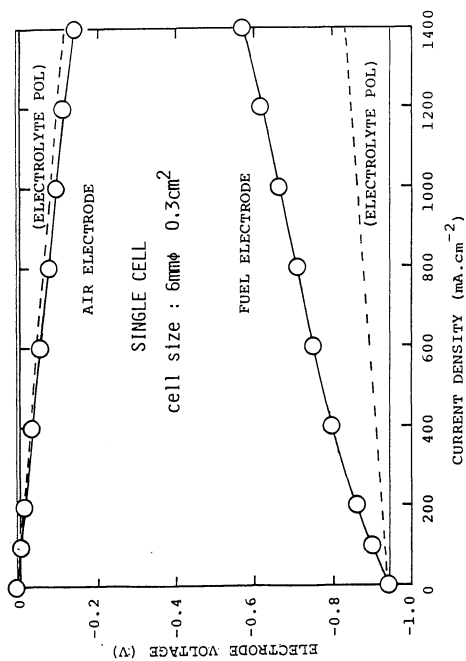


Fig.7 Single Cell Performance with 0.17 mm FSZ Disk (6 mm diameter)

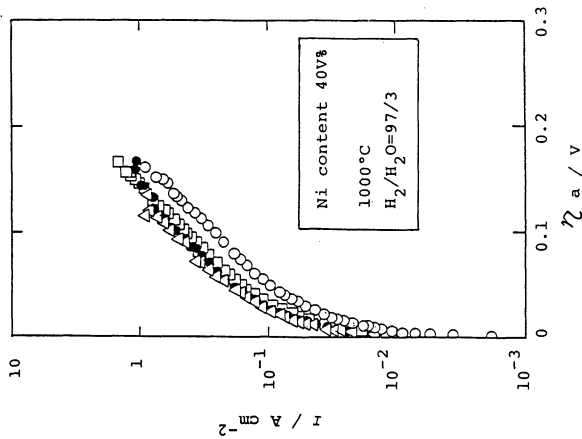


Fig.9 Polarization of Ni-FSZ Cermet Anode:
 ○: NiO, powder mixing, pre-sintered at 1673 K,
 sintered at 1673 K.
 ●: NiO, powder mixing, pre-sintered at 1673 K,
 sintered at 1773 K.
 ▲: NiCO₃H₂O, powder mixing, pre-sintered at
 1723 K, sintered at 1673 K.
 □: Ni(C₂O₄), mixed in slurry, pre-sintered at
 1773 K, sintered at 1773 K.

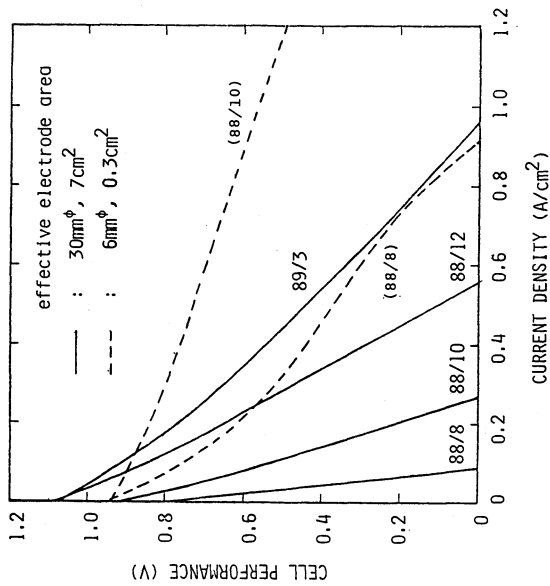


Fig.10 Single Cell Performances
 with FSZ Plates of
 Different Sizes.

FABRICATION TECHNOLOGIES FOR A PLANAR SOLID OXIDE FUEL CELL

P.A. Lessing, L.W. Tai and K.A. Klemm

Materials and Metallurgical Engineering Department
New Mexico Institute of Mining and Technology
Socorro, New Mexico, 87801, USA

ABSTRACT

Promising methods for fabrication of a planar SOFC stack are reviewed. A processing sequence under study at NM Tech utilizes methods selected to minimize layer interdiffusion by keeping substrate temperatures low during fabrication while producing the optimum density (low or high) required in each component. Results of a low temperature CVD study using organometallic precursors to produce ZrO_2 doped with Y_2O_3 and a sintering study in air of $LaCrO_3$ doped with SrO are presented.

1. INTRODUCTION

Since September 1986, the authors have been pursuing a program to develop new planar solid oxide fuel cell designs and appropriate fabrication technologies. A schematic of a typical planar design (Figure 1) shows utilization of very thin layers of zirconia based electrolyte, perovskite type materials for the air electrode (cathode) and interconnect, and a Ni- ZrO_2 cermet for the fuel electrode (anode). Properties required for the various components are given in Table I.

Many variations of the basic planar design and alternate materials are possible. It may be feasible to replace the ZrO_2 -Ni cermet anode with a "n-type" semi-conducting ceramic. Doped "n-type" conductive ceramics for use as fuel cell electrodes were studied by Lessing et. al.^[1]. The dc resistivities of the various compounds were measured under gas compositions and temperatures typical of high temperature fuel cells.

Oxide ceramics are much more tolerant to sulfur contamination in the fuel gas than nickel. Work at the Institute of

Gas Technology [2] clearly demonstrated that nickel is subject to severe degradation due to species like H_2S in the fuel gas at levels as low as 10 ppm. Conducting oxides like Nb doped TiO_2 were unaffected. Also, doped n-type conductors can be made from inexpensive raw materials and have been found to be catalytic like platinum for many fuel gas type reactions at elevated temperatures.

Some properties of candidate M^{+5} doped titanates (e.g. $CaTiO_3$ or $SrTiO_3$) are shown in Table II. Low resistivities were measured at high temperatures for all the titanate-based systems (such as $ZrTiO_4$, $MgTiO_3$, $CaTiO_3$, and $SrTiO_3$) [1] when: (a) doping with M^{+5} impurities such as Nb, and (b) when the atmosphere was reducing (low PO_2 simulated fuel gas). It was concluded that these materials should make excellent anodes. Resistivities measured on low density samples (50% TD) were comparable to those for p-type perovskites typically used for the air electrode and bi-polar plate in the SOFC (See Table III).

It is very important that the thermal expansion of the electrode match the other cell components. What enabled Westinghouse to successfully fabricate (prevent cracking of) their tubular design was the discovery and use of doped lanthanum manganites and chromites for the air electrode and interconnector [9]. These materials matched the CTE of the doped zirconia electrolyte fairly closely as is shown in Table III.

The $LaCrO_3$ has always been 10-20% low in its thermal expansion when compared to the zirconia electrolyte or the calcia doped zirconia support tube. The inclusion of the Al into the $LaCrO_3$ brings up the CTE but also lowers the electrical conductivity. The doped $LaMnO_3$ has a closer CTE match to the zirconia (even a little bit high) and has always performed very well.

The doped $ZrTiO_4$ was included in Table II for a particular reason. When the SOFC is operated at high temperatures for long periods of time there have been verified instances of interdiffusion. This interdiffusion can lead to the formation of non-conductive compounds such as $La_2Zr_2O_7$. Westinghouse reports have indicated that they have not observed any significant difficulties in the electrical performance of cells from this problem. If an anode (fuel electrode) were to be made from a titanate (e.g. $CaTiO_3$), interdiffusion would likely form a compound like $ZrTiO_4$ (a conductor when reduced on the fuel side of the cell). Also, Ca can exist as a substitutional cation dopant in zirconia and is normally compensated by oxygen vacancies which lead to enhanced oxygen conductivity.

Associated with the interdiffusion phenomena, rutile (TiO_2) perhaps deserves some attention. Reduced rutile and Nb or Ta doped rutile have very excellent electronic conductivity, even though its CTE appears to be somewhat low. There has been some recent work^[19] that indicates that solid solutions in the $\text{ZrO}_2\text{-Y}_2\text{O}_3\text{-TiO}_2$ system are single-phase with mixed electronic and oxygen ion conductivities. Up to about 15 mole percent TiO_2 can dissolve as a solid solution in single phase ZrO_2 with 12 mole percent Y_2O_3 . The electronic contribution appears to be PO_2 insensitive and is about the same order of magnitude as the ionic conductivity. Thus diffusion of Ti from either a TiO_2 or titanate (e.g. CaTiO_3) fuel electrode might result in a mixed electronic/ionic conductor. The natural application is for cathodes that are not required to be porous. However, anodes may also benefit by having a mixed electronic/ionic conducting region in close proximity to the fuel gas/electrode/electrolyte line interfaces. This might aid the reaction rate by effectively widening the reaction area. This would reduce polarizations at high current densities.

Figure 1 shows the gas channels formed in the bi-polar plate, which require the bi-polar plate to be relatively thick (layers not shown at true thicknesses). The channels could also be in the porous electrode layer(s) which typically have lower resistivities (if measured on the high density materials most often cited in literature). However, "as-fabricated" electrodes are normally only around 50 % dense and hence their actual resistivities are higher than tabulated values. Resistivities on actual electrode structures are rarely reported. Therefore locating the channels in the dense bi-polar plate might prove advantageous. Either counter-flow or cross-flow gas channels are possible depending upon the fabrication method.

Recent efforts at Argonne National Lab (the monolithic design) have been directed primarily at producing a high energy density design. This design is fabricated by green forming thin layers via tape casting, then laminating and co-firing the layers into a structure that resembles a cross-section of a cut stack of corrugated cardboard boxes. This design is quite promising but has very difficult fabrication problems. These problems are only partially solved on prototypes using a small number of cells.

Some planar SOFC designs also utilize tape casting to fabricate the electrolyte layer. The challenge in tape casting is the difficulty in making the electrolyte as thin as is possible by using the CVD technique. Layers

deposited by CVD at Westinghouse have been about $13\text{--}25 \times 10^{-6}$ m thick while free-standing, fired tapecast structures usually have a minimum thickness of about $75\text{--}250 \times 10^{-6}$ m. The electrolyte layer must be very thin, yet continuous, because it is the highest resistivity component of the fuel cell stack and we want to reduce IR losses. Typically the zirconia has a resistivity of about 10 ohm-cm at 1000 °C, which is about 100 to 1000 times higher than that measured for dense air electrode or fuel electrode materials.

Other problems arise if the electrodes are deposited by a powdered slurry method. If the powder is not fired to high enough temperatures there will be poor bonding between the powder crystallites and poor adherence to the electrolyte. This will result in a high resistance electrode. Conversely, if the electrodes are fired to a very high temperature, the electrodes might densify and shrink too much with the possibility of delamination (high contact resistance). There might also be formation of a high resistance layer such as $\text{La}_2\text{Zr}_2\text{O}_7$. Therefore it is desirable to find a good "low temperature" method to form well-bonded electrodes.

2. NEW MEXICO TECH DESIGN

The NM Tech program is investigating an optimized planar SOFC design that can take advantage of a combination of advanced fabrication techniques. Features are:

[1] It is a flat bi-polar plate design utilizing thin layers.

[2] Methods are being investigated that avoid simultaneous shrinkage, including:

(a) Tape casting and sintering of a dense perovskite bi-polar plate prior to adding other layers.

(b) Various green forming methods for placing gas channels in the structures .

(d) Plasma spraying as the favored method of applying the porous electrodes.

(e) Chemical vapor deposition (CVD) to form dense thin layers of stabilized ZrO_2 .

[3] Materials used for the various components are very similar to those used by Westinghouse, with the exception

of the bi-polar plate which will be $\text{La}_{0.85}\text{Sr}_{0.15}\text{CrO}_3$. The strontium doping onto the A site rather than Mg on the B site in the perovskite (ABO_3) structure results in about an order of magnitude increase in the conductivity over the Mg doped material. The Sr doping has the added benefit of almost a perfect match of CTE with zirconia. The Mg doping has been used by Westinghouse because they have found it impossible to fabricate the Sr doped material when using the EVD method.

[4] Some ceramic/ceramic bonding techniques are being investigated for the stacked cell components.

[5] A limited amount of single cell performance testing is scheduled to be performed.

One possible fabrication sequence for a counter-flow design using the NM Tech approach would be:

[1] Tape cast, calendar/emboss and sinter a bi-polar plate of the strontium doped lanthanum chromite composition.

[2] Screen print stripes or fill in gas channels in the bi-polar plate with a thermally transient material.

[3] Plasma spray electrode (likely air electrode using strontium doped lanthanum manganite) onto the bi-polar plate. This will result in a good bond between the bi-polar plate and the air electrode.

[4] The possible use of a proprietary process to fill in the electrode porosity.

[5] Use CVD to form a very thin (approx. 10×10^{-9} m) electrolyte (simultaneous deposition of zirconia and stabilization dopant to form a solid solution). Both cold wall apparatus utilizing organo-metallic precursors and hot wall apparatus utilizing high vapor pressure inorganic precursors are being investigated.

[6] Plasma spray (or other method) application of the fuel electrode. It is anticipated that a combination of zirconia and nickel would be used similar to the Westinghouse and Argonne designs. The addition of pore formers during the plasma spraying process is being investigated.

[7] Stack and creep flatten for enhanced bonding of the repeat units at moderate temperatures using low stresses.

We note that other slightly varying sequences would be possible for a cross-flow channel design.

3. CVD OF ZrO₂

Klemm[20] has recently published a review of zirconia chemical vapor deposition (CVD) literature. CVD of zirconium and yttrium oxides by the oxidation of ZrCl₄ and YCl₃ has been accomplished by several groups to yield continuous high quality films. For CVD of pure zirconium oxide, supply of the chloride vapor is made by simply heating ZrCl₄ to 160-200°C. Co-deposition of ZrO₂ and Y₂O₃ is much more complicated primarily because YCl₃ is volatile only at or above 800°C. For chloride CVD of ZrO₂ the substrate temperatures reported are 800-1600°C, with no deposition at temperatures below 800°C. Oxidants are necessary using such vapors as O₂, H₂O, and CO₂/H₂ mixtures. Low pressures have reportedly increased the growth rates.

The complexity of the high temperature systems necessary to supply both zirconium and yttrium chloride, along with the noxious and corrosive nature of the reactant and exhaust vapors have stimulated efforts to use volatile organometallic compounds. The organometallic reactants have the advantages of volatility for low delivery temperatures, exhibit lower deposition temperatures, and absence of extremely hot and corrosive vapors. Two classes of compounds that have been used for metal-organic chemical vapor deposition (MOCVD) of metal oxides are the metal alkoxides and the beta-diketone chelates. Compounds from both of these classes of organometallics have been used to CVD zirconium oxide films, while only the diketone chelates (not alkoxides) have demonstrated the volatility necessary for vapor transport of yttrium. A paper detailing Klemm's MOCVD of ZrO₂+Y₂O₃ will be published in the near future.

4. SINTERING OF LANTHANUM CHROMITE

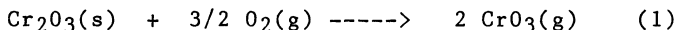
The NM Tech processing sequence calls for tape casting and sintering of bipolar plates made from lanthanum chromite doped with strontium. Since the tape cast body contains large amounts of organics and binders it is preferable to sinter the parts during a single-step firing in an air atmosphere furnace.

The primary difficulty encountered in sintering lanthanum chromite in air is the volatilization of chromium oxide species in oxidizing atmospheres. Previous studies suggested that the maximum densification of a Sr-doped lanthanum

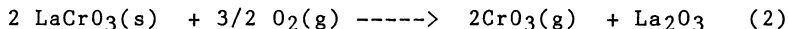
chromite (LSC) without using a sintering aid could only be achieved at low oxygen activities (10^{-11} to 10^{-12}) and a temperature above 1700°C .^[14] Anderson reported the densities of air fired LSC (Sr=16 mol%) were 71.4% and 77.6% T.D. at 1625°C and 1720°C respectively, while 99.85% T.D. was obtained at 1740°C using a PO_2 of 1.0×10^{-11} atm. Firing tape cast bodies in a reducing atmosphere would require a two-step firing schedule that includes binder burnout in air and then final sintering in a reducing atmosphere.

Theoretically several factors should aid in producing a LSC body that will sinter in air. Very fine unagglomerated powders are desirable. The fine powders have a higher driving force and shorter diffusion paths for sintering and should sinter at lower temperatures and shorter times. The lowered temperature should help minimize vaporization effects. It is well known in the sintering of LaCrO_3 compacts in air that the mass transport is dominated by vaporization-condensation and/or surface diffusion mechanisms. Rapid neck and grain growth with little shrinkage is always observed. Therefore it should also be beneficial to use a high heating rate accompanied by a short soaking time. This should minimize the effects of vaporization-condensation and surface diffusion while maximizing volume and grain boundary diffusion which have higher activation energies. The rate limiting volume diffusion coefficient can sometimes be increased by appropriate doping techniques. Dopants have been used in the studies of sintering lanthanum chromite by means of either increasing the point defects or stabilizing the chromium ions in a +3 oxidation state. However, degradation in electrical conductivity and large changes in CTE resulted.

The most volatile Cr oxide specie is CrO_3 which exists in gas form at high temperatures in air. When Cr_2O_3 is heated to above 1000°C in an oxidizing atmosphere, the following reaction^[15] takes place:



The evaporation of CrO_3 from LSC at high temperature in air is believed to degrade the material by the following reaction:



Since the equilibrium vapor pressure of CrO_3 over LSC is only about 1/5 of its pressure over Cr_2O_3 at high temperatures, a $\text{CrO}_3(\text{g})$ saturated atmosphere can be maintained over LSC in a "closed" system containing Cr_2O_3 .^[16] With an excess of $\text{CrO}_3(\text{g})$ being generated by reaction

(1), reaction (2) can be retarded or perhaps even reversed. The same method has been utilized in sintering of beta alumina by utilizing a soda-rich atmosphere^[17].

5. EXPERIMENTAL PROCEDURE

The apparatus used for the organometallic CVD is shown in the schematic drawing of Figure 2. The CVD of ZrO_2 was investigated at atmospheric and reduced (7-12 torr) pressures, at temperatures between 450 and 750°C, without oxidant, and using H_2O and O_2 as oxidants. Later co-deposition of yttria doped zirconia was accomplished. The organometallic beta-diketone chelate compounds zirconium trifluoroacetylacetonate [$Zr(tfacac)_4$] and yttrium 2,2,6,6-tetramethylheptanedionate [$Y(thd)_3$] precursors were used.

LSC powders were prepared for this study by a modified Pechini resin-intermediate method with a final calcining temperature of 800°C. Details of the complete powder preparation study will be reported in an upcoming paper.

Powders were weighed, mixed with a little distilled water as a lubricant, and then uniaxially pressed in a 1/2 inch cylindrical die at 30 kpsi. One group of pellets was pre-pressed uniaxially and then pressed isostatically to 207 MPa. The green density of the isostatically pressed samples were about 65% T.D.

A Lindberg 1700 °C box furnace and a CMVHT 1700 tube furnace were used for air firings in this study. A single-step firing was designed to duplicate sintering of tape cast parts. One set of samples were fired in an Astro furnace in Ar gas for comparison purposes.

Five configurations for firing LSC pellets in a chromia-rich atmosphere established inside an inverted alumina crucible on a setter plate were used: 1) Covering green pellets with LSC powder, 2) Covering green pellets with Cr_2O_3 powders, 3) Pellets surrounded with Cr_2O_3 powders but without physical contact, 4) Pellets fired between two fired Cr_2O_3 plates, and 5) For comparison, pellets fired in air without any external source of Cr.

After the most promising sintering configurations were selected, parameters like sintering temperature, heating rate, and soaking time were then studied by modifying the firing schedules. Bulk density of each fired sample was measured by the Archimedes method. The theoretical density for 15 mol% SrO doped $LaCrO_3$ was identified as

6.586 g/cm³[18] and was used to calculate the relative density. A Rigaku x-ray diffraction system was used for phase identification and a Hitachi HHS-2R with Tracor Northern 5400 attachment was used for SEM and EDS investigations.

6. RESULTS AND DISCUSSION

Sintering Study:

Pellets pressed from LSC powder made from the modified Pechini process sintered to about 98% theoretical density when fired in a reducing atmosphere (Ar) at 1700°C for 1 hour. Figure 4 shows that a similar pellet when sintered under an alumina crucible in air to about 1675°C achieved only about 74% T.D. However, LSC samples can be sintered to over 80% T.D. when covered with Cr₂O₃ powder or placed between fired Cr₂O₃ plates. The Cr₂O₃ powder tended to bond tightly to the LSC pellets when it was in intimate contact and inconsistent results were obtained when Cr₂O₃ was kept under the alumina crucible but not in contact with the LSC pellet. Overall, the best results were obtained using the Cr₂O₃ plates as shown in Figure 6.

All fired samples were cooled from the sintering temperature to room temperature "in-situ". The cover crucible worked as a cold trap when gaseous CrO₃ was reduced back to Cr₂O₃ during cooling which successfully prevented condensation of Cr₂O₃ on the fired LSC.

Three different heating rates were used in sintering LSC pellets placed between Cr₂O₃ plates. The results are shown in Figure 5 and all cases suggest that higher heating rates are very desirable for enhanced sintering. Higher densities (up to 94% T.D.) and less grain growth were observed in the samples fired with the higher heating rates.

A most interesting observation of polished cross sections showed that densification proceeded from the exterior towards the interior of the LSC pellets. This effect is shown in Figure 7a while Figure 7b shows the spatial relationship between the densified layer at the surface, the porous region in the interior and a transition region. Figure 7b also shows a speculation that Cr ions may be diffusing in from the surface. The surfaces of samples sintered up to 16 hours at 1670°C showed no evidence of second phases when examined by XRD. Results from EDS analysis on polished cross sections of the LSC pellets showed no signs of phase separations in the densified region.

Figure 8 shows the microstructure of the dense layer formed near the surface adjacent to the Cr_2O_3 plate. The sintering/densification was accompanied by grain growth as can be seen by comparison with the microstructure of the largely undensified interior shown in Figure 9. The microstructure of Figure 9 is almost identical to those of LSC pellets sintered in air (no Cr_2O_3 packing).

Boiling phosphoric acid was used as an etchant for the LSC microstructures. A preferential etching of the porous area was observed. After etching and rinsing in deionized water, a strontium or lanthanum deficient region was detected on the porous surface by EDS. We feel that H_3PO_4 preferentially reacted with residual SrO and La_2O_3 left in the porous area (See reaction 2) when LSC decomposed at the surface of the unsintered powder. The phosphoric acid reaction formed water soluble phosphate salts which were later washed away. We feel that when an atmosphere of CrO_3 is established at the surface, Cr and O ions must diffuse from the surface through the dense layer and reconstitute the LSC.

The thickness of the dense layer as a function of time at the "soak" or sintering temperature was determined by examining polished cross sections with a calibrated optical microscope. Figure 10 shows a parabolic time dependence for the thickness of the dense layer at various sintering temperatures. Since the plot fits a parabolic-rate law it appears the densification or growth rate of the densified layer is diffusion controlled. All lines were fitted by a least-square method. The line drawn from data obtained at 1670°C does not pass exactly through the zero point. This can be explained by the fact that the heating rate used was not very high ($15^\circ\text{C}/\text{min}$), so there was no clear distinguishable point between heating and soaking steps for points with a short overall sintering time. Most likely the densified layer started to form even before the "sintering temperature" was reached. The effect is small and can be neglected for longer soaking or "sintering" times.

The width of the densified layer could be measured rather easily at a low magnification, but there was no sharp transition in the microstructure when observed at high magnifications. A gradient in the degree of densification and grain sizes was observed using a SEM. Figure 7b shows a sketch of the general trend in the change in grain size and density from the Cr_2O_3 interface through the dense LSC region and then into the porous interior. The set of LSC samples fired in an Ar atmosphere showed no such dense surface layer.

A simple model of the sintering mechanism of pressed LSC contained in a Cr_2O_3 "sandwich" can be developed. The evaporation of Cr_2O_3 from LSC compacts at high temperatures causes a chromium-deficient perovskite or possibly phase separation everywhere in the sample. In this state the powders will not sinter. The deficiency of chromium ions at the interior of the compact in conjunction with a constant vapor pressure of chromium ions from a good exterior source (Cr_2O_3) results in a concentration or chemical potential gradient from the exterior to the interior. This concentration gradient of chromium ions is the driving force for mass transport.

At high temperatures the chromium species force a reversal of reaction (2) to reconstitute stoichiometric LSC and the surface powders sinter. The Cr ions (and possibly O ions) then diffuse through the dense layer into the interior in response to the chemical potential gradient. This might be either grain boundary or lattice diffusion. Since the parabolic rate law seems to hold at long times it appears that the grain growth we measured does not appreciably affect the diffusion constant. This might be an argument for lattice diffusion or it might imply the grain growth primarily takes place prior or during the densification. Since oxygen diffusion is often rapid in the grain boundaries of metal oxides it is logical that the ionic specie limiting the diffusion rate is Cr diffusion in either the grain boundary or the lattice.

We assume that the diffusion coefficient is independent of composition and the system can be compared to the diffusion of Cr from a constant source into a semi-infinite solid. Grain growth and shrinkage occur in the porous region during densification which makes the real situation complicated. However, we can approximate the situation by fixing the origin of our coordinate system at the outer surface such that the origin moves as the sample sinters and consider the densified region to be added in discrete layers such that the diffusion always takes place through a dense homogeneous region.

Under the above assumptions, the boundary conditions then lead to equation (3) as the solution to Fick's second law.

$$C(x,t) = C'' [1 - \text{erf}(x/2 \sqrt{Dt})] \quad (3)$$

where C = concentration at a certain point x and time t
 C'' = constant concentration of solute (e.g. Cr)

provided by Cr₂O₃ at the interface
x= distance (cm)
D= diffusion coefficient (cm²/sec)
t= time (sec)

Logically the concentration (C) at the visible front of the densified layer should be fairly low and also constant for all samples. It is convenient to set this C value to 0.1573xC" such that the relation $x=2\sqrt{Dt}$ would hold true at the front of the densified layer. Then the apparent diffusion coefficient D can be extracted by a measurement of the x value of the front for a given time t. The apparent diffusion coefficients for 0.15 mole % SrO doped LaCrO₃ at various temperatures were then calculated by a graphical method and plotted as an Arrhenius plot in Figure 11.

The activation energy calculated was 56.5 kcal/mole for the diffusion process. Since there is a lack of literature for diffusion coefficient values (tracer, sintering, or creep) of various ions in lanthanum chromite or LSC it is impossible to compare our measured diffusion values and activation energy. However, since the activation energy is moderate in value we might venture a guess that the process is grain boundary diffusion of Cr ions.

A sintering schedule in an air furnace was subsequently designed for sintering a tape-cast LSC plate with a thickness of 2 mm and using a diffusion coefficient of 1.94x10⁻⁷ cm²/sec at 1670 °C with Cr₂O₃ "sandwich" plates. From this sintering run, a sample of 92% T.D. was obtained after sintering at 1670°C for 7 hours.

CVD study:

Coatings deposited at atmospheric pressure using Zr(tfacac)₄ without the aid of an oxidant as well as with up to 10% H₂O vapor in the CVD chamber were amorphous with varying concentrations of organic impurities in the films. Deposition of coatings at reduced pressure (7-12 torr) using O₂ as oxidant and low Zr(tfacac)₄ partial pressure (<30 mtorr) resulted in heterogeneous growth of crystalline ZrO₂ coatings suitable for SOFC use. Figure 3 shows microstructures of the ZrO₂ films deposited at 600-750°C using scanning electron micrography. The changes in morphology with substrate temperature can be explained using a structure zone model. Similar structures were found when co-depositing ZrO₂+Y₂O₃, although the deposition rate was suppressed.

7. CONCLUSIONS

Two major fabrication techniques have been developed in support of the planar solid oxide fuel cell.

The first technique is CVD of dense, fully oxidized films of ZrO_2 stabilized with Y_2O_3 using volatile organo-metallic precursors in a cold-wall chamber. It was found that temperatures greater than $650^\circ C$, reduced total pressures, addition of gaseous oxidants, and limiting the reactant partial pressures are necessary to make acceptable electrolytes.

A technique was developed for sintering dense strontium-doped lanthanum chromite bi-polar plates in an air atmosphere furnace. The $Cr_2O_3/LSC/Cr_2O_3$ "sandwich" configuration appears to be a feasible way to sinter tape-cast LSC bi-polar plates. Grain growth always accompanied the densification. A faster heating rate and a higher sintering temperature than possible with the Lindberg furnace are suggested for enhancing the sintering to produce a sample with greater than 92% T.D. and suppressing the grain growth. The sintering conditions can be optimized further as diffusion mechanisms involved in this system are better understood. Detailed quantitative analysis on the final composition of fired LSC would ensure that stoichiometry and hence electrical conductivity is maintained.

ACKNOWLEDGEMENTS

This work was supported by New Mexico Institute of Mining and Technology and the Electric Power Research Institute, under Contract No. RP2706-3, Dr. Glen Cook Technical Monitor.

REFERENCES

- [1] P.A. Lessing, G.R. Miller, and H. Yamada, " Conducting Ceramic Oxides for Use as Molten Carbonate Fuel Cell Electrodes", Journal of the Electrochemical Society, 133, 8(1968) p. 1537-1541.
- [2] T.D. Claar, L.G. Marianowski, and A.F. Sammells, " Development of Sulfur-Tolerant Components for Second-Generation Molten Carbonate Fuel Cells", I.G.T. Interim Report July 1979- EM-1114 on Research Project 1085-2 prepared for EPRI. (See especially page 1-4).
- [3] R.L. Eichelberger, U.S. AEC Report NP-5432 (1954).

- [4] E.N. Bunting, et.al., "Properties of Barium-Strontium Titanate Dielectrics", J. Am. Cer. Soc., 30, (1947) p. 114-125.
- [5] U. Balachandran and N.G. Eror, "Electrical Conductivity in Strontium Titanate", J. Solid State Chem., 39, (1981) p. 351-359.
- [6] R.W. Ricker and F.A. Hummel, "Reactions in the System TiO_2-SiO_2 ; Revision of the Phase Diagram", J. Am. Cer. Soc., 34 (1951) p. 271.
- [7] W. Feduska, et. al. Westinghouse Annual Fuel Cell Report for 1981-82, Doc. 82-9D1-SOEFRC-R5, Westinghouse R&D Center, Pittsburgh, PA, 15235.
- [8] J.L. Henry and G.G. Thompson, "Thermal Expansion Match Between Molybdenum (TZM Alloy) and Oxides of the Perovskite and Spinel Types" Bull. Am. Cer. Soc., 55, No. 9 (1976) p. 281.
- [9] H.U. Anderson, R. Murphy, S. Semachaibovorn, B. Rossing, Al Alred, W. Procarione and R. Ackermann, "Electrical Conductivity, Volatilization and Preparation of $LaCrO_3$ Based Oxides," Conf. on High Temperature Science Related to Open-Cycle, Coal Fired MHD systems, Argonne National Laboratory, Argonne, IL, April 1977.
- [10] D.B. Meadowcraft and J.M. Wimmer, "Oxidation and Vaporization Processes in $LaCrO_3$ ", Am. Cer. Soc. Bull., 58, [6] (1979) p. 610-15.
- [11] H.U. Anderson et. al. "Fabrication and Properties of $LaCrO_3$ Based Oxides" in Processing of Crystalline Ceramics, Edited by H. Palmour, R. Davis, and T.M. Hare. Plenum, New York, (1978) p.469-477.
- [12] Measured at Harrop Laboratories for P. Lessing
- [13] S.C. Singhal, R.J. Ruka, and S. Sinharoy, "Interconnection Materials Development for Solid Oxide Fuel Cells", Final Report Sept. 1985, Westinghouse Electric Corp., DOE/MC/21184-1985(DE86003941).
- [14] L. Group and H.U. Anderson, "Densification of $La_{1-x}Sr_xCrO_3$ ", J. Am. Ceram. Soc., 59 [9-10], (1976) p. 449-450.
- [15] C.S. Tedmon, Jr., "The Effect of Oxide Volatilization on the Oxidation Kinetics of Cr and Fe-Cr Alloys," J. Electrochem. Soc., 113 [8], (1966) p. 766-68.

[16] T. Sasamoto and T. Sata, " Vaporization of Lanthanum Chromite at High Temperature in Vacuum", Yogyo Kyokai Shi, 79 [915] (1971) p. 408-18.

[17] R. Stevens, J.G.P. Binner, "Review: Structure, Properties and Production of beta-Alumina," J. Mater. Sci., 19 (1984) p.695-715.

[18] L. Group, Influence of Oxygen Activity in the Sintering of Strontium Doped Lanthanum Chromite, M.S. Thesis, University of Missouri at Rolla, August, 1975.

[19] W.L. Worrell and S.S. Liou, "Electrical Properties of Novel Mixed-Conducting Oxides", Meeting Abstract, Journal of the Electrochemical Society, 135, (8), page C382.

[20] K.A. Klemm, Chemical Vapor Deposition of Yttria-Doped Zirconia Films for Solid Oxide Fuel Cell Applications, Master's Degree Thesis, Dept. of Materials and Metallurgical Engineering, New Mexico Institute of Mining and Technology, Socorro, NM, 87801 (1989).

TABLE I.

PROPERTIES FOR PLANAR SOFC COMPONENTS

<u>COMPONENT</u>	<u>POROSITY</u>	<u>CONDUCTIVITY</u>	<u>ATMOSPHERE</u>
Electrolyte	Dense, gas tight	>99.9% Ionic Oxygen	Fuel/Air
Bi-polar plate	Dense, gas tight	>99.9% Electronic	Fuel/Air
Anode	Approx. 50% Interconnected pores	Primarily Electronic	Fuel
Cathode	Approx. 50% Interconnected pores	Primarily Electronic	Air

Coefficients of thermal expansion of components must match very closely

TABLE II.

CANDIDATES FOR SOFC FUEL ELECTRODES

Resistivities for a PO_2 of approx. 10^{-20} to 10^{-24} atm at $1000^\circ C$.

Samples were about 50% dense unless otherwise stated.

<u>COMPOSITION</u>	<u>RESISTIVITY ohm-cm</u>	<u>CTE $^\circ C^{-1}$</u>	<u>REFERENCE</u>
$CaTi_{0.99}Nb_{0.01}O_3$	$<2.5 \times 10^{-2}$	10.4×10^{-6} ($25-1000^\circ C$)	3
$SrTi_{0.99}Nb_{0.01}O_3$	9.1×10^{-1}	11.1×10^{-6} ($93-1400^\circ C$)	4
$SrTiO_3$ (dense)	5×10^{-1}		5
TiO_2		8.82×10^{-6} ($25-1500^\circ C$)	6
$ZrTiO_4 +$ 0.01% Ta	4.9×10^{-1}		1

TABLE III.

Selected CTE's of Various SOFC materials

Resistivities measured at 1000°C in air, CTE's 25-1000°C

<u>COMPOSITION</u>	<u>RESISTIVITY ohm-cm</u>	<u>CTE °C⁻¹</u>	<u>REF.</u>
La _{0.9} Sr _{0.1} MnO ₃	7.5 x 10 ⁻³ (dense in air)	12.0 x 10 ⁻⁶	7
La _{0.8} Sr _{0.2} MnO ₃	6.7 x 10 ⁻³ "	"	7
LaCrO ₃	1.4-10 x 10 ⁰ "	8.92x10 ⁻⁶	7,8,13
LaAlO ₃		11.5x10 ⁻⁶	8
La _{0.95} Mg _{0.05} Cr _{0.75} Al _{0.25} O ₃	3.1x10 ⁻¹	9.9x10 ⁻⁶	7,9,10, 11,13
La _{0.84} Sr _{0.16} CrO ₃	3 x 10 ⁻²	10.9x10 ⁻⁶	9
ZrO ₂ + 8 m% Y ₂ O ₃ + Al ₂ O ₃ sintering aid		10.14x10 ⁻⁶	12
Zircar ZrO ₂ (8.3 m% Y ₂ O ₃)	Approx. 10 (ionic)	11.31x10 ⁻⁶	12

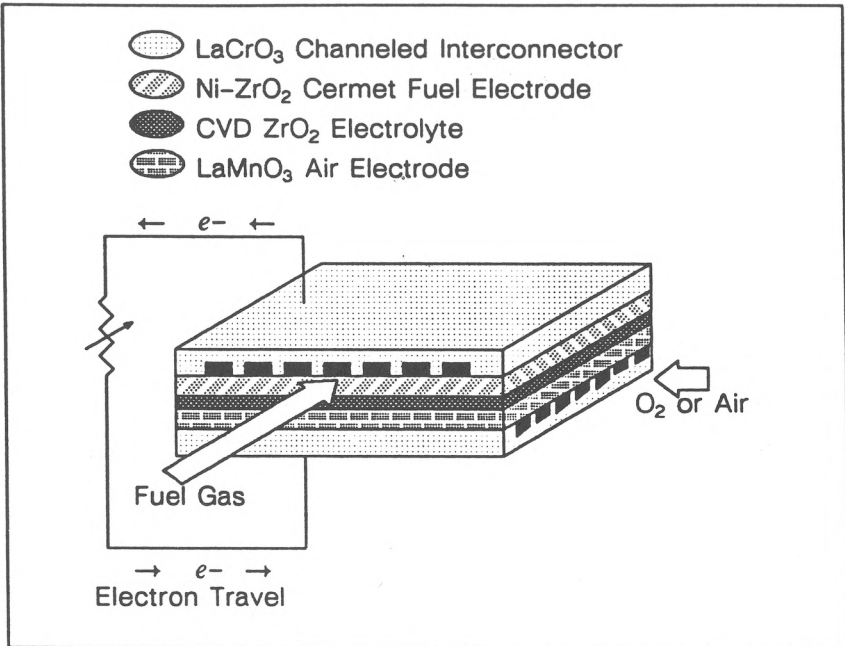


Figure 1. Advanced flat plate solid oxide fuel cell design

(components not shown to scale)

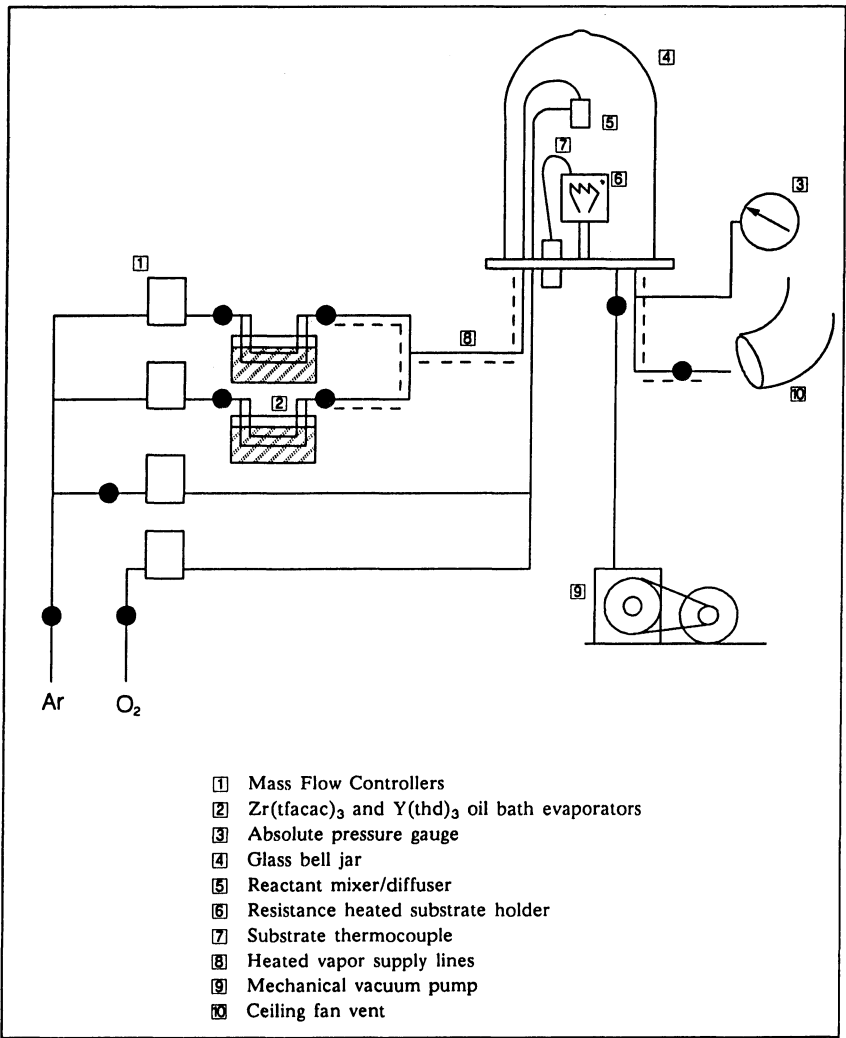
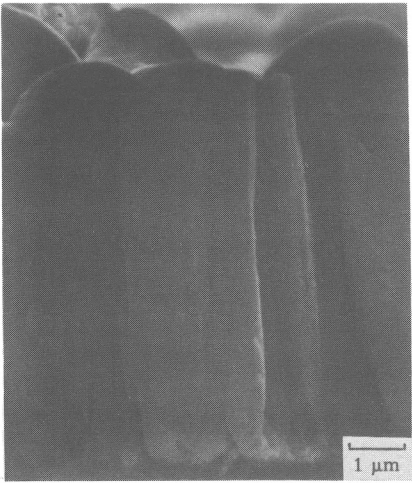
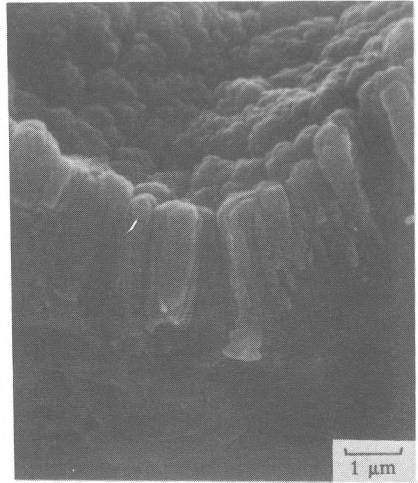


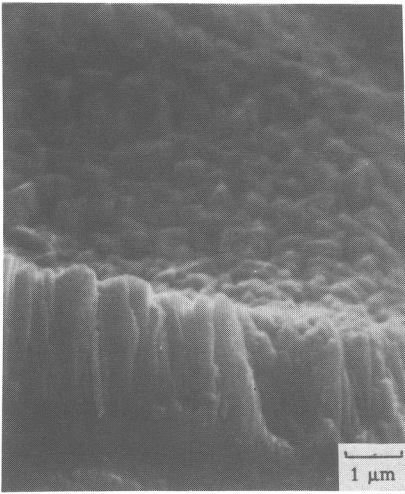
Figure 2. Cold-wall Chemical Vapor Deposition Apparatus



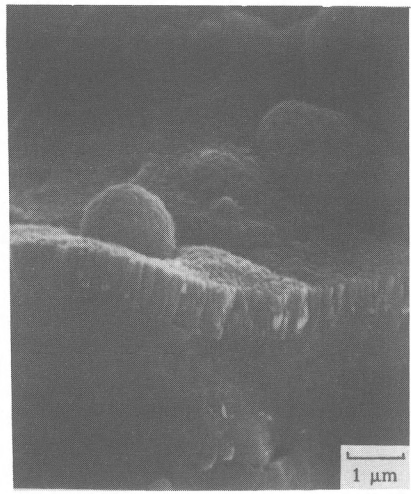
(a)



(b)



(c)



(d)

Figure 3.

Scanning electron micrographs of microstructures of heterogeneously deposited ZrO_2 (RPCVD) films. Coating in figure (a) was deposited at $600^\circ C$, (b) at $650^\circ C$, (c) at $700^\circ C$, and (d) at $750^\circ C$.

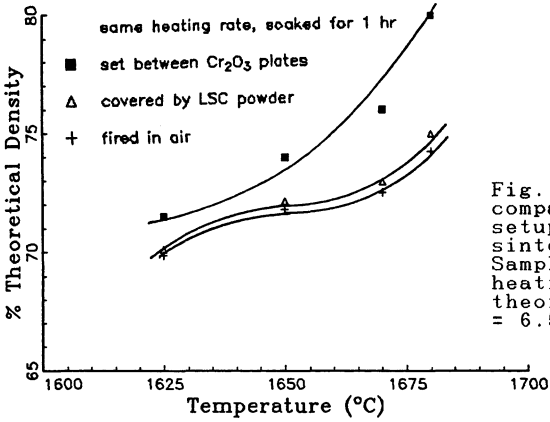


Fig. 4 - Density of LSC compacts fired by various setups as function of sintering temperature. Sample thickness = 2 mm; heating rate = 15 C/min; theoretical density = 6.586 g/cm³.

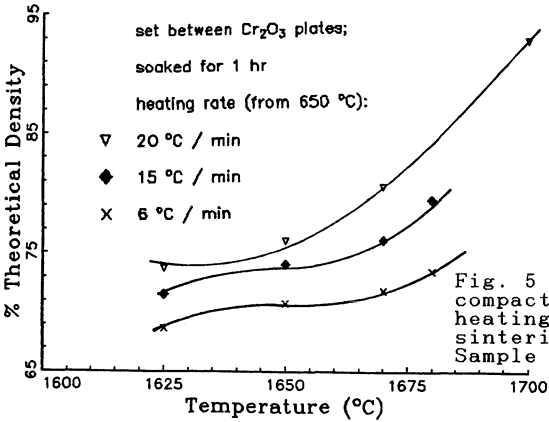
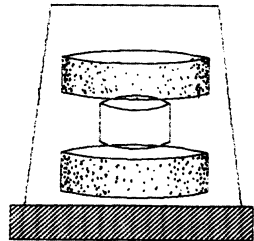


Fig. 5 - Density of LSC compacts fired with various heating rates as function of sintering temperature. Sample thickness = 2 mm.

Fig. 6 - Schematic drawing of the Cr₂O₃/LSC/Cr₂O₃ sandwich-type setup covered by an alumina crucible.



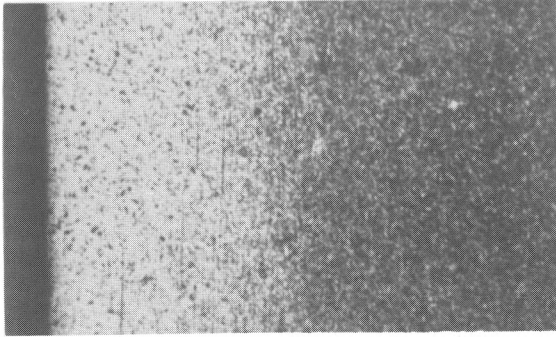


Fig. 7-a Optical micrograph of the polished cross section of LSC sintered by a sandwich-type setup. Bright region is near the surface and densified. 50X.

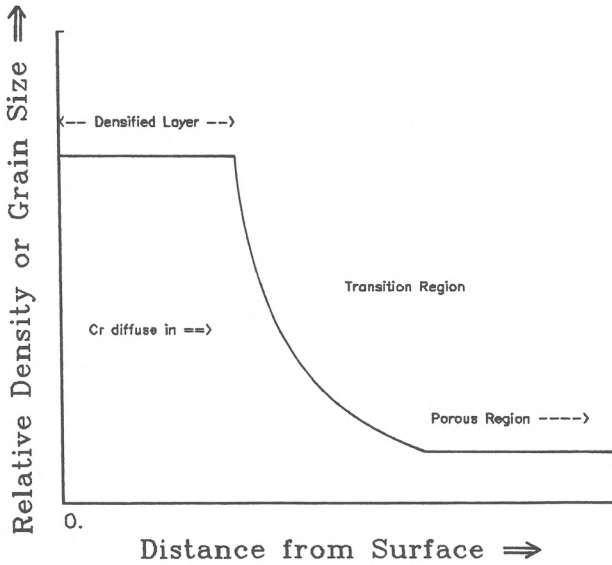


Fig. 7-b Schematic drawing corresponding to Fig. 7-a represents the observed trend on changes of density and grain size.

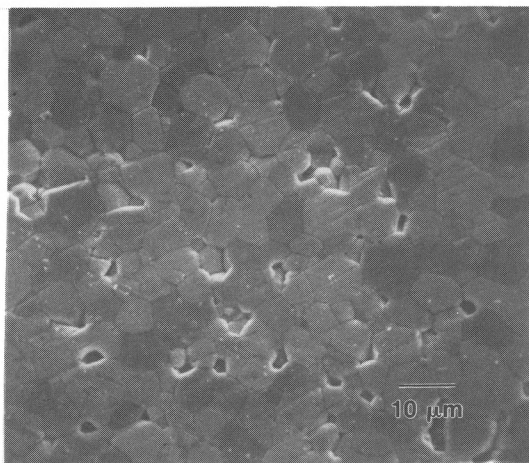


Fig. 8 Scanning electron micrograph of the densified region on the polished and etched cross section. Sample was sintered at 1670 C for 3 hours.

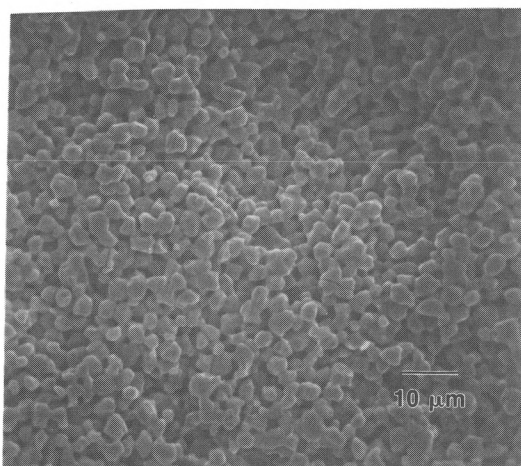


Fig. 9 Scanning electron micrograph of the porous interior on same LSC sample shown on Fig. 8.

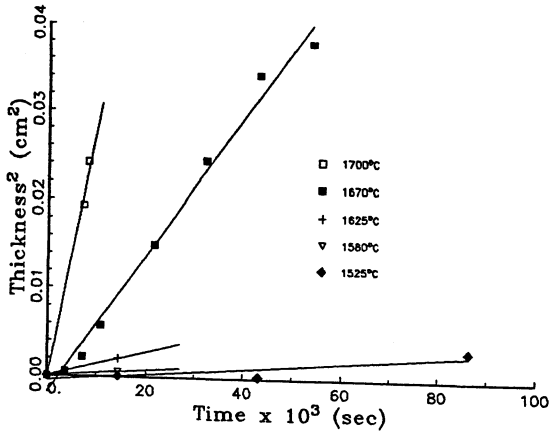


Fig. 10 Thickness of the densified layer formed in LSC compacts as a function of time for various sintering temperatures. Heating rate = 15 C/min.

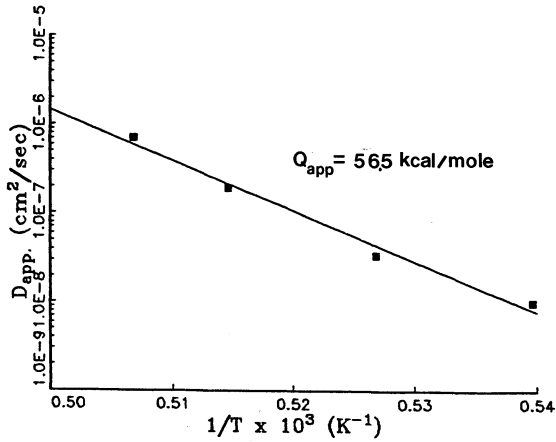


Fig. 11 Arrhenius plot of the apparent diffusion coefficients obtained from present study shows an activation energy of 56.5 kcal/mole.

FABRICATION OF INTEGRAL FLOW-FIELD / INTERCONNECTS FOR PLANAR SOFC STACKS

Christopher Milliken and Ashok Khandkar

Ceramatec, Inc.
2425 South 900 West
Salt Lake City, Utah 84119

Abstract

Acceptor doped LaCrO_3 materials have been used for interconnects in SOFCs for about 20 years owing to their high conductivity and thermodynamic stability. These materials present fabrication challenges especially related to sinterability. This paper reports on investigations of the effect of processing conditions on the microstructure and properties of doped LaCrO_3 ceramics. LaCrO_3 was green formed by tape casting as well as by uniaxial die pressing. Samples were densified by pressureless sintering in air. Liquid formers were added as sintering aids. Samples were also hot pressed in inert atmosphere in graphite dies. Microstructural examination of the sintered ceramics revealed that in reducing conditions the material reacts with graphite forming complex carbide phases. Such decompositions were found to affect the mechanical stability by propagating microcracks in order to relieve stresses arising from volume changes associated with phase reconstitution. The electrical conductivity of sintered compacts is reported. Conditions for obtaining high densities and thermal and mechanical stability against both structural and chemical phase changes are discussed.

Introduction

Development of planar geometry SOFC stack technology hinges critically on the ability to stack single cells connected electrically in series, with a ribbed bipolar separator serving as the interconnect. The interconnect, with integral flow-fields must channel the anodic and cathodic reactant gases to the electrode/electrolyte interfaces, prevent the direct chemical oxidation of the fuel gas and provide adequate electrical conductance from one cell to the adjacent cell. In a planar bipolar SOFC stack operating at 1273K, the interconnect is exposed to fuel gases which have low oxygen activity ranging between 10^{-20} to 10^{-15} on the anode side and oxidant gases with high oxygen activities ranging from 10^{-4} to 10^{-1} on the cathode side. In addition, there may be temperature variations present from the inlet to the outlet side leading to fairly large gradients in current density across the planar interconnect. Thus, the interconnect is typically subjected to extreme environmental conditions of high temperatures, chemical environments and thermal stresses arising from current density variations.

Doped LaCrO_3 , currently the interconnect material of choice, presents special difficulties in meeting the simultaneous functional requirements of high density, controlled stoichiometry and phase stability during fabrication and fuel cell operating conditions. The primary difficulty in air sintering of LaCrO_3 based materials arises from the volatility of Cr from the structure at temperatures in excess of 1400°C , causing porosity to develop. This is minimized by sintering in reducing atmospheres, with oxygen activities of 10^{-12} - 10^{-10} at 1500 - 1700°C , as reported by Group and Anderson (1). Meadowcroft (2) used SrCO_3 and Flandermeyer et. al. (3) used low melting oxide eutectics as well as La, Y and Mg fluorides upto 8-10 % by weight to increase density of sintered compacts. In an alternate approach, Balkevich et al. (4) have doped Ca (0.05 atom fraction per LaCrO_3 and Anderson (5) have incorporated various dopants, on both A and B sites of the perovskite structure, to enhance the sinterability in air. These dopants presumed to give a hitherto unidentified transient liquid phase, which help sinterability, in air at temperatures below 1500°C . In the fabrication of thin planar LaCrO_3 ceramics these sinterability problems pose rather severe challenges in reducing porosity to

acceptable levels. Incorporation of liquid phase sintering aids can lead to variations in sintered density of thin structures as well as to deleterious surface reactions with other materials in direct contact during the sintering process.

A detailed fabrication study on doped LaCrO_3 was carried out with a view to determine the effect of processing conditions on microstructure and properties. Methods to obtain high density including variations in fabrication processes, and transient liquid sintering aids were examined. The resulting microstructure and measured properties were correlated with processing conditions. On the basis of the experimental results, the influence of specific processing conditions on the fabrication of the thin planar interconnects and evolution of the microstructure were examined. General conclusions on fabrication and long term stability of LaCrO_3 are made. This paper reports on the influence of various fabrication process conditions on the microstructure, properties and phase composition of interconnects.

Experimental

Strontium doped LaCrO_3 , $\text{La}_{1-x}\text{Sr}_x\text{CrO}_3$ with $x=0.1$ and 0.2 , was made by the liquid mix method (6). Briefly, this process involves dissolving soluble salts of the cations in a citric acid solution (1.14 % by weight), adding ethylene glycol and heating the solution carefully to dryness. The resulting polymer char is calcined at temperatures of between $800\text{-}1000^\circ\text{C}$ to burn off all traces of organic residue and form the crystalline powder structure. The composition was characterized to be single phase using XRD. Typically these powders had a surface area of between $14\text{-}18\text{ m}^2/\text{g}$ when calcined at temperatures of between $700\text{-}850^\circ\text{C}$. Densification studies were carried out on pressureless sintered powder compacts, tape cast substrates as well as on compacts sintered under controlled heating rates and temperature, pressure and atmosphere. The starting powders were milled in ethanol or acetone with the binders (1 - 2 % by weight poly-vinyl butyrol, B-78, Monsanto). The powders were dry screened -80 mesh after evaporation of the solvents. Powder compacts were made by uniaxial and/or isostatic pressing at 35 and 200 MPa, respectively,

to the desired shape. Specimens were sintered in air and controlled atmospheres at temperatures between 1400-1650°C. The heating rate was kept constant at 2°/min and 10°/min. Samples were held at temperature for two hours. A ZrO₂ crucible was used to cover the specimens. (This was essentially to "contain" the Cr vapors). Sintering studies were also conducted on doped LaCrO₃ samples obtained from Anderson (Dept. of Mat. Science, University of Missouri, Rolla). Alternatively, hot pressing was performed at temperatures between 1200-1600°C in an Ar environment, using graphite dies loaded uniaxially under a pressure of 28-30 MPa. Densities were measured by the Archimedean method and correlated with porosity measurements on polished cross-sections observed by optical microscopy and scanning electron microscopy. The effect of sintering aids and process conditions was determined from examination of the microstructures using scanning electron microscopy (SEM) complemented with measurement of electrical conductivity (2- and 4-probe AC and DC methods), determination of phase assemblage by X-ray diffraction (XRD) , analytical microscopy such as scanning electron microscopy (SEM) and electron probe micro-analysis (EPMA) and thermal expansion characteristics.

Results and Discussion

Liquid Phase Sintering

Sr-doped LaCrO₃ compacts made by uniaxial compaction at 35 MPa gave typical green densities of about 42 - 45% of theoretical. Specimens pressed uniaxially followed by iso-static pressing at 200 MPa gave somewhat higher green densities of about 45 - 48% of theoretical. Sintered densities at temperatures between 1500 and 1650°C yielded densities of 58-80% of theoretical, consistent with the literature. Microstructural examination of polished cross-sections revealed a gradation in porosity with increased porosity at the surface. A greater amount of porosity was observed at the higher sintering temperatures. This is to be expected owing to the greater volatility of Cr at the higher sintering temperatures. Specimens compacted using iso-static pressing sintered to greater densities (upto 80% of theoretical) compared to those compacted by uniaxial pressing alone. No significant effect of heating rate was

observed. The $\text{La}_2\text{O}_3\text{-Cr}_2\text{O}_3$ phase diagram (7) suggests that transient liquid phase sintering may not occur below about 1900°C and hence no major effect of heating rate is to be expected. SEM examination of the calcined powders showed that they were porous agglomerates (15-20 μm mean size) with rather well formed necks between sub-micron sized primary particles. Figure 1(a) shows the morphology of $\text{La}_{0.9}\text{Sr}_{0.1}\text{CrO}_3$ calcined at 850°C and milled for 6 hours in ethanol using ZrO_2 media. Figures 1(b) and (c) show particle morphology after milling for 8 and 24 hrs. While the mean particle diameter has reduced there appears to be a substantial fraction of hard agglomerated particles. Sinterability studies on these milled powders are incomplete, however preliminary results show that green powder compacts have densities similar to those of powders milled for 8 hrs. Addition of lubricants such as polyethylene glycol helped to increase both green density and sintered density. These results are tabulated in Table 1.0

Several sintering aids were selected, from among transition metal and alkaline earth halides, on the basis of melting point, valence and ion size. The sintering aid ideally would assist in mass transport aiding the sintering process and would then completely

Table 1.0

Density of $\text{La}_{0.9}\text{Sr}_{0.1}\text{CrO}_3$ Specimens Pressed with Binder and Lubricant

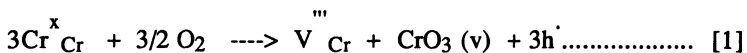
Compaction	Density (% Theoretical)		Comments
	Green	Sintered	
Uniaxial	40	58	1 % PVB
Uniaxial+ Iso-static	47	66	1 % PVB
Uniaxial	47	72	1% PVB + PEG
Uniaxial + Iso-static	53	80	1% PVB + PEG
Uniaxial + Iso-static	55	90	1% PVB,; powder milled for 24 hrs.

volatilize off without contaminating the grain boundaries (with a deleterious effect on the conductivity). With regard to the possible chemical effects, formation of insulating phases at the grain boundaries may not be entirely ruled out. Since the thermodynamic properties of many possible phases are not known, selection was made on the assumptions that any slight solubility of cations from the sintering aid should not be deleterious from the standpoint of conductivity. From prior literature as well as on the basis of initial trials, about 2 % (atom fraction) of the sintering aid was milled into the LaCrO_3 powders as described above. Densification was clearly aided by the use of the fugitive sintering aids. Figure 2 shows the fired density for the selected sintering aids and Figure 3 shows the density variation as a function of the melting temperature and ionic size. Among the different sintering aids evaluated, MgF_2 was shown to be the best sintering aid. In order to determine an optimal MgF_2 content, various amounts of MgF_2 were added and sinterability was investigated. Figure 4 shows that about 2 % (atom fraction) of MgF_2 is adequate in densifying LaCrO_3 . EPMA results on polished cross-sections of such specimens revealed clean grain boundaries with no Mg concentration at internal surfaces. Measured conductivities, plotted in Figure 5, on cylindrical specimens using standard 2-probe ac impedance methods and on bar specimens using 4-probe dc techniques were in agreement with previously reported literature values (8,9) indicating no effect of the sintering aid on the electronic conduction properties. The bulk thermal expansion coefficient measured using a dilatometer was also in agreement with the literature.

Sintering of Thin Planar Interconnects

Sintering of thin (100-150 μm thick) tape cast LaCrO_3 interconnects resulted in a graded porosity microstructure similar to that described earlier. The sintered ceramic interconnects were fragile and exhibited systematic differences in surface conductivity which could be correlated with changes in stoichiometry of the surface layers compared to the bulk. Figure 6 shows the profile of normalized elemental Cr, Sr and La map across a 120 μm thick interconnect. The top surface shows Cr depletion and an associated La enrichment. The Sr content is uniform across the specimen. The

arrows point to a Cr enriched area (with a corresponding La depleted area) along the profile. This is due to the presence of a large pore in the thin planar structure where Cr enrichment occurs most probably by the predominant evaporation-condensation mass transport mechanism operative at the sintering temperatures. Previous studies on volatilization of Cr_2O_3 (10) suggest that Cr volatilizes off by forming CrO_3 vapor. Assuming a similar volatility mechanism to be operative, the defect reaction can be written as:



Electronic conductivity in LaCrO_3 materials is p-type arising from charge compensation of Cr^{3+} to Cr^{4+} (electron holes) upon divalent ion substitution on the La^{3+} sites. The proposed conductivity mechanism is due a small polaron hopping on the Cr sites. This hole carrier density is sensitively affected by non-stoichiometry arising from Cr volatility. Associated with the Cr loss and the resulting Cr vacancies $\text{V}_{\text{Cr}}^{\text{'''}}$, additional p-type defects may be formed in the lattice. This causes an increase in conductivity at the surface as was determined using the van-der Pauw technique. The above reaction assumes some non-stoichiometry being permitted on the Cr sub-lattice in the perovskite structure. The phase diagram shows that LaCrO_3 is a line compound and therefore Cr loss must be accompanied by precipitation of La_2O_3 . Although the exact surface concentrations could not be estimated and while no La_2O_3 or $\text{La}(\text{OH})_3$ was detected in XRD examination, clear evidence of non-stoichiometry in the Cr sub-lattice was seen from the EPMA results.

The above results suggest that in tape cast structures where the surface is a greater fraction of the ceramic compared to powder compacts, vapor transport and surface diffusion effects dominate the initial sintering process. This is because these processes generally tend to have lower activation energies and greater values than other mass transport processes. During the temperature regime where the sintering aid is molten, some particle rearrangement is expected. At higher temperatures, once the liquid evaporates from the ceramic, the dominant mechanism that will contribute to densification will be bulk diffusion. The build up of the CrO_x rich phase in inter-particle necks with concomitant loss in grain surface area must greatly reduce the driving force for

sintering. This can be inhibited by two factors: the diffusion distances are greater because of neck growth (possibly resulting in pore isolation also) as well as increased Cr volatility at the higher temperatures. The implications for sintering of thin planar interconnects, with or without integral flow-fields, are that a minimum amount of sintering aid must be used so as to minimize porosity caused by decomposition and volatility of the sintering aid. Further, in case of liquid phase assisted sintering, the sintering aid must be uniformly dispersed not only between agglomerates but also within each agglomerate. This will ensure uniform wetting of individual crystallites thus greatly aiding in densification. Alternative fabrication methods which give more uniform and high density green bodies with smaller interstices between agglomerates may alleviate densification problems. Ideally, appropriate dopants in LaCrO_3 which have a transient eutectic liquid phase at temperatures below 1500°C , would be the best choice. Development in the latter direction is being carried out by Anderson (5) as well as by the authors.

Hot Pressed LaCrO_3

Extensive work was performed to establish optimal hot pressing temperatures and time schedules required for densifying LaCrO_3 . Some hot pressing was also done with dies machined with flow-field grooves. Typical densification curves are shown in Figure 7. The powders were pressed for a minimum of 40 min. after reaching the desired highest temperature. Hot pressing could be accomplished at a minimum temperature of 1450°C at pressures of about 28 MPa. Generally, densification stopped after about 40 minutes at temperature. Typical densities obtained were in excess of 98% of theoretical in the bulk of the specimens. This is attributed to particle sliding and rearrangement upon application of pressure. Further, the reducing conditions suppress the volatility of Cr thus enabling the densification process. Figure 8 shows the strain rate as function of temperature. The curve shows two densification regimes at about 1200°C and at 1500°C . XRD of the surface of the as hot pressed specimens revealed the presence of additional phases such as La_2O_3 , and the complex carbide Cr_{23}C_6 . XRD of the bulk of the hot pressed specimens did show peaks attributable to LaCrO_3 alone suggesting that the LaCrO_3 may have

reacted with graphite at the surface only. Examination of the microstructure for phase composition using EPMA revealed some La enrichment associated with pores both in the bulk as well as at the surface. Long term exposure of such hot pressed specimens to ambient air at room temperature caused the surface to form a powdery film which was identified by XRD as $\text{La}(\text{OH})_3$. Eventually, these specimens disintegrated. These latter observations support the XRD results.

The phase assemblage in hot pressed specimens can be understood by considering the thermodynamic stability of LaCrO_3 during the hot pressing process. The oxygen activity in the hot-press is controlled by C/CO equilibrium given by the reaction:



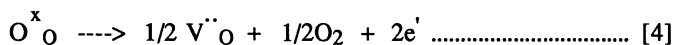
The equilibrium oxygen partial pressures for reaction [2] are plotted in Figure 9. Also plotted are the oxygen partial pressures for reaction [3] as below:



Although thermodynamic data for Sr-doped LaCrO_3 are not known, reaction of LaCrO_3 to form the complex Cr carbide phase appears to be favored under the experimental condition used. The reaction pathway is difficult to predict in the absence of available thermodynamic data. Based on the present results it appears likely to proceed directly by the carbothermal decomposition of LaCrO_3 to form the carbide phase at the surface. Figure 10(a) shows the microstructure of a hot-pressed specimen exhibiting high density in the bulk and surface porosity at the graphite/ ceramic interface. In Figure 10(b), the light contrast specks seen in the micrograph confirm the presence of Cr rich inclusions in the bulk. From the EPMA results the normalized Cr/C molar ratio can be calculated to be 1.7:1. This could result from a mixture of Cr and Cr-carbides or a mixture of Cr carbides of differing stoichiometry ranging from 1.5:1 to 3.83:1. A La/Cr molar ratio about 2:1 was detected in association with these Cr rich areas, suggesting that La_2O_3 lies in the vicinity of the Cr-rich inclusions. The possibility that LaCrO_3 could dissociate to form La_2O_3 and Cr_2O_3 with a simultaneous reaction to

form Cr_2C_6 may not be discounted. In iso-structural compounds such as Sr-doped LaMnO_3 as well as spinels such as MgCr_2O_4 such dissociations are well documented.

Conductivities of the as hot pressed surface, measured at room temperature by the Van-der Pauw method, indicated that the conductivity was about two orders of magnitude below that of specimens sintered in air. This degradation is due to the surface reactions of LaCrO_3 with the graphite die hardware. On grinding off this surface layer, the conductivity was measured to be lower compared to specimens sintered in air. This is readily understood by considering that in low activities of oxygen, the defect structure of p-type LaCrO_3 will be dominated by oxygen vacancies with charge compensation given by:



On annealing these hot pressed specimens at 1000°C in air for about 8 hours, the conductivity recovered to values similar to that of specimens sintered in air. This is consistent with the microstructural observations. However, after annealing, the specimens warped presumably due to volume expansion of the lattice caused by oxygen uptake. This caused micro-cracking in the ceramic especially in ribbed interconnects with integral flow-fields. This is not surprising since differential stresses caused by volume expansion will be greater at regions where the cross-section of the ceramic changes.

These results suggest that the defect structure of hot pressed specimens is dominated by effects of oxygen non-stoichiometry in the LaCrO_3 lattice. Even if the interconnect material is "reduced" during hot pressing, the amount of La_2O_3 and Cr_2O_3 phases present in the microstructure are below detectable limits of XRD and ,in any case, do not affect conductivity. The effects on long term stability are currently unknown and are being assessed by in-cell tests.

Conclusions

Powder compacts of Sr doped LaCrO_3 can be sintered to high densities with closed porosities by incorporating liquid formers such as MgF_2 . The benefit of such liquid formers is difficult to realize for thin tape cast bodies, where a porosity gradient is formed with the surface layers having greater porosity. The volatility of Cr appears to be the main factor inhibiting densification of such structures.

Hot pressing was used primarily as a method of obtaining fine grained well sintered specimens of near theoretical density and as a tool to study sinterability of LaCrO_3 ceramics. While the technique is cumbersome and most likely not commercially viable for fabrication of SOFC interconnects, sinterability was shown to be greatly enhanced by the combined use of reducing atmospheres and pressure. The reaction products with graphite are localized at the surface of the ceramic and the graphite die interface and do not affect the conductivity after removal of the surface layers by grinding and annealing in air. The phase assemblage in the bulk of hot pressed LaCrO_3 ceramics can be controlled to give oxygen deficient LaCrO_3 . The conductivity can be as high as air sintered specimens after annealing in air. However, stresses arising from differential expansion can cause microcracking of interconnects, especially those with integral flow fields.

Acknowledgements

The authors wish to thank the Gas Research Institute for supporting this research. Discussions with Prof. A. Virkar, Dept. of Materials Science and Engineering, Univ. of Utah and Prof. H. Anderson, Dept. of Ceramics Engineering, Univ. of Missouri, Rolla are also acknowledged.

References:

- 1) L. Group and H.U. Anderson, J. Am. Cer. Soc. 59, No.9-10, 449, (1976).
- 2) D.B.Meadowcroft, Brit. J. Appl. Phys. D2, 1255 (1969).
- 3) B.K. Flandermeyer et al., Fuel Cell Seminar Abstracts, p.68, (1986).
- 4) V.L.Balkevich, A.V. Satanovskii, Yu. M. Mosin, V.E.Sotnikov and M.V.Andrianov, (Trans. from Russian), Steklo i Keramika, No. 12, 16,. (1981).
- 5) H.U. Anderson, private communications.
- 6) M. Pechini, U.S. Patent No:3,330,697, July 11, 1967.
- 7) R. Berjoan, Rev. Int. Hautes Temp. Refract., 13, [2], 119 (1976).
- 8) J.B.Webb, M. Sayer and A. Mansingh, Can. J. Phys. 55, 1725, (1977).
- 9) B.K. Flandermeyer, M.M. Nasrallah, A.K. Agarwal and H.U. Anderson, J. Am. Cer. Soc., 67, 1951, (1984).
- 10) D. Caplan and M. Cohen, J. Electrochem. Soc., 108, [5], 438,(1961).

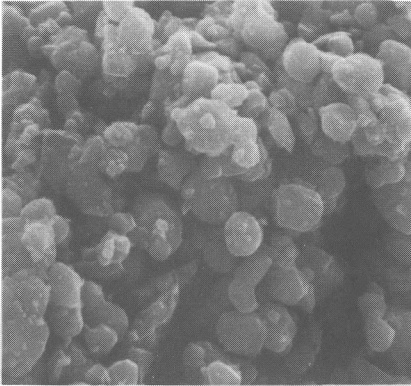


FIGURE 1(a) - TYPICAL MORPHOLOGY OF $\text{La}_{0.9}\text{Sr}_{0.1}\text{CrO}_3$ CALCINED AT 800°C AND MILLED IN ETHANOL FOR 6 HRS.

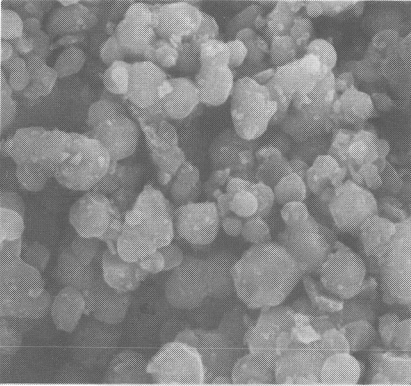


FIGURE 1(b) - POWDER MORPHOLOGY OF $\text{La}_{0.9}\text{Sr}_{0.1}\text{CrO}_3$ CALCINED AT 800°C AND MILLED IN ETHANOL FOR 8 HRS.

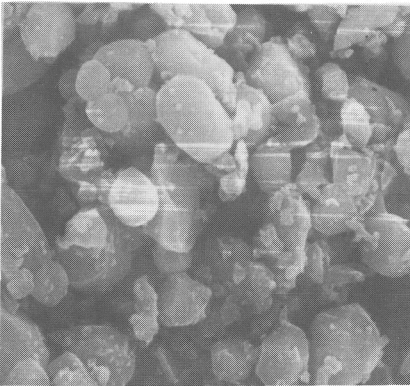


FIGURE 1(c) - POWDER MORPHOLOGY OF $\text{La}_{0.9}\text{Sr}_{0.1}\text{CrO}_3$ CALCINED AT 800°C AND MILLED IN ETHANOL FOR 24 HRS.

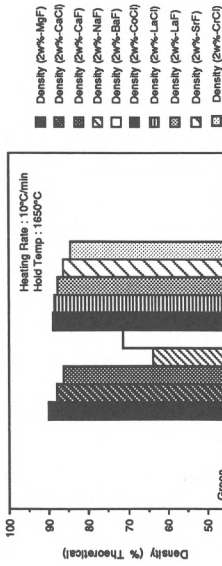


FIGURE 2 - FIRED DENSITY FOR SELECTED SINTERING AIDS

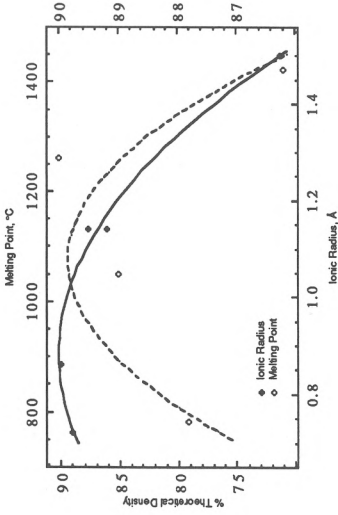


FIGURE 3 - DENSITY VARIATION AS A FUNCTION OF DOPANT MELTING POINT AND ION SIZE

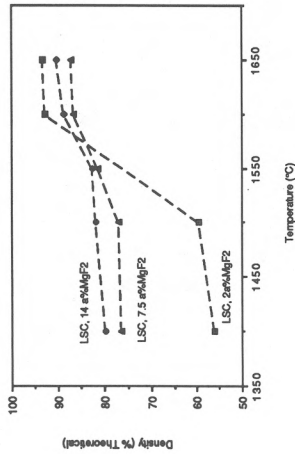


FIGURE 4 - EFFECT OF MgF₂ CONCENTRATION ON FIRED DENSITY OF LSC

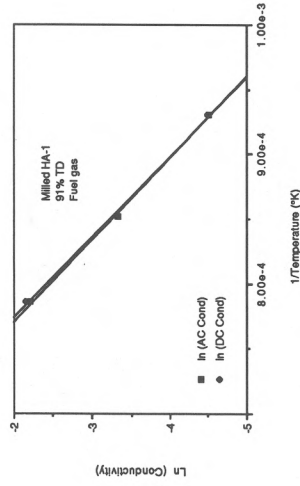


FIGURE 5 - CONDUCTIVITY OF LSC AS A FUNCTION OF TEMPERATURE

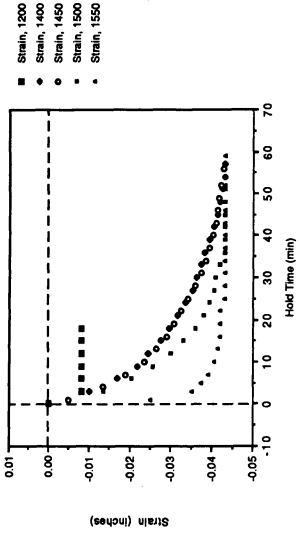


FIGURE 7 - DENATIFICATION STRAIN RATES FOR ISOTHERMALLY HOT PRESSED LSC

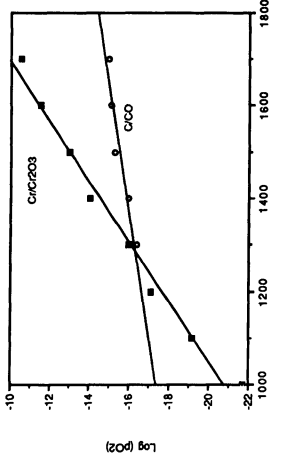


FIGURE 9 - EFFECT OF TEMPERATURE ON THE EQUILIBRIUM OXYGEN PARTIAL PRESSURE OF C/CO AND C/CO₂

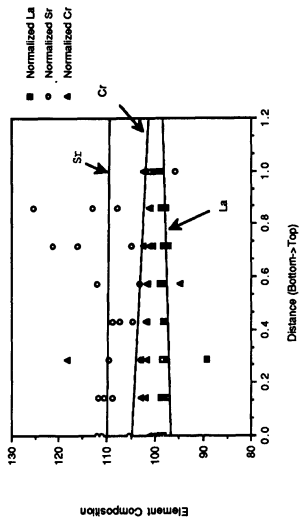


FIGURE 6 - ELEMENTAL COMPOSITION VS. CROSS SECTION FOR AIR FIRED LSC.

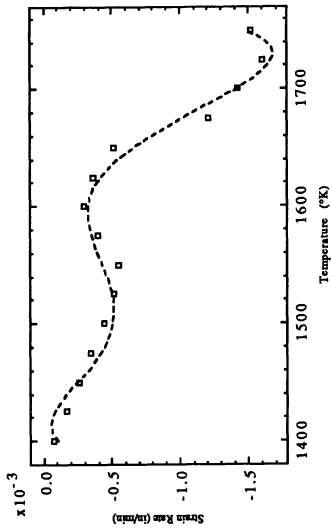


FIGURE 8 - STRAIN RATE AS A FUNCTION OF TEMPERATURE FOR NON-ISOTHERMALLY PRESSED LSC

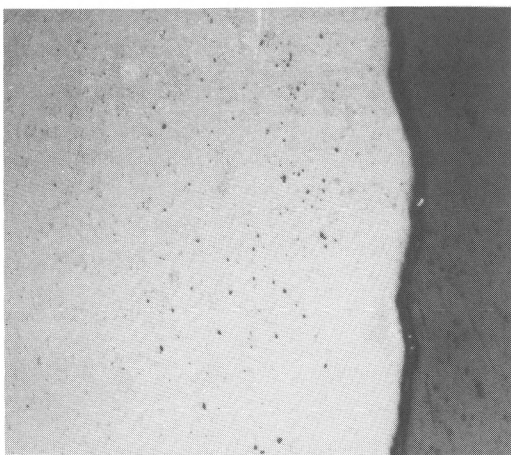


FIGURE 10(a) - MICROGRAPH OF HOT PRESSED LSC SHOWING DENSITY GRADIENTS AND SURFACE REACTION LAYER (133X)

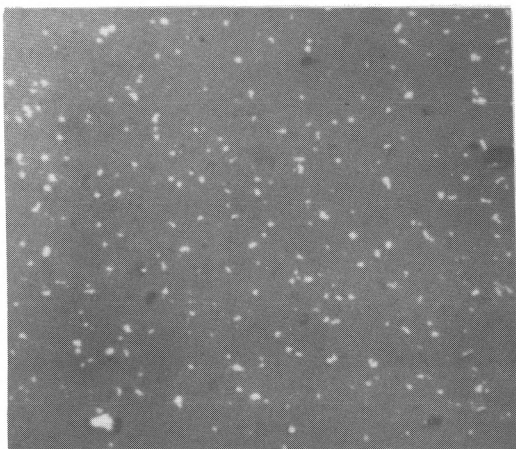


FIGURE 10(b) - MICROGRAPH OF HOT PRESSED LSC SHOWING Cr RICH INCLUSIONS (LIGHT CONTRAST SPECKS, 1330X)

ELECTRODE PERFORMANCE AT PLANAR SOFC INTERFACES

Ashok C. Khandkar, Kevin L. Stuffle
and
S. Elangovan

Ceramatec, Inc.
2425 South 900 West
Salt Lake City, Utah 84119

Abstract

Development of planar geometry Solid Oxide Fuel Cells has received increasing attention recently due to their ability to perform at very high efficiencies as a high power density energy conversion device. Low cost fabrication techniques of planar SOFC devices are an added attractive feature. In order to derive the maximum performance it is necessary to achieve good interfaces between the electrolyte and the electrodes. Characterization of planar SOFC interfaces thus becomes necessary to optimize the fabrication methodology. In the present study the electrode/electrolyte interfaces are characterized by ac impedance spectroscopy. Single cell performance characteristics are correlated to interface characteristics which were observed to be a function of fabrication methods. Scanning Electron Microscopy of the interfaces with various fabrication techniques are currently underway. A quantitative model is being developed.

Introduction

Planar SOFCs offer the potential for high efficiency, high power density energy conversion devices. In addition, the current processing technology to fabricate planar cells is fairly

inexpensive. In this process the electrodes are applied to a predensified zirconia electrolyte and fired at a temperature high enough to effect bonding but prevent the formation of deleterious interface reaction products. This process provides for intermediate inspection of electrolytes before the electrode/electrolyte sub-assembly is fabricated. It also eliminates co-sintering of materials of different sintering characteristics and has the potential of maintaining the electrode morphology required for efficient electrode kinetics. However, the various available techniques for application of electrodes may lead to varying electrode morphology and interfacial characteristics. Understanding performance characteristics of SOFCs requires correlation of morphological characteristics of electrodes with electrical properties of cell components as well as various intercomponent interfaces that connect them. This would then enable one to optimize the fabrication process to achieve high performance planar SOFCs.

Electrolyte/electrode interfaces in SOFCs represent an abrupt change in conduction mechanism, from ionic conduction in the electrolyte to electronic or mixed conduction in the electrode. Heterogeneous charge transfer across such interfaces causes loss of efficiency in an electrochemical system(1). In order to achieve fast electrode kinetics, it is essential for the electrodes to be well bonded to the electrolyte. Such well bonded interfaces usually result in linear I-V curves dominated by ohmic polarization losses(2). However, application of porous electrodes on to a densified zirconia electrolyte by methods such as screen printing or slurry coating followed by high temperature bonding often leads to poor interfacial bonding at the microscopic level. This phenomenon often manifests at the anode/electrolyte interface largely due to high thermal expansion mismatch between Ni/ZrO₂ anode and the ZrO₂ electrolyte. Earlier studies have shown that the interface morphology plays an important role in dc polarization characteristics of solid electrolytes(3,4). In the present study, the dc polarization characteristics of planar single cells were observed to be dependent upon the interfacial characteristics.

EXPERIMENTAL

AC impedance spectroscopy(5-8) was used to characterize the electrode interfaces in planar SOFCs under fuel cell operating conditions. The impedance spectra were analyzed using Nyquist as well as Bode plots to identify the impedance contribution from the electrode interfaces. Current-Voltage performance curves were also obtained as a function of temperature. Solartron 1250 FRA and 1286 ECI were used in obtaining ac and dc characteristics of the cells.

Two different techniques were used to obtain varying bonding characteristics between the electrode (anode) and the electrolyte. The first technique is screen printing of electrode slurries on to the electrolyte with subsequent firing. The other improved technique provides superior bonding due to better bonding of the zirconia of the anode cermet with the electrolyte.

DISCUSSION

In the development of planar cells, a very interesting feature in cell I-V characteristics was observed. A non-linear 200-400 mV polarization drop, similar to an activation polarization behavior of low temperature cells, was observed at low current densities (see Figure 1). Beyond this threshold current density, the I-V characteristics were linear with a slope that corresponds to the ohmic i-R losses. This behavior however is not unique to planar SOFCs and other developers of SOFCs have reported similar behavior (9). In a computer simulation of SOFCs, Dunbar et al. (10) assumed an activation polarization at low current densities and employed the Tafel equation to characterize the non-linear segment of the I-V curve in the cell performance data provided by Westinghouse. However, at the operating temperatures of SOFCs (~1000° C) losses due to activation polarization are expected to be negligible (see the references cited in 10).

Further study into the origin of this steep polarization drop was found to be very instructive in correlating interfacial morphology with observed dc and ac response characteristics of

planar cells. This behavior is attributed to poor electrode interface, especially the anode/electrolyte interface. The complex impedance spectrum indicated a high interfacial resistance (Figure 2). Conversely, at anode/electrolyte interfaces with good bonding characteristics, the interfacial component is small (figure 3) and the I-V characteristics indicate a smaller non-linear region (Figure 4). Figure 5 Shows the I-V behavior of the well bonded cell at 1000° C exhibiting a very small non-linear region.

The significant difference observed in dc polarization curves of various cells at low current densities can thus be attributed to variations in anode/electrolyte interface. A poorly bonded interface between the anode and the electrolyte constitutes a sudden decrease in reaction area across the interface for reduction of oxygen ions. This requires focussing of the oxygen ions towards a narrower anode/electrolyte interface for the charge transfer reaction and spreading of electrons in the anode. The resistive component due to focussing and spreading of conducting species may change as a function of current density introducing non-linearity in the I-V characteristics. Furthermore, the poor electrode/electrolyte contact would contribute a capacitive reactance to the interfacial component. Thus, the nature of interface is expected to play a major role in the dc polarization behavior. A quantitative model is being developed to explain this behavior.

ACKNOWLEDGEMENT

The authors wish to thank the Gas Research Institute for supporting this research.

REFERENCES

- (1) J.R. Macdonald, ed., Impedance Spectroscopy, John Wiley & Sons, NY (1987).
- (2) S.S. Penner, ed., Assessment of Research Needs for Advanced Fuel Cells, DOE/ER 30060-T1, July 1985.
- (3) T.M. Gür et al., J. Electrochem. Soc. 127, 2620 (1980).

- (4) T.M. Gür and R.A. Huggins, *J. Applied Electrochem.* **17**, 800 (1987).
- (5) J.E. Bauerle, *J. Phys. Chem. solids* **30**, 2657 (1969).
- (6) M. Kleitz, *Solid State Ionics* **3/4**, 513 (1981).
- (7) J. Sasaki et al., *Solid State Ionics* **3/4**, 531 (1981).
- (8) S.P.S. Badwal et al., *Solid State Ionics* **9/10**, 973 (1983).
- (9) J.T. Brown, Presentation at EPRI Workshop No. 13, Palo Alto, CA, August 1986.
- (10) W.R. Dunbar, R.A. Gaggioli, Paper no. 889203, *Proceedings of 23rd IECEC Conference Volume II*, Denver, Co, July 31, 1988.

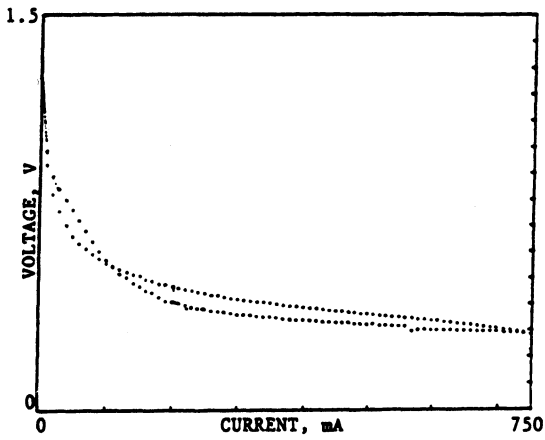


Figure 1. I-V Characteristics of Weakly Bonded Electrode (Temperature 900° C, Cell Area 5 cm²)

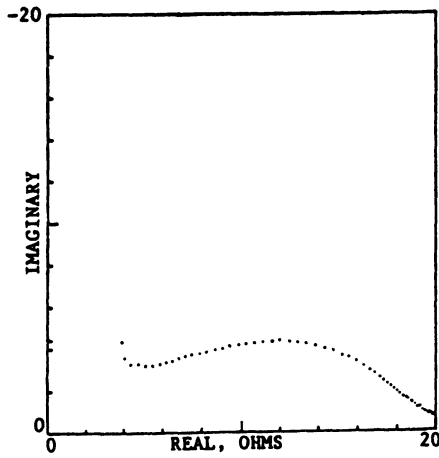


Figure 2. AC impedance Spectrum of cell in Figure 1

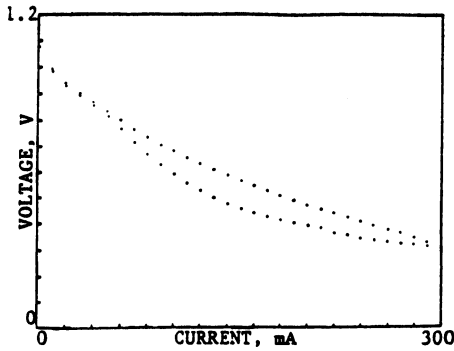


Figure 3. I-V Characteristics of Well Bonded Electrode (Temperature 900° C, Cell Area 5 cm²)

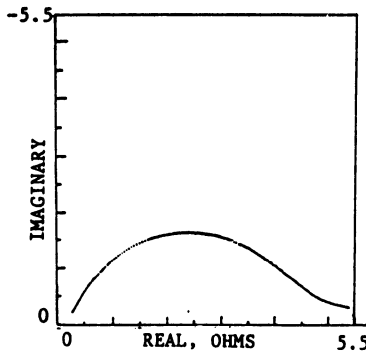


Figure 4. AC impedance Spectrum of Cell in Figure 3

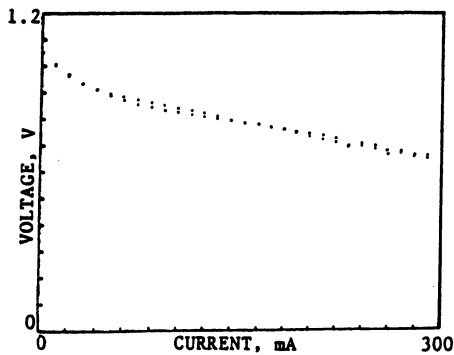


Figure 5. I-V Characteristics of Well Bonded Cell at 1000° C

GENERAL

PRESENT STATE OF SOFC IN JAPAN

Tetsuo Yazawa
Glass and Ceramic Department
Ministry of International Trade and Industry
Government Industrial Research Institute
Osaka, Japan

ABSTRACT

This review deals with the present state of solid oxide fuel cells (SOFC) in Japan. In a national project (Moonlight Project), feasibility study on SOFC started in 1989 and will last for three years. National institutes which promote R & D on SOFC are the Electrotechnical Laboratory and the National Chemical Laboratory for Industry; universities are Yokohama National University, Mie University, Kyoto University, Tottori University and Kyushu University; and the companies are Mitsubishi Heavy Industry, Mitsui Engineering and Shipbuilding and the Tokyo Electric Power Company. The research on SOFC operation is promoted in the Tokyo Gas and the Osaka Gas Companies.

1. INTRODUCTION

The R & D on fuel cells by research organizations and industrial firms in Japan has been underway for over 30 years. This R & D on fuel cells accelerated since 1981 when a national R & D program was started in the "Moonlight Project" by MITI (1). In addition, the activities of many industrial companies and organizations contributed to the recent progress in solid oxide fuel cells.

The Agency of Industrial Science and Technology, MITI, started research on fuel cells in Fiscal year 1981 as a part of "Large-Scale R & D Projects for Energy conservation" (Moonlight Project), and it is presently engaged in research mainly on the phosphoric acid and molten carbonate fuel cells, but also on the solid oxide fuel cells. Figure 1 shows the R & D program for developing fuel cell power generation technologies. The fuel cell R & D project is scheduled to be a 15-year program lasting until Fiscal year 1995 and the total R & D budget is estimated to be about ¥57 billion.

In the Moonlight Project, The Electrotechnical Laboratory is engaged in research to develop a 500-MW class solid oxide fuel cell based on a cylindrical configuration. The National Chemical Laboratory for Industry is conducting research to develop a planar type fuel cell in the same project.

Some private corporations are also very active in this field. Tokyo Gas and Osaka Gas Companies signed contracts in 1986 with Westinghouse to purchase 3 kW solid oxide fuel cell generators and have conducted demonstration tests on these generators since November 1987.

Fundamental research on SOFC is being conducted at universities such as Tottori University, Kyoto University, Mie University, Kyushu University and Yokohama National University.

A feasibility study on SOFC power generation system was conducted in FY 1987, and a report on this study published in March 1988 (2). The present status of SOFC research at various organizations is discussed in the following sections.

2. ELECTROTECHNICAL LABORATORY

The Electrotechnical Laboratory started R & D on SOFC in FY 1974; this R & D has continued as part of the Moonlight Project since FY 1981.

Figure 2 shows the cross-sectional view of a solid oxide fuel cell stack developed at the Electrotechnical Laboratory. Materials used in this cell design are:

Electrolyte : $(ZrO_2)_{0.92}(Y_2O_3)_{0.08}$ (YSZ)
Air electrode : $LaCrO_3$, $La_{1-x}M_xCoO_3$, $La_{1-x}M_xMnO_3$ (M = Sr or Ca)
Fuel electrode : Ni, NiO - YSZ
Interconnector : NiAl, $LaCrO_3$
Gas-tight layer: Al_2O_3
Substrate : Calcia-stabilized zirconia or Al_2O_3

Gas-tight films are made by plasma spray and the porous films are made by flame spray or slurry painting method. Laser spray/vapor deposition and chemical vapor deposition using organic precursors are also under development.

Cell and stack performance tests were conducted for solving problems of cell materials and configuration and long-term tests of 1000 hours were conducted for the inspection of chemical reactions between the YSZ electrolyte and the electrode materials. In FY 1986, the 500 W power generation experiment was conducted to evaluate the plasma spray fabrication method and the performance of the SOFC. The specifications for the stacks developed for 500 W test were as follows:

Number of cells connected in series: 15
Unit cell length: 24 mm
Interconnector length: 12 mm

The typical performance of a stack with 4 l/min hydrogen gas flow was as follows:

Open circuit voltage: 0.986 volt per cell
Current density : 140 mA per square cm
Power output : 26.6 W at the cell voltage of 0.8 volt

The 500 W power generation test was conducted with 48 SOFC stacks connected in parallel. At the beginning of the test, the output power of 500 W was obtained at the cell voltage of 0.76 volt and the current density of 63 mA per square cm with hydrogen supply of 190 l/min and air supply of 1100 l/min.

3. NATIONAL CHEMICAL LABORATORY FOR INDUSTRY

The planar type SOFC is expected to be better suited than tubular type SOFC for large scale power plants because of its higher power generating efficiency, higher power density, lower production cost, etc. The National Chemical Laboratory for Industry (NCLI) has focused its research activity on planar type SOFC in the following fields:

- (a) New separator material
- (b) Design and feasibility of internal gas-manifold structure
- (c) Material processing for cells with the above structure

The electrical resistances of the cells were measured with several Ni-Cr alloy separators in air at 1000 C with 100 mA per square cm current. It was found that the electrical resistance of the cell with Inconel-600 separator decreased during 600 hours testing. In this test, the YSZ membrane was reinforced by a framework and the gases sealed by inconel packing and silica cement; the evaluation of this design is presently under progress. Another type of internal gas-manifold was designed for a cell with corrugated lanthanum chromite separator as shown in Figure 3. The processing technology for this design is also presently under investigation.

4. TOKYO ELECTRIC POWER COMPANY, INC.

The Tokyo Electric Power Company, Inc. started investigating fuel cells in 1960's and has already achieved many successes including that in the generation of 4.5 MW electric power by phosphoric acid fuel cells. In 1980's, the company began the study of solid oxide fuel cells; at present, they are working on the development of this type of fuel cell jointly with Mitsubishi Heavy Industries, Ltd.

Their basic research efforts have concentrated on the investigation of cell component materials and their physical properties, methods for forming thin membrane and other flow fields, and trial production of cells. For the time being, these investigations employ tubular multi-cell type cell elements which can be made and evaluated easily in terms of basic technology. In the future, the development activities will focus on producing highly efficient and durable cells by improving

their electrical properties, preventing cracking, peeling and chemical changes, as well as by solving the problems of modularization.

5. MITSUI ENGINEERING AND SHIPBUILDING COMPANY, LTD.

With the aid of the Japan Shipbuilding Industry Foundation, Mitsui Engineering and Shipbuilding Company is currently developing SOFC, which is being considered for the next generation ship propellant power plant, jointly with the Japan Marine Machinery Development Association. SOFC is better suited as a power unit on board a ship because it is all solid state and composed only of ceramic materials. Maintenance of a SOFC is also very easy because there is no fear of outflow of any corrosive liquids as is the case with electrolytes in fuel cells of other types. A SOFC can utilize hydrogen, carbon monoxide and air, and also can tolerate more impurities in these gases than other types of fuel cells. Thus, SOFC is expected to be easy to handle and highly resistant to vibrations and oscillations on board a ship. If a power system composed of SOFC's with a DC motor is employed to propel a LNG ship, then the total weight can be reduced to about 30% of that of a conventional boiler and turbine system. Furthermore, the total volume will be reduced to about 20%.

SOFC's operate at a temperature as high as 1000 C. This high operating temperature helps recover exhaust heat but it also could cause instability of materials and requires the selection of special materials for peripheral parts. It is therefore desirable to lower the operating temperature of a SOFC to accelerate its practical use. The operating temperature of a SOFC is determined by ionic conduction in the electrolyte and reaction kinetics in the electrodes. One objective of this research is to develop a SOFC that can operate at a lower temperature by using a suitable electrolyte material and improving the shape of the electrolyte film.

6. OSAKA GAS COMPANY, LTD.

Osaka Gas Company is interested in solid oxide fuel cell for on-site power generation because of its high electrical efficiency, high temperature exhaust heat and expected long life. They have tested a 3 kW SOFC generator system from Westinghouse Electric Corporation since 1987 to evaluate the state of the art SOFC. After test of the first generator was finished on March 18, 1988, a second generator was placed on test. This second generator has been running since its start-up on March 29, 1988 (2). The generator is shown in Figure 4. The results of the first generation operation were as follows:

Operating period: October 2, 1987 to March 18, 1988
Operating time : 3,012.5 hours
Availability : 97.9%
Average power : 2.02 kW

REFERENCES

1. "The Moonlight Project," (1988), Japan Industrial Technology Association, Japan.
2. "FY 1987 Report on Coal Gas Utilization for High Efficiency of Electric Power Generation," (1988), Nihon Sangyo Kikai Kogyo Kai.
3. "Report of IEA Workshop on Advanced Fuel Cell," (1988), IEA.
4. "Fuel Cell News," (1984 onwards), Fuel Cell Association.
5. "FC News Letter," (1986 onwards), Fuel Cell Development Information Center, Japan.

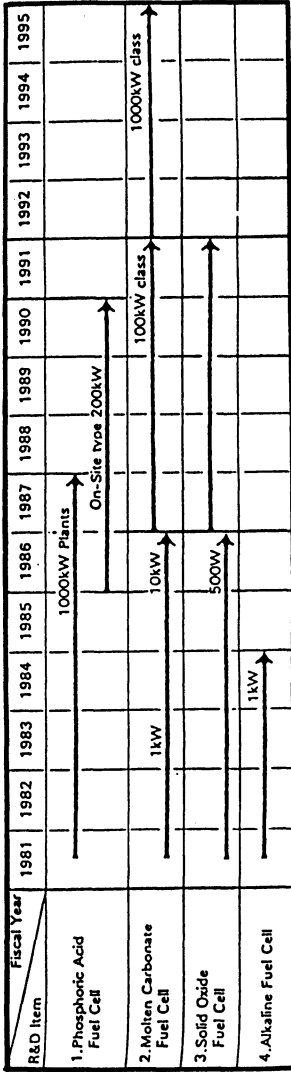


Figure 1. Timetable of the Moonlight Project

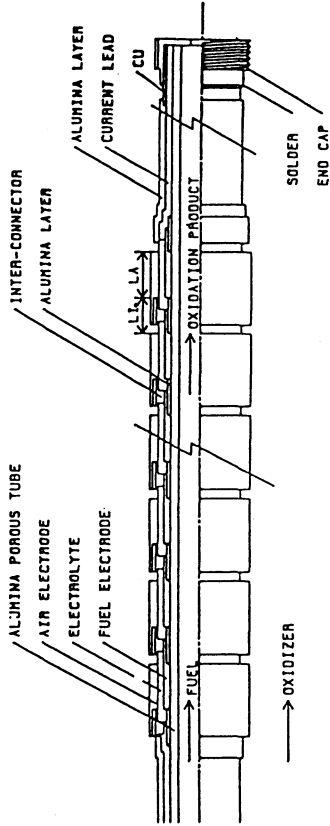


Figure 2. 500 W SOFC generator

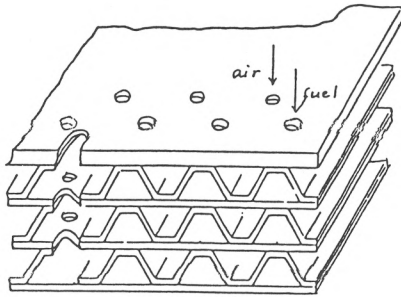


Figure 3. Gas-manifold for corrugated type planar SOFC

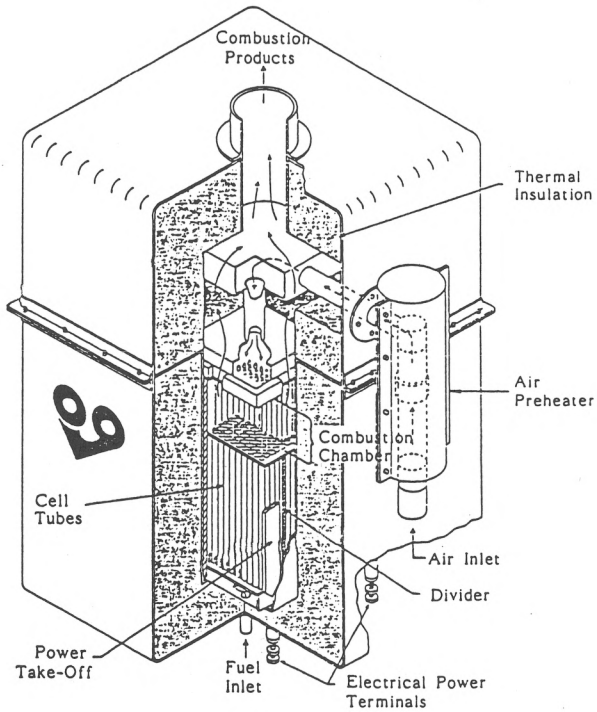


Figure 4. Westinghouse 3 kW SOFC generator

SUBJECT INDEX

- Anode (fuel electrode),
 by flame spraying, 72
 cyclic voltammetry on, 90, 101
 mixed conducting, 81, 99
 morphology, 90
 Ni/zirconia, 90, 129, 280, 308,
 317, 327, 337, 378
 NiO, 188, 288
 Oxidation of CH_4 on, 99
- Bismuth oxide,
 conductivity, 15, 31
 conductivity aging, 19
 differential thermal analysis,
 19
 Er_2O_3 -stabilized, 15
 oxygen kinetics, 15
- Cathode (air electrode),
 Ca-doped LaMnO_3 , 254
 conductivity, 114, 145, 164,
 199, 205, 221, 256
 defect structure, 112
 deposition, 188, 198
 In_2O_3 - $\text{PrO}_{1.83}$ - ZrO_2 , 141
 interactions with zirconia, 242,
 254, 265
 LaCoO_3 , 188, 388
 LaCuO_3 , 157
 LaMnO_3 , 111, 188, 197, 388
 $(\text{La,Sr})(\text{Cr,Mn})\text{O}_3$, 220, 326
 mixed conducting oxides, 81
 morphology, 197, 205, 256
 oxygen diffusion, 214
 Pt additions, 204
 Seebeck coefficient, 116, 146
 sintering, 221
 Sr-doped LaCuO_3 , 157
 Sr-doped LaMnO_3 , 72, 111,
 188, 198, 204, 214, 242, 265,
 280, 308, 388
- stability, 111, 148, 162, 242
 structure, 143, 189, 198, 221
 synthesis, 116, 130, 143, 159,
 205, 221, 243, 255
 thermal expansion, 129, 148,
 163
- Cerium oxide, 31, 100, 288
- Chemical vapor deposition, 41,
 57, 67, 342
- Defect structure
 LaCrO_3 , 112, 370
 LaMnO_3 , 112
 $\text{Gd}_2(\text{Zr}_x\text{Ti}_{1-x})_2\text{O}_7$, 32
 yttria-stabilized zirconia, 46,
 59
- Electrode,
 anode (*see Anode*)
 blocking, 81
 cathode (*see Cathode*)
 interactions with zirconia (*see Interactions*)
 mixed conducting, 81, 99, 141
 performance, 377
- Electrolyte,
 bismuth oxide, 15, 31
 CeO_2 -based, 31, 288
 $\text{Gd}_2(\text{Zr}_x\text{Ti}_{1-x})_2\text{O}_7$, 30
 pyrochlore structure, 30
 zirconia-based (*see Zirconia*)
- Glycine/nitrate process, 170
- Ion plating, 288
- Impedance measurements,
 at $\text{La}_{0.6}\text{Ca}_{0.4}\text{MnO}_3/\text{YSZ}$, 254
 in monolithic SOFC, 317
 in planar SOFC, 379
 on Er_2O_3 -stabilized Bi_2O_3 , 17
 on $\text{Gd}_2(\text{Zr}_x\text{Ti}_{1-x})_2\text{O}_7$, 34

- on $\text{ZrO}_2\text{-Y}_2\text{O}_3$, 4
- on $\text{ZrO}_2\text{-Y}_2\text{O}_3\text{-TiO}_2$, 83
- Interaction,
 - at $\text{La}_{0.6}\text{Ca}_{0.4}\text{MnO}_3/\text{YSZ}$ interface, 254
 - at $\text{LaSrMnO}_3/\text{YSZ}$ interface, 242, 265
 - in monolithic SOFC, 317
 - in planar SOFC, 377
- Interconnection,
 - Al-doped LaCrO_3 , 131, 170
 - conductivity, 116, 221
 - defect structure, 112, 370
 - hot-pressing, 368
 - $(\text{La}_{1-x}\text{Ca}_x)(\text{Cr}_{1-y}\text{Ca}_y)\text{O}_3$, 326
 - LaCrO_3 , 111, 170, 368
 - $(\text{La,Sr})(\text{Cr,Mn})\text{O}_3$, 220
 - Mg-doped LaCrO_3 , 116, 132, 280, 310
 - NiAl, 388
 - Seebeck coefficient, 116
 - sintering, 174, 223, 326, 342, 366
 - Sr-doped LaCrO_3 , 116, 131, 170, 310, 363
 - stability, 112, 132
 - structure, 221
 - synthesis, 116, 130, 170, 221
 - thermal expansion, 129, 179
- Internal reforming, 99, 293
- Lanthanum chromite
 - (see *Interconnection*)
- Lanthanum cobaltite, 188, 388
- Lanthanum cuprate, 157
- Lanthanum manganite,
 - (see *Cathode*)
- Laser evaporation, 71
- Liquid-mix process, 34, 116, 221, 363
- Mixed-conducting oxides, 30, 81, 99, 141
- Monolithic solid oxide fuel cell,
 - design, 307
 - fabrication, 308
 - interfacial effects, 317
- NiAl, 388
- Planar solid oxide fuel cells,
 - bipolar plate for, 339
 - design, 340
 - electrode performance in, 377
 - fabrication of, 328, 337, 361
 - materials for, 325
 - performance of, 377, 389
- Plasma spraying, 71, 288, 341
- Pyrochlore, 30
- Seebeck coefficient, 116, 146
- Sulfur, 312, 337
- Thermal expansion, 129, 148, 163, 338, 378
- Thermogravimetric analysis, 162
- Tubular solid oxide fuel cell,
 - design, 41, 280, 288, 293, 388
 - partial pressures distribution, 294
 - performance, 280, 289
 - temperature distribution, 293
 - voltage stability, 283
- Zirconia
 - aging, 30
 - alumina addition, 3
 - bending strength, 4
 - calcia-stabilized, 280
 - chemical vapor deposition, 41, 57, 67, 342
 - conductivity, 5, 35, 41, 73
 - defect structure, 46, 59
 - detonation spraying, 71

electrochemical vapor
 deposition, 41, 57, 67, 280
grain size, 3
growth kinetics, 43, 57
laser evaporation, 71
oxygen semi-permeability, 49
partially-stabilized, 188
plasma-spraying, 71, 288
titania addition, 81
vacuum evaporation, 189
V-I characteristics, 6, 73
yttria-stabilized, 3, 30, 41, 57,
 67, 71, 215, 242, 265, 280,
 288, 293, 308, 317, 337, 388

AUTHOR INDEX

Anderson, H.U.	111, 129, 220	Middleton, P.H.	90
Arai, H.	288	Mihara, H.	71
Balachandran, U.	317	Milliken, C.	361
Bates, J.L.	141, 170	Minh, N.Q.	307
Belzner, A.	214	Mizusaki, J.	254
Bentzen, J.J.	99	Mogensen, M.	99
Burggraaf, A.J.	67, 197	Moon, P.K.	30
Chick, L.A.	170	Mori, M.	325
de Haart, L.G.J.	67, 197	Nakagawa, H.	71
de Vries, K.J.	67, 197	Namikawa, T.	188
Dees, D.W.	317	Pal, U.B.	41
Dekker, J.P.	57	Pederson, L.R.	170
Dokiya, M.	325	Picciolo, J.J.	317
Dorris, S.E.	317	Priestnall, M.A.	157
Eguchi, K.	288	Sakai, N.	325
Elangovan, S.	377	Sakurada, S.	3, 204
Griffin, C.W.	141	Sato, Y.	71
Gur, T.M.	214	Sawata, A.	254
Hammou, A.	265	Schilling, D.P.	129
Hammouche, A.	265	Schoonman, J.	57
Heiberger, J.J.	317	Seiersten, M.E.	90
Horne, C.R.	307	Setoguchi, T.	288
Howard, S.A.	220	Siebert, E.	265
Huggins, R.A.	214	Singhal, S.C.	41
Inoue, T.	288	Sparlin, D.M.	111, 220
Ishizaki, F.	3	Srilomsak, S.	129
Itoh, H.	288	Staszak, P.R.	307
Iwata, T.	325	Steele, B.C.H.	90, 157
Jiang, N.	15	Stevenson, D.A.	15
Kanamura, K.	293	Stillwagon, T.L.	307
Kanno, R.	242	Stuffle, K.L.	377
Kawada, T.	325	Tagawa, H.	254
Khandkar, A.	361, 377	Tai, L.W.	337
Kissinger, H.E.	170	Takeda, Y.	242
Kiwiet, N.J.	57	Takehara, Z.	293
Kleitz, M.	265	Tenmei, H.	188
Klemm, K.A.	337	Tsuneizumi, H.	71
Koc, R.	220	Tsuneyoshi, K.	254
Kojima, T.	242	Tsunoda, A.	204
Kosuge, S.	71	Tuller, H.L.	30
Kuipers, R.A.	197	Van Ackeren, J.J.	307
Kuo, J.H.	111	Wachsman, E.D.	15
Lessing, P.A.	337	Weber, W.J.	141
Lin, Y.S.	67	Worrell, W.L.	81
Liou, S.S.	81	Yamamoto, O.	242
Liu, F.	307	Yamazaki, Y.	188
Maskalick, N.J.	279	Yazawa, T.	387
Mason, D.M.	15	Yokokawa, H.	325
Matsuda, E.	71	Yoshida, T.	3, 204
McPheeters, C. C.	317	Yoshioka, S.	293
Michibata, H.	188		